Multipapameter Radar Case Studies of the Microphysical and Kinematic Evolution of Lightning Producing Storms

by
Lawrence D. Carey

Department of Atmospheric Science
Colorado State University
Fort Collins, Colorado

Steven A. Rutledge, P.I.
NSF Grant ATM-9015485, ATM-9321361
And CSU-CHILL Cooperative Agreement ATM-8919080
National Science Foundation

Colorado State University

Department of Atmospheric Science

Paper No. 567

MULTIPARAMETER RADAR CASE STUDIES OF THE MICROPHYSICAL AND KINEMATIC EVOLUTION OF LIGHTNING PRODUCING STORMS

by

Lawrence David Carey

Department of Atmospheric Science

Colorado State University

Fort Collins, CO 80523

Research Supported by

National Science Foundation

under Grant ATM-9015485, ATM-9321361 and

the CSU-CHILL Cooperative Agreement ATM-8919080

September, 1994

Atmospheric Science Paper No. 567

ABSTRACT

We examine the co-evolving microphysical, kinematic, and electrical characteristics of a multi-cell thunderstorm and a developing squall line observed during May 1993 along the Front Range of Colorado using data collected with the 10.7 cm, multiparameter, CSU-CHILL Doppler radar. The measured polarimetric variables provide information on the size, shape, orientation, and thermodynamic phase of hydrometeors. Recent modeling and observational advances in weather radar polarimetry now permit the inference of bulk-hydrometeor types and mixing ratios, and the measurement of precipitation rate in mixed-phase (i.e., hail and rain) environments.

In the first case study, we have combined these techniques with dual-Doppler analyses to investigate the correlation between the convective life cycle of a multi-cell storm and the evolution of lightning type and flash rate. The observations suggest a strong correlation between the radar-inferred graupel volume suspended in a vigorous updraft in upper-portions of the storm and the in-cloud (IC) lightning flash rate. Our analyses reveal that maxima in the hail rate are related to peaks in the cloud-to-ground (CG) lightning flash rate. Both correlation's are consistent with the non-inductive charging mechanism which relies on collisions between graupel particles and ice crystals in the presence of supercooled water to separate charge in thunderstorms. Peaks in storm outflow are shown to lag or to be coincident with maxima in both the CG flash rate and hail rate. The fate of ice in this storm was also related to the strength and polarity of the electric field through observations of a Field Excursion Associated With Precipitation (FEAWP) and a

subsequent microburst. We demonstrate that the FEAWP was coincident with the descent of graupel below the charge reversal level consistent with the non-inductive charging mechanism, and that the further descent of graupel below the melting level aided in the generation of a microburst near the surface. Using observations of the FEAWP, we present a comparative speculation between the microphysics of the associated lower positive charge center and the applicability of the reviewed laboratory charging studies.

In the second case study of a developing squall line, multiparameter radar observations and dual-Doppler analyses further support the correlation between ice processes and lightning type and frequency. We present observations of positive differential reflectivity, Z_{dr}, columns which formed in response to a low-level updraft within convergence along the squall line gust front. Using multiparameter radar data, we infer the presence of mixed phase precipitation, or a mixture of supercooled rain drops and wet ice, suspended within these columns above the freezing level. We argue that the source of these large supercooled drops was the result of the recycling of melted graupel into the vigorous low-level updraft. Unique observations of a local minimum in the correlation coefficient collocated with a maximum in the reflectivity and specific differential phase at the top of the positive Z_{dr} column are presented. We suggest that this was a region of high liquid water content consisting of supercooled drops, wet frozen drops, and rapidly growing hail. We demonstrate that the emergence of the Z_{dr} columns within the developing squall line was coincident with the rapid increase in both the IC and CG lightning flash rates. This correlation is attributed to 1) the prodigious hail producing capabilities of these columns, 2) the increase in the updraft velocity caused by latent heat release associated with the freezing of drops, and 3) favorable conditions for ice multiplication processes.

ACKNOWLEDGMENTS

I would like to thank my advisor Dr. Steve Rutledge for the expert guidance that he has given to me over the last two years. I thank Dr. Graeme Stephens and Dr. Raymond Robinson for being on my graduate committee. I would like to thank the entire CSU-CHILL staff for their assistance in obtaining the multiparameter radar data and installing the flat plate antenna and corona point sensor. Specifically, I would like to recognize Dave Brunkow for his expert software support and Pat Kennedy for his aid in planning the scanning strategies for this project and his insight into polarimetric radar data processing. I thank Mr. Bob Rilling of NCAR/ATD for making MHR data available to me, Mr. Kelly Dean of CIRA for providing Front Range mesonet data, Mr. Steve Finley for supplying upper-air and surface data, and Ms. Glenda Wahl of NOAA/FSL for furnishing LLP data. I would also like to thank Dr. V. N. Bringi and Ms. Shanthala Mudegowda of the CSU Department of Electrical Engineering (CSU/EE) for their insight into the impact of sidelobes and antenna-pattern mismatch on polarimetric data. I am thankful to Dr. V. Chandrasekar also of CSU/EE for allowing me to borrow the flat plate antenna. I am grateful to Dr. Dusan S. Zrnic and Dr. Earle Williams for their invaluable suggestions on several aspects of this research. I also thank Dr. Williams for supplying the corona point sensor. I am deeply grateful to "the group" for their friendship, encouragement, and advice over the last two years: Lisa Berg, Doug Burks, Rob Cifelli, Charlotte Demott, Tom Rickenbach, Walt Petersen, Terry Schuur, and Jamie Scott. Finally, I thank my wife and best friend, Shawna Fox, for her support, patience, encouragement, and love. This research was supported by the National Science Foundation under the grant ATM-9015485 and the CSU-CHILL Cooperative Agreement ATM-8919080.

TABLE OF CONTENTS

LIST OF TABLES

LIST OF FIGURES

CHAPTER 1

INTRODUCTION

1.1 Background Motivation

Significant advances in the discrimination of precipitation type and in the estimation of precipitation rates in mixed-phase environments using multiparameter radar data have occurred in recent years. Some of the most successful techniques have been developed with polarization diverse radars, featuring alternating polarization states which are most commonly horizontal and vertical. The additional information provided by polarization diverse radars allows measurement of important hydrometeor characteristics such as particle size and shape, spatial orientation, and thermodynamic phase.

This information has been used for the identification of mixed-phase hydrometeors (Zrnic′ et al., 1993a), estimation of rain and hail rates in mixed-phase precipitation (Sachidananda and Zrnic′, 1987; Balakrishnan and Zrnic′, 1990a), the detection of hail and discrimination of its size (Bringi et al., 1986a; Aydin et al., 1990; Balakrishnan and Zrnic′, 1990b), and the discrimination of ice forms (Zrnic′ et al., 1993a). Much of the knowledge obtained from these and other studies have been used to form an algorithm to deduce bulk-hydrometeor types and amounts from multiparameter radar data as presented in Doviak and Zrnic′ (1993) and Straka and Zrnic′ (1993). Recently, Zrnic′ et al. (1993a) applied this algorithm to deduce particle types and mixing ratios in a severe hailstorm. Although polarimetric signals are sometimes not unique, the simultaneous use of all available multiparameter variables in combination with knowledge of the melting level can provide significant insight into the type and amount of precipitation that is not available from co-polar reflectivity alone. Multiparameter techniques have been used to reveal the evolution of some hydrometeor types in convective storms (e.g., Wakimoto and Bringi,

1988; Tuttle et al., 1989; Herzegh and Jameson, 1992; Conway and Zrnic', 1993) and in stratiform precipitation (e.g., Herzegh and Jameson, 1992; Zrnic' et al., 1993b; Zrnic' et al., 1994).

In this study, we use these multiparameter techniques cast within the framework of dual-Doppler derived flow fields to investigate the integrated microphysical, kinematic, and electrical evolution of deep convection along the Front Range of Colorado. As noted by Goodman and Raghavan (1993), few detailed case studies have examined these co-evolving properties of deep convection, especially along the Front Range. Earlier studies (e.g., Goodman et al., 1988; Williams et al., 1989a) suggest a strong correlation between the convective life-cycle of storms and lightning type and frequency. Goodman et al. (1988) demonstrated that lightning activity is strongly related to echo volume in the mixed-phase region of storms. Williams et al. (1989a) found regular relationships between the stage of convective growth and the lightning type (in-cloud vs. cloud-to-ground). Based on their observations, Williams et al. (1989a) hypothesized that in-cloud (IC) lightning is associated with the updraft accumulation of graupel and cloud-to-ground (CG) lightning is related to the descent of ice in the storm. This correlation between ice processes and cloud electrification is consistent with laboratory studies of the non-inductive charging mechanism (e.g., Takahashi, 1978; Jayaratne et al., 1983; Saunders et al., 1991) which relies on collisions between graupel and ice crystals (in the presence of supercooled water) to separate charge in thunderstorms.

Utilizing recent advances in multiparameter radar techniques which enable the discrimination and quantification of hydrometeors, we present observations which support the hypothesis that electrification in mid-latitude, deep convection is correlated to ice processes as suggested by laboratory experiments of the non-inductive charging mechanism. Earlier studies using a limited subset of these techniques have provided useful insight into thunderstorm electrification. Using the Z-Z_{dr} pair to indicate ice-phase precipitation, Goodman et al. (1988) found that a rapid increase in lightning flash rates

was immediately preceded by the initial presence of ice during a period of vigorous vertical growth. Similar observations have been reported in the initial findings from the Convection and Precipitation/Electrification (CaPE) experiment conducted in the vicinity of Cape Canaveral, Florida in 1991 (Bringi et al., 1993; Goodman and Raghavan, 1993). Bringi et al. (1993) found that a rapid increase in the in-cloud electric field was associated with the glaciation of a positive Z_{dr} column (indicative of large supercooled drops). In this research, we hope to confirm these initial findings, significantly expand the multiparameter methods used, and thereby provide an improved understanding of thunderstorm electrification.

1.2 Overview of the Data

Data for this thesis were collected during a small, highly focused field project. The primary observational platform was the 10.7 cm, multiparameter, CSU-CHILL Doppler radar. During this project, the CSU-CHILL radar measured the radial velocity (V_r), horizontal reflectivity (Z_h), differential reflectivity (Z_{dr}), differential propagation phase shift (ϕ_{dp}), and correlation coefficient at zero-lag between horizontally and vertically polarized waves $|\rho_{hv}(0)|$. Additional instruments located at the CSU-CHILL site included a flat plate antenna, used to measure the total lightning flash rate, and a corona point sensor, configured to measure the electrostatic field strength and polarity of nearby charge structures. Cloud-to-ground (CG) lightning flash rates and ground strike positions were provided by a network of three magnetic direction finders (DF's) of medium-high gain. In-cloud lightning (IC) rates were determined by subtracting the CG rates from the total lightning rate. When appropriate, dual-Doppler observations were obtained by synchronous operations between the CSU-CHILL and the National Center for Atmospheric Research (NCAR) Mile High (10 cm) radars. Collectively, these data are used to correlate the lightning type and frequency, and electrostatic field strength and polarity, to the evolution of storm kinematics (based on single- and dual-Doppler analyses)

and cloud microphysical processes (as inferred from CSU-CHILL multiparameter variables).

In this thesis, we present two detailed case studies of the electrical evolution of deep convection along the Front Range. In the first case study, a multi-cell storm, observations suggest a strong correlation between the radar-inferred graupel storm volume suspended in a vigorous updraft and the IC lightning flash rate. The analyses also reveal that maxima in the hail rate are related to peaks in the CG lightning flash rate and the storm outflow. We also demonstrate that an observed electric field excursion was coincident with the descent of graupel and small hail below the charge reversal level as explained by the non-inductive charging mechanism (Jayaratne et al., 1983). In the second case study, a developing squall line, we confirm the above correlations between the evolution of precipitation sized ice and the lightning type and frequency. We present observations of positive Z_{dr} columns within low-level convergence zones of the developing squall line. We analyze the kinematic and microphysical characteristics of these columns in detail, compare these traits to previous studies, and hypothesize on positive Z_{dr} column origins in this storm. We provide evidence to suggest that these columns are prodigious producers of hail. Lastly, we demonstrate that the emergence of the differential reflectivity columns and the production of large hail is coincident with the rapid increase in the total lightning flash rate to over 30 flashes min^{-1}.

1.3 Scientific Objectives and Organization of the Thesis

The scientific objectives of this research are

1) to provide detailed case studies which examine the morphology of the co-evolving electrical, microphysical, and kinematic properties of deep convection;

2) to provide new insight into and confirmatory evidence for the role of ice in the electrification of deep convection by utilizing the latest multiparameter radar techniques to identify and quantify precipitation sized ice;

3) and to provide further understanding of the origins, microphysical characteristics, and meteorological significance of a particular multiparameter radar signature in developing deep convection, the positive Z_{dr} column.

This thesis is organized into seven chapters. Following this introductory chapter, chapter 2 contains background material on electrification theories and the characteristics of lightning producing storms. We then present an overview of the field project conducted with the CSU-CHILL multiparameter radar in Ch. 3. In Ch. 4, we define the polarimetric radar observables and present the analyses methods used to correlate ice processes to electrification in the two case studies presented. The first case study of the electrical evolution of a multi-cell storm is discussed and analyzed in Ch. 5. The second case study is presented in Ch. 6 where a detailed account of the development of a squall line along the Front Range is given. In addition to correlating ice-phase precipitation to storm electrification, we present and analyze observations of positive Z_{dr} columns within the developing squall line and assess their impact on electrification. Finally, Ch. 7 presents conclusions and recommendations for future research.

CHAPTER 2

ELECTRIFICATION THEORIES AND CHARACTERISTICS OF LIGHTNING PRODUCING STORMS

2.1 Review of Electrification Theories

The physical origin of thunderstorm electrification is an old and, as yet, an unresolved problem. Mechanisms suggested to explain cloud electrification and subsequent lightning in thunderstorms can be grouped into two opposing categories: 1) the precipitation-based theories (non-inductive and inductive), and 2) the convective theory. In this section, we present a brief overview of evidence which suggests that the non-inductive charging mechanism is the most viable theory for explaining the presence of lightning in deep convection, which is the focus of this thesis. For more complete reviews of these theories, we suggest Vonnegut (1963) or Moore (1977) which concentrate on the convective theory and Krehbiel (1986) or Williams (1989) which focus on a precipitation based mechanism for storm electrification.

Many laboratory studies have been conducted to investigate the non-inductive charging mechanism. We present a brief review of one subset of these experiments which suggest that collisions between graupel (or hail) particles and ice crystals in the presence of supercooled liquid water separates sufficient charge to account for recent observations of thunderstorm electrification (Reynolds, 1957; Church, 1966; Takahashi, 1978; Jayaratne et al., 1983; Keith and Saunders, 1990; Saunders et al., 1991) We then discuss possible correlations between the microphysical growth state of riming graupel particles and the sign of the separated charge (Williams et al., 1991, 1994). We survey recent theories put forward to explain the physical mechanism(s) responsible for non-inductive charging. Lastly, we present observational evidence (both in-situ and large scale) that

support the feasibility of the non-inductive charging mechanism. A comprehensive review of non-inductive charging laboratory experiments and theories can be found in Saunders (1994).

2.1.1 Precipitation vs. convective theories

A fundamental issue to thunderstorm research is whether the electrification is caused by the gravitational fall of charged precipitation particles or whether it results primarily from the convective transport of charge by the air motions of the storm. Convective theories for cloud electrification (e.g., Vonnegut, 1953; Wagner and Telford, 1981) invoke the vertical transport of space charge against the local electric field by thunderstorm air motions. Unlike the precipitation-based mechanisms, the electric charge is hypothesized to originate from regions outside of the cloud. According to Vonnegut (1953), there are two sources of electric charge: 1) positive charge from corona emission at the Earth's surface, and 2) negative charge from the conductive atmosphere surrounding the cloud top which is produced by cosmic radiation. In the convective theory, it is suggested that thermals, or warm air currents, carry the positive charge released at the earth's surface to the top of the cloud. The negative charge in the vicinity of the cloud top is attracted to this positive charge and thereby attach themselves to cloud particles, forming a negative screening layer. Downdrafts within the cloud or along the cloud boundary are assumed to transport the negative charge downward, forming a positive dipole, with positive charge situated above negative charge.

However, the convective theory does not adequately explain the observed charge structures in thunderstorms nor does it produce lightning on time scales relevant to a developing thunderstorm (Williams, 1989). Measurements of corona point discharge from the Earth's surface beneath thunderstorms by Standler and Winn (1979) suggest that this current is small compared to the time integrated lightning current. Another problem with this lower source of positive charge is that observations (Standler and Winn, 1979; Markson and Anderson, 1987) do not support a deep vertical column of positive charge

above the Earth's surface as required by the convective theory. Assuming that this source could produce sufficient positive charge to explain the observed upper positive charge in thunderstorms, theoretical calculations by Moore et al. (1983) suggest that the transport time for this positive charge would be too long to account for the first lightning in a developing thunderstorm. The ability of air motions to transport the negative charge contained in screening layers at cloud top to the observed mid-level location in positive dipole thunderstorms is also in question. According to Vonnegut (1953), the negative charge is transported downward in screening layers along the cloud boundary. For this to explain the observed mid-level altitude stability of the negative charge region (Krehbiel et al., 1984), there would need to be convergence at this level in thunderstorms. Observations from 27 thunderstorms in Huntsville, Alabama presented in Williams (1989) suggest that the typical level of mid-level inflow is significantly lower than observed altitudes of the main negative charge. According to Wagner and Telford (1981), the negative charge descends within the central region of developing thunderstorms. As will be shown in this study (Ch. 5 and Ch. 6) and as demonstrated in Lhermitte and Williams (1985), dual-Doppler derived air and particle motions are typically upward in the central portion of developing and mature thunderstorms.

Precipitation based theories can be subdivided into the non-inductive (e.g., Takahashi, 1978; Jayaratne et al., 1983; Saunders et al., 1991) and inductive (Elster and Geital, 1913; Illingworth and Latham, 1977) charging mechanisms. In the induction charging theory, a downward-directed electric field polarizes precipitation particles such that their lower surfaces are positively charged and the upper surfaces are negatively charged (Fig. 2.1a). This downward directed field which is strong enough to polarize precipitation particles may result from the normal fair weather field or could be initially generated by another charging process such as the non-inductive charging mechanism. When hydrometeors (liquid or ice) collide at a moderate angle, the smaller particle which is moving upward in an updraft acquires positive charge while negative charge is transferred to the larger,

downward-moving precipitation particle (Fig. 2.1b). Provided that the particles rebound, gravitational separation of the particles can result in a positive dipole (positive charge center above negative). It should be noted that the induction process is a positive feedback mechanism. As the two charge centers build up, they will reinforce the downward directed electric field within the cloud, increasing the magnitude of the separated charge. However, several researchers (e.g., Gaskell, 1979; Rawlins, 1982) have demonstrated that the inductive charging mechanism alone cannot produce large enough electric fields for breakdown to occur. The primary limitation for colliding ice particles is that the charge relaxation time is much longer than a typical contact time, significantly reducing the amount of charge transferred per collision. There is no such limitation on colliding water drops. Since the electric fields in developing warm rain clouds are typically small (< 1 kV m^{-1}), induction charging is ineffective. As a result, observations suggest that clouds dominated by warm rain processes produce little or no lightning (e.g., Chauzy et al., 1985; Williams, 1985; Rutledge et al., 1992). In comparison to convective and inductive charging theories, the non-inductive mechanism is considered to be a viable charging mechanism for electrification in thunderstorms (Williams, 1989).

2.1.2 Non-inductive mechanism

The non-inductive mechanism is an ice-based charging process. Laboratory experiments have determined that significant charge ($\geq$ 1 fC) is separated during the collision of a graupel particle with a smaller ice particle such as an ice crystal in the presence of supercooled liquid water. The sign and magnitude of the separated charge are a function of temperature, cloud liquid water content, relative particle velocity, and ice crystal diameter. In this section, we present a review of laboratory experiments which involve multiple ice crystal interactions with a riming target (to simulate graupel), a brief survey of recent theories to explain these laboratory results, and a discussion of field observations which suggest that the non-inductive charging mechanism is responsible for the electrification of deep convective storms.

Note that we do not consider two other groups of laboratory experiments because they do not appear to be relevant to the electrification of deep convection. The first group of experiments (e.g., Gaskell and Illingworth, 1980; Avila and Caranti, 1991; 1992) involve single collisions between a riming target and a small (100 μm) ice sphere. These experiments have resulted in primarily positively charged graupel which is at odds with the predominance of negatively charged graupel observed in thunderstorms. The second class of experiments (Findeisen, 1940; Latham, 1963; Rydock and Williams, 1991; Saunders et al., 1993 among others) have investigated the charge transfer when frost is broken off an ice surface during the impact of an airjet, ice crystal, or ice sphere with a frosted ice surface in the absence of supercooled liquid water. These experiments are not necessarily representative of the predominant conditions found in deep convection (i.e., which typically possess significant supercooled liquid water or mixed phase conditions).

2.1.2.1 Laboratory experiments

The non-inductive charging mechanism is based on the results of a series of laboratory experiments beginning with Reynolds et al. (1957). They rotated ice spheres (representing small graupel pellets) through a cloud of ice crystals and supercooled water droplets and measured the charge transferred to the spheres. Their objective was to simulate conditions inside thunderstorms in which falling graupel particles become charged by collisions with ice crystals. They found that riming graupel particles charge negatively at temperatures around -25° C during multiple collisions with ice crystals. Church (1966) conducted similar experiments and determined that the sign of the separated charge on graupel was a function of temperature and liquid water content (LWC). He found that graupel charged negatively at -15° C in low LWC conditions and positively for higher LWC and the same temperature.

Takahashi (1978) extended our understanding of the non-inductive charging mechanism by investigating the dependence of separated charge sign and magnitude on temperature and LWC over a wide range of values. As seen in Fig. 2.2, he found that

graupel charges positively, independently of LWC, at all temperatures above -10° C. Below -10° C, graupel charges negatively for intermediate values of LWC and positively at high and low values of LWC. The magnitude of separated charge per collision in Takahashi's experiment reached up to 40 fC (for negative rimer charge). A similar study was conducted in the Manchester labs by Jayaratne et al. (1983). They determined that the riming target (representing graupel) charged positively at temperatures above a certain value, called the "charge reversal temperature," and negatively below this temperature, while ice crystals separated charge of the opposite sign. This reversal temperature was dependent on cloud LWC and moved to higher (warmer) temperatures with a decrease in LWC (Fig 2.3). Jayaratne et al. (1983) also demonstrated that significant charge ($\geq$ 1 fC) is transferred only in the presence of supercooled liquid water. They found charging rates less than 0.25 fC for collisions in the absence of liquid water and up to 10 fC for those collisions with cloud liquid water present. Keith and Saunders (1990) extended the Manchester studies to larger ice crystal diameters and higher target speeds (representing graupel terminal fall speeds). They determined the mathematical dependence of transferred charge magnitude on rimer speed and ice crystal size. Further work in the Manchester lab by Saunders et al. (1991) investigated the dependence of ice crystal/graupel charge separation on the effective LWC (EW), which represents the fraction of the droplet spectrum captured by the riming target. The negative and positive regions of graupel charging for Saunders et al. (1991) are depicted in Fig. 2.4. The calculated magnitude of charge transfer per separation from Saunders et al. (1991) for experimental conditions similar to Takahashi (1978) reached up to 110 fC (for negative rimer charge).

Given the temperature dependence of the sign of separated charge illustrated in Fig. 2.2 - 2.4, Jayaratne et al. (1983) first suggested the process by which the non-inductive charging mechanism explains the observed charge structure in thunderstorms (see Fig. 2.5). Above the charge reversal temperature (region B) which is typically -10° to -20° C

(Williams, 1989), graupel colliding with small ice crystals in the mixed phase region are charged negatively. The ice crystals which are charged positively are lifted into the upper regions of the storm by updrafts (region C). Meanwhile, the negatively charged graupel remain in a relatively narrow layer (region B) of the mixed phase region defined by the particle balance level, or the level at which the terminal velocity of the graupel equals the updraft velocity (Lhermitte and Williams, 1985; Krehbiel, 1986). In this region, they continue to grow and charge negatively due to collisions with ice crystals. When the graupel particles grow large enough (or the suspending updraft weakens sufficiently), they fall through the level of the charge reversal temperature. In this region (region A), graupel particles charge positively and ice crystals charge negatively during glancing collisions in the presence of supercooled liquid water. The negatively charged ice crystals are carried above the level of the charge reversal temperature by the updraft where they contribute to the main negative charge center (region B). As a result, a net positive charge center is formed in the lower levels of the thunderstorm due to the falling, positively charged graupel particles (region A). The resulting charge distribution (lower positive charge, middle negative charge, and upper positive charge; Fig. 2.5) is in accord with the observed tripole charge structure discussed by Williams (1989).

It is interesting to compare the results of Takahashi (1978) in Fig. 2.2 with those of the Manchester studies (Jayaratne et al., 1983; Saunders et al., 1991) in Figs. 2.3 and 2.4. Given the wide range of experimental conditions and methods, the various laboratory experiments are in broad agreement as to the order of magnitude of the charge separated per collision in the presence of supercooled liquid water (10 - 100 fC). The physical explanation for the required role of supercooled liquid water in the non-inductive charging mechanism discussed above is still an active area of research. In general, supercooled liquid water may be required for significant charge separation during a graupel/ice crystal collision because: 1) cloud liquid water is required to allow the growth of the graupel particle to sufficient size via riming such that the differential terminal velocity between

colliding ice particles is significant, 2) several theories (See Sec. 2.1.2.2) rely on the surface rime characteristics of graupel for a physical explanation of non-inductive charging, and 3) the microphysical growth state of graupel, which has been hypothesized to control the sign and magnitude of non-inductive charging (See Sec. 2.1.2.2), is a function of the cloud liquid water content. Although there are some regions of agreement between the studies as seen in the above Figs., there are significant discrepancies in the sign of the separated charge for a given temperature and LWC between the Manchester results and those of Takahashi (1978). For example, Takahashi (1978) observed exclusive positive charging at temperatures above -10° C while the Manchester group found that the sign of the charge is positive or negative depending on the liquid water content. A second important difference between the two sets of results occurs at intermediate values of LWC (1-4 g m^{-3}). At T = -20° C, the Manchester results show a transition from negative to positive rimer charge at a LWC (or EW in Saunders et al., 1991) of less than 1 g m^{-3} whereas Takahashi's negative charging zone extends up to a LWC of 4 g m^{-3}. A third area of significant discrepancy is the positive charging of the simulated graupel particle at sufficiently high liquid water content to cause wet growth (i.e., LWC > 4 g m^{-3}) in Takahashi (1978). Saunders and Brook (1992) found that under wet growth riming conditions the charge transfer to the target falls to zero. They attribute this result to the complete collection of ice crystals by the wet target. These discrepancies have been attributed to differing experimental methods and laboratory conditions and are the subject of ongoing controversy (e.g., Saunders et al., 1991; Williams and Zhang, 1993; Saunders, 1993; Saunders, 1994; Williams et al., 1994).

2.1.2.2 Theories

In an effort to better understand both the areas of agreement and discrepancy in the above laboratory experiments, theories have been suggested by several authors to explain the physical mechanism(s) responsible for the charging measured in the above experiments. It is important to note that the observed charging in the above experiments

and possibly in thunderstorms could be due to either a single mechanism or two or more competing physical mechanisms. Although a detailed discussion of these theories is beyond the scope of this thesis, we present a brief survey. Critical reviews can be found in Williams et al. (1991) and Saunders (1994).

Williams et al. (1991) compared the laboratory results of Takahashi (1978) with the calculated microphysical growth state of graupel particles associated with the mixed phase region of deep convection. The growth state is defined by the ambient temperature, the cloud liquid water content, and the graupel size and associated terminal velocity. For fixed graupel size and velocity relevant to Takahashi's experiment (D=3 mm, V=9 m s^{-1}), Williams et al. (1991) identified three distinct growth regions based on microphysical calculations in the parameter space of temperature and liquid water content as depicted in Fig. 2.6. At low liquid water contents, vapor deposition is prominent according to the classic Bergeron process (Bergeron, 1935). At intermediate LWC, the graupel particles are warmed sufficiently by riming to minimize deposition and support sublimation. A further increase in LWC to very large values results in riming which is sufficiently vigorous to promote wet growth and evaporation of the liquid water surface. In Fig. 2.6, the two curves delineate these three regions.

Superimposed on these microphysical calculations are the laboratory results of Takahashi (1978) where solid circles indicate negative charging of the rimer (i.e., simulated graupel) and open circles indicate positive charging of the rimer. The broad correspondence between the sign of graupel charge and the microphysical growth state of graupel seen in Fig. 2.6 led Williams et al. (1991) to conclude that graupel charges negatively when in a sublimation state and positively when in both vapor deposition and wet growth. One notable area of significant discrepancy is the region in Fig. 2.6 for cloud temperatures between 0° and -10° C. Williams et al. (1991, 1994) suggest that the large scale observations together with in-situ measurements indicate that the most prevalent growth condition for large ice particles in active convection is sublimation during riming.

This is consistent with large scale electrical observations and in-situ precipitation charge measurements in active convection which indicate that graupel is usually negatively charged (e.g., Williams, 1989), forming the classical positive dipole in thunderstorms (Wilson, 1920). Saunders (1993, 1994) points out that the above correlations between the microphysical growth state of graupel and the sign of separated charge on graupel are not supported by the laboratory results of Saunders et al. (1991).

The riming of an ice surface gives it a negative contact potential relative to an unrimed ice surface, as noted by Caranti et al. (1985). In their experiment, the potential increased with decreasing temperature and reached a steady state of approximately -400 mV at temperatures below -20° C. If (unrimed) ice crystals have a less negative contact potential than riming graupel particles in thunderstorms, then graupel particles will charge negatively during ice crystal collisions, consistent with the positive dipole structure often observed beneath thunderstorms. The magnitude of the charge transfer is a function of the potential difference and the area of contact. Saunders (1994) shows that for a contact area of 100 μm^2, a contact potential of 100 mV, and a separation distance between the surfaces of 1 μm, the charge transfer is on the order of 10 fC in agreement with observations.

Keith and Saunders (1990) suggest that positively charged dislocations in the ice structure may be the source of the charge transfer during ice crystal and graupel collisions. Dislocation concentration within the ice structure depends on the vapor deposition rate (Hobbs, 1974). A rimer (graupel) surface which is growing faster than the ice crystals because of the additional vapor released by the freezing droplets will possess more positively charged dislocations than the ice crystals. As a result, the graupel particle could charge negatively and ice crystal positively by a transfer of these positively charged dislocations during collisions. Keith and Saunders (1990) estimate that for a typical number of positive dislocations per unit area ($5x10^9$ m^{-2}) each having a charge per unit length of $6x10^{-11}$ C m^{-1}, the charge available on an area of 55x55 μm^2 is 50 fC. If this

available charge is transferred during a graupel/ice crystal collision (possibly via a mass transfer), then this mechanism would be sufficient to explain the charge separated in the above experiments. With an increase in LWC or temperature, the droplet freezing time increases and so the rimer dislocation concentration decreases and the associated charging mechanism becomes less effective.

Based on recent ideas of surface melting, Baker and Dash (1989; 1994) derive a theoretical mechanism for the charge transfer between colliding ice and graupel particles. According to this theory, each of these ice particle surfaces is covered by a disordered, or quasi-liquid layer (QLL). The layer wets the solid-vapor interface such that the vapor-QLL-solid system has a lower free energy than the vapor-solid system. The thickness of the QLL can be estimated as a function of the temperature and local curvature. The fundamental premise of their theory is that charge transfer during collisions is associated with a mass transfer, or more specifically a transfer of QLL. They demonstrate that during contact of two ice particles, fluid will flow from the thicker to the thinner layer (i.e., from warm to cold, from regions of high surface curvature to those of smaller curvature, and from regions of high vapor growth to regions of lower growth or evaporation). If the fluid is negatively charged, then this flow would be consistent with the dependence of charge transfer on environmental conditions as observed in laboratory experiments of the non-inductive mechanism. Of the charging theories reviewed by Saunders (1994), he suggests that only the QLL theory can provide charge transfers of both signs as is required by the non-inductive charging mechanism (see Figs. 2.2 - 2.4). The transition from one charging regime to another would be a function of conditions on the riming graupel surface (i.e., temperature and local curvature).

2.1.2.3 Observational evidence

The non-inductive charging mechanism is supported by the following in-situ (airborne and balloon) and remotely sensed (radar, surface-based electric field and lightning measurements) observational studies:

1) In-situ observations of the charges on precipitation particles within thunderstorms have demonstrated that the integrated charge densities are sufficient to explain the observed electric fields (e.g., Gaskell et al., 1978; Marshall and Winn, 1982; Vali et al., 1984; Dye et al., 1986; Weinheimer et al., 1991; and Marshall and Rust, 1991).

2) In-situ measurements of supercooled LWC and ice particle (both ice crystals and graupel) sizes, concentrations, and collision rates within thunderstorms are sufficient to explain thunderstorm electrification via the non-inductive charging mechanism (e.g., Dye et al. 1986; Dye et al. 1988; Weinheimer et al., 1991).

3) In-situ measurements of the vertical charge structure in thunderstorms are consistent with expected temperatures of the main negative charge and the charge reversal temperatures of the various laboratory studies shown in Figs. 2.2 - 2.4 (e.g., Moore, 1976; Winn et al., 1978; Marshall and Winn 1982; Weber et al., 1983; Marshall, 1985; Byrne et al., 1987; Dye et al., 1988; Selvam et al., 1991).

4) Remote measurements (i.e., via analysis of the electric field changes associated with lightning and sounding data) of the inferred temperatures associated with main negative charge in thunderstorms are consistent with the non-inductive mechanism (e.g., Jacobson and Krider, 1976; Krehbiel et al., 1979; Krehbiel, 1981; Maier and Krider, 1986).

5) Observations suggest that clouds dominated by warm rain processes and weak mixed phase regions produce little or no lightning (e.g., Chauzy et al., 1985; Williams, 1989; Selvam et al., 1991; Rutledge et al., 1992).

6) Radar studies demonstrate consistent correlations between the evolution of precipitation structure (as inferred from reflectivity) in the mixed-phase region and the evolution of lightning type and frequency, and the electric field strength and polarity (e.g., Workman and Reynolds, 1949; Lhermitte and Krehbiel, 1979; Lhermitte and Williams, 1984; Goodman et al., 1988; Dye et al., 1989; Williams et al., 1989a;

Williams et al., 1989b; Williams, 1990; Petersen et al., 1993; Kitagawa and Michimoto, 1994; Rutledge and Petersen, 1994).

7) Polarimetric radar studies strengthen the above evidence (6) by specifically demonstrating that precipitation sized ice (i.e., graupel and hail) is highly correlated to the lightning flash rate and electric field measurements of thunderstorms (e.g., Goodman et al., 1988; Bringi et al., 1993; Goodman and Raghavan, 1993).

Since this thesis is a polarimetric radar study of lightning producing storms, we present a brief review of items 6 and 7 in the next section. Williams (1989) presents a comprehensive review of items 1 - 5.

2.2 Electrification and the convective life-cycle

The apparent correlation between the convective life-cycle, as seen in kinematic and microphysical fields, and the evolution of lightning and electric fields in thunderstorms has been well documented. Investigators have found consistent relationships between the stage of the convective growth and the lightning type (IC vs. CG) and polarity of the surface electric field. Similarly, strong correlations have been observed to exist between the vertical extent of storms and the magnitude of the lightning flash rate and surface electric field. Both the electrical and kinematic events in a storm's convective life-cycle can be attributed (to some extent) to microphysical processes involving ice.

The development period for thunderstorms is characterized by strong updrafts which permit ice particles to undergo accretional growth due to the presence of sufficient supercooled liquid water. With the growth of larger ice particles, conditions become favorable for the particle scale separation of charge via the non-inductive charging mechanism. Collisions between large precipitation particles (such as graupel) with smaller ice particles (such as ice crystals) in the presence of cloud liquid water results in negative charge being transferred to the larger particle and positive charge to the smaller particle, since the bulk of these collisions are occurring above the charge reversal level during

periods of vertical growth. Gravitational sedimentation between the two particles results in storm scale separation of negatively charge graupel particles and positively charged ice crystals. Positive charge is then concentrated in the upper portions of the storm by the action of the strong updraft on the small ice crystals. Using triple-Doppler radar data, Lhermitte and Williams (1985) showed that this vertical development is associated with the persistent presence of a particle balance level at nearly constant altitude, characterized by a zero value of the mean precipitation particle vertical velocity. The creation of such a balance level allows the concentration of negative charge carried by the large precipitation particles and can explain observations of the altitude stability of the main negative charge center (Krehbiel, 1986). The final product of particle scale microphysics and cloud scale kinematics during periods of vertical development is the formation of the classic positive dipole with positive charge above negative within the thunderstorm (Wilson, 1920). Once enough charge is concentrated within the two regions, dielectric breakdown can occur and cause an in-cloud lightning flash. In Lhermitte and Williams (1985), this concentration of large precipitation particles was nearly coincident with a negative charge center which participated in IC lightning. Similarly, Lhermitte and Krehbiel (1979) found that the sources of negative charge participating in IC lightning were shown to be approximately collocated with enhanced reflectivity signatures and maxima in the updraft velocity. It is in this way that cloud vertical development can be related to the IC flash rate and the (near-storm) surface electric field.

Several studies (Lhermitte and Krehbiel, 1979; Lhermitte and Williams, 1984; Goodman et al., 1988; Dye et al., 1989; Williams et al. 1989a; and Kitigawa and Michimoto, 1994 among others) have demonstrated that both the sub-cloud electric field and the IC lightning flash rate rise in parallel with the cloud vertical development. As presented in Goodman et al. (1988), Figs. 2.7a-b depict the radar and lightning evolution of an isolated microburst-producing thunderstorm in Huntsville, Alabama collected during the Cooperative Huntsville Meteorological Experiment (COHMEX). The total flash rate

(Fig. 2.7a) increases simultaneously with the emergence of a rising core of reflectivity (Fig. 2.7b) in the mixed phase region (0° C ≥ T ≥ -40° C). Williams (1990) attributes the appearance of this ascending high reflectivity core to the rapid growth of graupel particles in the mixed phase region. Note that the peak in the IC flash rate is nearly coincident with the time of peak vertical development.

Williams et al. (1989a) attribute the increase in the IC lightning flash rate as seen in Fig. 2.7 with the updraft-driven accumulation of charged (via the non-inductive mechanism) graupel and hail in the central dipole region. Williams et al. (1989a) suggest that CG lightning may be initiated by the descent of graupel and hail particles below the height of the main negative charge (-10° C ≥ T ≥ -20° C; Williams, 1989) where the action of charge reversal microphysics causes these large ice particles to charge positively. This lower positive charge center combined with the already established main negative charge region and upper level positive charge region forms the electric tripole often observed in mature thunderstorms (Williams, 1989). This lower positive charge could then result in the electrical bias necessary for a cloud-to-ground discharge to occur.

This hypothesis has been supported by several radar studies of electrified storms. Workman and Reynolds (1949) showed that the first CG flash in a New Mexico thunderstorm occurred several minutes after the descending phase of the radar echo aloft. In a Florida storm, Lhermitte and Krehbiel (1979) found that the onset of CG lightning was well correlated with the initial descent of a 55 dBZ reflectivity core beneath the level of inferred main negative charge. As seen in Figs. 2.7a and b, Goodman et al. (1988) observed six cloud-to-ground discharges from 1914 - 1922, during the descent of a 60 dBZ reflectivity core below the level of inferred negative charge (which is -15° C ≥ T ≥ -22° C for storms in the southeastern US; Williams, 1989).

Goodman et al. (1988) and Williams et al. (1989a) demonstrate that the final stage in the convective life-cycle of Alabama thunderstorms is typically a microburst at the surface. As seen in Figs. 2.7a and b, the initial occurrence of significant outflow (radial velocity

differential, $\Delta V > 10$ m s^{-1}, as measured by a Doppler radar at 0° elevation) was nearly coincident with the onset of CG lightning and the descent of the high reflectivity core. The peak storm outflow ($\approx$ 30 m s^{-1}) lagged the peak total flash rate by approximately 6 minutes. Observations in Williams et al. (1989b) suggest that descending ice may aid in driving the outflow associated with a microburst, by virtue of the melting process. Williams et al. (1989b) show that storm outflow is often accompanied by an excursion in the electric field at the surface from foul- to fair-weather polarity in the vicinity of the microburst. They also speculate that this Field Excursion Associated With Precipitation (FEAWP; Krehbiel, 1986), or reversal in polarity of the charge aloft during the onset of heavy precipitation and strong winds, could be attributed to charge reversal microphysics as graupel particles descend below the charge reversal level to the melting level.

Recently, these electrification studies have been supplemented with polarimetric radar studies of electrified storms (e.g., Goodman et al., 1988; Goodman and Raghavan, 1993; and Bringi et al., 1993). For example, Goodman et al. (1988) used reflectivity and differential reflectivity to infer the presence of graupel and hail aloft during the rapid increase in the total flash rate from 1910 to 1917 (Fig. 2.7b). Similarly, Bringi et al. (1993) employed polarimetric radar data to demonstrate that the rapid increase in the electric field beneath a Florida storm during CaPE was associated with the development of graupel and hail aloft. In this thesis, we extend the work presented in this section with the multiparameter radar techniques presented in chapter four in an attempt to add new insight to the understanding of lightning producing storms in Colorado.

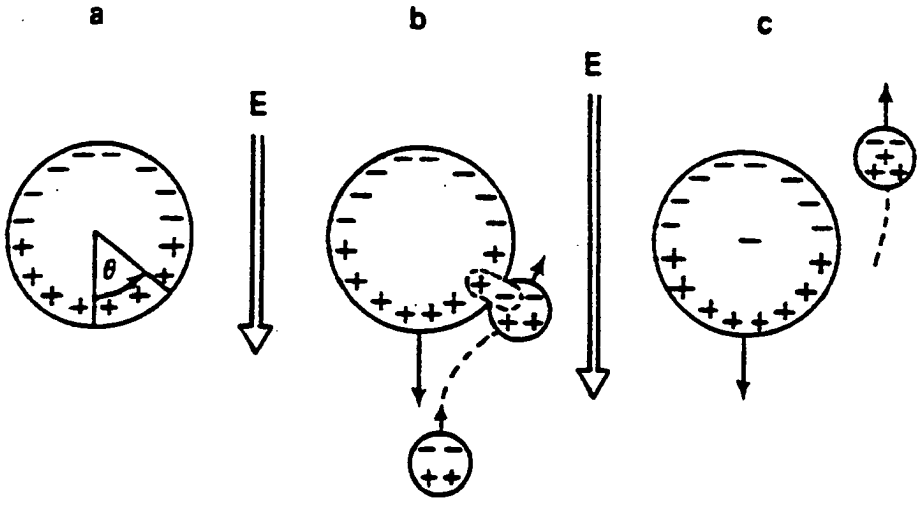

Fig. 2.1 Charge transfer by the induction mechanism for colliding drops in a downward-directed field. Adapted from Beard and Ochs (1986). a) charge distribution on a polarized drop; b) precipitation particle contact at a moderate angle; c) charge generation after drop separation.

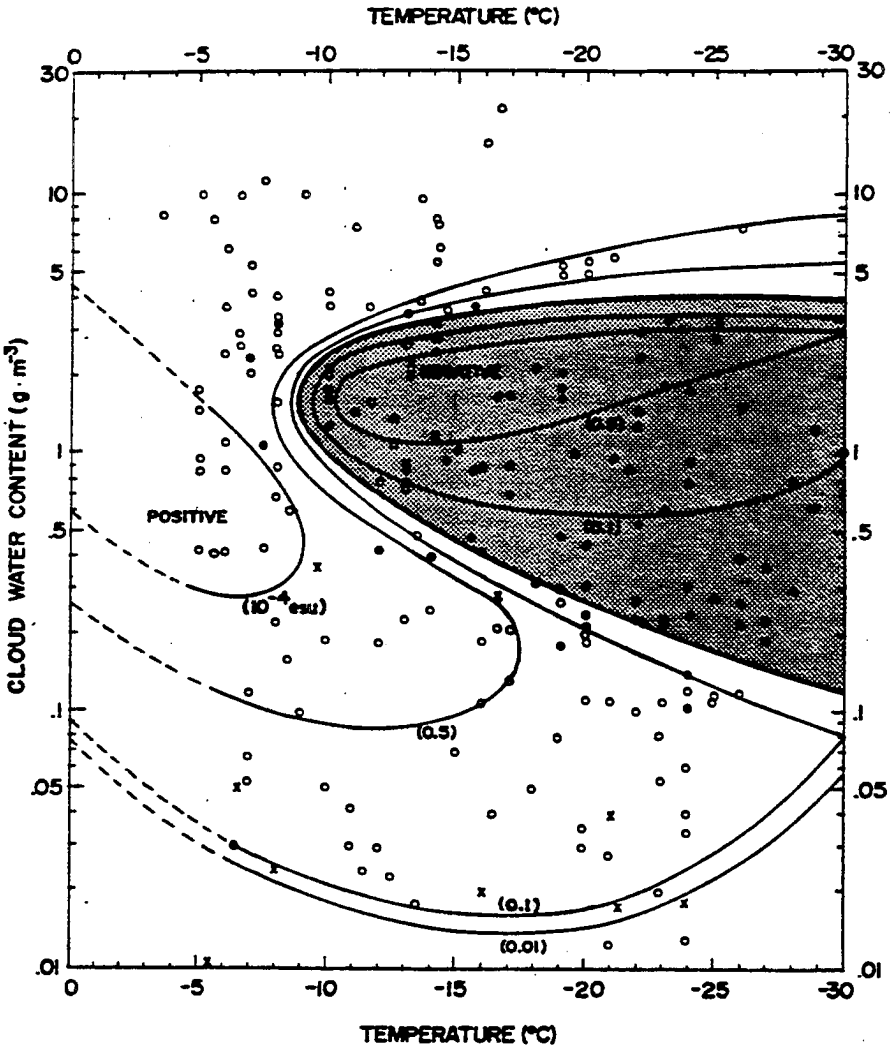

Fig. 2.2 Positive and negative rime charging zones as a function of temperature (° C) and cloud water content (g m^{-3}) for the laboratory experiment of Takahashi (1978). Open circles represent positive charge, solid circles negative charge, and crosses represent uncharged cases. The electric charge transferred to the rime per ice crystal collision is shown in units of 10^{-4} esu.

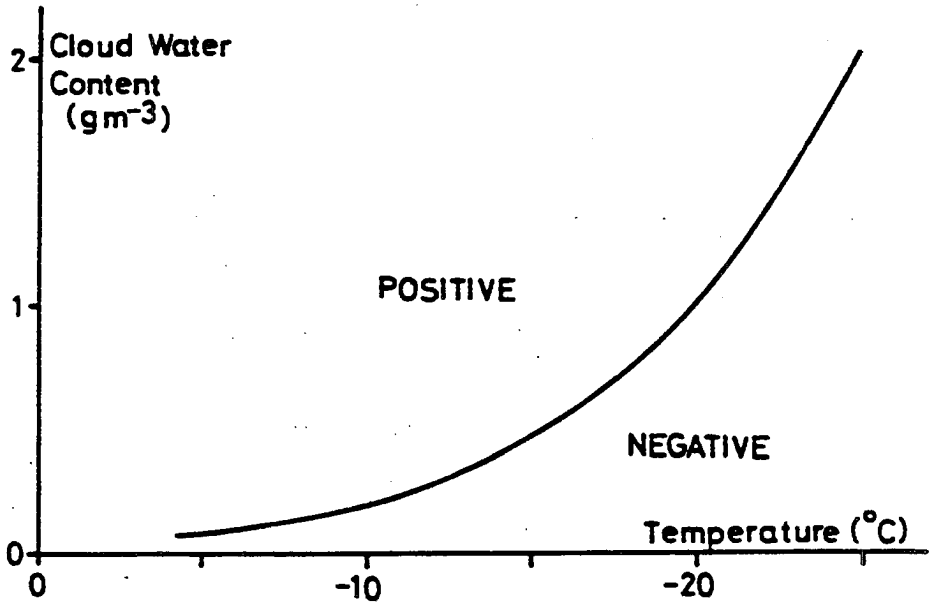

Fig. 2.3 Positive and negative rime charging zones as a function of temperature (° C) and cloud water content (g m^{-3}) for the laboratory experiment of Jayaratne et al. (1983).

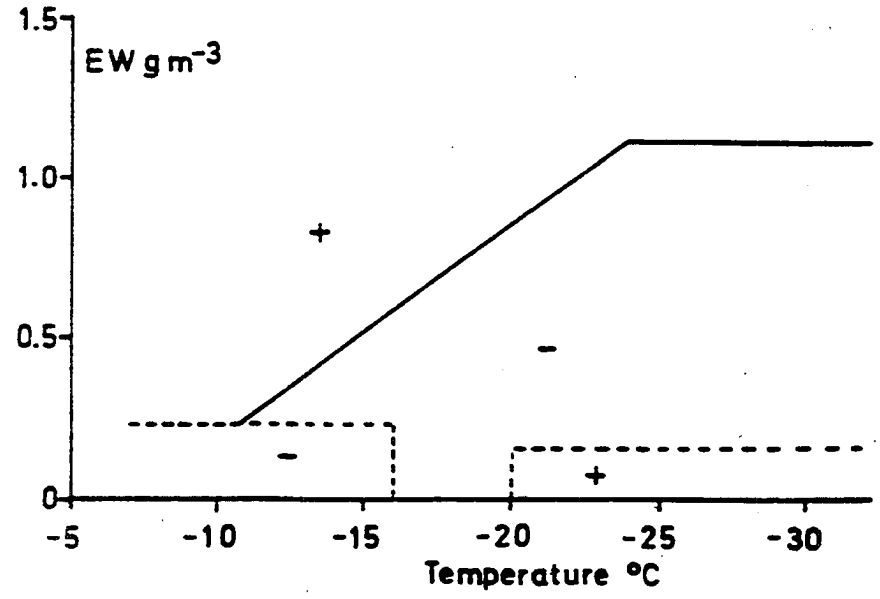

Fig. 2.4 Positive and negative rime charge zones as a function of temperature (° C) and effective liquid water content (g m^{-3}) for the laboratory experiment of Saunders et al. (1991).

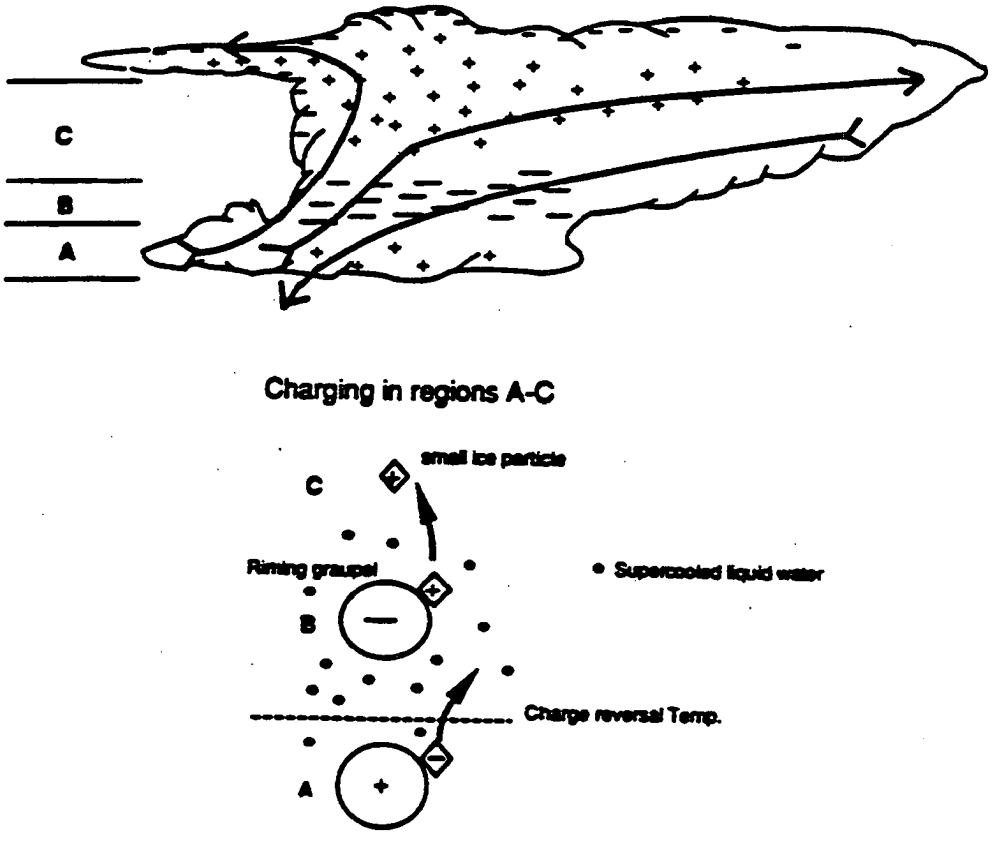

Fig. 2.5 Illustration of the non-inductive charging process for a graupel/ice crystal collision in the presence of supercooled liquid water. See text for a detailed explanation.

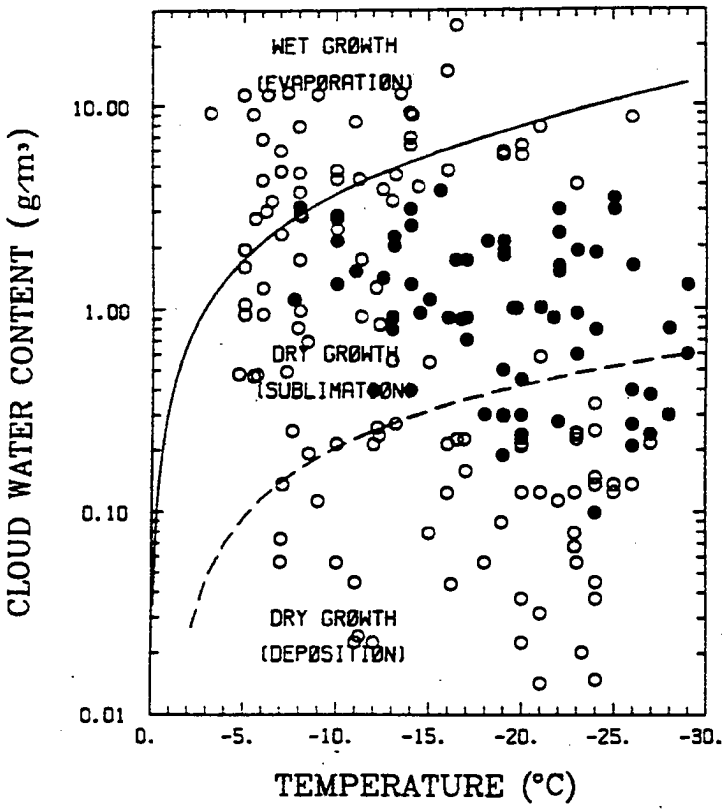

Fig. 2.6 Diagram depicting three microphysical growth states for graupel in a mixed phase region and comparison with laboratory results of Takahashi (1978). Open circles indicate negative graupel charging and solid circles indicate positive charging as in Fig. 2.2. Adapted from Williams et al. (1991).

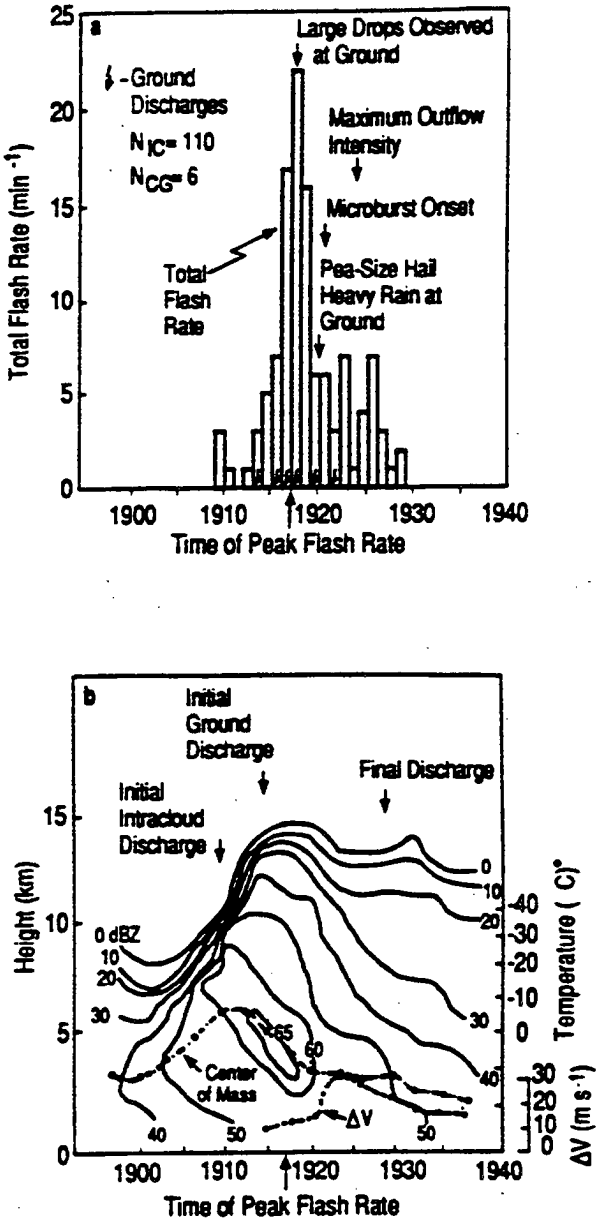

Fig. 2.7 Lightning and precipitation history of the 20 July 1986 microburst at Huntsville, Alabama from Goodman et al. (1988). a) Total lightning flash rate versus time where N_{IC} is the number of in-cloud lightning flashes and N_{CG} is the number of cloud-to-ground lightning flashes during the entire storm history. b) Time-height cross-section of maximum horizontal reflectivity, Z_h, in dBZ, the storm center of mass, and the 0° C elevation Doppler radar radial velocity differential, ΔV, in m s^{-1}.

CHAPTER 3

OVERVIEW OF THE FIELD PROJECT

3.1 Observational Network

The primary observational platform was the 10.7 cm, multiparameter, CSU-CHILL Doppler radar. System characteristics for the radar are given in Table 3.1. During this project, the CSU-CHILL radar measured the radial velocity (V_r), horizontal reflectivity (Z_h), differential reflectivity (Z_{dr}), differential propagation phase (ϕ_{dp}), and correlation coefficient at zero-lag between horizontally and vertically polarized waves $|\rho_{hv}(0)|$. The CSU-CHILL radar is located in the South Platte River Valley approximately 35 km east of the foothills at the base of the Front Range as seen in Fig. 3.1.

This location is ideal for observing thunderstorms which develop in the foothills during the early afternoon hours in response to terrain induced circulations and differential heating over the elevated terrain and then advect eastward by mid-afternoon (Karr and Wooten, 1976; Toth and Johnson, 1985). Frequently, decayed convection over the foothills forms cold-pools which rapidly flow down into the valley east of the CSU-CHILL radar, triggering new storms or enhancing pre-existing convection along an eastward advancing convergence zone (Hane, 1986). Using upper-air sounding data for Denver, National Weather Service (NWS) surface observations, and Front Range mesonet observations to supplement available radar data, we will demonstrate that both the 28 May squall line and the 21 May multi-cell storm studied in this thesis were generated by these terrain related mechanisms. The Front Range meso-network is operated by the National Oceanographic and Atmospheric Administration Forecasting System Laboratory (NOAA/FSL).

Additional instruments located at the CSU-CHILL site included a flat plate antenna, used to measure the total lightning flash rate, and a corona point sensor, configured to measure the electrostatic field strength and polarity of nearby charge structures. Cloud-to-ground (CG) flash rates were provided by a network of three magnetic direction finders (DF's) of medium-high gain. In-cloud lightning (IC) rates were determined by subtracting the CG rates from the total lightning rate. The location and areas of coverage by these instruments are depicted in Fig. 3.1. Additional information on these instruments are provided in the next section.

Given the operational range of the electrical instruments in Fig. 3.1 and keeping in mind the nature of the terrain induced convection under study, a scanning strategy was developed which provided both temporally and spatially high resolution multiparameter radar data. Surveillance scans were begun by late morning with an emphasis on activity over the foothills to the west. When a convective cell moved to within 60 km of the CSU-CHILL radar, sector scans with azimuthal widths dictated by the horizontal extent of the storm were begun. The CSU-CHILL was operated with the polarimetric switch engaged, a pulse repetition time (PRT) of 1000 μs, a gate spacing of 150 m, azimuth (α) and elevation intervals of approximately 1°, and 128 transmitted pulses (P) per integration cycle in order to allow for the proper estimation of the polarimetric observables. Since the antenna rotation rate, α', is defined by the above parameters, $\alpha' = \alpha/[(P)(PRT)]$, the maximum volume that could be sampled in a given time was fixed. In our study of electrification, it was critically important to obtain a complete spatial sample within three to six minutes so that the electrical evolution would be captured in sufficient detail and so that the "steady-state" approximation for the radar observables could be assumed during scanning. Since it was equally important to sample the entire storm (i.e., "top the storm"), a constant compromise between sector size, temporal resolution, and horizontal and vertical resolution was necessary. In general, the above parameters were altered slightly such that the spatial resolution was constrained to be 1 km or less out to 40 km in range.

While the CSU-CHILL was performing sector scans, the MHR surveillance scan was monitored in real time to insure that the entire storm volume was included in the sector scan and that no other storm was present within range of the flat plate and corona point, eliminating a potential source of electrical contamination caused by other storms not being scanned by the CSU-CHILL radar.

When appropriate, dual-Doppler observations were obtained by synchronous operations between the CSU-CHILL radar and the National Center for Atmospheric Research (NCAR) Mile High (10 cm) radar, located approximately 63 km to the south-southwest of the CSU-CHILL radar as shown in Fig. 3.1 The dual-Doppler lobes formed by the 30° radar beam crossing angle are also depicted. Since the dual-Doppler analysis in this study was primarily focused on the relation between kinematics and electrification, we narrowed the dual-Doppler analysis area to the intersection of the dual-Doppler lobes and the operational area of the flat plate antenna. As a result of the large dual-Doppler baseline and the limited range of the flat plate, radar echoes were typically 50 - 85 km from MHR. Davies-Jones (1979) derived a simple expression for the dual-Doppler spatial resolution, S, given the half-power beamwidth, Δ, and the maximum range, R, from the echo to the furthest of the two radars: $S = (R\pi\Delta)/180$. Using $\Delta = 1°$ and R = 85 km, we estimate that the spatial resolution in our dual-Doppler domain was S = 1.5 km. Although this was too large to resolve many convective scale circulations, it was of sufficient size to estimate the horizontal and vertical motion field on scales relevant to electrification.

3.2 Lightning and Electrical Data

3.2.1 Flat plate antenna

The flat plate antenna, or "field change meter," measured the electrostatic field change due to both in-cloud and cloud-to-ground lightning and was therefore used to obtain total lightning flash rate (Uman, 1987). The antenna consisted of a disk shaped conductor of effective area *A* mounted on a tripod facing the earth. As governed by Gauss' Law, a

change in the electric field, ΔE, terminating on the plate was accompanied by a change in the induced charge, $\Delta Q = \varepsilon_o A \Delta E$. An operational amplifier maintained the plate at ground potential by charging a feedback capacitor, C, so that a potential difference ΔV appeared across the output. From the definition of capacitance, the output voltage can be expressed as $\Delta V = \Delta Q/C = (\varepsilon_o A/C)\Delta E$. Sensitivity was adjusted by varying C. A resistor was placed in parallel with the capacitor such that the time constant, $\tau = RC = 30$ ms, was long enough to reproduce accurately the field changes associated with both IC and CG lightning. However, the time constant was short enough to bring the output voltage back to zero between flashes. The antenna was over-sampled at approximately 1 kHz (in order to avoid sampling errors) with an Analog-to-Digital (A/D) converter which was controlled via a Personal Computer (PC). In order to avoid saturation due to nearby lightning, one of four sensitivity channels (or different feedback capacitors) could be selected via the PC. The range of values for the feedback capacitors allowed a maximum effective range of about 40 to 50 km.

Data from the flat plate antenna was post-processed with an equally weighted, running mean filter specifically designed to eliminate a known source of 60 Hz noise. The data was then analyzed for lightning strikes by comparing the amplitude of the signal to the average amplitude of any remaining noise, determined from data collected during several fair-weather days. If the signal-to-noise ratio (SNR) exceeded some pre-determined threshold (typically 2 - 3.5 times depending on the channel), then the signal was tallied as a lightning flash. Return strokes were handled by requiring 500 ms to pass before the next signal could be considered a separate flash.

3.2.2 Corona point sensor

The polarity and strength of the electrostatic field were measured with a single corona point sensor. The instrument consisted of a conducting rod with a sharply pointed tip which was mounted on an instrument tower approximately 7 m AGL and fed into an A/D converter via an operational amplifier. This corona point measured the small currents

(microamperes) which flowed from elevated points in response to the electrostatic field of charge regions within approximately 15 km. Gradual changes (order of a minute) in the corona current were associated with changes in the charge structure aloft due to charge generation and/or advection. Sudden discontinuities (order of a second) in the corona current were associated with changes in the E-field due to both IC and CG lightning. The corona current was input into an operational amplifier through a 0.56 MΩ input resistor. This allowed for a maximum input current of approximately ± 9 μA for an appropriate output voltage ($\pm$ 5 V) for A/D conversion. Using the same PC which controlled the flat plate antenna, the corona point was sampled at sufficient temporal resolution (1 Hz) to detect both types of lightning. Corona point sensors have been used successfully by Williams et al. (1989a,b) in their investigations of lightning type and convective state of storms and by Engholm et al. (1990) in their study of positive CG lightning.

3.2.3 Magnetic direction finder network

Cloud-to-ground lightning information, including ground strike location and signal strength, were obtained from the NOAA/FSL network of three magnetic DF's of medium-high gain located in northeastern Colorado (López and Holle, 1986). The DF's which were manufactured by Lightning, Location and Protection Inc. (LLP) consisted of a wideband system of two orthogonal magnetic loop antennas and a flat plate electric antenna (Krider et al., 1976). The magnetic field produced by a lightning flash induces a signal in the circuit of each of the loops which is proportional to the field strength and the cosine of the angle between the plane of the loop and the direction from which the field is coming. From the ratio of these two signals, the flash direction is determined except for a 180 degree ambiguity. The flat plate antenna is used to resolve this directional ambiguity and determine CG flash polarity. The DF's discriminate against in-cloud flashes and noise by comparing the magnetic field wave shapes of the observed flash against a range of shapes of typical CG flashes. The position of a CG ground strike was determined by triangulation, using data from the two closest responding DF's. The probability of

detection of the DF's has been estimated at 70 - 85% for ranges less than 100 km (which includes this study's area of operation as seen in Fig. 3.1). Positioning errors for this network have been calculated at about 2-16 km, as discussed in López and Holle (1986). As a result, accuracy of the cloud-to-ground strike locations were adequate to assign each flash to the storms of interest. However, no attempt was made to associate individual CG lightning strikes to particular convective features since the positioning errors are of the same spatial scale as the horizontal extent of these features.

3.3 Case Studies

During the period from 15 May to 15 June 1993, six potential case studies of electrified storms were collected. On 21 May, the entire convective and electrical life-cycle of a long-lived multi-cell storm which was moderately electrified (peak flash rate $\approx$ 10 flashes min^{-1}) in a low ($\leq$ 1000 J/kg) CAPE (Convective Available Potential Energy) and moderate shear environment were observed. From one of the cells closest to the CSU-CHILL radar, corona point observations of a Field Excursion Associated with Precipitation (FEAWP) were collected along with CSU-CHILL radial velocity data of the accompanying microburst near the surface.

On 26 May, the Front Range of CO was under the drying influence of a lee-side pressure trough and south-southwest flow at the surface. The morning sounding was characterized by low CAPE and a classic "inverted-V" at low levels resulting in high-based thunderstorms which were weakly electrified (peak total flash rate < 5 flashes min^{-1}) and produced dry microbursts at the surface. Several storms moved through the northwest periphery of the observational network, allowing some limited observations. On 27 May, data were collected from two weakly electrified isolated cells which produced light to moderate rain in a low CAPE and low shear environment.

On 28 May, a severe squall line with tops reaching 15 km AGL formed in a high CAPE (2000 J/kg) and low shear environment within 40 km of the CSU-CHILL and

moved eastward through the data network. Explosive storm growth occurred when an outflow boundary from decayed convection collided with the strong updraft of developing convection producing funnel clouds and an F0 tornado approximately 20 km west of the CSU-CHILL radar. The tornado producing mechanism in this case was similar to that proposed by Wakimoto and Wilson (1989). Unique observations of several positive Z_{dr} columns (Illingworth et al., 1987) embedded within the developing squall line were collected as the total lightning flash rate rapidly increased. The storm produced golf-ball sized hail at the CSU-CHILL site, heavy rain causing local flooding, and peak total flash rates near 50 flashes per min. On 2 and 3 June, portions of the convective and electrical life-cycle of a weakly electrified, isolated storm in a low CAPE and moderate shear environment were recorded.

Due to limitations in data coverage in several of the possible case studies (26, 27 May and 2, 3 June), we have focused this research on the 21 and 28 May 1993 case studies. The 21 May case (Ch. 5) was analyzed in detail because two hours of comprehensive multiparameter radar and electrical observations of the entire life-cycle of a multi-cell storm were obtained. Unfortunately, these ideal conditions were not repeated in the other potential case studies. The 28 May case (Ch. 6) was of particular interest because of the unique multiparameter radar observations of a developing severe squall line which was highly electrified.

Table 3.1: System Characteristics of the CSU-CHILL Radar.
(Adapted from Rutledge et al., 1991).

Antenna	
type:	fully steerable, prime focus parabolic reflector
size:	8.5 m
feed:	scalar horn
3 dB beamwidth:	1.0°
directivity :	45 dB
sidelobe level (any ϕ-plane):	≤ -27 dB
cross-pol. level (any ϕ-plane):	≤ -30 dB
polarization radiated:	Horizontal or Vertical
Transmitter	
type:	klystron, modernized FPS-18
wavelength:	10.7 cm
peak Power:	700 $\sim$ 1000 kW
pulse width:	steps of 0.1 μs up to a max. of 1 μs
PRT:	800 $\sim$ 2500 μs
max. unambigu. range:	375 km
max. unambigu. velocity:	$\pm$34.3 m/s
Receiver	
noise figure:	$\sim$ 4 dB
noise power:	$-$ 114 dBm
transfer function:	linear
dynamic range:	90 dB, 0 $\sim$ 60 dB IAGC in 12 dB steps
min. detectable signal:	$-$110 dBm (SNR = 0 dB)
Data Acquisition	
signal processor:	SP20 made by Lassen Research
number of range gates:	64 $\sim$ 2048
range gate spacing:	0.2 μs or 1μs
sampling rate/avg. option:	under micro-code control
video digitizer:	12-bit, in the SP20 input card for I, Q and logP
time series capability:	up to 150 range gates.
Variables Available	
• Reflectivity at H polarization (Z_h)	
• Differential Reflectivity (Z_{dr})	
• Mean Doppler Velocity ($\bar{v}$) and Spectral Width (σ_v)	
• Differential Phase between H and V states (Ψ_{dp})	
• Copolar Correlation Coefficient ($\rho_{hv}(0)$)	
• Linear Depolarization Ratio (LDR)	
• Doppler Spectra from FFT processing	
• I, Q and logP for every pulse in time series mode (upto 150 gates)	

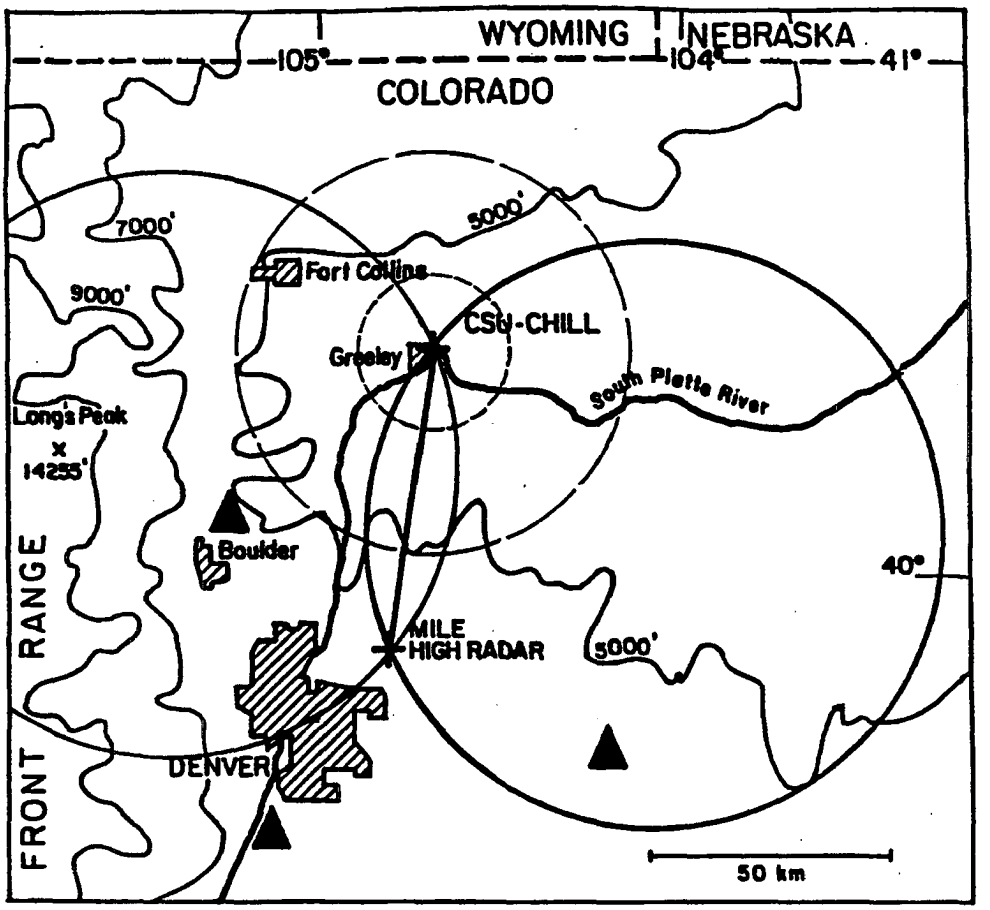

Fig. 3.1 Schematic of the observational network used in this study. CSU-CHILL Doppler radar (11 cm, dual-polarized) is shown along with the dual-Doppler lobes formed with the NCAR Mile High Radar (10 cm). The maximum operating range (40 - 50 km) for the slow antenna which was used to measure total flash rates is shown as the outer dashed ring around the CSU-CHILL at a radius of 40 km. The inner dashed ring depicts the maximum operational range (15 km) for the corona point sensor which was used to measure the electrostatic field and polarity. A network of three magnetic direction finders of medium-high gain used to record CG lightning flash rates and ground strike locations are depicted as triangles.

CHAPTER 4

POLARIMETRIC DOPPLER RADAR OBSERVABLES AND ANALYSIS METHOD

The primary source for kinematic and remotely-sensed microphysical data was the CSU-CHILL, multiparameter Doppler radar which was capable of computing and displaying in real-time the differential reflectivity (Z_{dr}), correlation coefficient at zero-lag between horizontally (h) and vertically (v) polarized echoes $|\rho_{hv}(0)|$, and differential propagation phase (ϕ_{dp}), in addition to the more conventional horizontal reflectivity (Z_h), and radial velocity (V_r) as described in Bringi et al. (1994). In this study, the phrase "multiparameter radar observations" is limited to observations of ideally the same pulse volume made at two orthogonal linear polarizations (Seliga and Bringi, 1976).

In this chapter, we begin by presenting an expression for the backscattering matrix and covariance matrix. These expressions will provide a framework from which a mathematical definition and brief qualitative description of each of the dual-polarimetric variables can be given. We then present an overview of radar analysis methods employed in our investigation of storm electrification. A succinct description of radar data editing and gridding methods is given. Several sections are then devoted to the discrimination and quantification of ice and liquid precipitation using all available multiparameter radar data: 1) the reflectivity factors, and 2) the specific differential phase. The knowledge gained from these methods is then combined together to form a multiparameter decision process that partitions the four-dimensional space of Z_h, Z_{dr}, $|\rho_{hv}(0)|$, and K_{dp} (the specific differential phase) such that each partition uniquely corresponds to a particular precipitation type. Since precipitation sized ice such as graupel and hail are essential for

the particle scale and storm scale separation of charge in deep convective storms according to the non-inductive charging mechanism (e.g., Reynolds, 1957), these ice detection and quantitative methods are the foundation upon which our multiparameter radar case studies of electrification are built. Lastly, a brief overview of the dual-Doppler method of retrieving the three dimensional wind field is presented with an emphasis on the assumptions and boundary conditions used and the expected sources of error in our analyses.

4.1 The Backscattering Matrix

A pulsed meteorological radar such as the CSU-CHILL illuminates a radar resolution volume (RRV) which is defined by range to target, pulse width, and antenna pattern. A typical RRV for the CSU-CHILL is about 0.1 km^{-3} for a range of 50 km, a 1 degree half power beam width, and a 1 μs pulse width (Doviak and Zrnic, 1993). Within this RRV, the hydrometeors are assumed to be randomly positioned and therefore constitute a random medium from which radar measurements are taken. Since the fractional volume concentration of the scattering particles is typically very small (<< 1%), the independent backscatter approximation is valid and the backscattered power is proportional to the sum of the incoherent powers backscattered by each particle within the RRV.

As discussed earlier, the CSU-CHILL is a polarization diverse radar which has a variable transmitted and received wave polarization, allowing for measurement of hydrometeor characteristics such as size, shape, spatial orientation, and thermodynamic phase. To understand how these physical characteristics of hydrometeors are measured from the backscattered power, it is crucial to establish a mathematical basis for the polarimetric radar observables. These characteristics are described in terms of the backscattering matrix [**S**] that relates the backscattered electric field $[\mathbf{E}]^b$ at the antenna to the incident electric field $[\mathbf{E}]^i$. Elements of the backscattering matrix are complex scattering amplitudes that are dependent on size, shape, orientation, and dielectric

constant. The symmetric backscattering matrix in a linear polarization basis for an individual target can be expressed as (Doviak and Zrnic, 1993)

$$\begin{bmatrix} \mathbf{E_h} \\ \mathbf{E_v} \end{bmatrix}^b = \begin{bmatrix} S_{hh} & S_{hv} \\ S_{vh} & S_{vv} \end{bmatrix} \begin{bmatrix} \mathbf{E_h} \\ \mathbf{E_v} \end{bmatrix}^i \frac{\exp(-jkr)}{r} \tag{4.1}$$

where $k = 2\pi/\lambda$ is the free space propagation constant and r is the range or distance between the antenna and the scatterer. By convention, the first and second subscripts of the backscattering elements, S, refer to the receive and transmit polarization states respectively where h represents horizontal and v represents vertical. Since a distribution of hydrometeors can be considered a reciprocal medium, we will assume that $S_{hv} = S_{vh}$ throughout the rest of this study.

In the above equation, we have purposely neglected propagation effects in order to clearly identify the backscattering properties of the hydrometeors in the RRV. Both attenuation and phase shift can affect the received signals at the radar. The effect of specific attenuation on the reflectivity due to rain and dry hail is negligible (less than a few dB) for S-band ($\lambda \approx 10$ cm) radars such as the CSU-CHILL (Battan, 1973). Although it is possible for large wet hail to cause significant attenuation for a 10.7 cm radar, detailed analyses of the multiparameter radar data failed to reveal its presence in this study. Differential attenuation is typically small for S-band radars and its effect on differential reflectivity can be considered negligible (Doviak and Zrnic, 1993). Differential phase shift can be broken down into two components: 1) a backscatter component and 2) a range cumulative, forward propagation component. For S-band radars, only very large hail ($\geq$ 5 cm) can cause the resonance in the Mie scattering regime that is necessary for significant backscatter differential phase, δ, (Balakrishnan and Zrnic, 1990b). Following the filtering techniques of Hubbert et al. (1993), an attempt was made to separate δ from the total phase shift in all analyzed radar volumes. No evidence of significant δ was found in either case study. As a result, the measured phase shift can be entirely attributed to the forward

propagation component: the specific differential phase, or K_{dp}. Since attenuation, differential attenuation, and backscatter differential phase are negligible in this study, we will not present a more in-depth discussion of propagation effects. For a detailed mathematical treatment of propagation on polarimetric radar observables and a presentation of the propagation matrix, see Bringi et al. (1994).

Using the backscattering matrix in Eqn. (4.1) and neglecting propagation effects for now, we can define the backscattering covariance matrix. If a vector $\mathbf{A} = \{S_{hh}, S_{hv}, S_{vv}\}$ is defined from its constituent elements, the 3 x 3 covariance matrix of vector **A** is $\mathrm{Cov}(\mathbf{A}) = \langle \mathbf{A}^t, \mathbf{A}^* \rangle$ where t stands for the matrix transpose and * stands for the complex conjugation. Expanding the backscattering covariance matrix, we obtain

$$\mathrm{Cov}(\mathbf{A}) = \begin{bmatrix} \left\langle |S_{hh}|^2 \right\rangle & \left\langle S_{hv} S_{hh}^* \right\rangle & \left\langle S_{vv} S_{hh}^* \right\rangle \\ \left\langle S_{hh} S_{hv}^* \right\rangle & \left\langle |S_{hv}|^2 \right\rangle & \left\langle S_{vv} S_{hv}^* \right\rangle \\ \left\langle S_{hh} S_{vv}^* \right\rangle & \left\langle S_{hv} S_{vv}^* \right\rangle & \left\langle |S_{vv}|^2 \right\rangle \end{bmatrix} \tag{4.2}$$

where the angle brackets, $\langle\rangle$, denote ensemble averages over the distributions of particle size, shape, orientation, and dielectric constant within the RRV (Doviak and Zrnic, 1993).

4.2 Equations and Definitions

Since attenuation, differential attenuation, and backscatter differential phase are negligible, the backscattering covariance matrix shown in Eqn. (4.2) is sufficient to extract equations for Z_h, Z_{dr}, and $|\rho_{hv}(0)|$. After consideration of the phase constants at horizontal and vertical polarizations, an equation for K_{dp} will also be given. These equations will then be used as a basis for qualitative discussions on the characteristics and applications of each polarimetric observable.

4.2.1 Reflectivity, $Z_{h,v}$

Using a horizontal/vertical polarization basis, we define the copolar radar reflectivity factors with respect to the backscattering covariance matrix elements in Eqn (4.2) as

Reflectivity factor at horizontal polarization:

$$\mathbf{Z_h} = \left(4\lambda^4/\pi^4|K_w|^2\right)\left\langle|S_{hh}|^2\right\rangle \tag{4.3}$$

Reflectivity factor at vertical polarization:

$$\mathbf{Z_v} = \left(4\lambda^4/\pi^4|K_w|^2\right)\left\langle|S_{vv}|^2\right\rangle \tag{4.4}$$

where λ is the radar wavelength and $|K_W|^2 = 0.93$ is the complex index of refraction for water. In this study, reflectivity factors will be distinguished by bold characters and have units of $mm^6\ m^{-3}$. Since values of $\mathbf{Z_{h,v}}$ commonly encountered in weather observations span many orders of magnitude, radar meteorologists use reflectivity with a logarithmic scale and units of dBZ.

$$Z_{h,v} = 10\log_{10}(\mathbf{Z_{h,v}}) \quad [\text{dBZ}] \tag{4.5}$$

Reflectivity is typically accurate to 1 dB or less (Doviak and Zrnic, 1993).

4.2.2 Differential reflectivity, Z_{dr}

The differential reflectivity, Z_{dr}, is a good indicator of hydrometeor shape (i.e., oblateness) and orientation. Neglecting propagation effects, we use Eqn. (4.2) to define Z_{dr} as

$$Z_{dr} = 10\log\left(\left\langle|S_{hh}|^2\right\rangle/\left\langle|S_{vv}|^2\right\rangle\right) \quad [\text{dB}] \tag{4.6}$$

Comparing Eqn. (4.6) to Eqns. (4.3) and (4.4), we find that differential reflectivity is related to the decibel difference between the reflectivity factor at horizontal polarization, $\mathbf{Z_h}$, and the reflectivity factor at vertical polarization, $\mathbf{Z_v}$, and can be expressed as

$$Z_{dr} = 10\log_{10}(\mathbf{Z_h}/\mathbf{Z_v}) \quad [\text{dB}] \tag{4.7}$$

The differential reflectivity is typically accurate to 0.25 dB or less (Doviak and Zrnic, 1993).

Since differential reflectivity is a measure of precipitation particle oblateness, it is useful in distinguishing between large rain drops, large hail, and graupel/small hail due to differences in shape and orientation. Since raindrops larger than about 1 mm in diameter

are deformed into oblate spheroids by aerodynamic forces (Pruppacher and Beard, 1970) with a preferred orientation of their maximum dimension in the horizontal direction (and therefore $Z_h > Z_v$), Z_{dr} is positive and increases for larger raindrop sizes. Large hail can result in a $Z_{dr} \approx 0$ if the hailstones are spherically symmetric or exhibit random tumbling behavior. Alternatively, it could also be possible for the hailstones to be oblate with their longest dimension in the vertical such that $Z_h < Z_v$ and $Z_{dr} < 0$. Although this fall mode has yet to be substantiated in a wind tunnel experiment, Zrnic et al. (1993b) present theoretical arguments that suggest this is a stable fall mode for elongated or large oblate hailstones.

Small hail and graupel particles (especially hexagonal and lump graupel) often tend to be more spherically symmetric such that $Z_h \approx Z_v$, resulting in $Z_{dr} \approx 0$. It is important to note that graupel particles in northeastern Colorado thunderstorms can be conically shaped with mean axis ratios ranging from 0.75 to 0.90 for sizes in excess of 1 mm (Heymsfield, 1978). Despite this deviation from sphericity, the Z_{dr} for a graupel particle is significantly lower than that for a similarly shaped raindrop because Z_{dr} sensitivity to hydrometeor shape varies with the dielectric constant of the scattering particle. For example, graupel particles with a range of bulk densities of 0.3 to 0.6 g cm^{-3} and an axis ratio of 0.75 has a range of Z_{dr} from 0.4 to 0.8 dB compared to similarly shaped raindrops with a Z_{dr} of 2.8 dB (Herzegh and Jameson, 1992). As a result, Z_{dr} is related to the *reflectivity* weighted mean axis ratio. In order to avoid confusing a highly conical graupel particle with a less oblate raindrop, analysis is limited to radar data with $Z_h > 40$ dBZ such that raindrops with a typical drop-size distribution and equilibrium size-to-shape relationship are characterized by $Z_{dr} > 1$ dB (e.g., Bringi et al., 1991). Even with this precaution, some ambiguities can occur below the melting layer. Melting ice may produce enhanced Z_{dr} (Aydin et al., 1984) because the water coating forms a torus around the particle's equator, giving it a more oblate shape, (Rasmussen et al., 1984) and because a melt water radius of only 10% of the total melting ice particle radius results in a reflectivity that is 90% that of an all-water drop of the same radius (Battan, 1973). As a

result, we rely on the combined information inferred from Z_h, Z_{dr}, K_{dp}, and $|\rho_{hv}(0)|$ below the melting layer.

Differential reflectivity has been used extensively to analyze precipitation types and amounts. For example, Z_{dr} was used in combination with Z_h by Illingworth et al. (1987) to detect the presence of large supercooled drops in updrafts during initial convective development, and by Wakimoto and Bringi (1988) to infer the presence of melting hail in the precipitating downdraft of a microburst producing storm. The differential reflectivity in conjunction with reflectivity has also been used to provide good estimates of moderate to heavy rainfall (20 - 70 mm hr^{-1}) in convective storms (Chandrasekar and Bringi, 1988).

4.2.3 Correlation coefficient at zero-lag, $|\rho_{hv}(0)|$

The correlation coefficient at zero-lag between reflectivity at horizontal and vertical incidence, $\rho_{hv}(0)$ (we will use this abbreviated symbol throughout the rest of the study), depends on the orientation and shape of hydrometeors and decreases from near unity for a distribution of irregularly shaped particles. Neglecting propagation effects and using Eqn. (4.2), we define $\rho_{hv}(0)$ as

$$\rho_{hv}(0) = \left\langle \mathbf{S_{vv}}\,\mathbf{S_{hh}^{*}} \right\rangle \Big/ \left[\left\langle \left|\mathbf{S_{hh}}\right|^2 \right\rangle^{1/2} \left\langle \left|\mathbf{S_{vv}}\right|^2 \right\rangle^{1/2} \right] \tag{4.8}$$

The correlation coefficient at zero-lag is primarily affected by the variability in the ratio of the vertical-to-horizontal size of individual hydrometeors because the intensity of backscattering for the Rayleigh condition ($2\pi r/\lambda << 1$) depends monotonically on the dimension of the hydrometeor in the direction of the electric field. This relation is more complicated in the Mie scattering regime because it involves the differential phase shift on scattering, δ. Several effects can lower the correlation coefficient below unity: distributions of shape and orientations, differential phase shift on scattering, irregular shapes of hydrometeors, and mixtures of two types of hydrometeors. (Balakrishnan and

Zrnic, 1990b). In order to effectively utilize $\rho_{hv}(0)$, it is necessary to understand each of these possible effects.

In rain, the eccentricity distribution is related to the distribution of equivalent volume diameter D_e, because of the well known size-to-shape relationship for raindrops. Small and continuous changes in the drop-size distribution within the RRV can reduce $\rho_{hv}(0)$ because increments in reflectivities at horizontal and vertical polarizations are not equal for the same increment in D_e. Sachidananda and Zrnic (1985) determined that the shape effects in rain are small, and compute theoretical values larger than 0.99. Balakrishnan and Zrnic (1990b) measured the correlation coefficient in Oklahoma rainstorms and found that the mean correlation coefficient from pure rain is larger than 0.97 with a standard error of about 0.01. Measured values of $\rho_{hv}(0)$ are typically lower than the theoretical calculations above because of the effects of canting angle variations, sidelobes, and receiver noise. Balakrishnan and Zrnic (1990b) found that shape effects on the correlation coefficient for graupel and hail were negligible for Rayleigh conditions.

Variations in the canting angle distribution can lower $\rho_{hv}(0)$ because canting changes the effective shape of the hydrometeors as seen by the radar. Observational evidence show that the degree of common alignment is much less in hail medium than in rain. As a result, the effect of canting should be more significant in hail storms. However, theoretical calculations by Balakrishnan and Zrnic (1990b) demonstrate that canting angle effects are also insignificant for dry hail (reduction less than 0.01) and minimal for wet hail with diameters less than 5 cm. As a result, if shape and orientation are the only considerations, we would expect the following typical values of $\rho_{hv}(0)$: pure rain with $\rho_{hv}(0) > 0.97$, pure graupel with $\rho_{hv}(0) > 0.99$, and pure hail (dry or wet with < 5 cm diameter) with $\rho_{hv}(0) > 0.96$ (i.e., Balakrishnan and Zrnic, 1990b; Doviak and Zrnic, 1993).

Changes in the backscatter differential phase, δ, can lower $\rho_{hv}(0)$ when entering the Mie scattering regime for a specific pairing of (large) diameter and dielectric constant. This can be understood mathematically by inspection of Eqn. (4.8). Variations in δ cause

the composite horizontally and vertically polarized signals to fluctuate differently, thus lowering the ensemble average covariance in the numerator of Eqn. (4.8). This effect is negligible in rain for S-band radars such as the CSU-CHILL (Jameson, 1985). Balakrishnan and Zrnic (1990b) showed that this effect can lower $\rho_{hv}(0)$ significantly for wet or spongy hail with diameters in the range of 5 cm or greater. No surface evidence of such large hail was reported for either of the case studies presented and no significant values of backscatter differential phase ($\delta \geq 5°$) were measured. As a result, we do not feel that backscatter differential phase affected $\rho_{hv}(0)$ in the following case studies.

Highly irregular shapes of hydrometeors is another factor that can lower the correlation coefficient. Larger hailstones (4-10 cm diameter) are typically irregularly shaped with small and large protuberances (List, 1985). Balakrishnan and Zrnic (1990b) demonstrated that hailstones with large lobes (protuberance-to-diameter ratio $\geq$ 0.1) would significantly lower the correlation ($\rho_{hv}(0) < 0.90$). Since there was no ground evidence supporting the presence of hail with large lobes and since storm reports and radar analyses suggest that all hail was less than 4 cm in diameter, we will assume that irregularly shaped hydrometeors did not exist in our storms.

The final factor that can significantly lower the correlation coefficient is the presence of a mixture of hydrometeor types in the radar resolution volume. In a mixture of precipitation types, the reduction of $\rho_{hv}(0)$ is due to the broader spread in the composite distribution of shapes, sizes, orientations and dielectric constants compared to a distribution of a single precipitation type. The drop in $\rho_{hv}(0)$ is largest if the reflectivity weighted distributions of the two hydrometeor types are comparable. If either one of the precipitation types dominate the reflectivity in the RRV, then $\rho_{hv}(0)$ will tend to be similar to the intrinsic value for that hydrometeor type. Zrnic' et al. (1993b) demonstrated that $\rho_{hv}(0)$ decreases in regions of mixed phase hydrometeors such as at the bottom of the melting layer. This is because the distribution of sizes, shapes, canting angles, and phase shift upon scattering from hydrometeors consisting of a rain and ice mixture broadens with

increasing ice particle size, thus decreasing the correlation. Similarly, the correlation coefficient has also been used to infer the presence of large (> 2.5 cm) and small (< 1 cm) hail in mixed-phase precipitation below the melting layer (Balakrishnan and Zrnic', 1990b) by noting that $\rho_{hv}(0)$ decreases with increasing hail size. Large hail in mixed-phase precipitation is typically characterized by $\rho_{hv}(0) \leq 0.95$ while small hail mixed with rain usually results in $\rho_{hv}(0) > 0.95$ (Balakrishnan and Zrnic, 1990b; Doviak and Zrnic, 1993).

4.2.4 Specific differential phase, K_{dp}

Specific differential phase is defined as the difference between the ensemble average propagation phase constants for horizontally and vertically polarized electromagnetic waves.

$$K_{dp} = \left(\langle k_h \rangle - \langle k_v \rangle\right) \tag{4.9}$$

Note that this definition is for one way propagation per current convention whereas original studies defined K_{dp} for two-way propagation (e.g., Sachidananda and Zrnic, 1986 and 1987). The specific differential phase can be directly calculated from the range derivative of ϕ_{dp} which is measured in real time. In theory, measurements of ϕ_{dp} at two ranges r_1 and r_2 are sufficient to obtain a finite difference estimate of K_{dp}.

$$K_{dp} = \frac{1}{2}\frac{d\phi_{dp}}{dr} \approx \frac{\phi_{dp}(r_2) - \phi_{dp}(r_1)}{2(r_2 - r_1)} \tag{4.10}$$

In practice, the range profile of ϕ_{dp} is filtered first before estimating K_{dp} in order to reduce errors to an acceptable level ($\leq 0.4°$ km^{-1}) as discussed in Hubbert et al. (1993).

Specific differential phase has the unique property that it allows discrimination between statistically isotropic (i.e., hailstones) and anisotropic (i.e., raindrops) hydrometeors. The phase constants can be written as (Oguchi, 1983)

$$\langle k_h \rangle = k_0 + \langle k_{hR} + k_{hH} \rangle \tag{4.11a}$$

$$\langle k_v \rangle = k_0 + \langle k_{vR} + k_{vH} \rangle \tag{4.11b}$$

where k_0 is the free-space propagation constant and the subscripts R and H refer to the contributions made by rain and hail respectively to the phase constants at each polarization. Hail can be considered isotropic if it is approximately spherical in shape or tumbles as it falls such that $\langle k_{hH} \rangle = \langle k_{vH} \rangle$. With the assumption of isotropic hail, we subtract Eqn. (4.11b) from Eqn. (4.11a) to obtain the specific differential phase.

$$K_{dp} = \left(\langle k_h \rangle - \langle k_v \rangle \right) = \left(\langle k_{hR} \rangle - \langle k_{vR} \rangle \right) \tag{4.12}$$

Isotropic hydrometeors such as hail produce equal phase shifts for either polarization so that any phase difference is due only to the anisotropic particles in the radar resolution volume such as rain. As a result, K_{dp} is affected typically by measurably oblate rain only in a rain and hail mix.

Jameson (1985) demonstrated theoretically that the specific differential phase between horizontally and vertically transmitted waves is proportional to the precipitation liquid water content (W) times a shape factor (1 - $\Re$) where $\Re$ is the mass weighted mean axis ratio over the drop size distribution. Since K_{dp} is relatively insensitive to the presence of hail and proportional to the precipitation liquid water content, it is very useful in the discrimination and quantification of precipitation types. Chandrasekar et al. (1990) have shown that K_{dp} provides a robust and accurate estimate of heavy rainfall (> 60 mm hr^{-1}) because it is 1) independent of receiver/transmitter calibration, 2) insensitive to beam filling, 3) independent of attenuation, 4) relatively insensitive to drop size distribution, and 5) not biased by the presence of hail. In addition, K_{dp} can be used in combination with Z_h to distinguish between frozen and liquid precipitation. By separating the rain and hail contribution to the reflectivity factor, K_{dp} and Z_h can provide estimates of the hail and rain rates in mixed phase environments as shown by Balakrishnan and Zrnic' (1990a).

4.3 Analysis Methods

4.3.1 Data processing: editing and gridding of radar data

Before interpreting the polarimetric data, all measurements obtained from the CSU-CHILL were carefully edited using the Research Data Support System (RDSS) software developed at the National Center for Atmospheric Research (NCAR) (Oye and Carbone, 1981). Ground clutter was manually removed since it has a deleterious effect on the quality of multiparameter measurements at low elevation angles. All aliased Doppler radial velocities were corrected using RDSS. The differential phase was filtered with a low-pass, infinite impulse response (IIR) filter that is designed such that gate-to-gate fluctuations are attenuated while physically meaningful trends are preserved (Hubbert et al., 1993). The specific differential phase was then calculated from the IIR filtered ϕ_{dp} using a finite differencing approximation. The impact of mismatched sidelobe patterns on the differential reflectivity was minimized as explained in the following paragraphs. The multiparameter observables were then interpolated onto a Cartesian grid using the REORDER software package also developed at NCAR. Grid resolution was different for each case study. For the 21 May 1993 case (Ch. 5), the grid resolution was 1 km in the horizontal and 0.5 km in the vertical. The radius of influence for the Cressman filter (Cressman, 1959) employed in the interpolation process was 0.87 km in the horizontal and 0.5 km in the vertical for this case. For the 28 May 1993 case (Ch. 6), the grid resolution in the horizontal and vertical was 0.5 km and the Cressman filter radius of influence was 0.7 km for all dimensions.

The accuracy of polarimetric radar measurements, especially Z_{dr}, is critically dependent on the matching of the antenna illumination function at both polarizations. Herzegh and Carbone (1984) noted that when the main antenna beam sampled an area of weak reflectivity in the vicinity of a strong reflectivity gradient, Z_{dr} measurements were often dominated by the large sidelobe contributions of the two copolarized patterns from a more strongly reflecting region. Therefore, an understanding of the effects of mismatched

illumination patterns at horizontal and vertical polarizations is crucial for the proper interpretation of multiparameter radar data.

During the spring of 1993, the CSU-CHILL radar antenna had relatively high sidelobes with some beam-pattern mismatch as discussed in Xiao et al. (1993). A high performance antenna was installed in December 1993 which now provides excellent matching of the antenna illumination function between horizontal and vertical polarization states. As a result, we used an approximate yet objective and efficient method to mitigate the potential errors in Z_{dr} due to the deficiencies of the old antenna. Sample radar data was input into a one-dimensional simulation run by the Colorado State University (CSU) Electrical Engineering Department that calculates the Z_{dr} bias caused by beam-pattern mismatch, using the CSU-CHILL antenna patterns and horizontal reflectivity profiles as input (V. N. Bringi, private communication). Using the results from these simulations, we determined the maximum acceptable horizontal reflectivity (Z_h) gradient that insured reliable Z_{dr} data, ($|Z_{dr}$ bias $| < 0.5$ dB), as a function of range and removed Z_{dr} data from any range gate which exceeded this threshold. For example, we eliminated any differential reflectivity data at 30 km in range if the horizontal reflectivity gradient exceeded 22 dB km^{-1} and at 60 km in range if the Z_h gradient exceeded 14 dB km^{-1}. We used this Z_h gradient threshold to quality control all Z_{dr} data employed in this study and visually inspected the results. Anomalous Z_{dr} patterns often found along the edges of intense convective cores and along outer, low reflectivity echo boundaries were successfully deleted. As a result; we have interpreted the remaining Z_{dr} data with confidence.

4.3.2 Discrimination between ice and liquid precipitation

As discussed in Sec. 2.1.2, precipitation sized ice such as graupel and hail are crucial components of the charge separation process in deep convective clouds that leads to lightning. As a result, multiparameter radar methods which can remotely infer the presence and amounts of these ice hydrometeors should provide an excellent tool in studying storm electrification. In this section, we discuss three such methods using the

multiparameter observables (Z_{dr}, Z_{dp}, and K_{dp}) in combination with the horizontal reflectivity.

4.3.2.1 Differential reflectivity method, Z_h and Z_{dr}

The simultaneous use of Z_h and Z_{dr} provides an effective means of distinguishing between pure rain and pure hail. Leitao and Watson (1984) established a statistical relationship in the Z_h - Z_{dr} space that separates rain from hail using linear-polarized radar data as depicted as the dashed-line boundary "1" in Fig. 4.1. Bringi et al. (1984) demonstrated that hail can be characterized by low Z_{dr} (i.e., $Z_{dr} < 0.5$ dB) and high Z_h (i.e., $Z_h \geq 50$ dBZ). This anticorrelated pattern of high reflectivity coupled with near zero or negative Z_{dr} defines a Z_{dr} hail signal. Using rain data from surface disdrometers, Aydin et al. (1986) also established a boundary between rain and hail in Z_h - Z_{dr} space as shown in Fig. 4.1 as the thick solid line (boundary "2"). They proposed a hail detection signal H_{dr} which is the departure of the observed Z_h from the above rain-hail boundary and is defined as

$$H_{dr} = Z_h - F(Z_{dr}) \quad [\text{dB}]$$

where,

$$F(Z_{dr}) = \begin{cases} 60; & Z_{dr} > 1.74 \\ 19 Z_{dr} + 27; & 0 < Z_{dr} \leq 1.74 \\ 27 & Z_{dr} \leq 0 \end{cases} \qquad (4.13)$$

Radar data below the melting level with $H_{dr} > 0$ is indicative of hail. Above the freezing level, H_{dr} detects all forms of precipitation sized ice and cannot be used alone as a hail signal. On the other hand, Bringi et al. (1986a) found that large oblate (vertically oriented) hail yields slightly negative differential reflectivity in the range $-1 \leq Z_{dr} \leq 0$ dB throughout the storm.

These studies have demonstrated the effectiveness of Z_h and Z_{dr} as a tool for detecting pure rain and pure hail. However, these methods often break down in mixed-phase

precipitation (i.e., mixture of rain and ice). The large spread of Z_{dr} around a mean value due to variations in the drop-size distribution makes it difficult to establish a clear boundary between rain and ice.

4.3.2.2 Difference reflectivity method, Z_h and Z_{dp}

An alternate method to handle mixed-phase precipitation was introduced by Golestani et al. (1989). They proposed that the logarithm of the difference between horizontal and vertical reflectivity factors (boldface; units of $mm^6\ m^{-3}$), or difference reflectivity (Z_{dp}), be used to estimate the fraction of ice in rain/ice mixtures and defined it as

$$Z_{dp} = 10 \log(\mathbf{Z_h} - \mathbf{Z_v}) \ [dB] \quad (\text{where } \mathbf{Z_h} > \mathbf{Z_v}) \tag{4.14}$$

This method assumes that ice (i.e., graupel and hail) contributes to both Z_h and Z_v equally. In other words, graupel and hail are assumed to be spherical on average. Deviations from the assumption of sphericity for graupel and hail are mitigated by the effects of tumbling and wobbling (e.g., Pflaum et al., 1978; Knight and Knight, 1970) and by the significantly lower dielectric constant for ice as discussed earlier. Therefore, Z_{dp} would be due solely to rain which is known to deform into oblate spheroids. They demonstrated that the relationship between Z_{dp} and Z_h is nearly linear for simulated gamma drop-size distributions as represented by the dashed line in Fig. 4.2 which is given by

$$Z_{dp} = 1.2\, Z_h - 15.4 \ [dB] \tag{4.15}$$

Significant deviation below the rain line would be caused by the presence of ice in mixed-phase precipitation. If the reflectivity factors (boldface) are a sum of the reflectivity due to rain, "R", and ice, "I", ($\mathbf{Z_h}=\mathbf{Z_{hR}} + \mathbf{Z_{hI}}$ and $\mathbf{Z_v}=\mathbf{Z_{vR}} + \mathbf{Z_{vI}}$) and it is assumed that $\mathbf{Z_{hI}}=\mathbf{Z_{vI}}$, then the difference of the reflectivity factors is due solely to measurably oblate rain or $\mathbf{Z_h} - \mathbf{Z_v}=\mathbf{Z_{hR}} - \mathbf{Z_{vR}}$. Using the dashed line in Fig. 4.2, $\mathbf{Z_{hR}}$ can by inferred from a measured Z_{dp} since $\mathbf{Z_{hR}}=\mathbf{Z_h}$ for pure rain. The fraction of rain can thus be defined as

$$f = \frac{Z_{hR}}{Z_h} \tag{4.16}$$

and hence the reflectivity weighted fraction of ice and rain particles is obtained as

$$\frac{Z_{hI}}{Z_{hR}} = \left(\frac{1-f}{f}\right) \tag{4.17}$$

To estimate the linear relationship between Z_h and Z_{dp} in this study, Z_{dp} was plotted versus Z_h for data from the lowest grid level (0.5 km AGL) at 1735 MDT on 21 May 1993 (Fig. 4.2). The overall storm intensity had decreased significantly by this time so that possible contamination by ice is assumed to be negligible. The validity of this assumption will be verified later in Ch. 5 (e.g., see Figs. 5.8 or 5.9). The least-squares fit line to the points in Fig. 4.2 (solid line) is

$$Z_{dp} = 1.10\, Z_h - 9.36 \quad [\text{dB}] \tag{4.18}$$

As can be seen in Fig. 4.2 or by comparing Eqns. (4.15) and (4.18), the empirical rain line for this data set is similar to the theoretical line deduced by Golestani et al. (1989). This result is also very similar to the findings of Conway and Zrnic (1993) who found the slope m = 1.13 and intercept b = -9.1 in the decaying stage of a severe Front Range, Colorado hailstorm. The slight differences in the equations for these three lines could be due to inaccuracies in radar/antenna calibration and/or differing drop-size distributions. Since Eqn. (4.18) and that of Conway and Zrnic (1993) are so similar, we speculate that rain in Colorado hailstorms exhibit similar drop-size distributions which are somewhat different than the simulated gamma drop-size distribution used by Golestani et al. (1989). The empirical rain line in Z_h - Z_{dp} space given by Eqn. (4.18) and depicted as a solid line in Fig. 4.2 will be used throughout the rest of this study to analyze radar data in mixed-phase precipitation.

4.3.2.3 Specific differential phase method, Z_h and K_{dp}

The discrimination between ice and liquid hydrometeors is also effectively accomplished by examining scatter plots of K_{dp} and Z (where Z is an average of the horizontal and vertical reflectivity) as demonstrated by Balakrishnan and Zrnic' (1990a). They determined an empirical relationship for a boundary in K_{dp}-Z space that distinguishes

pure rain from mixed-phase and hail from observations of Oklahoma (OK) storms which is given by

$$Z = 8 \log(2K_{dp}) + 49 \ \ [dBZ] \tag{4.19}$$

The curve depicting this boundary is shown as a solid line in Fig. 4.3. This empirical boundary is relatively independent of local climatological effects since K_{dp} is not biased by the presence of hail and is relatively insensitive to drop size distribution. The lower the measured K_{dp} for a given Z from that given by Eqn. (4.19), the higher the probability that the precipitation contains hail. The data points shown in this scatter plot are from actual radar data taken in an OK rainstorm. Consequently, all but two of the K_{dp}-Z pairs fall below the given rain/mixed-phase boundary.

Balakrishnan and Zrnic' (1990a) also presented several simple models of mixed-phase precipitation in order to better detect and possibly quantify the amount of hail. A set of curves in the K_{dp}-Z plane (Fig. 4.4) illustrate the effects of various amounts of spherical hail in mixed-phase precipitation. These theoretical curves were calculated from the Cheng-English hail-size distribution and the Marshall-Palmer drop-size distribution. The hailstones are assumed to be spherical and dry (refractive index = $1.78 + j0.007$) or water-coated (wet with refractive index = $9.0585 + j1.3421$). Figure 4.4 indicates that it is possible to estimate the hail fraction (R_h/R_e) from the K_{dp}-Z pairs and hence quantify individual contributions due to rain and hail. This estimate is only valid to the extent that the assumptions used in the model are representative of real conditions. Balakrishnan and Zrnic' (1990a) presented results from several other models with different assumptions about hailstone shape and refractive index. The key results from all of these modeling studies, including the one depicted in Fig. 4.4, are: 1) Precipitation that is comprised primarily of hail results in a tight clustering of points around the line with $K_{dp} \approx 0$; 2) As the amount of hail decreases toward zero, the K_{dp}-Z points should cluster around curves similar in shape to those in Fig. 4.4 that approach the mixed-phase boundary ($R_h/R_e = 0$, also depicted in Fig. 4.3).

Since K_{dp} is influenced by anisotropic hydrometeors only (i.e., rain) as described earlier, K_{dp} and Z can also provide a quantitative estimate of precipitation liquid water and ice in mixed-phase precipitation. This is accomplished by separating the rain and hail contributions to the reflectivity factor (Balakrishnan and Zrnic', 1990a). To obtain the portion of the reflectivity factor due to hail, $\mathbf{Z_H}$, the contribution due to rain, $\mathbf{Z_R}$, must be subtracted from the measured **Z**. An indirect estimate of $\mathbf{Z_R}$ can be obtained by combining known K_{dp}, R and $\mathbf{Z_R}$, R relationships as shown in Doviak and Zrnic' (1993). They have derived the following K_{dp}, $\mathbf{Z_R}$ relationship:

$$Z_R = 65{,}800\left(K_{dp}\right)^{1.386} \quad (\text{mm}^6\ \text{m}^{-3}) \tag{4.20}$$

The contribution of hail to the reflectivity factor is thus $\mathbf{Z_H} = \mathbf{Z} - \mathbf{Z_R}$ ($\text{mm}^6\ \text{m}^{-3}$). This is then substituted into the following R_H, $\mathbf{Z_H}$ relationship based on the Cheng and English (1983) hail size distribution to yield the precipitation rate (liquid equivalent) from hail:

$$R_H = \frac{88}{\exp\left[\left(5.38\times10^{-6}\,\mathbf{Z_H}\right)^{-0.30}\right]} \quad (\text{mm h}^{-1}) \tag{4.21}$$

The accuracy of this estimate is dependent on three key assumptions: 1) the validity of the $\mathbf{Z_R}$, R relationship used, 2) the applicability of the Cheng and English hail size distribution, and 3) updrafts and downdrafts are insignificant compared to the terminal velocity (i.e., $|w| \ll V_t$) at the level of measurement.

4.3.3 Method of bulk hydrometeor identification

The experience gained from the above techniques for distinguishing hydrometeor types and amounts using pairs of polarimetric measurements can be extended to include all available multiparameter variables. Doviak and Zrnic' (1993) and Straka and Zrnic' (1993) have proposed a multiparameter decision process that partitions the five-dimensional space of Z_h, Z_{dr}, K_{dp}, $\rho_{hv}(0)$, and LDR (Linear Depolarization Ratio) so that each partition uniquely corresponds to a distinct hydrometeor type. This method of bulk-

hydrometeor identification is based primarily on modeling studies in addition to observational studies and the experience of various investigators, and relies on the successful partitioning of two-dimensional subspaces such as K_{dp} and Z as seen in Fig. 4.3 and Z_h and Z_{dp} (Fig. 4.2). Combining the methods discussed in the previous three sections with the knowledge of $\rho_{hv}(0)$ presented in Sec. 4.2.4, it is possible to infer the presence of precipitation sized ice in the RRV.

We have adapted this method to identify graupel and hail particles above and below the melting level using the four polarimetric variables available in our study [Z_h, Z_{dr}, K_{dp}, and $\rho_{hv}(0)$]. Since LDR was not available for our study, it was necessary to make some adjustments to the partitioning found in Doviak and Zrnic' (1993). The resulting four-dimensional partitioning is shown in Table 4.1. Note that these values are for ideal conditions (i.e., low sidelobes and minimal noise) and are only applicable to deep convection in the mid-latitudes. To support the validity of bulk-hydrometeor identification, we use the Z_{dp}/Z_h and K_{dp}/Z techniques presented above to independently corroborate the presence of graupel and hail in the multi-cell storm being studied (Ch. 5).

In order to clarify the terminology used in Table 4.1, we note that hail is defined as a type of precipitation often composed of concentric spheres of alternating clear (riming with wet growth) and opaque (riming with dry growth) ice, having diameters of up to 50 or more mm (Encyclopedia of Climatology, 1987). In the encyclopedia, they recognize three general types of hail: graupel (or soft hail), small hail, and "true" hail. The key difference between graupel and hail is the lack of any wet growth stages for the former. The key difference between small and true hail is size. It is typically not possible to infer the presence of wet growth hail with the multiparameter observables in this study (the positive Z_{dr} columns discussed in Ch. 6 are noticeable exceptions). Since the dielectric constant, shape, orientation, and size are the most dominant effects of hail on the multiparameter variables, we have organized Table 4.1 as shown. In this study, an expanded definition of graupel is utilized which includes small hail (< 2 cm) and soft hail.

We make the simplifying assumption that all ice below the melting level is wet and all ice above the freezing level is dry. This assumption appears to be a valid one in all situations except within the positive Z_d columns where rain and ice were mixed above the freezing level.

4.3.4 Dual-Doppler analysis

Limited opportunities for dual-Doppler analyses using radial velocity data from the CSU-CHILL and MHR radars were available for both case studies. In order to conduct dual-Doppler analysis, the following criteria had to be met: 1) approximately synchronous scanning times (within tens of seconds) for both radars, 2) sufficient temporal resolution for studying the electrification of deep convection ($\leq$ 6 minutes), 3) sufficient horizontal and vertical spatial coverage (this will be discussed more in the following sections), and 4) the storm must occur within an area defined by the intersection of the flat plate antenna range of operation and one of the dual-Doppler lobes (outside the baseline) as depicted in Fig. 3.1.

4.3.4.1 Brief review of method

The theoretical basis for estimating the three dimensional wind velocity field from the precipitation particle radial velocity data from two radars and the equation of mass continuity for air has been established for some time now (e.g., Armijo, 1969). In this study, we utilized the interactive version of CEDRIC (Custom Editing and Display of Reduced Information in Cartesian space) developed at NCAR to synthesize the radial velocity data into Cartesian space, filter radar fields when necessary, and execute the necessary algebraic functions and integrations (Mohr and Miller, 1983). A brief overview of the general method utilized to calculate the 3-D wind field using CEDRIC will now be given.

Using CEDRIC the radial velocity field from the CSU-CHILL and MHR radars were synthesized onto a Cartesian grid using a differential advection correction scheme. Storm speed and direction were determined from a detailed inspection of the CSU-CHILL

reflectivity field. Next, utilizing the notation of Mohr and Miller (1983) CEDRIC relates the radar beam crossing angle, β, to the velocity error variances in order to define the acceptable area for dual-Doppler analysis.

$$\frac{\sigma_u^2 + \sigma_v^2}{\sigma_1^2 + \sigma_1^2} = \csc^2 \beta \equiv b \tag{4.22}$$

where σ_u^2 and σ_v^2 are the error variances in the dual-Doppler velocity estimate, σ_1^2 and σ_2^2 are the velocity error variances from radars 1 and 2, and b is the parameter input into CEDRIC. In general, the more orthogonal the crossing beams are from each radar, the smaller the error. For beam crossing angles, β, less than about 30°, error variances for u and v increase rapidly (Doviak and Zrnic, 1993). We choose to input b = 3.75 into the CEDRIC software package which corresponds to a beam crossing angle of β = 31.1°. Assuming that the velocity error variances from radar 1 and 2 are approximately 1 m s^{-1} each, this would result in a combined dual-Doppler error variance of $\sigma_u^2 + \sigma_v^2 = 7.5\,\mathrm{m\,s^{-1}}$. Recovery of the 3-D wind field using only 2 radars requires knowledge of the terminal fallspeed, V_t, of precipitation particles in the RRV. This was accomplished in CEDRIC using a specific V_t vs. Z_h relationship above and below the melting level.

Initial estimates of the horizontal velocities were then computed assuming that the vertical velocity was zero. From these estimates of the horizontal velocities, a horizontal divergence field was then calculated. An initial estimate of the vertical velocity field was computed from this horizontal divergence field by integrating the mass continuity equation. A downward integration was performed with an upper boundary condition of w = 0 m s^{-1} at storm echo top ($Z_h \approx 0$ dBZ). A downward integration is preferred since exponentially decreasing air density with height decreases errors associated with wind estimate errors (Bohne and Srivastava, 1975). With the new estimate of the vertical velocity, CEDRIC was used to re-compute the horizontal velocity field.

Successive iterations of the procedure described in the above paragraph were performed until the change in the calculated horizontal velocity was less than the expected measurement error. Computation was halted when the average (over all vertical levels in the grid) change in each calculated horizontal velocity was ≤ 0.1 m s^{-1}. Typically, only 2 or 3 iterations were necessary to achieve the above criteria. Finally, CEDRIC was used to calculate an adjusted divergence and adjusted vertical velocity by redistributing mass associated with errors in the vertical velocity throughout the dual-Doppler domain as discussed in Biggerstaff and Houze (1993). Assuming $w = 0$ m s^{-1} at storm top and integrating downward, these errors are determined by estimating distributions of vertical velocity at the ground where w should be zero.

4.3.4.2 Sources of error

A complete discussion of errors associated with 3-D wind field estimation from dual-Doppler radar measurements can be found in Doviak et al. (1976). In this section, we present a brief outline of some of these sources of error.

1) Intrinsic variance in the mean Doppler velocity and reflectivity estimates from each radar caused by the statistical nature of a weather echo.

2) Non-uniform shear and asymmetric reflectivity factor within the radar resolution volume (RRV).

3) The use of an incorrect V_t, Z relationship. The presence of large hail can often cause significant errors in fall speed estimation if not considered in the calculation.

4) Inaccuracies in the beam position or location of the RRV due to errors in assumed azimuthal or elevation position.

5) Bias caused by velocity editing procedures.

6) Uneven terrain features between the radar and the storm.

7) Evolution of the storm during scanning. An attempt was made to correct for this source of error with the differential advection correction scheme.

8) Echoes received through sidelobes that contaminate signals associated with the RRV.

9) Increases in the vertical velocity variance with each integration step due to error in the divergence used in the continuity equation. This can occur due to the incomplete sampling of low-level or upper-level divergence or an improper top boundary condition specification.

No attempt was made to quantify the actual magnitude of errors in the computed horizontal and vertical wind field in this study. Given the above sources of error, we believe that the horizontal velocity estimates are accurate to within 2-4 m s^{-1} (Nelson and Brown, 1982). The vertical velocity field is the most difficult to reliably estimate of the three components of the wind and errors can be fairly substantial. Doviak et al. (1976) calculated a theoretical standard deviation of the vertical velocity, σ_z, of 6 - 7 m s^{-1} with a boundary condition of w = 0 m s^{-1}at storm top and downward integration. Several studies (e.g., Nelson and Brown, 1982; 1987; Vasiloff et al., 1986) have estimated σ_z and found values ranging from 5 - 10 m s^{-1} which are close to the theoretically expected values given above. The errors in w associated with these relatively large standard deviations can be reduced by using a variational adjustment technique to produce an adjusted wind field that satisfies both top and bottom boundary conditions (w = 0 at echo top and at the ground) in addition to the continuity equation (Zeigler, 1978). In the dual-Doppler analyses in this thesis, the mass redistribution scheme discussed by Biggerstaff and Houze (1993) was employed.

Table 4.1. Bulk-hydrometeor identification using multiparameter radar variables. (Adapted from Doviak and Zrnic', 1993)

Precipitation Type	Zh (dBZ)	Zdr (dB)	$\|\rho hv(0)\|$	Kdp (deg km-1)
Graupel, (T < 0° C)	40 to 50	-0.5 to 0.5	> 0.99	-0.5 to 0.5
Graupel, (T ≥ 0° C)	50 to 60	-0.5 to 1	> 0.95	-0.5 to 0.5
Hail, ≥ 2 cm (T < 0° C)	≥ 55	< -0.5	> 0.95	-0.5 to 0.5
Hail, ≥ 2 cm (T ≥ 0° C)	≥ 55	< -0.5	≤ 0.95	-1.0 to 1.0

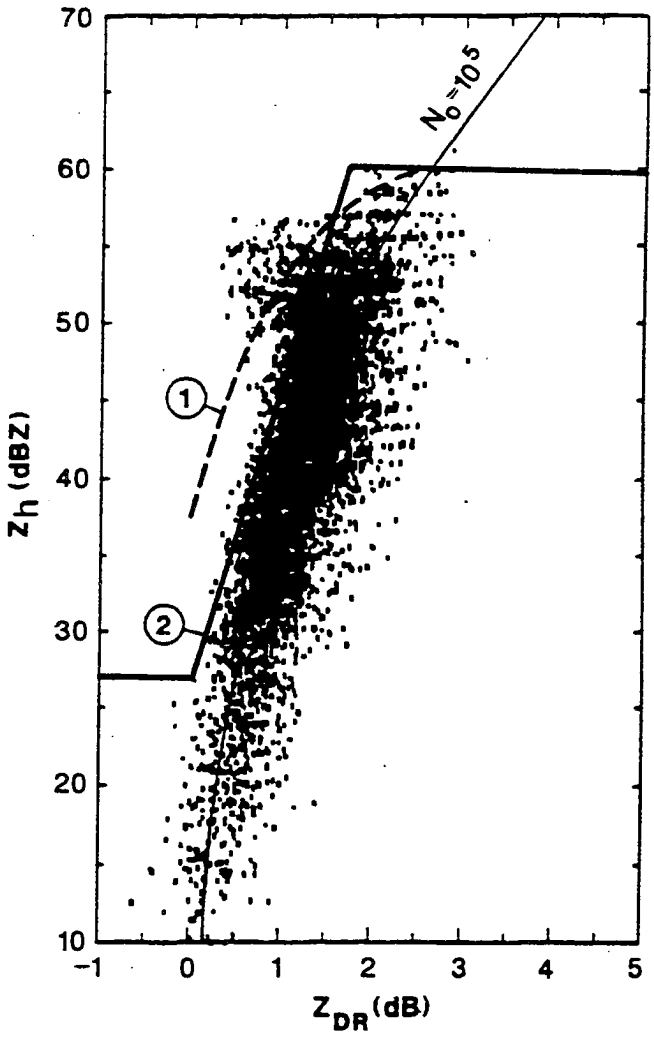

Fig. 4.1 Scatter plot of Z_h vs. Z_{dr} for rainfall at 1° elevation in an Oklahoma rainstorm on 10 June 1986. The thin solid curve for $N_0 = 10^5$ mm^{-1} m^{-3} is plotted from Steinhorn and Zrnic (1986). The dashed line labeled (1) is the rain-hail boundary in the Z_{dr} / Z_h plane proposed by Leitao and Watson (1984) and the thick solid line labeled (2) is a similar boundary from Aydin et al. (1986). Adapted from Doviak and Zrnic (1993).

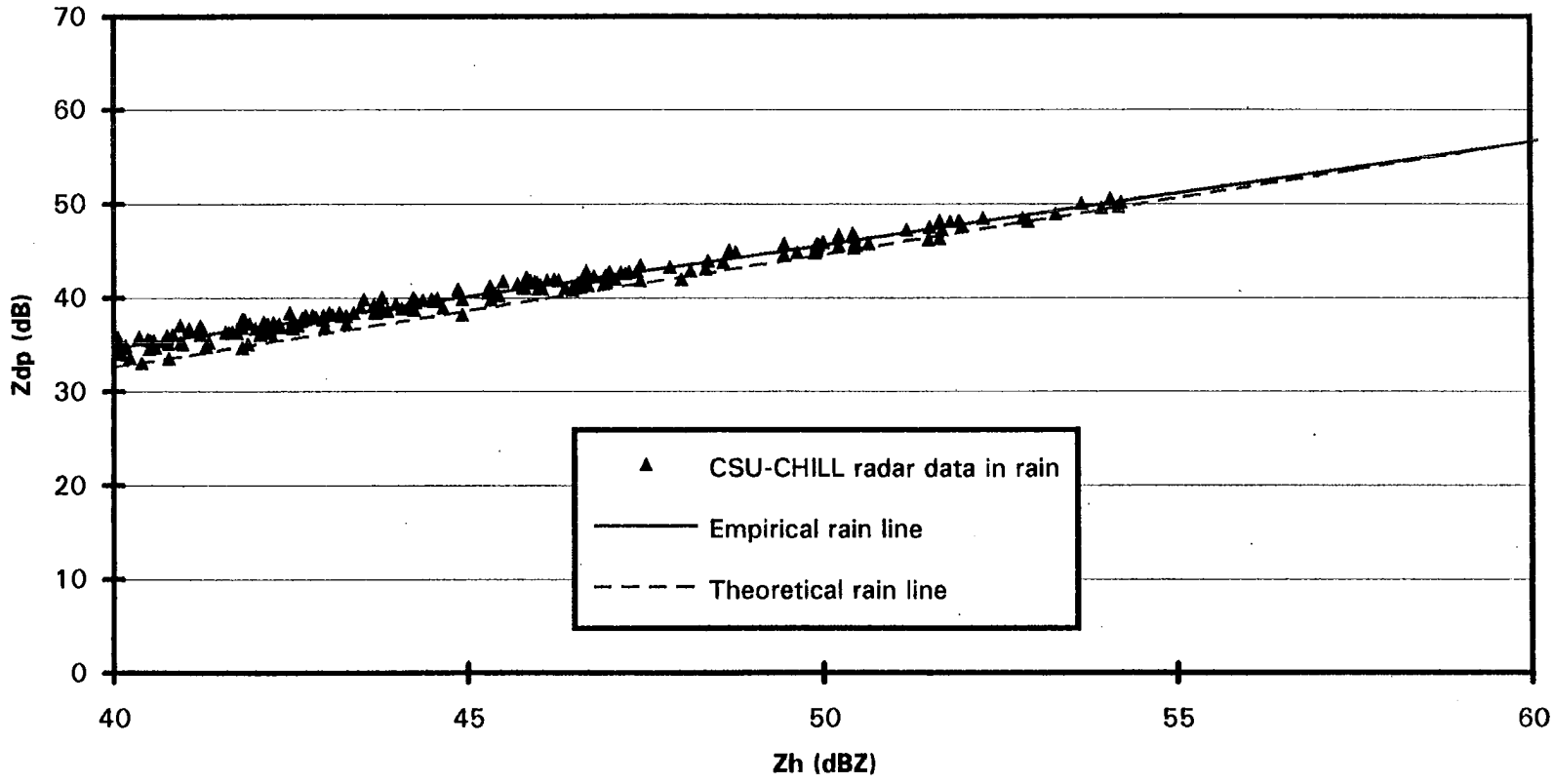

Fig. 4.2 Scatter plot of $Z_{dp} = 10 \log (\mathbf{Z_h} - \mathbf{Z_v})$ [dB] vs. Z_h [dBZ] for CSU-CHILL radar data at 0.5 km AGL in rain on 21 May 1993 at 1735 MDT. The solid line is the least-squares fit line (linear correlation coefficient, r = 0.98) to the CSU-CHILL radar data. The dashed line depicts the best fit line for simulated gamma raindrop size distributions from Golestani et al. (1989).

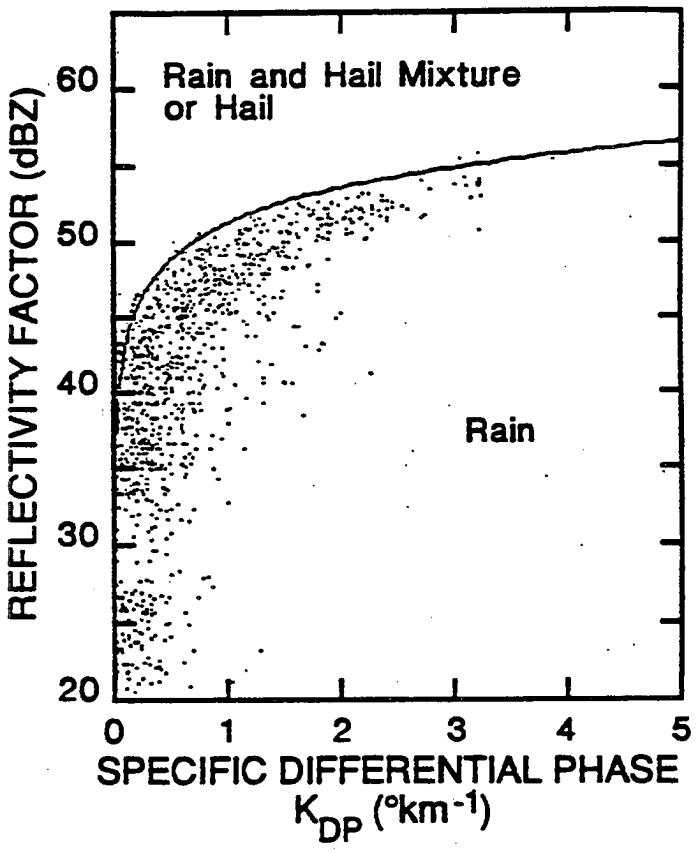

Fig. 4.3 Scatter plot of Z-K_{dp} of about 1400 radar measurements for an Oklahoma rainstorm on 10 June 1986. The empirical boundary between rain and mixed phase or hail is shown as a solid line. Z is an average of reflectivity factors at horizontal (Z_h) and vertical polarizations (Z_v). (Adapted from Balakrishnan and Zrnic', 1990a)

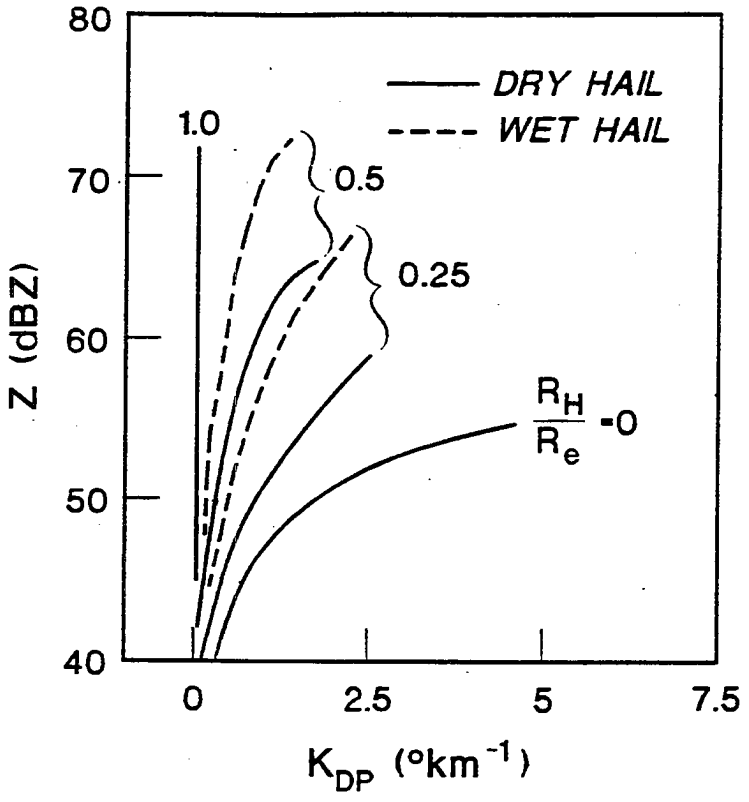

Fig. 4.4 Z - K_{dp} variations in simulated mixtures of rain and both wet and dry spherical hail. See text for more details concerning model. R_h is the liquid equivalent hailfall rate. R_e is the sum of rainfall and hailfall rates. The curve for wet hail and $R_h / R_e = 1$ coincides with the $R_h / R_e = 1$ curve for dry hail. (Adapted from Balakrishnan and Zrnic', 1990a)

CHAPTER 5

CASE STUDY 1

A MULTI-CELL THUNDERSTORM

We examine the co-evolving microphysical, kinematic, and electrical characteristics of a multi-cell thunderstorm observed on 21 May 1993 along the Front Range of Colorado. Recent modeling and observational advances in weather radar polarimetry now permit the inference of bulk-hydrometeor types and mixing ratios, and the measurement of precipitation rate in mixed-phase (i.e., hail and rain) environments. We have employed these and other radar techniques, such as dual-Doppler analyses, to investigate the correlation between the convective life cycle of a multi-cell storm and the evolution of lightning type and flash rate, and electric field strength and polarity.

5.1. Atmospheric conditions

As shown in Fig. 5.1, the afternoon Denver, CO sounding on 21 May 1993 (22 May 1993/0000 GMT) was characterized by an "inverted-V" just above the surface, with dry air up to 3.0 km AGL (above ground level) and deep moisture through the rest of the troposphere. The sounding showed low (< 1000 J kg^{-1}) convective available potential energy (CAPE) and moderate westerly shear due to westerly flow aloft (above 2 km AGL) at about 7 - 10 ms^{-1} and deep surface upslope (lowest 2 km) out of the east at 3 - 5 ms^{-1}. These upper-air sounding conditions were conducive to the formation of long-lived, multi-cell storms which are typically not severe (Bluestein, 1993) As a result of the east-southeasterly upslope flow observed at the surface in Front Range mesonet data at 1530 MDT (2130 UTC, Fig. 5.2), near surface conditions were relatively moist with dewpoints

of about 7° C (45° F). A dissipating surface warm front was oriented N-S in eastern Colorado and a weak ridge of high pressure dominated the upper-levels of the western United States at 500 hPa (or mb) with no evidence of any short waves influencing the weather. With ample mid-level moisture, dry low-level conditions (beginning just above the surface), and upslope winds at the surface, the atmosphere along the Front Range of the Rocky Mountains was primed for diurnally-forced thunderstorms with the potential for producing strong microbursts (Caracena et al., 1983; Wakimoto, 1985).

5.2. Kinematic and microphysical evolution of a typical cell

Comprehensive multiparameter, Doppler, and electrical observations of the evolution of the multi-cell storm were obtained as it moved through the observational network during a two hour period. During this time, the storm produced a total of 507 IC flashes with a peak flash rate of about 10 min^{-1}. A total of 34 CG flashes were recorded, resulting in an inferred IC/CG ratio of about 15. This ratio is about five times larger than values typically reported for average midlatitude thunderstorms (Price and Rind, 1993, for $\lambda = 40°$) and is therefore an interesting aspect of this storm. Multiparameter radar data were collected at six minute intervals for this entire period and dual-Doppler analyses were possible during the initial thirty minutes while the storm precipitation ice mass grew exponentially with time.

This multi-cell storm which produced marble-sized hail (1 - 1.5 cm in diameter), heavy rain, and several microbursts in addition to frequent lightning entered the CSU-CHILL network (within range of the flat plate antenna) at about 1514 MDT (Mountain Daylight Time). First lightning was detected at 1535 MDT in response to rapidly developing cells aloft in the forward anvil region of decayed convection. The most vigorous cell was located 48 km to the west-southwest (x = - 44 km and y = - 19 km) at 1532 MDT as shown in the horizontal cross-section of reflectivity at 2 km AGL (Fig. 5.3a). Explosive convective growth occurred within range of the flat plate antenna (50 km) during the next

eighteen minutes as can be seen from the significant increase in area of Z_h > 40 dBZ by 1550 MDT (Fig. 5.3b). This rapid development can be clearly seen in vertical cross-sections of reflectivity and storm relative velocity through the most vigorous cell at 1532 MDT (Fig. 5.4a) and 1550 MDT (Fig. 5.4b).

During this period, the total storm flash rate increased from 0.3 min^{-1} to 0.9 min^{-1} while the maximum height of the 40 dBZ contour increased from 9.5 km at 1532 MDT to 11 km AGL at 1550 AGL. As seen in Fig. 5.4b, an enhanced reflectivity feature (> 55 dBZ) developed between 5 km and 7.5 km AGL in the storm updraft centered on x = -33 km. The maximum updraft in this cell increased from 11 ms^{-1} at 1532 to 16 ms^{-1} by 1550 MDT and was consistently found in the upper-half of the storm (5.5 to 9.5 km). If the graupel and small hail which are responsible for the enhanced reflectivity feature are the primary source of negative charge at these heights as suggested by the non-inductive charging mechanism, then these observations are consistent with the findings of Lhermitte and Krehbiel (1979) who showed that the sources of negative charge centers were located in the vicinity of a maximum reflectivity feature aloft co-located with strong upward motion.

This region of enhanced reflectivity co-located with the maximum updraft was a persistent feature in the dual-Doppler analysis from 1532 to 1559 MDT (not shown) and was typically centered at about z = 6.5 km AGL (T = -25°C). This persistent feature is suggestive of a "particle balance level," as observed by Lhermitte and Williams (1985) at 6-7 km MSL in Florida thunderstorms.

This level is characterized by a balance between particle terminal fall speeds and the storm updraft. The observations of Lhermitte and Williams suggested that large precipitation particles were suspended in the updraft at this level and were possibly responsible for the lightning negative charge centers that were less than 1 km above this level (generated through the non-inductive charging process). The multiparameter radar variables in the enhanced reflectivity region of Fig. 5.4b (not shown), with reflectivity

between 45 and 60 dBZ, Z_{dr} ranging from -0.5 to 0.5 dBZ, and near zero K_{dp} implied the presence of large graupel and small hail, as can be seen by comparing these values to the K_{dp}-Z rain-hail boundary found in Fig. 4.3 and the Z_{dr}-Z_h rain-hail boundaries proposed by Leitao and Watson (1984) and Aydin et al. (1986) found in Fig. 4.1. Matson and Huggins (1980) developed a terminal velocity equation for hailstones in Colorado thunderstorms, using diameter, D, as input: $V_t = 3.62\sqrt{D}$ m s^{-1}. By balancing the particle terminal velocity, the maximum vertical velocity at 1550 MDT of 16 m s^{-1} (Fig. 5.4b) would be capable of suspending a 2 cm hailstone according to the above equation. As a result, both dual-Doppler synthesized vertical velocities and multiparameter radar variables suggest the possibility of hail within the enhanced reflectivity feature aloft.

From 1550 to 1611 MDT, the entire storm continued to grow slowly in areal extent as inferred from the horizontal cross-section of reflectivity seen in Fig. 5.3c. Much of this growth was the result of the development of a second cell centered on Y = - 10 km (see Figs. 5.3b and c). Meanwhile, the total lightning flash rate increased exponentially from 0.9 min^{-1} to 7.5 min^{-1}. The cell centered on y = -19 km entered the mature phase by 1611 MDT with 40 dBZ echo tops descending to 9 km AGL (Fig. 5.4c). Note in Fig. 5.4c that the enhanced reflectivity feature identified in Fig. 5.4b descended below the -10° C level (4 km) with all of the Z > 60 dBZ echo below the melting layer.

The descent of this enhanced reflectivity feature below the -10° C level was associated with a peak in the CG flash rate of 0.58 min^{-1} at 1611 MDT. Since Williams et al. (1989a) hypothesized that CG lightning is associated with the descent of graupel and hail particles below the height of the main negative charge (typically near -10° C for areas climatologically similar to Colorado; Williams, 1989), it is worthwhile to use multiparameter radar data to infer the presence of hail in this enhanced reflectivity feature. To this end, contours of differential reflectivity are in included in Fig. 5.4c. At x = - 24 km and z = 0.5 km, Z_h and Z_{dr} are anti-correlated with a maximum in Z_h (> 60 dBZ) and a minimum in Z_{dr} (< 0.5 dB). Bringi et al. (1984) identified this pattern as being

associated with hail below the melting level. This finding is supported by comparing values in the hail shaft (Z_h = 60 dBZ and Z_{dr} = 0.5 dB) with the rain-hail boundaries proposed by Leitao and Watson (1984) and Aydin et al. (1986) shown in Fig. 4.1. Using Eqn. (4.13), we find that the Aydin et al. (1986) hail detection signal for this region is H_{dr} = 23.5, clearly identifying the presence of hail. On either side of the hail shaft, there are maxima in Z_{dr} (1.5 - 3 dB) with reflectivities near 40 dBZ associated with rain shafts (as is verified with comparison to Fig. 4.1).

Range profiles (azimuth = 231°, elevation = 0.5°) of Z_h, Z_{dr}, $\rho_{hv}(0)$, and K_{dp} through this cell are shown in Figs. 5.5a and b. The Z_{dr} hail signature ($-1 \leq Z_{dr} \leq 0$ dB) associated with large oblate hail (Bringi et al., 1986a) is clearly seen with Z_h = 60 dBZ in Fig. 5.5a at a range, R, of 30.3 km. As in Fig. 5.4c, maxima in Z_{dr} occur on either side of the hail shaft. The correlation coefficient and specific differential phase depicted in Fig. 5.5b have more complex patterns in and around the hail shaft. Notice that ρ_{hv} has a relative maximum (0.98) coincident with the minimum in Z_{dr} and maximum in Z_h at R = 30.3 km. On either side of this point, there are relative minima in $\rho_{hv}(0)$ ($\rho_{hv}(0)$ = 0.945 at R = 29.7 km and $\rho_{hv}(0)$ = 0.96 at R = 31.0 km) coincident with significant increases in Z_{dr} and decreases in Z_h. Since $\rho_{hv}(0)$ is mainly affected by the variability in the ratio of the vertical-to-horizontal size of individual hydrometeors within the RRV, it is consistent for minima in $\rho_{hv}(0)$ to be associated with rapid changes in Z_{dr} which is a measure of the reflectivity weighted axis ratio. The specific differential phase has a maximum (1.3° km^{-1}) that is nearly coincident with the minimum in $\rho_{hv}(0)$ between 29 and 30 km in range. It is important to note that although K_{dp} decreases through the previously identified hail shaft at R = 30.3 km, it still has a value of 1° km^{-1}. Since Jameson (1985) demonstrated that K_{dp} is proportional to W, the precipitation liquid water content, the hail must be mixed with rain. Using the rain rate equation, $R = 40.7(K_{dp})^{0.866}$ mm h^{-1} (Sachidananda and Zrnic, 1987), K_{dp} = 1° km^{-1} is equivalent to a rain rate of 40 mm h^{-1}. Since the correlation coefficient still has the intrinsic value for pure hail despite the presence of rain,

we must conclude that the hail dominates the reflectivity factor as also inferred from a negative Z_{dr}.

Moving radially outward from the center of the precipitation shaft, the reflectivity weighted distribution of rain and hail must be approximately equal at R = 29.7 km where the correlation coefficient is a minimum. To support this premise, the reflectivity due to rain is calculated using both the Z_h-Z_{dp} and Z-K_{dp} methods as discussed in Secs. 4.1.2 and 4.1.3. Using Eqn (4.20) with $K_{dp} = 1.2°$ km and converting to decibels, the contribution of rain to the reflectivity is Z_R = 49 dBZ. Since the measured total reflectivity is 52 dBZ, the hail contribution is also about Z_H = 49 dBZ, satisfying the criteria for a local minimum in $\rho_{hv}(0)$ (Balakrishnan and Zrnic, 1990b). A reflectivity of 52 dBZ and Z_{dr} = 1.2 dB is equivalent to Z_{dp}= 46 dB. Substituting this value into Eqn. (4.18) results in Z_{hR} = 50 dBZ (since $Z_h = Z_{hR}$ in pure rain). A rain fraction of f = 0.6 is obtained using Eqn (4.16) which is in relatively close agreement with the expected value of f = 0.5. Both methods support the conclusion that the $\rho_{hv}(0)$ minimum at R = 29.7 km is caused by mixed-phase precipitation in which the reflectivity weighted distribution of rain and hail is about equal. Moving further outward toward R = 28 km, rain is now the dominant hydrometeor type as indicated by the increase in $\rho_{hv}(0)$ above 0.97, the large values of Z_{dr} (2.5 - 4.0 dB), and the significant K_{dp} ($\approx 1°$ km^{-1}). Through a detailed analysis of the polarimetric radar data, the presence of hail has been inferred. The observed double $\rho_{hv}(0)$ minima centered on a coincident minimum in Z_{dr} and a maximum in Z_h in the presence of significant K_{dp} has been interpreted as a mixed phase precipitation shaft with the hail contribution to reflectivity dominating within the center of the shaft and decreasing radially outward. It is interesting to note that the observed minima in $\rho_{hv}(0)$ (0.94 - 0.95) are associated with hailstones in the size range of 1 to 2 cm when mixed with rain (Balakrishnan and Zrnic, 1990b). This range of sizes is consistent with the observed updraft that could have suspended a hailstone up to 2 cm in diameter as discussed earlier.

In this section, we presented the evolution of the kinematic and precipitation structure of a typical cell within the multi-cell storm. The total flash rate increased during a period of vertical growth as inferred from the ascent of the 40 dBZ echo. As the storm grew vertically, dual-Doppler synthesized upward vertical velocities continued to increase in magnitude. Multiparameter radar data of an enhanced reflectivity feature aloft was discussed. Both the dual-Doppler derived winds and the multiparameter radar data within the feature were consistent with the presence of large graupel and hail suspended in the updraft. The descent of this enhanced reflectivity feature below the inferred level of main negative charge was coincident with a maximum in the CG flash rate. We provided further multiparameter radar data at low elevation suggesting the presence of hail within the descending precipitation shaft. With an understanding of the evolution of a typical cell within the storm, we can now present correlations between microphysics, kinematics and electrification on the storm scale.

5.3. Correlation between convective life-cycle and lightning type

5.3.1 IC lightning and the updraft accumulation of graupel and hail

In this section, we provide strong evidence that the storm-wide, updraft-driven accumulation of graupel above the melting level is highly correlated to the in-cloud flash rate. The method of bulk-hydrometeor identification as presented above was used to infer the relative amount of graupel in the storm. Any grid volume above the melting level ($T < 0^{\circ}C$) which satisfied the given ranges of the multiparameter variables in Table 4.1 for graupel was added to the graupel storm volume. Recall that our expanded definition of graupel includes soft hail and small hail (< 2 cm). Note that no grid points above the melting level satisfied the criteria for hail ($\geq$ 2 cm) shown in Table 4.1. The graupel volume cannot be simply multiplied by a representative graupel density to calculate total graupel mass since it is merely the echo volume which is dominated by the multiparameter variables indicative of graupel and small hail. It can be shown however that this volume is

proportional to the total graupel mass and is therefore a reliable measure of the location and amount of graupel in an evolving storm.

The results were calculated at twelve minute intervals (frequency of volume scan data) and plotted on a logarithmic scale with the average in-cloud flash rate (min^{-1}) during the period centered on the radar time (Fig. 5.6), and indicated the graupel volume was strongly correlated to the IC flash rate. Both the graupel storm volume and the IC flash rate increased exponentially (linearly on a logarithmic scale) during initial stages of the storm. On closer inspection, the exponential growth of graupel volume from 1535 MDT to 1547 MDT preceded the exponential growth of the IC flash rate from 1547 to 1611 MDT. Also, note that the peak in the graupel volume occurred twelve minutes before the peak in the IC flash rate. Both of these observations are consistent with the findings of Goodman et al. (1988) which showed an exponential growth of precipitation mass aloft for several minutes before first lightning. In an investigation of the correlation between precipitation development and the initial electrification of New Mexico thunderstorms, Dye et al. (1989) found that the average time delay between the development of precipitation aloft with $Z_h > 40$ dBZ and the first lightning flash was about 17 minutes. The average time delay was closer to 11 minutes for storms which were experiencing significant convective growth during electrification. Assuming that the above reflectivity threshold can be used as a crude indicator for graupel, the 11 minute time delay between graupel formation aloft and first lightning is very similar to the 12 minute lag between graupel volume and the IC flash rate shown in Fig. 5.6. This apparent lag could be attributed to the time necessary to allow the gravitational sedimentation of enough graupel particles from oppositely charged, smaller ice crystals to produce an electric field sufficiently large for dielectric breakdown.

To support this hypothesis, we have estimated the scale of vertical charge separation, z_{cs}, that would have occurred due to gravitational sedimentation during this twelve minute lag in electrical startup. We have assumed that the terminal fall speed for graupel particles

is significantly larger than that of ice crystals ($V_{tg} >> V_{ti}$). Using triple-Doppler observations of the early development of a New Mexico thunderstorm, Raymond and Blyth (1989) measured particle terminal velocities of 4-8 m s^{-1} in a mixed phase region characterized by low reflectivities. On the other hand, Heymsfield (1978) calculated the terminal fall speeds of graupel particles in northeastern Colorado cumulus congestus clouds using in-situ measurements and found that the majority of values fell between 1 and 4 m s^{-1}. Using $V_{tg} = 4$ m s^{-1} as a representative value for our calculation, we estimate the vertical charge separation as $z_{cs} = (V_{tg} - V_{ti})t \approx (V_{tg})t = 3$ km. Krehbiel et al. (1984) inferred the heights of the negative and positive charge centers participating in lightning in a small Florida thunderstorm. They determined that the separation distance between these charge centers was about 3 km (with the negative charge center at about 7 km and the positive charge center at about 10 km) at the time of first lightning, lending some credence to our rough estimate.

Following the initial exponential growth of both graupel volume and IC lightning, both storm parameters in Fig. 5.6 remained relatively constant for 48 minutes before decreasing more rapidly after 1659 MDT. This approximate steady state in the electrical activity of storms after initial exponential growth was also noted by Williams (1989). It is interesting to note that both the graupel volume and the IC flash rate decreased by a factor of two during the approximate steady state stage (1623 - 1659 MDT). In contrast, the dissipating stage (1659 - 1735 MDT) was characterized by an IC flash rate that decreased twice as fast as the graupel volume (IC decrease/graupel volume decrease = 16/8 = 2). This seems to suggest that the charge separation per unit mass was fairly constant during the steady state stage but was reduced by a factor of two during the dissipating stage.

In past studies, the IC flash rate has been well correlated with the cloud vertical development as quantified by radar cloud top height and time-height cross-sections of radar reflectivity (e.g., Williams, 1985; Krehbiel, 1986; Goodman et al., 1988; Williams et al., 1989a). If the non-inductive charging mechanism is the primary means of charge

separation in thunderstorms, then a more direct measure of the cloud vertical development relevant to electrification would be the evolution of the vertical profile of graupel volume per unit interval of height as seen in Figs. 5.7a and b. Fig. 5.7a shows this evolution during a period of exponential growth in the IC flash rate as depicted in Fig. 5.6. Both the vertical extent and the total graupel volume increased with the IC flash rate. The maximum graupel volume was consistently between 5 and 6.5 km AGL (corresponding to a range of temperatures between -17 and -27°C).

Interestingly, this temperature range is similar to the range of temperatures measured for the negative charge regions participating in lightning for storms in various geographical regions in the United States (Williams, 1985). This consistent peak of negatively charged graupel and hail volume (negative charge as inferred from the laboratory non-inductive charging studies for these temperatures) within a 1.5 km thick layer could help explain the altitude stability of the negative charge region observed by Krehbiel et al. (1984) for a small Florida thunderstorm.

This consistent peak in graupel volume does however occur at temperatures somewhat cooler (or higher in height) then the range of temperatures (or heights) measured for negative charge regions in New Mexico (-10° C to -20° C; Krehbiel et al., 1979) which should be climatologically similar to Colorado. This apparent discrepancy can be explained by charge reversal microphysics and the inclusion of ice crystals into the charge budget of the negative charge region. There should be a predominance of negatively charged particles in the updraft near the charge reversal level due to negatively charged graupel falling from above combined with negatively charged ice crystals being carried from below. At some distance above the charge reversal level, any remaining negative charge on ice crystals should be neutralized such that all of them are charged positively. The presence of these upward moving, positively charged ice crystals would tend to reduce the magnitude of the net negative charge below that of the negative charge residing on the graupel alone. By including ice crystals into the charge budget with a non-

inductive charging mechanism, it is possible to explain how the level of peak graupel volume could be displaced slightly above the negative charge center.

The rapid decrease in the IC flash rate from 1717 to 1747 MDT (Fig. 5.7b) was associated with a decrease in the vertical extent and total volume of graupel and small hail within the storm as would be expected if rimed ice was the primary source of negative charge. This is also consistent with previous findings using reflectivity measurements (Krehbiel, 1986; Williams, 1985; Goodman et al., 1988; Williams et al., 1989a).

5.3.2 CG lightning and the descent of graupel and hail

Williams et al. (1989a) proposed that IC lightning dominates during initial stages of storm growth while negatively charged graupel and hail particles accumulate at mid-levels (as seen in Figs. 5.6 and 5.7a) because it is not energetically favorable to transfer negative charge to ground in CG lightning with this storm structure. Williams et al. went on to propose that CG lightning may be initiated by the descent of ice particles (i.e., graupel and hail) below the level of main negative charge where the action of charge reversal microphysics causes these large ice particles to charge positively. This lower positive charge may result in the electrical bias which allows for the transfer of negative charge to ground in CG lightning as first suggested by Clarence and Malan (1957). This hypothesis was supported by observations of electrical discharges in laboratory-scale space charge structures (Williams et al., 1985). The study demonstrated that laboratory discharges extended favorably into regions of concentrated space charge.

To further test this hypothesis, we compare the graupel volume at low levels (below the melting level) using the bulk-hydrometeor identification scheme in Table 4.1 to the CG flash rate. Fig. 5.8 shows the graupel volume and CG flash rate at twelve minute resolution. The correlation between descending ice and CG lightning suggested by Williams et al. (1989a) is confirmed in Fig. 5.8 with both peaks in ice volume accompanied by peaks in CG lightning. The peak at 1611 MDT was likely due to the collapse of the strongest of the initial cells (seen in Figs. 5.3c and 5.4c) which developed within the CSU-

CHILL data network while the second peak at 1723 MDT was the result of another vigorous cell which formed to the south-southeast of the radar in response to colliding outflow boundaries from two of the original cells (not shown).

To provide further evidence for this correlation, we calculated the peak precipitation rate associated with graupel and small hail in the lowest 1 km using K_{dp} and Z as outlined in Sec. 4.3.2.3 at six minute resolution. Fig. 5.9 shows that the liquid equivalent hail rate was well correlated with the number of CG flashes per six minute period. (Note that the differential radial velocity presented in this figure will be discussed later in the paper). The peaks in the graupel volume at 1611 and 1723 MDT in Fig. 5.8 are mirrored by peaks in the graupel rate in Fig. 5.9. The increased temporal resolution (from 12 to 6 minute) reveals another relative maxima in the hail rate coincident with a smaller peak in the number of CG flashes at 1635 MDT. This smaller peak is likely due to the collapse of a weaker cell which first entered the data network centered at y = -10 km (see Figs. 5.3b and c).

The accuracy of the graupel volume using Table 4.1 and the hail rate using Eqns. (4.20) and (4.21) are crucially dependent on the capability of multiparameter radar data to identify the presence of ice in mixed-phase precipitation. To insure that the two previous methods properly quantified ice below the melting level, it is useful to look at the evolution of K_{dp}/Z and Z_h/Z_{dp} plots as discussed in Secs. 4.1.2 and 4.1.3. We show the plots for z=0.5 km at the times following the identified hail peak at 1723 MDT to verify that the graupel amount did indeed decrease.

Fig. 5.10 is a plot of K_{dp} vs. Z for the period from 1723 to 1741 MDT. Recalling that a plot of K_{dp} vs. Z for pure rain would appear similar to Fig. 4.3, it is apparent that the amount of hail in mixed-phase precipitation did actually decrease significantly from 1723 to 1741 MDT. At 1723 MDT, there are many grid points with values of K_{dp} significantly smaller than that predicted for pure rain as is indicated by the large scatter of points above the theoretical boundary between pure rain and mixed-phase precipitation. The number of

grid points above this boundary decreases significantly and the average deviation of K_{dp} from pure rain values also decreases by 1729 MDT. By 1735 MDT, there is only a slight hint of any ice in the storm as most points fall below the rain boundary. It is interesting to note that the number of pure rain points also decreases from 1723 to 1735 MDT. The reason for this can be seen in the vertical profile of graupel volume at these times (Fig. 5.7b). The amount of graupel which is available to melt into rain also decreases steadily from 1723 to 1735 MDT as the storm dissipates, resulting in a reduction of the number of pure rain points.

Figs. 5.11a-c reveal the evolution of Z_h versus Z_{dp} plots for the same time period. Recalling that the increased departure of points below the theoretical rain line indicates the presence of ice, it is qualitatively evident that the amount of ice decreases from 1723 to 1735 MDT. There is significant scatter below the rain line at 1723 MDT (Fig. 5.11a), especially for the cluster of grid points between Z_h=58 and 62 dBZ. Using Eqns. (4.16) and (4.17) for the grid point at Z_h=62 dBZ and Z_{dp}=51.5 dB (delineated by a solid arrow), the corresponding fraction of ice is 1 - f = 0.78 and the reflectivity weighted fraction of precipitation sized ice to precipitation liquid water is (1 - f) / f = 3.5. Similar calculations using the data point marked by a dashed arrow (Z_h = 58.4 dBZ and Z_{dp} = 53.3 dB) result in an ice fraction of 0.28 and a reflectivity weighted fraction of ice to precipitation liquid water of 0.4. These calculations suggest that the ice fraction for precipitation with Z_h > 58 dBZ ranges from about 30% to 80% at 1723 MDT. Deviation below the pure rain line decreases by 1729 MDT (Fig. 5.11b) and is almost non-existent in the tight cluster of points in Fig. 5.11c for 1735 MDT.

Similar K_{dp} vs. Z plots for the first peak in the CG flash rate and hail rate (Fig. 5.9) from 1541 to 1623 MDT are shown in Figs. 5.12a-b. The number of grid points in the mixed-phase precipitation region increases dramatically from 1541 to 1605 MDT as seen in Fig. 5.12a. Although the number of grid points in this region does not lessen significantly from 1611 to 1623 MDT as might be expected, the fraction of hail in the

mixed-phase precipitation decreases as can be seen from the proximity of the points to the mixed-phase boundary in Fig. 5.12b. Plots of Z_h versus Z_{dp} for this time period are presented in Figs. 5.13a - f. As with the previous procedure, the reflectivity factor method reveals that the number of mixed phase grid points and the ice fraction qualitatively increase from 1541 to 1611 MDT and that the trend is reversed from 1611 to 1623 MDT. This further supports the results presented in Fig. 5.8 and 5.9 and the correlation between descending ice and the CG flash rate.

5.4 The role of ice in storm outflow generation

After ice provides the impetus for CG lightning by descending beneath the charge reversal level, the graupel and hail particles then fall below the 0°C isotherm where they contribute to the negative buoyancy of the descending air parcel through melting and may therefore aid in the creation of a microburst at the surface (Srivastava, 1987). Roberts and Wilson (1984) speculated that microbursts produced by intense, deep hailstorms (similar to this case) are driven by precipitation loading, below cloud-base hailstone melting, and evaporation of water shed from hailstones. Using several two-dimensional cloud model simulations, Hjelmfelt et al. (1989) demonstrated that loading by graupel and hail, the melting of ice, and the evaporation of rain was important in driving storm outflow. Although it is difficult to quantify exactly how much ice melts in the downdraft of a storm from radar observations at six minute intervals, it is reasonable to propose that an increase in the precipitating ice mass will result in more melting and loading, increased negative buoyancy, and stronger storm outflow.

All microbursts for this storm were of the "wet" variety (total cumulative rainfall of $\geq$ 0.01 inches, or 0.025 cm, from the onset to cessation of high winds; Fujita and Wakimoto, 1983). A climatology of microbursts in this region collected during the summer of 1982 in the Joint Airport Weather Studies (JAWS) found that dry (< 0.025 cm rain) microbursts were more common than wet microbursts, with 81% of detected microbursts to be of the dry variety as discussed in Fujita and Wakimoto (1983). In a contrasting study, Biron and

Isaminger (1989) found that about one-half of all detected microbursts in the Denver area were of the wet variety (defined as $Z > 35$ dBZ where Z is the maximum surface reflectivity) during the summers of 1986 and 1987.

Despite this lack of consensus regarding characteristics (wet vs. dry) of Front Range microbursts, the findings from both field projects show that the microbursts in this study were unusual for the semi-arid climate of this area. For example, Biron and Isaminger (1989) found that less than 10% of Denver area microbursts were preceded by upper level divergence or by a descending reflectivity core which they defined as follows: 1) a maximum reflectivity of 50 dBZ or greater, 2) the maximum reflectivity must develop at a height of > 2.5 km AGL, 3) the depth of the reflectivity core must exceed 5.2 km, and 4) the core is considered to be descending when it falls below 2 km AGL. The reflectivity core centered on x = -34 km in Fig. 5.4b formed above the 2.5 km AGL level, had a $Z >$ 50 dBZ depth of about 6 km, and was accompanied by very strong upper-level divergence ($5 - 10 \times 10^{-3}$ s^{-1}). About twenty minutes later in the storm's evolution (Fig 5.4c), the reflectivity core descended well below the 2 km AGL level and as will be shown in the next paragraph, was associated with a strong microburst near the surface, a peak in the surface hail rate, and a maximum in the CG flash rate. The absence of dry microbursts and the presence of a descending reflectivity core in this storm can be attributed to the ample mid-level moisture in the atmosphere due to a decaying warm front in eastern CO.

A measure of the storm outflow (or microburst) strength was determined from single-Doppler radar data by calculating the maximum differential radial velocity (ΔV_r) which was calculated by taking the difference in the radial velocity between two peaks of diverging flow at the lowest elevation angle (0.5°). The distance between the peaks was constrained to be less than or equal to 4 km. A differential radial velocity of $\geq$ 10 m s^{-1} over this distance in diverging flow near the surface is defined as a microburst (Fujita and Wakimoto, 1983). The results are shown in Fig. 5.9 with the hail rate and number of CG flashes per radar volume time. The relative maxima in hail rate of 23.4 mm hr^{-1} at 1611

MDT was followed by a peak in the differential radial velocity of 20.75 m s^{-1} at 1617 MDT. Similarly, the secondary peak in the hail rate of 12.7 mm hr^{-1} at 1635 MDT was succeeded by a smaller maxima in the outflow strength (14.5 m s^{-1}) six minutes later. The final maxima in the hail rate (25.5 mm hr^{-1}) was also followed by a peak in the differential radial velocity, ΔV_r, of 19.5 m s^{-1}. Consistent with the idea that mass loading and melting of precipitation sized ice is the principal cause of microbursts associated with deep convection, each peak in the hail rate was closely followed by a microburst near the surface. This lag of approximately six minutes (at most) between the peak hail rate and the maximum outflow intensity is similar to the findings of Goodman et al. (1988) who found a four minute lag between the peak precipitation rate and storm outflow. Fig. 5.9 also reveals that maxima in storm outflow were either coincident with or preceded by peaks in CG activity similar to the results of Williams et al. (1989a). It is interesting to note that a temporal pattern emerged with the CG flash rate peaking first, followed by a peak in the graupel rate in the lowest 1 km, and ending with a maxima in the microburst strength near the surface (except for the third set of peaks in Fig. 9 around 1723 MDT which shows the hail rate peaking first, followed by coincident peaks in CG activity and storm outflow). Note that the peak hail rate in Fig. 9 did lag the CG flash rate by 2 minutes for the 1635 MDT peak and that the graupel volume in Fig. 8 also lagged the CG flash rate by 3 minutes for the 1723 MDT peak when considering one minute time resolution. This is not revealed by the time resolution of the two graphs.

This is consistent with the findings of Goodman et al. (1988), Williams et al. (1989a), and Williams (1990) who found a consistent pattern starting with peak IC flash rate, switching to peak CG flash rate, followed closely by a peak in the precipitation rate, and concluding with a maximum in the storm outflow. A comparison of Figs. 5.6 and 5.8 shows that the IC flash rate for the 21 May 1993 multi-cell storm did not appear to fit this pattern. This lack of agreement could stem from the complex interaction of multiple convective cells simultaneously contributing to the IC flash rate at different phases in their

convective life cycle. Fortunately, the three strongest cells collapsed at sufficiently different times to allow for the rest of the convective life cycle of each individual cell to be observed with some clarity as depicted in Fig. 5.9.

5.5. Radar and electrical observations of a FEAWP

A field excursion associated with precipitation (FEAWP) is a pronounced excursion of the electric field to negative values (fair-weather field) during the active stage of a thunderstorm that is coincident with the arrival of a strong downdraft and a transient burst of precipitation near the observing location (also known as a gradient excursion associated with precipitation, or GEAWP; Moore and Vonnegut, 1977). It is still unclear whether the FEAWP is caused by descending, positively charged precipitation or whether the downdrafts that accompany the precipitation transport other positive charge downward, thus causing the field excursion (Krehbiel, 1986). Williams et al. (1989b) presented observations of two FEAWP's accompanied by dry microbursts in the Denver, CO area. They speculated that excursions in the electric field could be attributed to charge reversal microphysics as graupel particles descend from -20°C to the melting level.

The 21 May 1993 multi-cell storm produced a FEAWP at approximately 1640 MDT within range of the corona point sensor located at the CSU-CHILL radar. The storm outflow associated with this FEAWP was detected by a nearby Greeley meso-network observing station operated by NOAA/FSL (located approximately 1 km SE of the CSU-CHILL radar). The cell which produced the recorded FEAWP and associated microburst was centered approximately 7 km to the southwest of the radar. Williams et al. (1989b) observed FEAWP's in Denver thunderstorms when a corona point sensor was within about 2 km of the associated microburst. The sensor used in this study was mounted 40% higher off the ground (7 m vs. 5 m) than those used in Williams et al. (1989b), allowing greater sensitivity. Corona point sensor observations of the FEAWP are shown in Fig. 5.14. The corona current was initially positive, indicating predominately negative charge aloft, and reached a maximum of just under 5 microamperes, similar to the findings of

Williams et al. (1989b). In-cloud flashes occurred approximately every two minutes as can be seen by the sudden discontinuities in the corona current. (The corona point sensor cannot distinguish between IC and CG flashes, thus magnetic DF data were used to differentiate between lightning types). This fairly regular interval in the IC flash rate is suggestive of the electrical steady-state achieved by thunderstorms after initial exponential growth and before storm collapse (Williams, 1989). It is important to note that most of these IC discharges before 1640 MDT neutralized negative charge as can be inferred from the sudden jump from large positive to near zero or negative values of corona current. The overall magnitude of the corona current (and hence the E-field) gradually decreased from 1623 to 1640 MDT as did the magnitude of the IC discharges (as inferred from the corona current data). At 1640 MDT, the corona current transitioned from positive to negative values, indicating a gradual transition from predominately negative to positive charge aloft. A weak microburst (with a differential radial velocity of 14 m s^{-1}) was detected in CSU-CHILL single-Doppler radar data at 1641 MDT in the cell centered 7 km southwest of the radar as indicated by the "MB" in Fig. 5.14. A large discontinuity in the corona data at approximately 1643 MDT indicated that positive charge was being neutralized aloft. The corona current returned to positive values, or predominately negative charge aloft, by 1649 MDT.

A record of the spatially averaged rain rate [derived using CSU-CHILL radar data and $R(K_{dp})=40.7(K_{dp})^{0.866}$ (mm hr^{-1}) from Sachidananda and Zrnic' (1987) with an averaging area equivalent to the operational area of the corona point sensor] and of the five minute peak wind gust from the mesonet site in the vicinity of the FEAWP are shown in Fig. 5.15. The transition from foul- to fair-weather field occurred at the same time as the peak in the spatially averaged rain rate. The maximum rain rate during the field transition was 47 mm hr^{-1} (not shown). The wind reached its maximum value (8 m s^{-1} gusting to 11 m s^{-1}) at approximately the same time as the peak in the fair-weather field at about 1645 MDT.

From this data, it is still uncertain whether the precipitation or the storm downdraft carried the electric charge responsible for the observed field excursion.

However, more evidence in favor of the role for precipitation (i.e., ice) in causing the FEAWP can be found in Fig. 5.16. This figure presents the evolution of the vertical profile of graupel volume in the cell responsible for the FEAWP. When the corona current was strongly positive at 1625 MDT (see "A" in Figs. 5.14 and 5.16), indicating the presence of predominately negative charge aloft, the vertical profile of graupel volume was similar in shape to those found in developing convection (c.f., Fig. 5.7a). During this period, the peak in graupel volume was at 5.5 km AGL (T = -20°C) similar to the most common altitudes and temperatures for the negative charge layer. From 1625 to 1631 MDT (see "B"), the graupel volume descended slightly and the electrostatic field began to weaken slightly in response. Since the bulk of the graupel volume was above the charge reversal level up to this point in time (T = -10°C; Takahashi, 1978), the graupel and hail particles would have charged negatively and therefore could have accounted for the foul-weather field.

By 1637 MDT (see "C"), the graupel volume had descended even further such that more than half of the volume was below the charge reversal level. The corona current was weakly positive at this point in time and transitioned to negative values three minutes later. Since there was very little graupel and hail above the charge reversal level at 1643 MDT (see "D"), the negative corona current might have been the result of positively charged graupel and hail particles aloft as explained by the non-inductive charging mechanism. Since a large volume of the graupel and hail descended through the charge reversal level at approximately the same time as the transition from foul- to fair-weather electric field, it is possible that the action of charge reversal microphysics on the descending graupel and hail was responsible for the FEAWP. The field excursion lasted for approximately nine minutes. By 1649 MDT (see "E"), the corona point returned to positive values, indicating predominately negative charge aloft. The return to foul electric field was associated with

a slight resurgence of the graupel volume above the inferred charge reversal level similar to the findings of Williams (1990).

Alternative explanations for the FEAWP have included the capture of positive corona ions by descending precipitation (Malan, 1952), the lateral displacement of negative charge aloft (Moore and Vonnegut, 1977), and the deposition of positive charge on precipitation by lightning (Holden et al., 1983). Since the cell was nearly stationary during the transition period (1637 - 1642 MDT) and did not become tilted significantly with height, it is unlikely that the field excursion was caused by the lateral displacement of negative charge in this case. The gradual nature (on the order of minutes) of the transition to fair-weather field appears to eliminate the deposition of positive charge by lightning as a possible explanation, since this process would occur on the order of a second. In this case, the field excursion was clearly linked to the gradual descent of the precipitation core as illustrated in Fig. 5.16. This is similar to the findings of Williams (1990) who presented time-height figures of reflectivity and mean Doppler velocity at vertical incidence of a FEAWP producing thunderstorm. Williams showed that the transition to fair-weather electric field and associated outflow at the surface was coincident with the descent of a region of maximum reflectivity from mid-levels in the storm. Although the capture of positive ions by precipitation cannot be dismissed, the available observations for this study strongly suggest that the descent of graupel and small hail below the charge reversal level was responsible for the field excursion at 1640 MDT.

Similarly, it is reasonable to speculate that the increased negative buoyancy caused by a large volume of ice descending below the melting level after 1637 MDT was partially responsible for the observed microburst at 1641 MDT and the gusty winds at the mesonet site which peaked at 1645 MDT. This melting process was manifest in the rapid decrease of graupel volume below the melting layer as seen in Fig. 11b. Further evidence for an active melting process was found in the decrease of the correlation coefficient below the melting level. The correlation coefficient decreased monotonically from 0.987 above the

melting layer to 0.955 near the surface (not shown), similar to the findings of Balakrishnan and Zrnic' (1990b). This suggests that a mixture of precipitation types, such as graupel and rain, was present below the melting level. The broader spread of sizes, shapes, canting angles, and phase shift upon scattering in a mixture of rain and graupel is the most probable cause for the decrease in the correlation coefficient. The gradual nature of this decrease in $\rho_{hv}(0)$ toward ground was probably caused by a progressively increasing amount of rain due to the melting of graupel and small hail (Balakrishnan and Zrnic', 1990b).

The large discontinuity which occurred at 1643 MDT while the graupel storm volume was rapidly descending was not detected by the magnetic DF network as a cloud-to-ground flash. This lightning flash would be more consistent with the convective life cycle observed by Williams et al. (1989a) and Goodman et al. (1988) if it were a CG flash since the bulk of the ice mass had descended below the charge reversal level. The large amplitude of this discontinuity in the corona point data and the fact that the detection efficiency of the DF network was about 70 to 85% at these distances leads us to suspect that the DF network may have missed this CG flash. An alternative possibility is that the large field change toward the end of the FEAWP could be a very close in-cloud discharge between the residual main negative charge and the lower positive charge center.

5.6 A comparison with laboratory charging studies

Observations of the FEAWP presented in the previous section allow for some comparative speculation on the microphysics of the associated lower positive charge center and the applicability of the various laboratory charging studies mentioned earlier (Takahashi, 1978; Jayaratne et al., 1983; and Saunders et al., 1991). The existence of a localized, lower positive charge center was first observed by Simpson and Scrase (1937). A detailed review of the various mechanisms that have been attributed to the presence of the lower positive charge was given by Williams (1989). The most recent hypothesis based on the non-inductive charging mechanism and associated charge reversal

microphysics was first suggested by Jayaratne et al. (1983). Graupel falling through an updraft below the Level of Charge Reversal, LCR could acquire positive charge when colliding with ice crystals, eventually neutralizing the negative charge obtained above the LCR and thus creating the lower positive charge center.

Although the level of charge reversal is a complex function of both cloud temperature and liquid water content (LWC), it is possible to compare the observations of the lower positive charge center in this study to the above laboratory charging experiments by making some assumptions regarding cloud LWC. During the National Hail Research Experiment (NHRE, 1976) centered on northeastern Colorado, the Wyoming Queen Air measured cloud LWC values that were 25% to 40% of the adiabatic LWC using a Johnson-Williams hot wire device at temperatures from -10° C to -15° C (Fankhauser et al., 1982). Using Denver sounding data from 21 May 1993, 1200 UTC, we estimate that the adiabatic LWC in this subset of the mixed phase region ranged from 4.5 to 5.5 g m^{-3}. Given the above percentages, we speculate that representative values of LWC in this study ranged from 1 - 2 g m^{-3}. This range is supported by NHRE measurements taken by the South Dakota School of Mines and Technology (SDSM&T) armored T-28 in 9 thunderstorms during the summers of 1975 and 1976. Using similar instrumentation and at similar temperatures as the Wyoming Queen Air, the T-28 measured a relative frequency peak in LWC from 1 to 1.5 g m^{-3} (Knight et al., 1982).

In our comparison, we will therefore assume a LWC of 1 g m^{-3} as a representative value. At this LWC, the charge reversal temperature is about -10° C for Takahashi (1978) and approximately -20° C for Jayaratne et al. (1983). Saunders et al. (1991) represent their results in terms of the effective liquid water content, EW, which is that fraction of the droplet spectrum caught by the rimer (simulated graupel particle). This subtle difference has been a significant issue in the on-going debate regarding the applicability of the various laboratory studies to large scale observations (e.g., Williams and Zhang, 1993; Saunders, 1993). The effective liquid water content is related to LWC

simply by the relation $EW=E_C$ (LWC), where E_C is the collection efficiency. By studying the formation of graupel from the riming of freely suspended frozen drops in a wind tunnel, Pflaum and Pruppacher (1979) found that graupel collection efficiencies can range from about 0.5 to 1.0. Using these values of E_C, we find that a LWC of 1 g m^{-3} results in a range of EW from 0.5 to 1.0 g m^{-3}. We can therefore deduce that the charge reversal temperature for Saunders et al. (1991) at a LWC of 1 g m^{-3} should range from -15° C to -22° C, depending on the value of the graupel collection efficiency.

In order to properly assess the applicability of the laboratory studies to our observations, it is important to get a rough estimate of the charging time scale for the non-inductive charging mechanism. The rate of graupel electrification (dQ/dt) during collisions with ice crystals is (Takahashi, 1978)

$$\frac{dQ}{dt} = \pi R^2 n(V - v_i) q E \qquad (6.1)$$

where R is the radius of the graupel particle, n the number concentration of ice crystals, V the graupel terminal fall speed, v_i the ice crystal fall velocity (assume $V >> v_i$), q the electric charge separated per ice crystal collision, and E the collision efficiency. As noted by Williams (1989), both n and q have order of magnitude variability with the ice concentration varying from 10^4 to 10^6 m^{-3} and the separated charge from 1 to 100 fC. Substituting the median values in these ranges and reasonable values for a mature thunderstorm for the result of the variables (R = 2.0 mm, n = 10^5 m^{-3}, V = 3 m s^{-1}, q = 50 fC, E = 0.5) into Eqn. (6.1), we estimate that the graupel charging rate is 9 x 10^{-14} C s^{-1}. The average magnitude of negative charge, $\overline{Q}$, on individual millimeter sized graupel particles during the mature stage of a hail producing storm is on the order of 10 pC (Latham, 1981). By dividing $\frac{\overline{Q}}{dQ/dt}$, we estimate that the negative charge residing on graupel would be neutralized within approximately 2 minutes after falling below the level of charge reversal. Assuming the above conditions are still representative below the LCR,

the graupel would then obtain a positive charge of 10 pC within another 2 minutes such that the entire charge reversal process would take only 4 minutes.

The observations shown in Figs. 5.14 and 5.16 support the hypothesis that the lower positive charge center associated with the transition from foul to fair weather electric field is coincident with the descent of graupel as also found by Kitagawa and Michimoto (1994) for winter thunderstorms over the Japanese coast. In our study, the transition from predominately negative to predominately positive charge aloft (1640 MDT) occurred while the vertical structure of graupel volume descended from profile C (1637 MDT) to profile D (1643 MDT). As seen in Fig. 5.16, a majority of the graupel volume had already descended below the 5 km (-17° C) level by 1631 MDT (profile B). The bulk of the graupel mass then preceded to fall below the 4.5 km (-14° C) level between 1631 MDT and 1637 MDT. After 1637 MDT, the majority of the graupel volume was below 4 km (or -10° C). Another observation for which any plausible charge reversal temperature must account is the persistent re-charging of the net negative charge aloft until 1637 MDT after each lightning discharge (Fig. 5.14). After 1637 MDT, the corona current began to systematically decrease, indicating a decrease in net-negative charge aloft.

For this comparison, only advection of charge or the generation of charge aloft via the non-inductive charging mechanism will be considered. The effects of lightning are also readily apparent in Fig. 5.14 as sudden discontinuities in the corona current. However, this discussion is limited to gradual, order of minute variations in the current. A stated earlier, the horizontal advection of charge was not a significant factor in this storm. Given the position of the corona point relative to the cloud (7 km SW) and assuming a peak altitude of the negative charge center below 5 km AGL, the vertical descent of the negative charge center would only have served to decrease the corona current toward zero (Uman, 1987 Fig. A.2). This is in contrast to the systematically increasing current up until 1637 MDT. As a result, the non-inductive charging mechanism was creating net negative charge aloft. This would have been impossible for a charge reversal temperature less

(cooler) than -17° C since the bulk of the graupel particles would have been charging positively after 1631 MDT. Given the previous charging calculations, the field transition should have occurred a couple of minutes later at 1633 MDT. As a result, the charge reversal temperature of Jayaratne et al. (1983) (T_R = -20° C) and good portion of the inferred Saunders et al. (1991) results (-22° C $\leq T_R <$ -17° C) do not appear to be consistent with these observations. Given the six-minute resolution of the radar data and the many assumptions necessary for this comparison, the higher (warmer) end of the Saunders et al. (1991) results (-17° C $\leq T_R \leq$ -15° C) represent a plausible range for this storm's charge reversal temperature.

On the other hand, the Takahashi (1978) charge reversal temperature of -10° C appears to be the most consistent with our observations. The majority of the graupel mass was still above the level of charge reversal associated with T = -10° C until 1637 MDT, in accordance with the observed persistent replenishment of net-negative charge aloft. Coincident with the descent of the bulk of the graupel volume below the -10° C level, the corona current began to systematically decrease. By 1639 MDT, the corona current was near zero and rapidly became negative (net-positive charge aloft) shortly thereafter. This is in good agreement with our rough estimate of the non-inductive charging time scale which suggests a 2 minute charge neutralization period. If the charge reversal temperature is not influenced by the initial charge on the colliding ice particles, then the laboratory determined charge reversal temperature should closely agree with the temperature associated with the height of the observed negative charge center. In mountainous New Mexico, the temperatures at negative charge height typically range from -8° C to -17° C (Williams, 1989), in close agreement with the inferred range of the charge reversal temperature in this Colorado thunderstorm (-17° C $\leq T_R \leq$ -10° C).

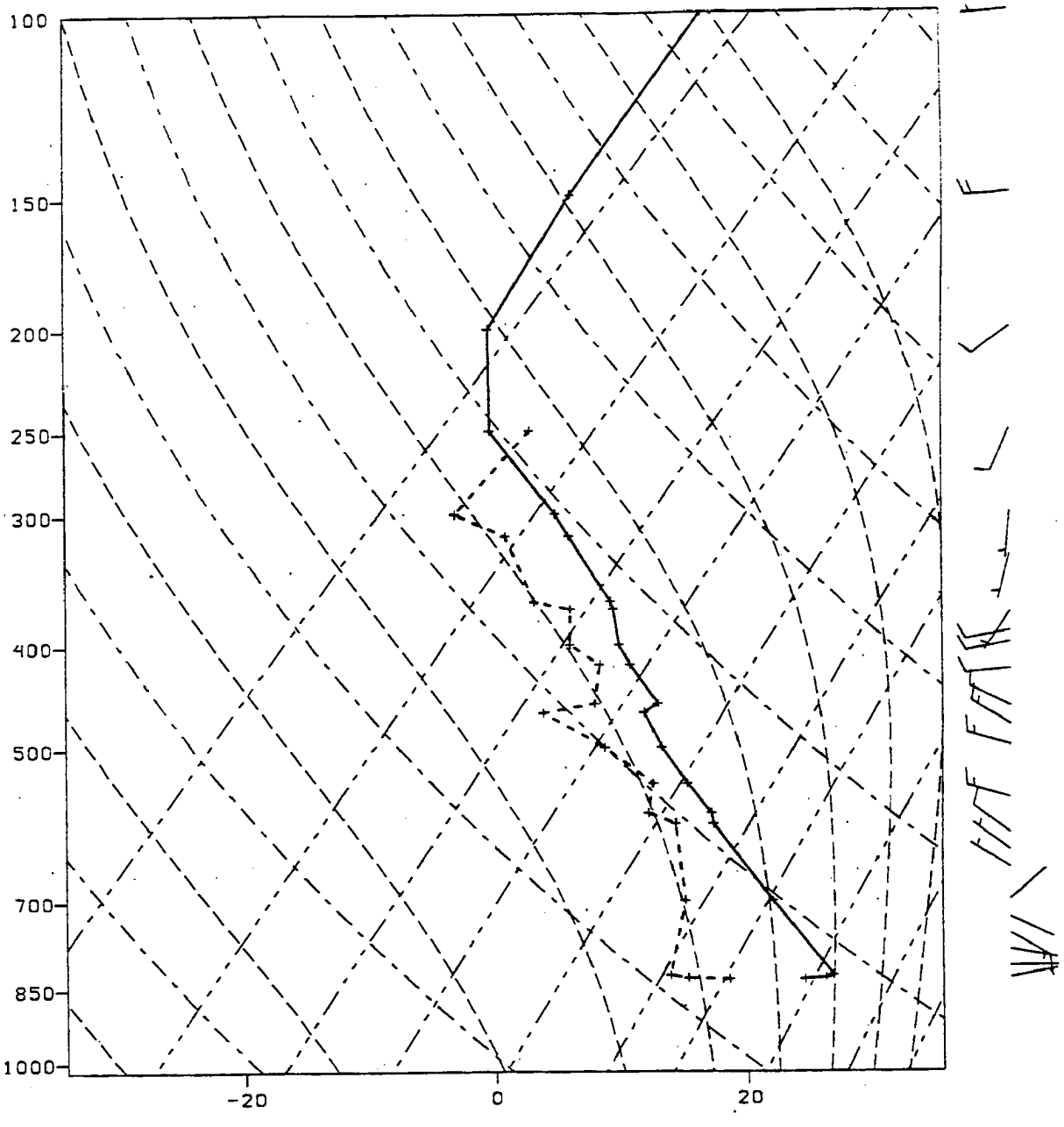

Fig. 5.1 Skew T - Log P plot of upper air sounding for Denver (DEN), Colorado on 22 May 1993 at 0000 UTC. Profiles of temperature (solid line) and dewpoint (dashed line) are given in degrees Celsius. Winds are in m s^{-1}.

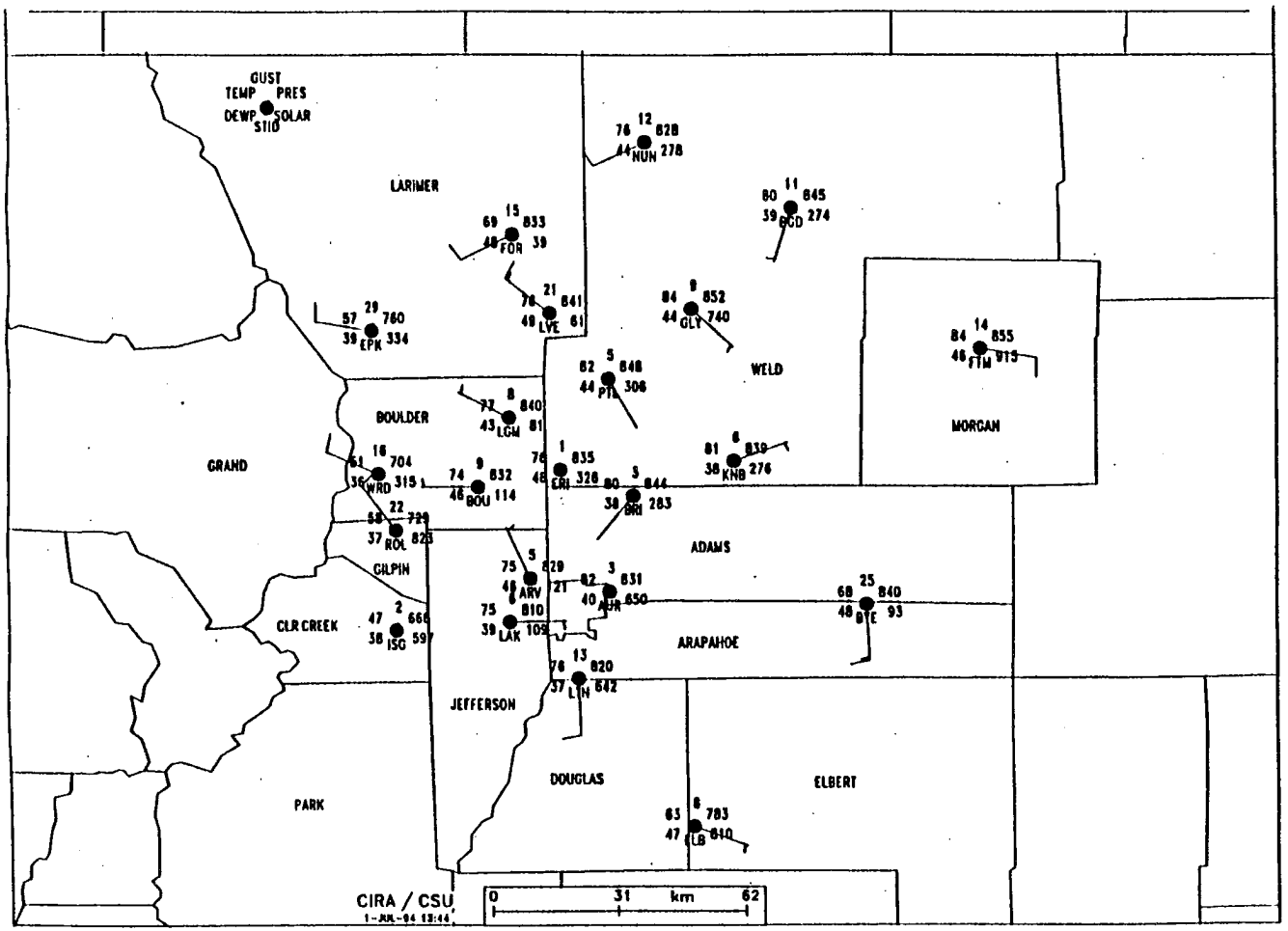

Fig. 5.2 Front Range Mesonet surface data for 21 May 1993 at 2130 UTC depicting temperature and dewpoint temperature in degrees Fahrenheit; wind direction; wind speed and gust magnitude in knots; pressure in millibars; and solar radiation in W m^{-2}. Note key at top left hand corner of figure.

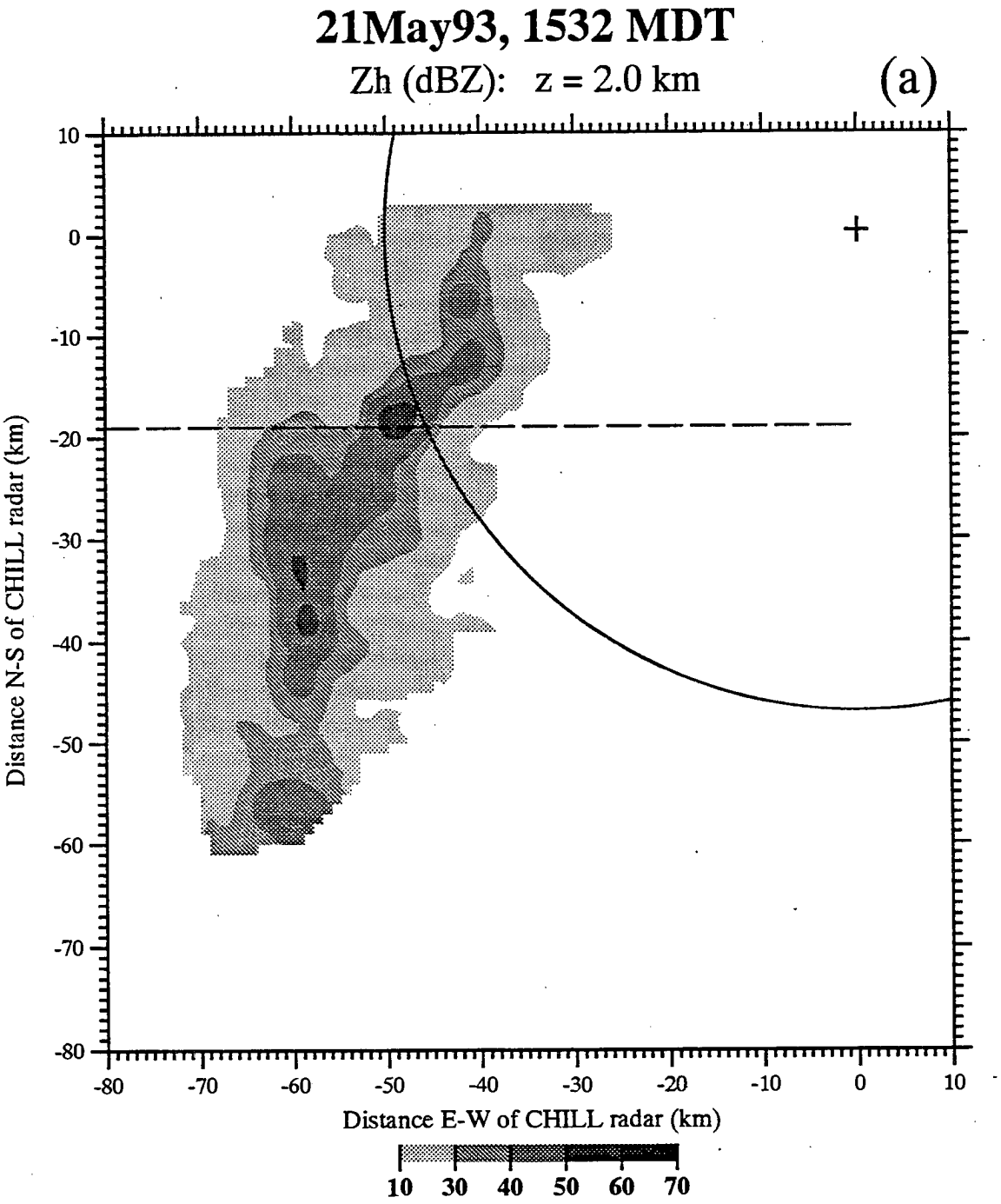

Fig. 5.3 Horizontal cross-section of reflectivity (dBZ) at 2 km AGL on 21 May 1993. The location of the CSU-CHILL radar is depicted by a "+" at the origin (x = 0, y = 0). The 50 km radius of operation for the flat plate antenna is shown by the solid line. The dashed line indicates the plane of the vertical cross-section illustrated in Fig 5. a) Results at 1532 MDT.

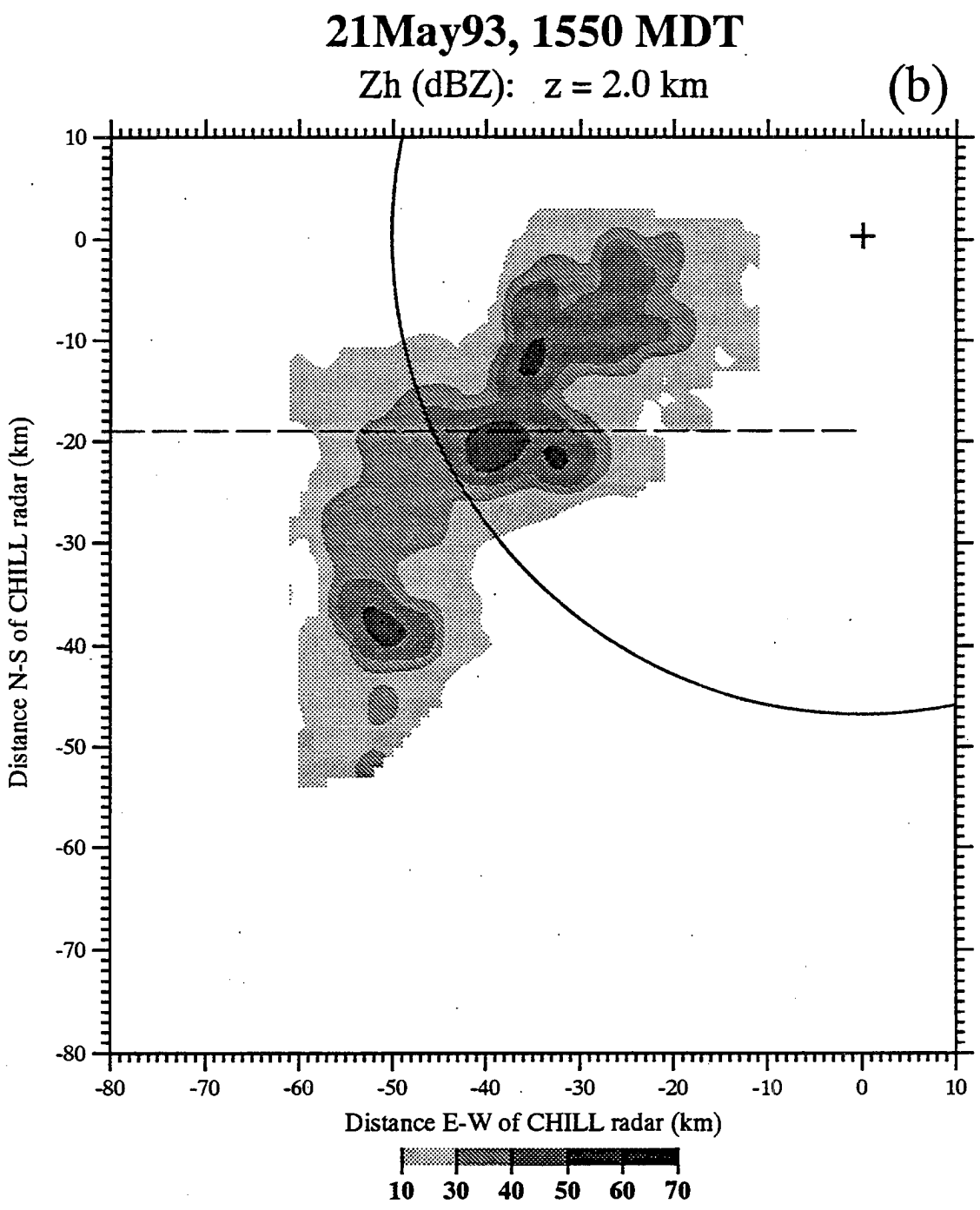

Fig. 5.3 b) Results at 1550 MDT.

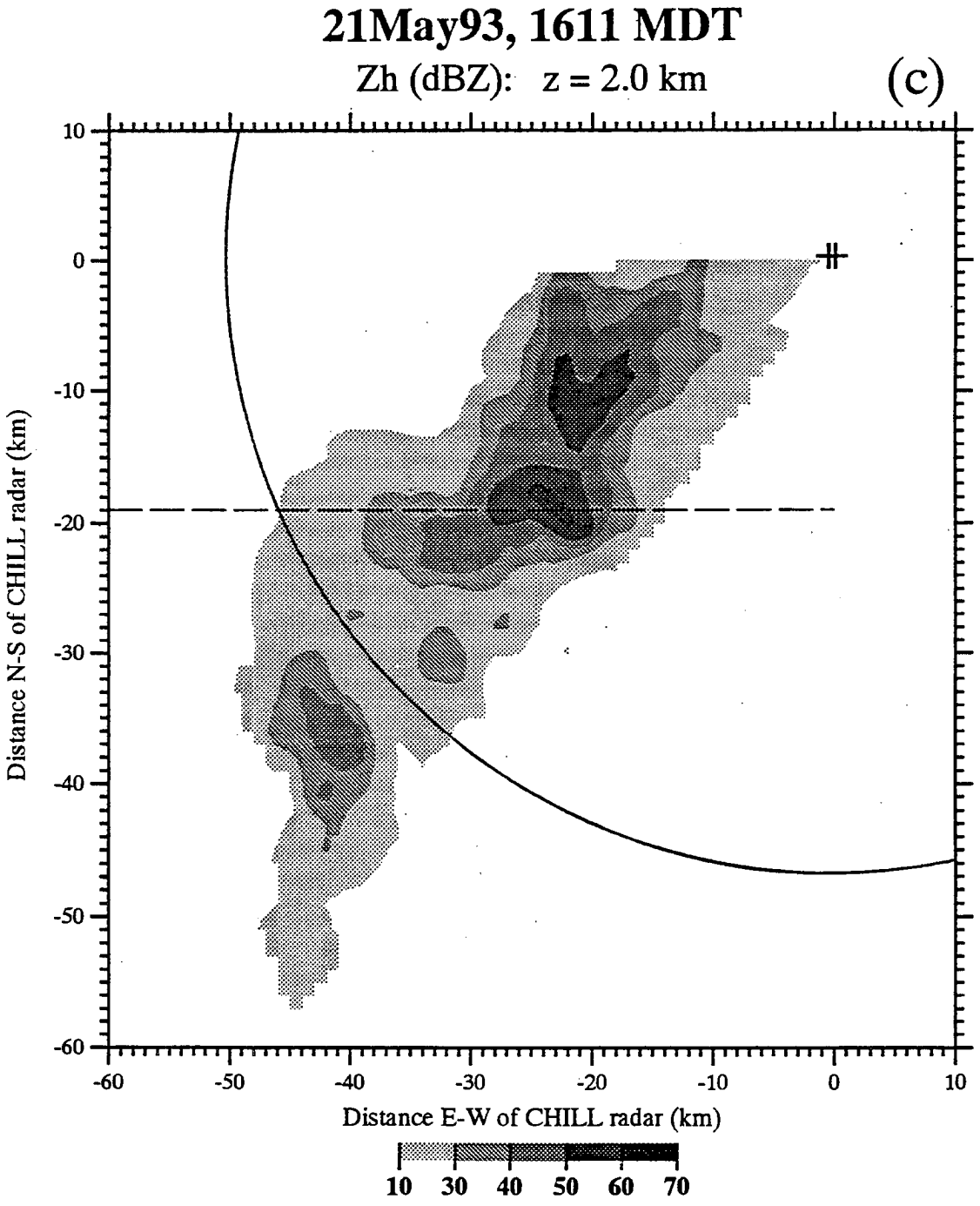

Fig. 5.3 c) Results at 1611 MDT (Note different scale than 5.3a-b).

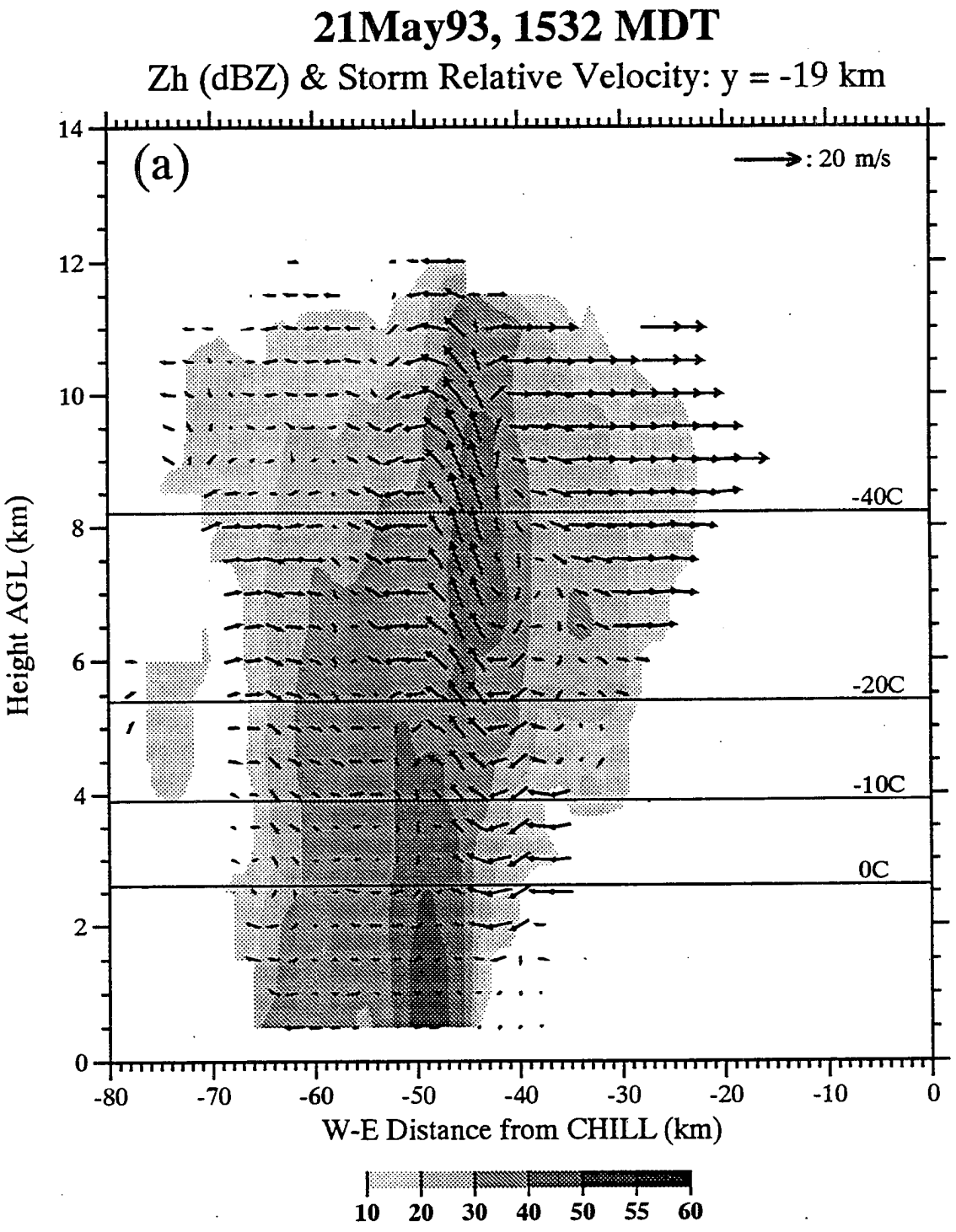

Fig. 5.4 East-west vertical cross-section of reflectivity (dBZ) and storm relative velocity from dual-Doppler analyses when available (vector length of 1 cm is approximately equal to 20 ms^{-1} as shown) through the most vigorous cell to initially enter the observational network on 21 May 1993. Where dual-Doppler synthesized winds were not available, differential reflectivity (dB) is contoured. The plane of the cross-section is depicted by a dashed line in Fig. 5.3. a) Results at 1532 MDT.

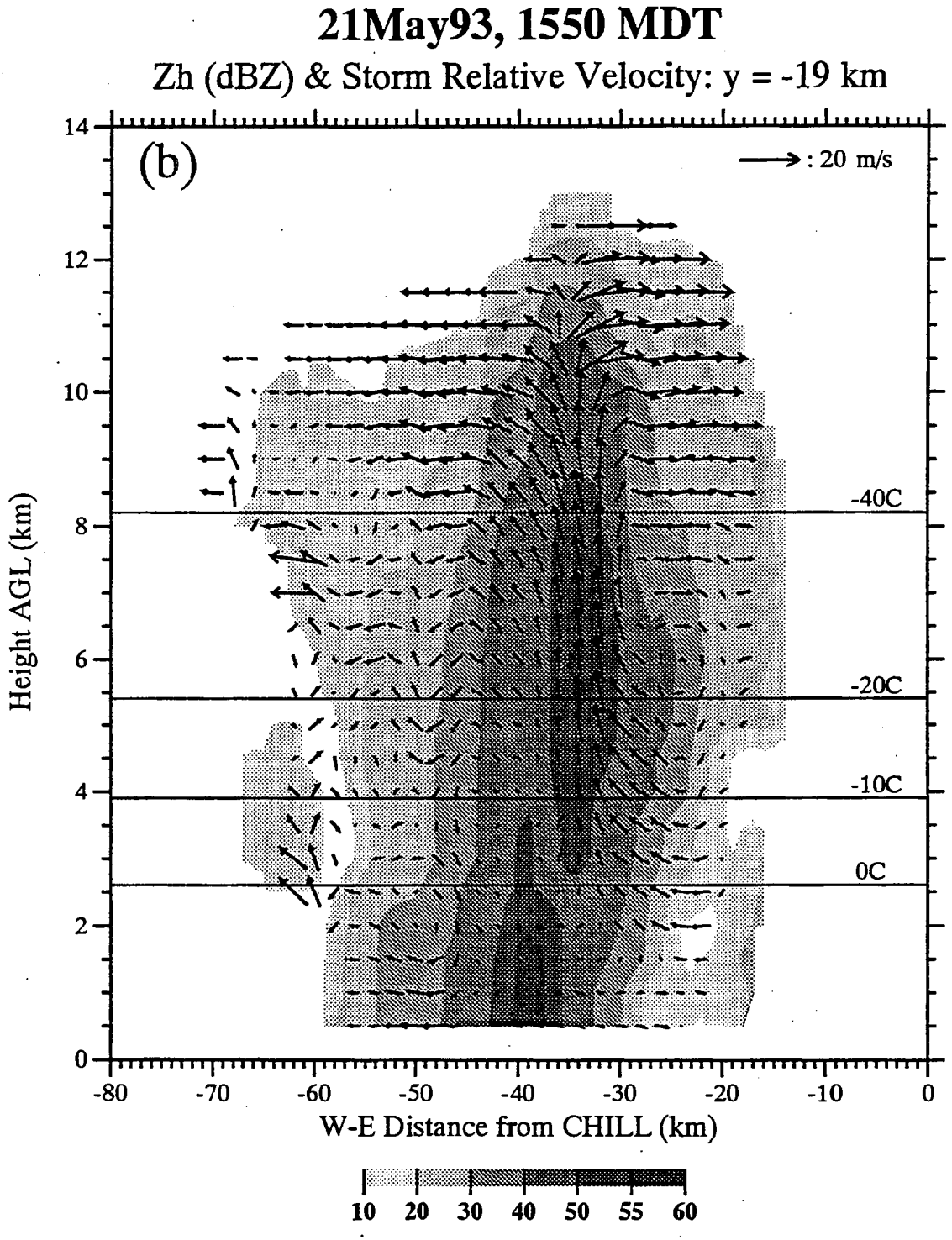

Fig. 5.4 b) Results at 1550 MDT.

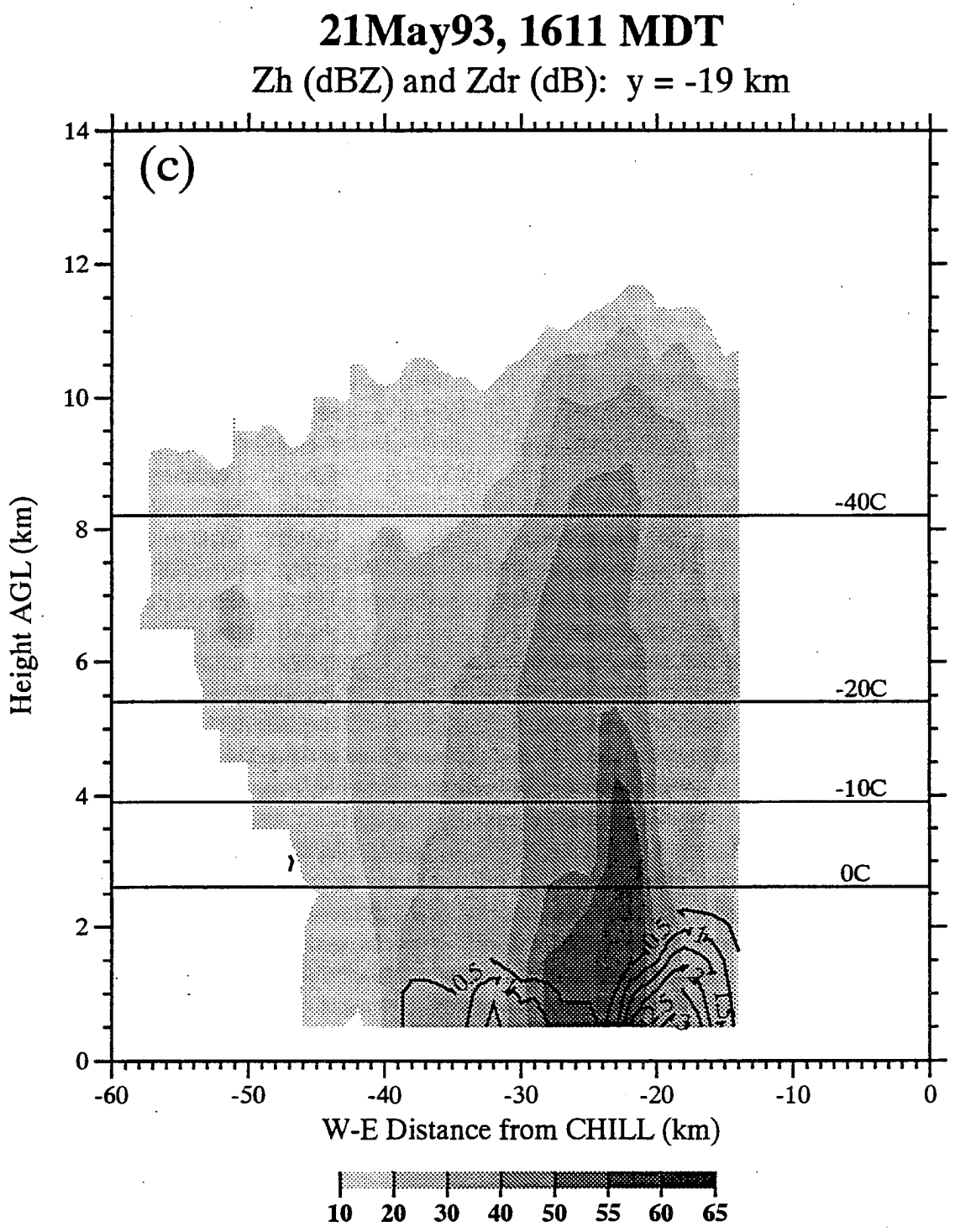

Fig. 5.4 c) Results at 1611 MDT. Dual-Doppler analysis was not available for this time. Instead, contours of differential reflectivity are plotted every 0.5 dB. (Note that horizontal scale is slightly different.)

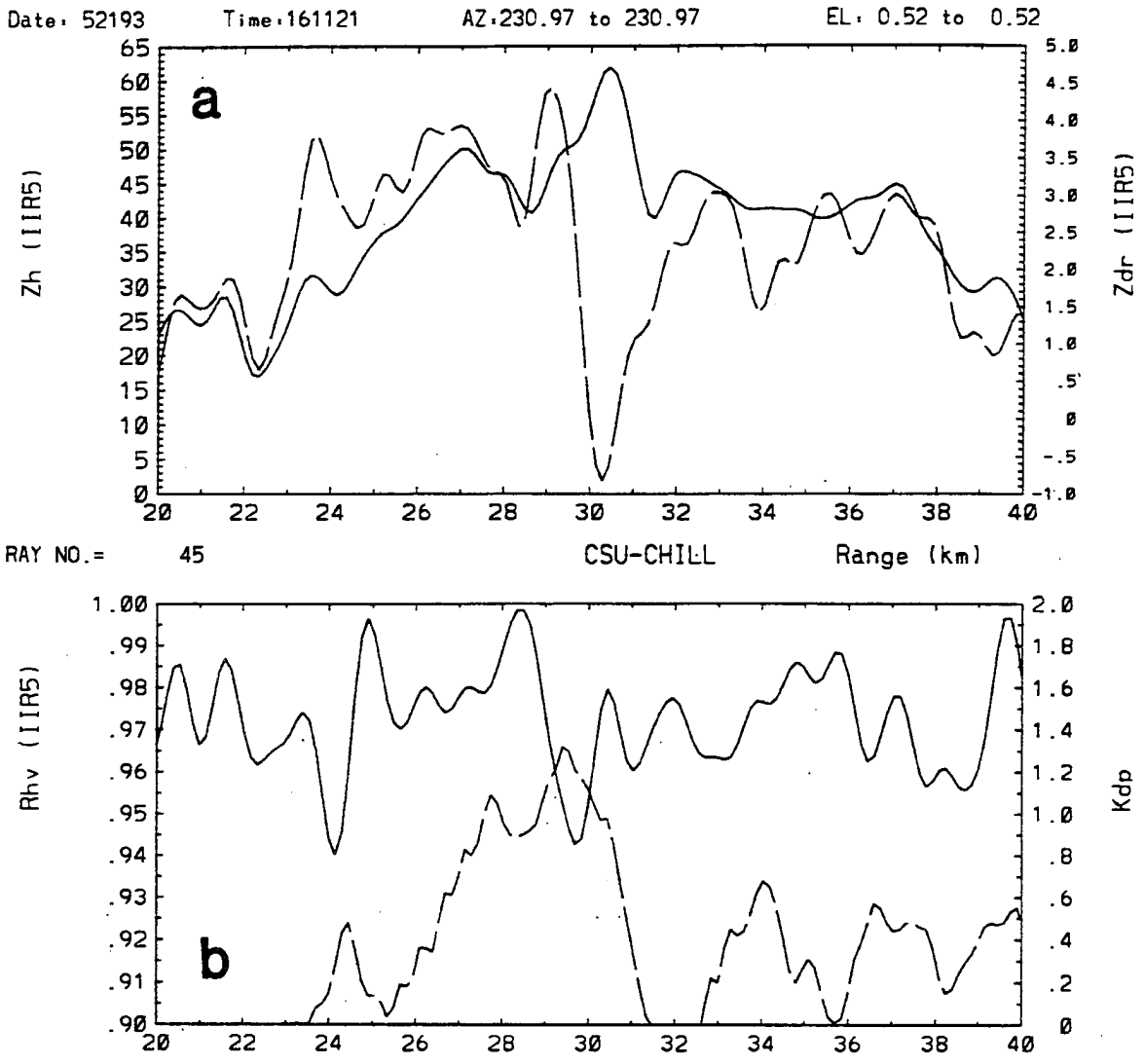

Fig. 5.5 Range plots for 21 May 1993, 1611 MDT at an azimuth of 230.97°, an elevation of 0.52°, and a range from 20 to 40 km through the convective cell depicted in Fig. 5.4c a) of Z_h (dBZ, solid line) and Z_{dr} (dB, dashed line). and b) of K_{dp} (° km^{-1}, dashed line), and $\rho_{hv}(0)$ (solid line).

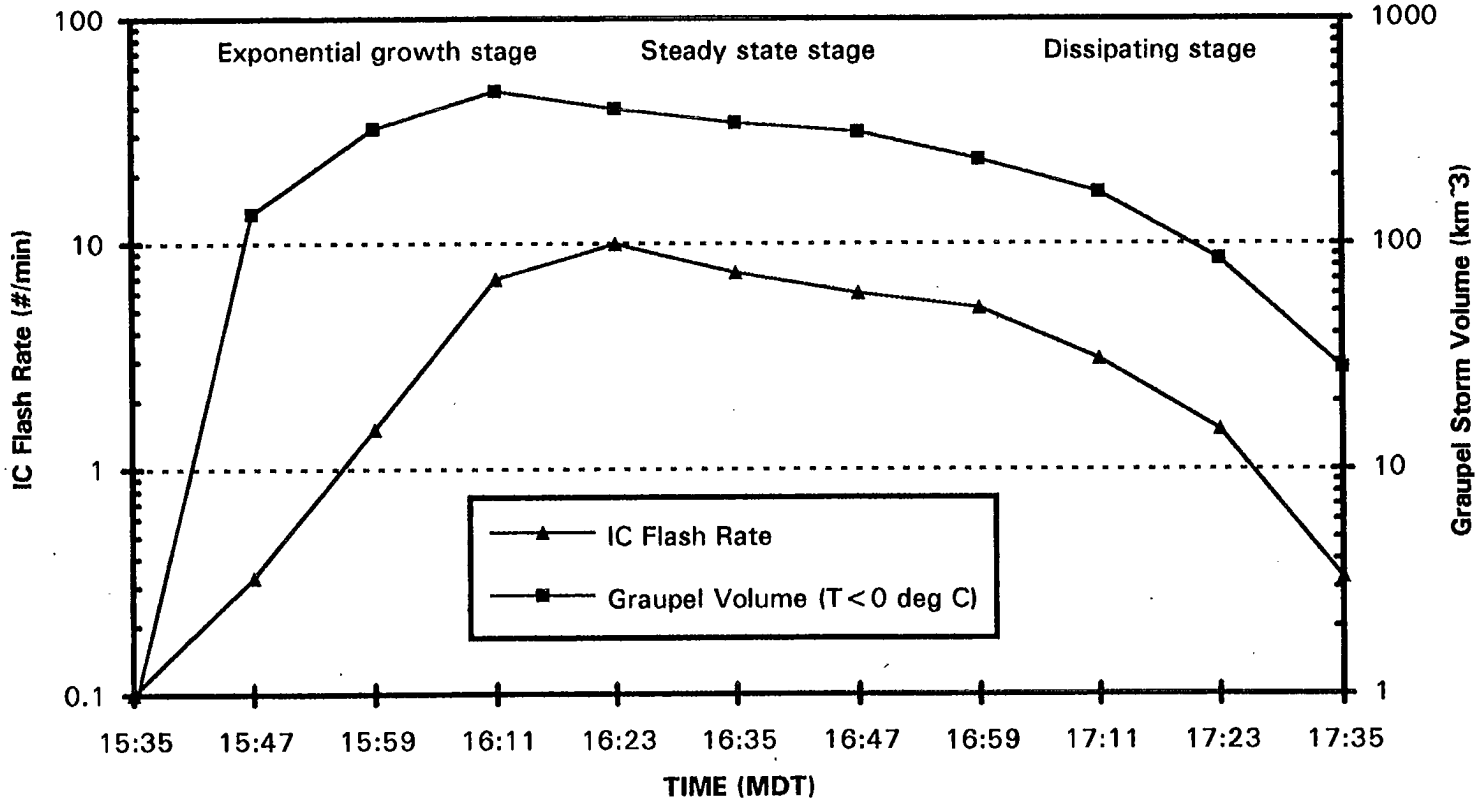

Fig. 5.6 Evolution of the IC lightning flash rate (flashes min^{-1}) and graupel storm volume (km^3) above the melting layer as inferred from multiparameter radar data for a two hour period on 21 May 1993 at 12 minute resolution.

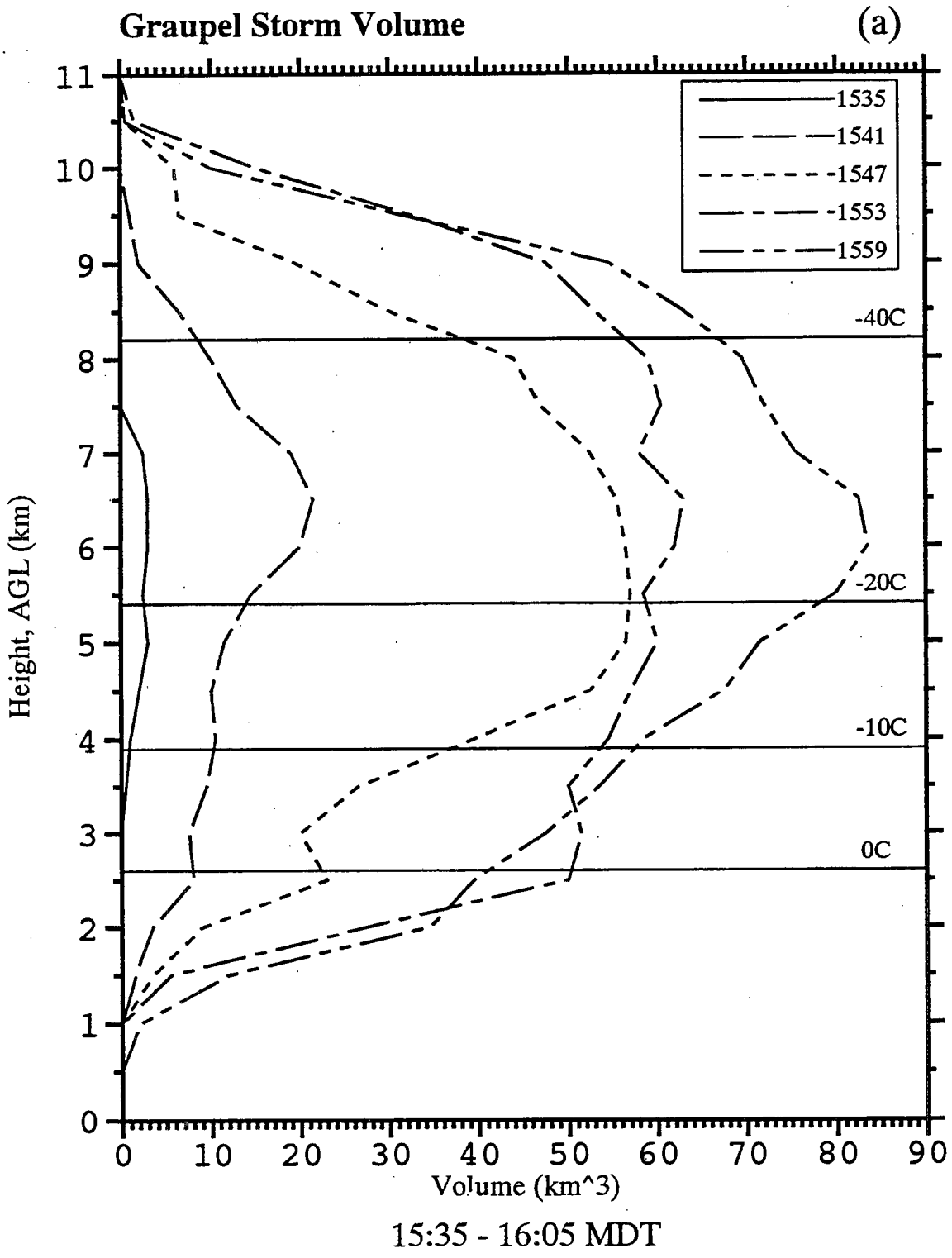

Fig. 5.7 Vertical profiles of graupel storm volume per unit interval of height (km^3) as inferred from multiparameter radar data. a) Graupel volume for the exponential growth of the IC flash rate.

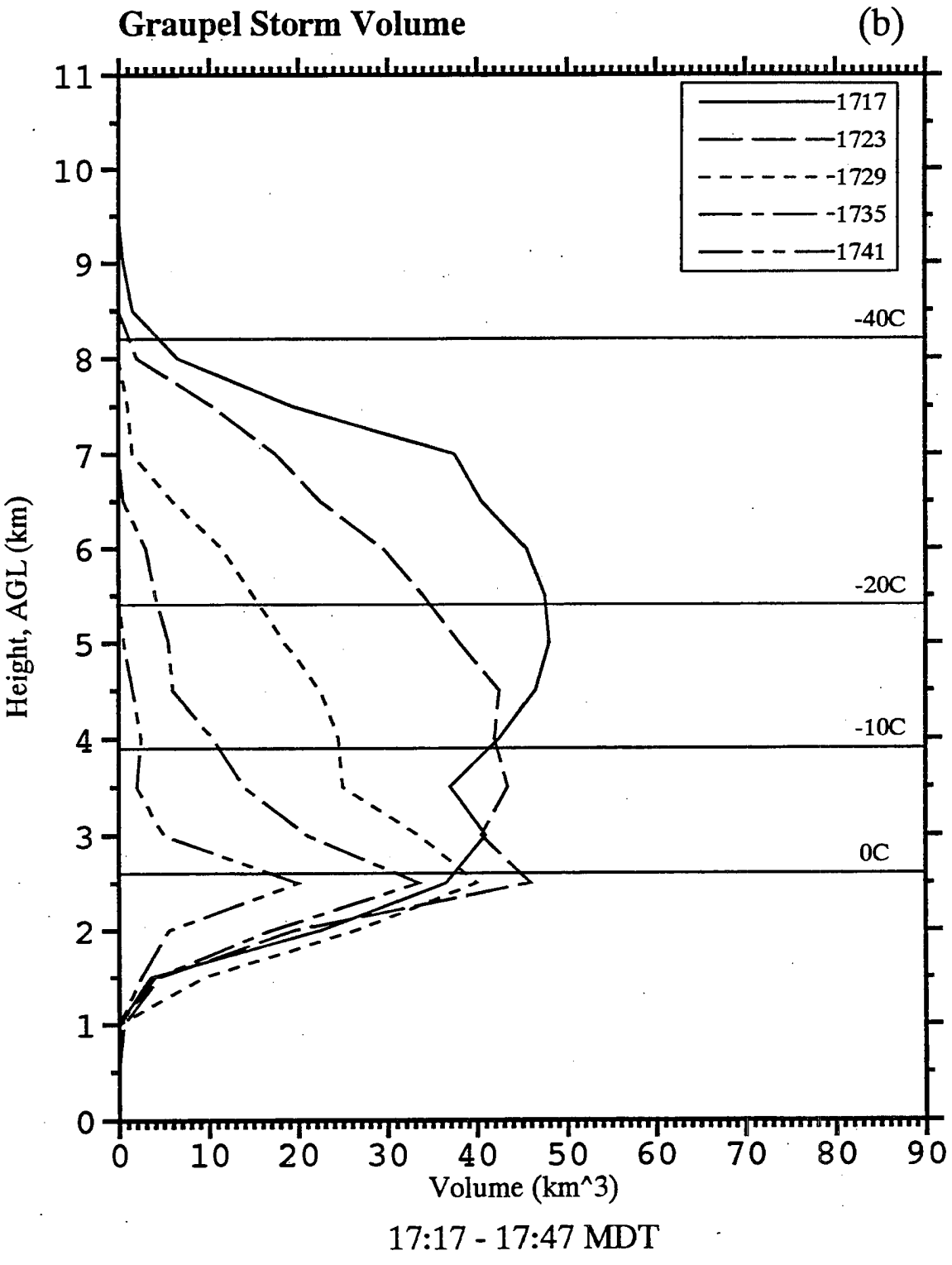

Fig. 5.7 b) Same as in a) except during the rapid decay of the IC flash rate.

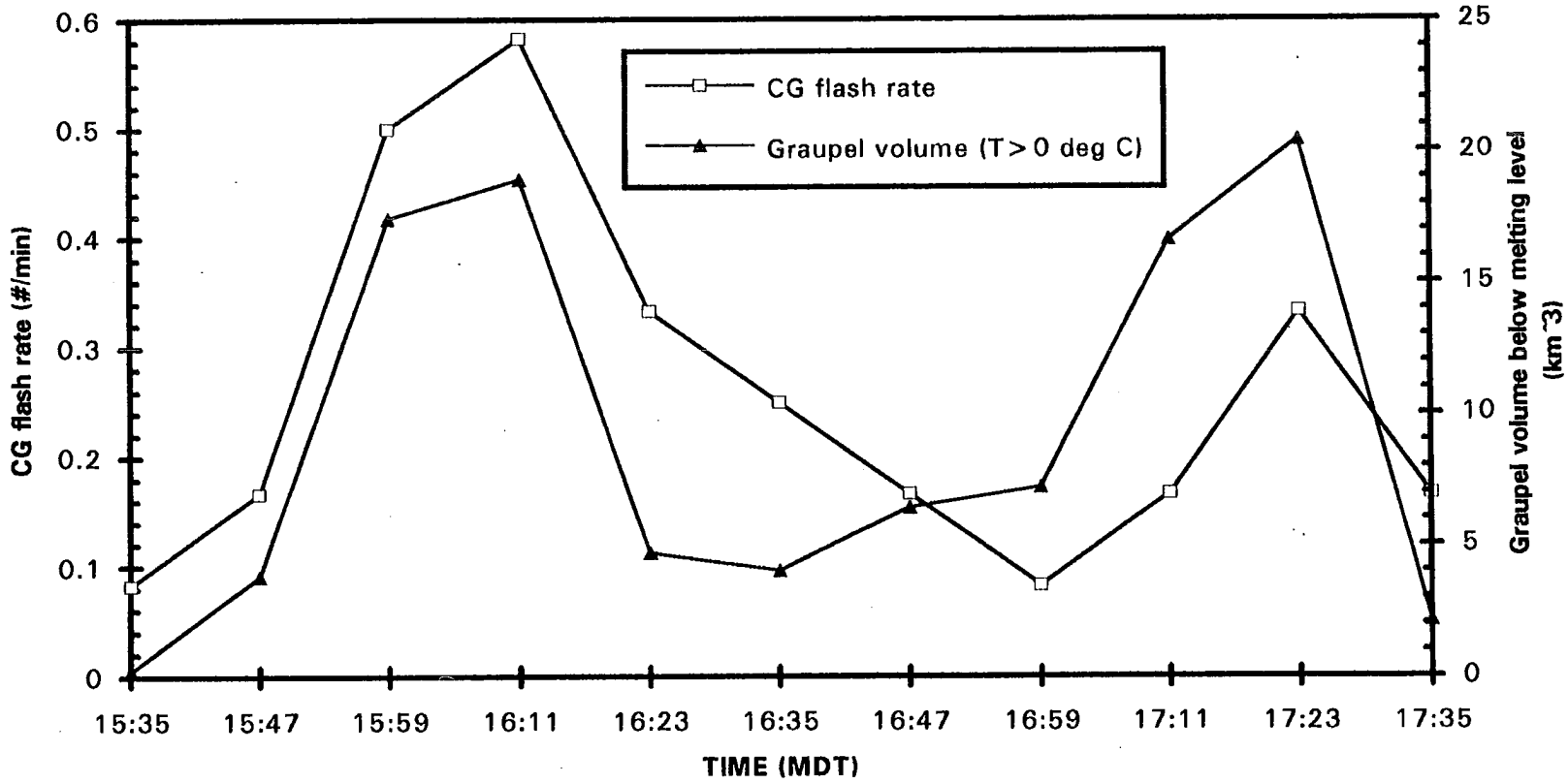

Fig. 5.8 Evolution of the CG lightning flash rate (flashes min^{-1}) and graupel storm volume (km^3) below the 0° C level as inferred from multiparameter radar data for a two hour period on 21 May 1993 at 12 minute resolution.

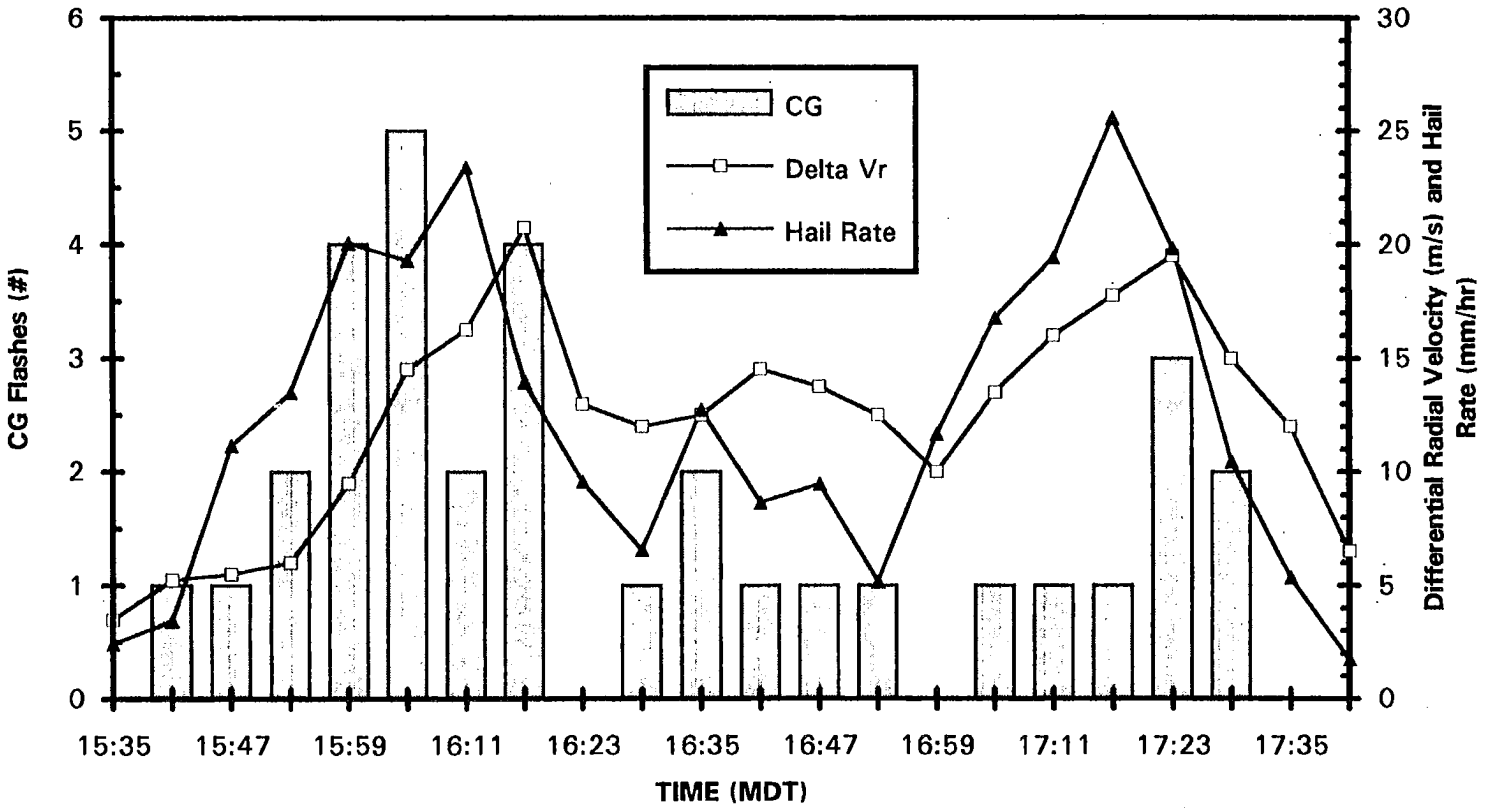

Fig. 5.9 Evolution of the maximum differential radial velocity, (ΔV_r, ms^{-1}; the difference in the radial velocity between two peaks of diverging flow over a distance of $\leq$ 4 km at the lowest elevation angle), as a measure of microburst strength, CG flash rate (min^{-1}), and liquid equivalent hail rate (mm hr^{-1}) for a two hour period on 21 May 1993 at six minute resolution.

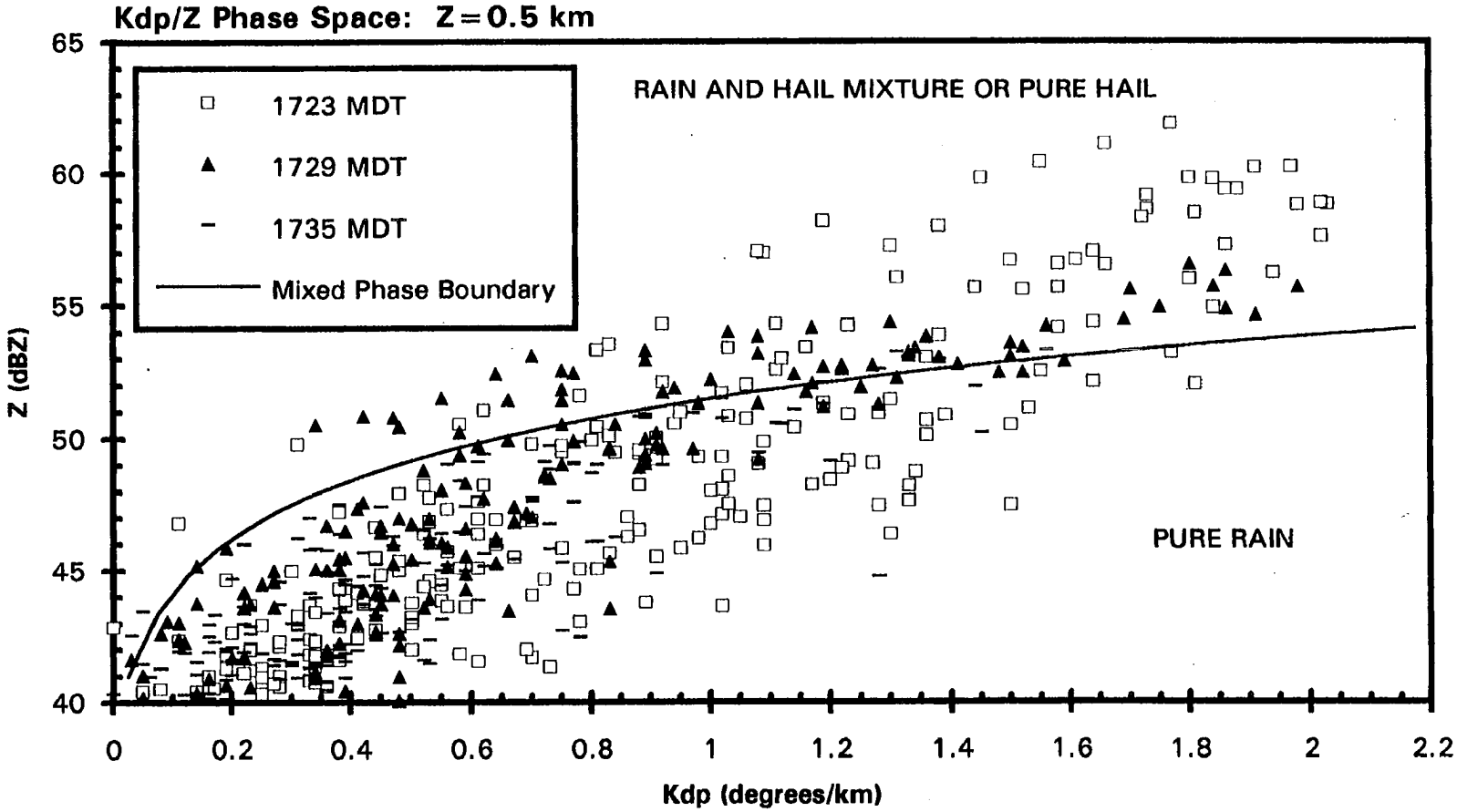

Fig. 5.10 Scatter plot of Z-K_{dp} for CSU-CHILL radar observations at z=0.5 km on 21 May 1993 from 1723 to 1741 MDT during which time the CG flash rate went from a peak of 0.5 to 0 min^{-1}. The empirical boundary between rain and mixed phase precipitation or hail is shown as a solid line. Z is an average of reflectivity factors at horizontal (Z_h) and vertical polarizations (Z_v).

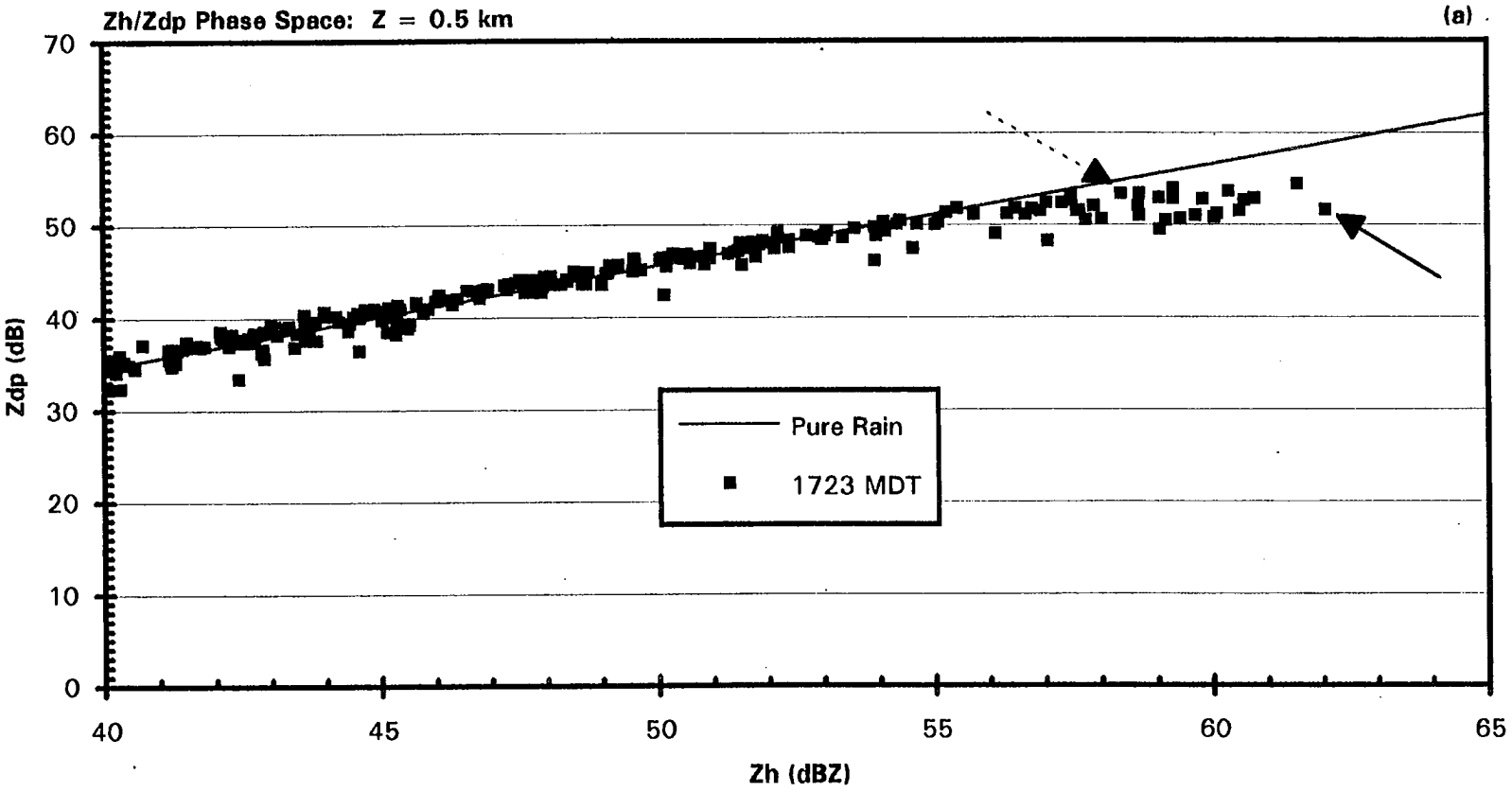

Fig. 5.11 Scatter plot of $Z_{dp} = 10\log(\mathbf{Z_h} - \mathbf{Z_v})$ [dB] vs. Z_h [dBZ] for CSU-CHILL radar observations at z=0.5 km on 21 May 1993. Solid line is the pure rain line. a) Results at 1723 MDT (CG flash rate = 0.5 min^{-1}).

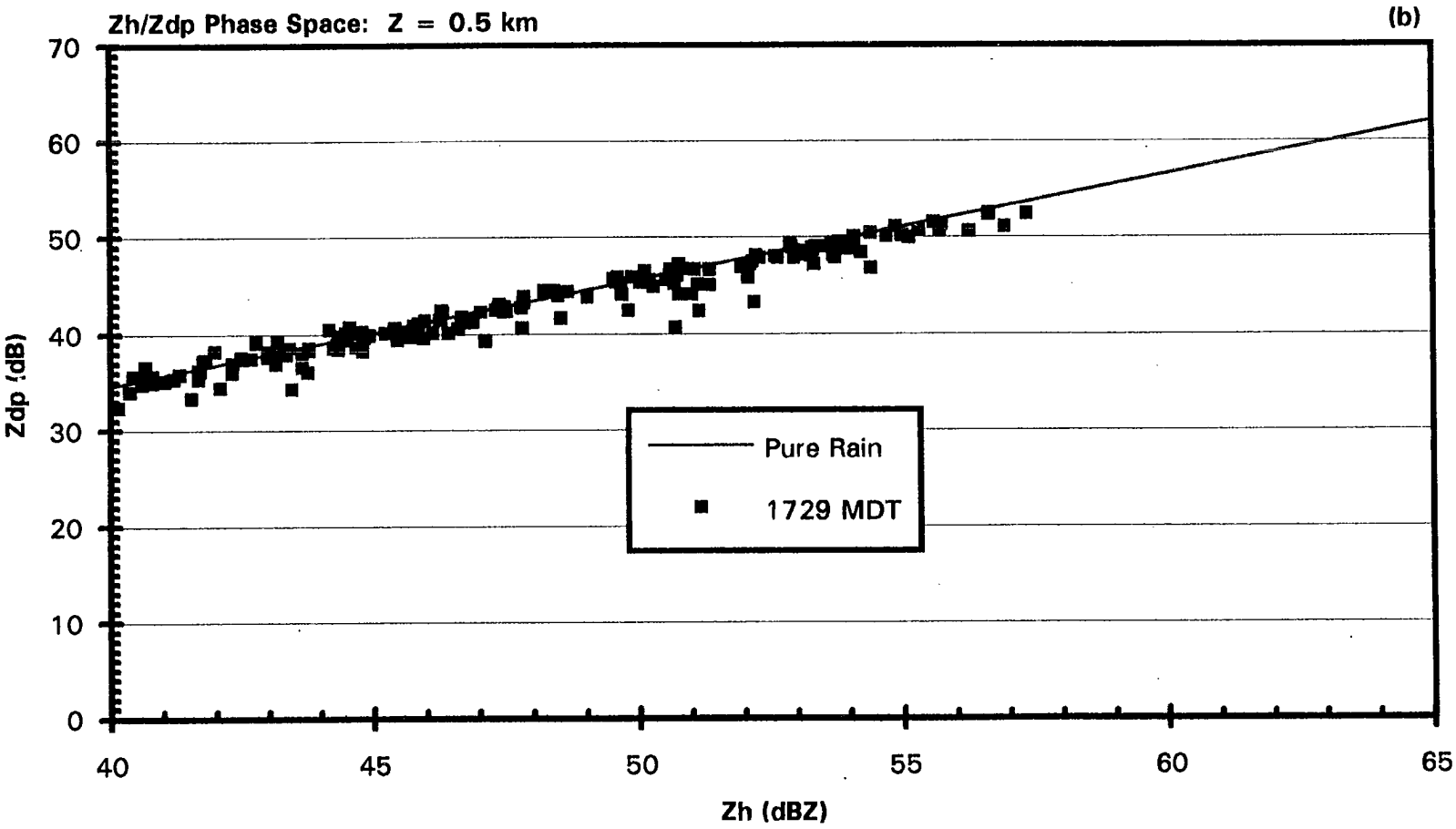

Fig. 5.11 b) Results at 1729 MDT (CG flash rate = 0.33 min^{-1}).

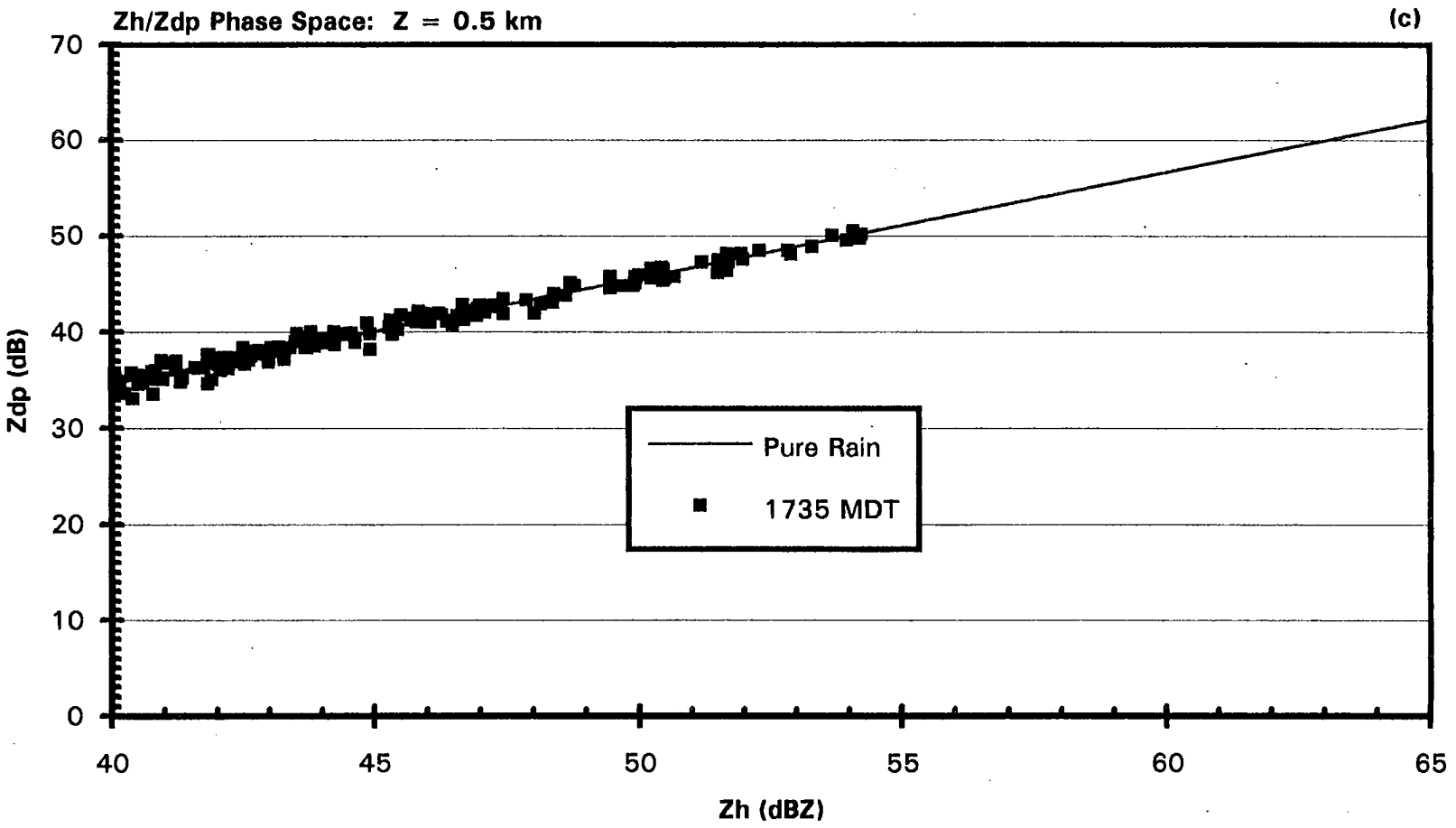

Fig. 5.11 c) Results at 1735 MDT (CG flash rate = 0 min^{-1}).

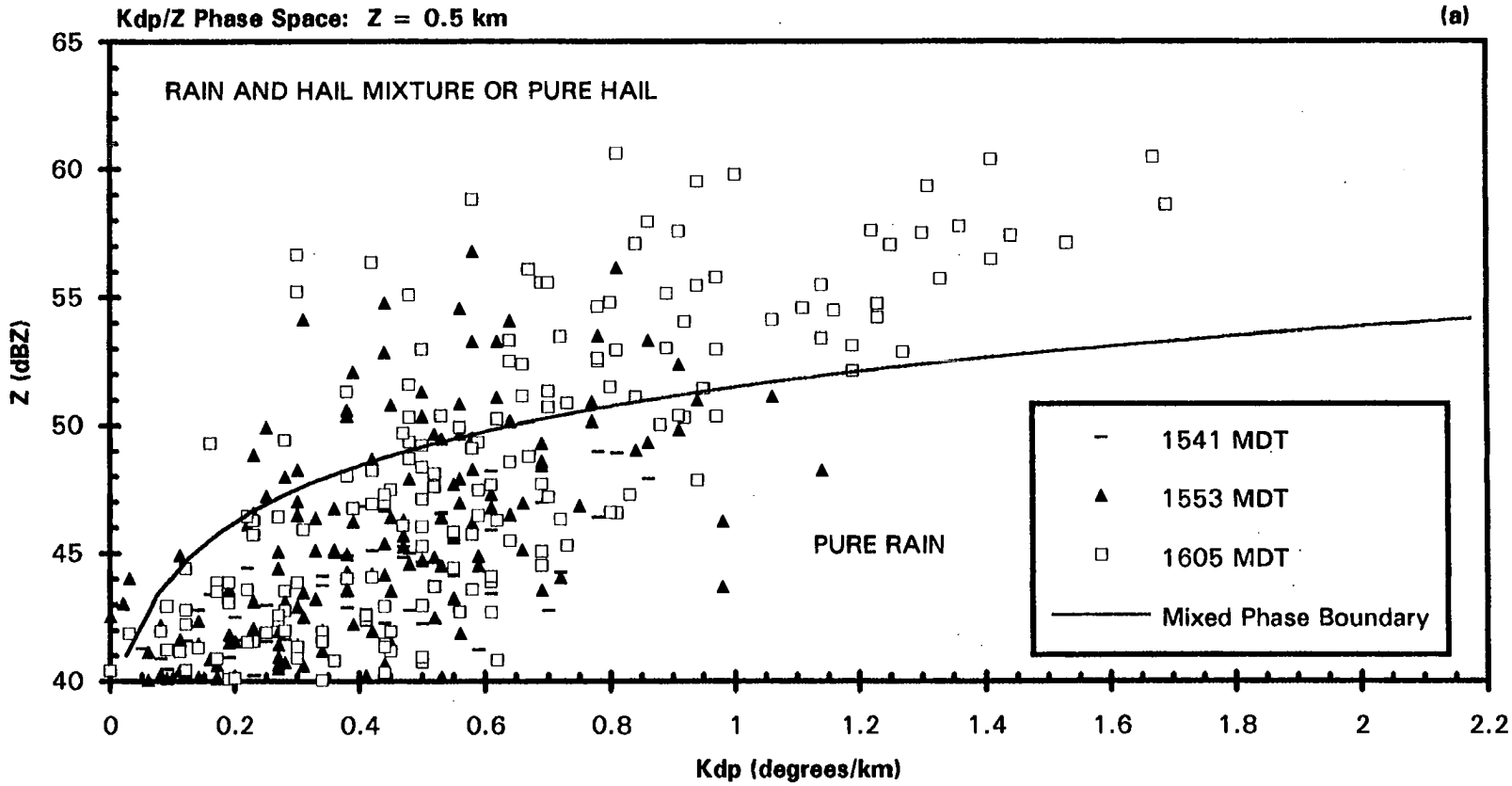

Fig. 5.12 Same as Fig. 5.10 with results from a) 1541 - 1605 MDT during which time the CG flash rate increased.

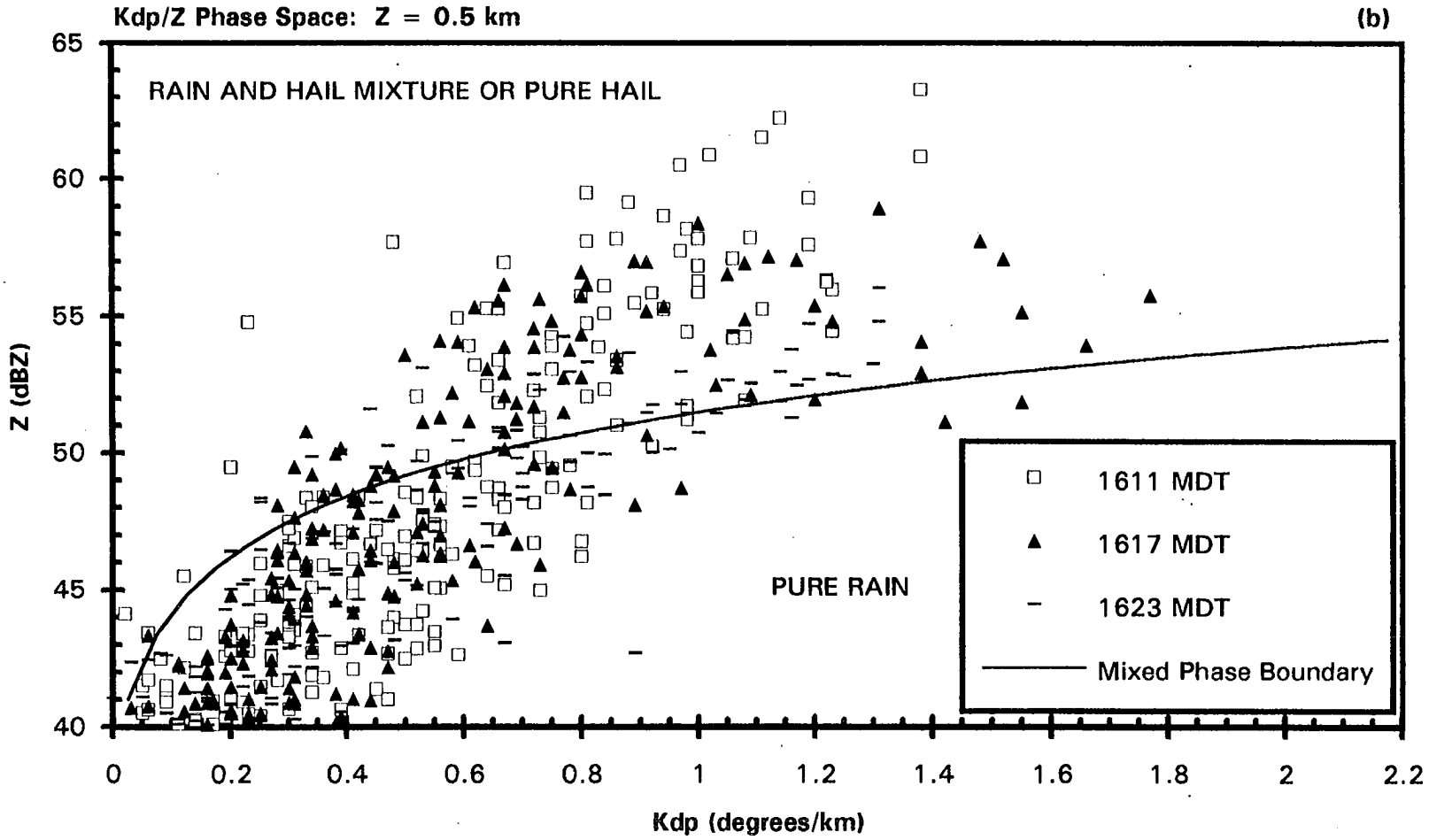

Fig 5.12 b) 1611 - 1623 MDT during which time the CG flash rate decreased.

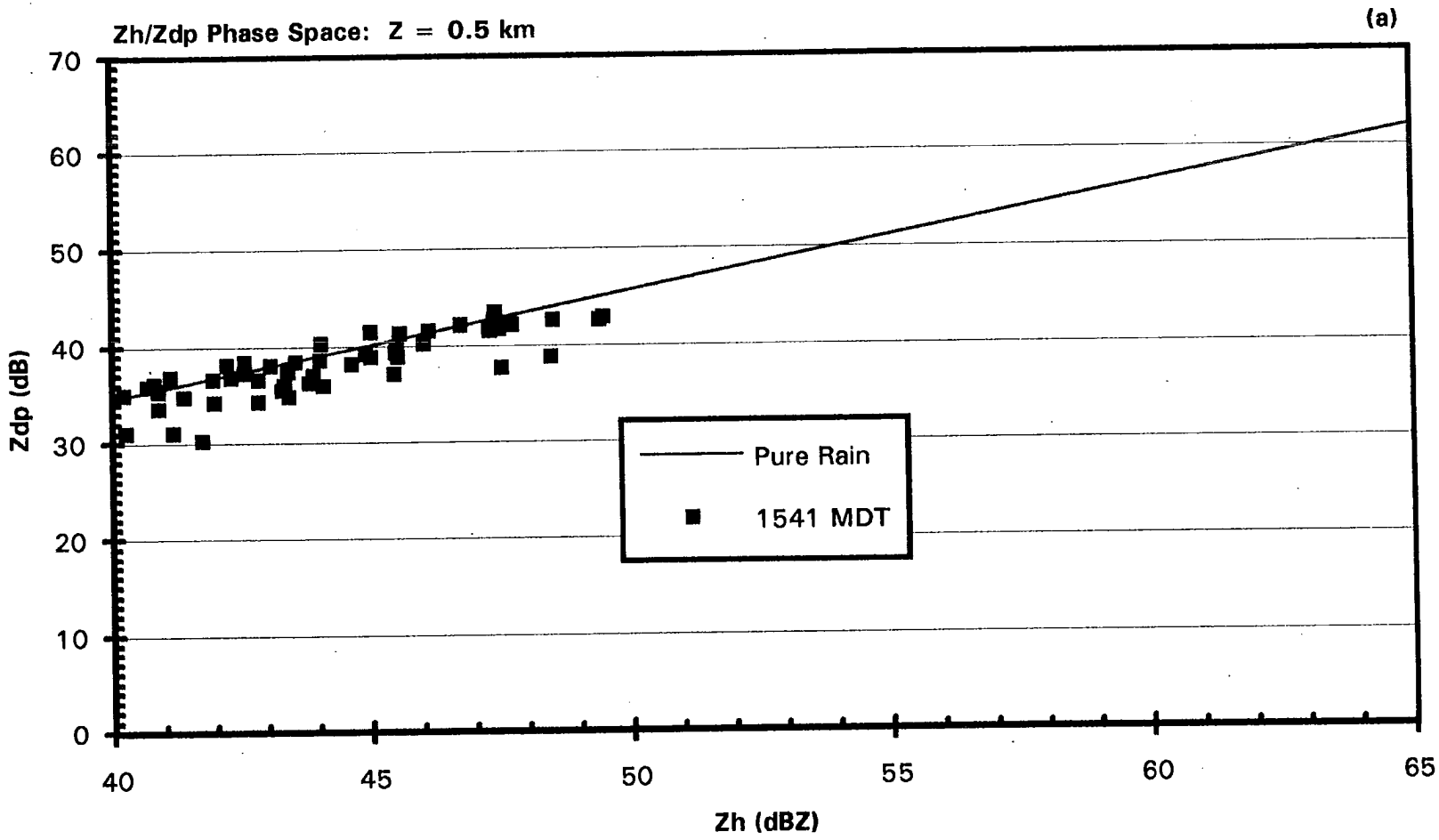

Fig. 5.13 Same as Fig. 5.11. a) Results at 1541 MDT.

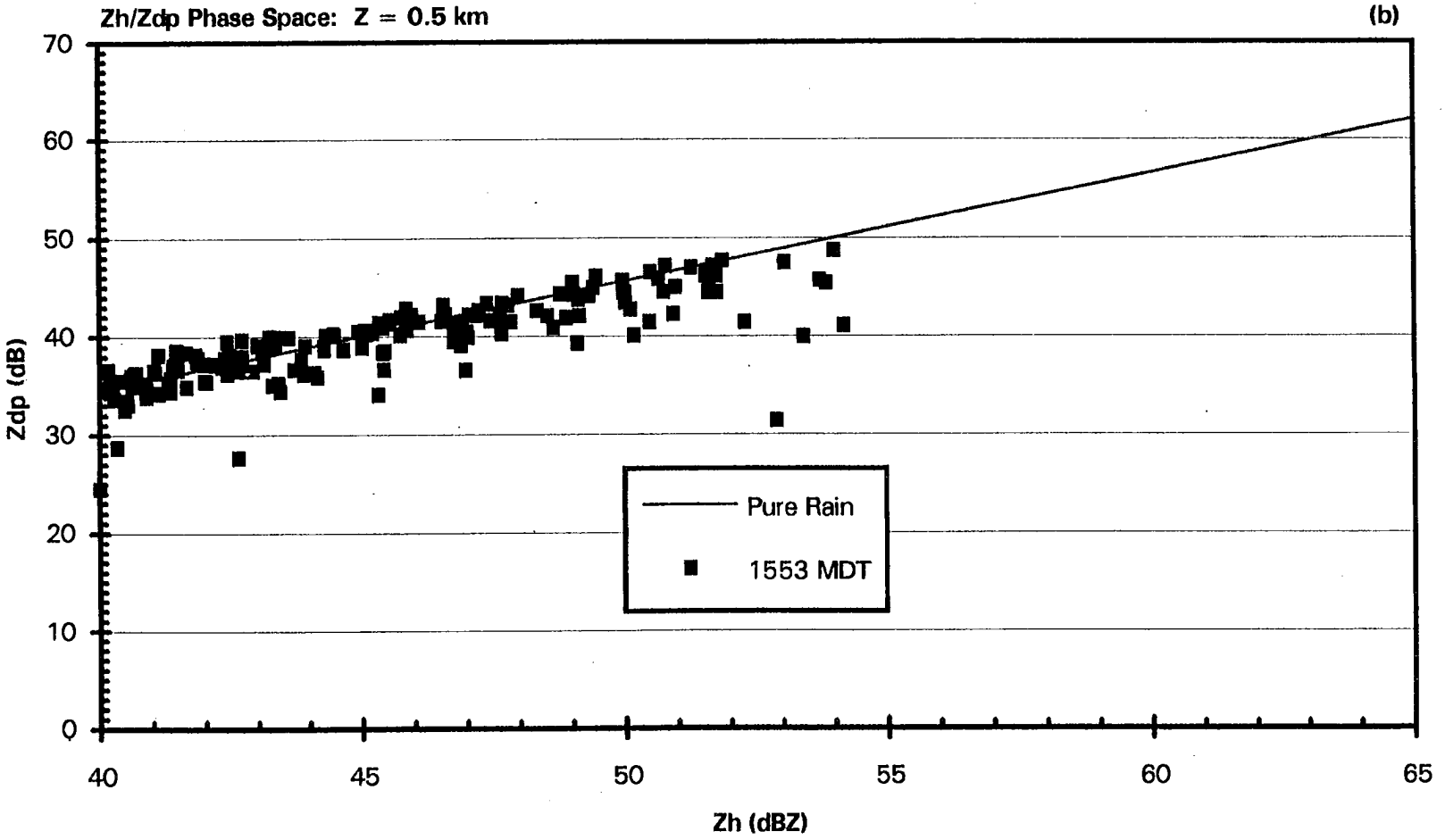

Fig. 5.13 b) Results at 1553 MDT.

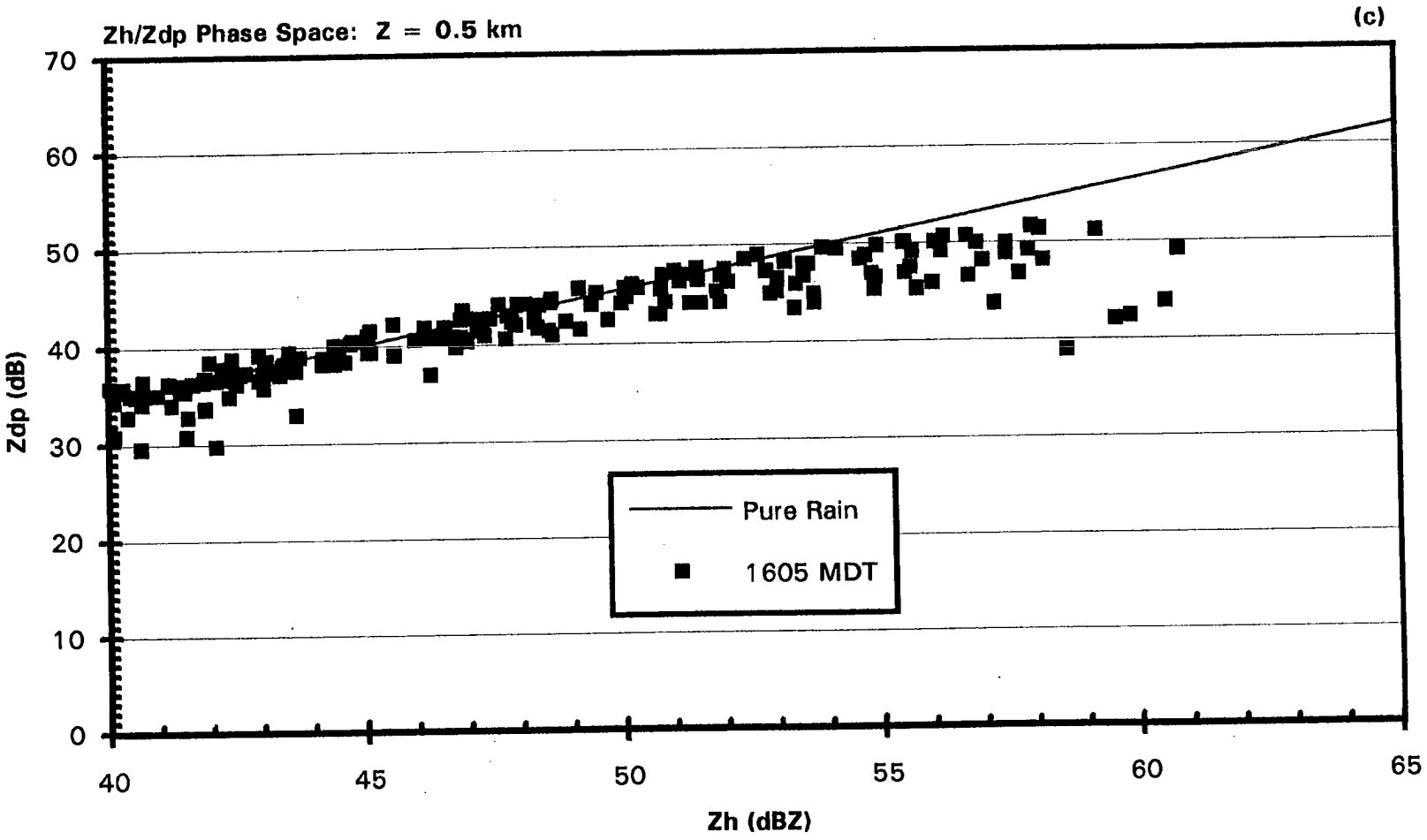

Fig. 5.13 c) Results at 1605 MDT.

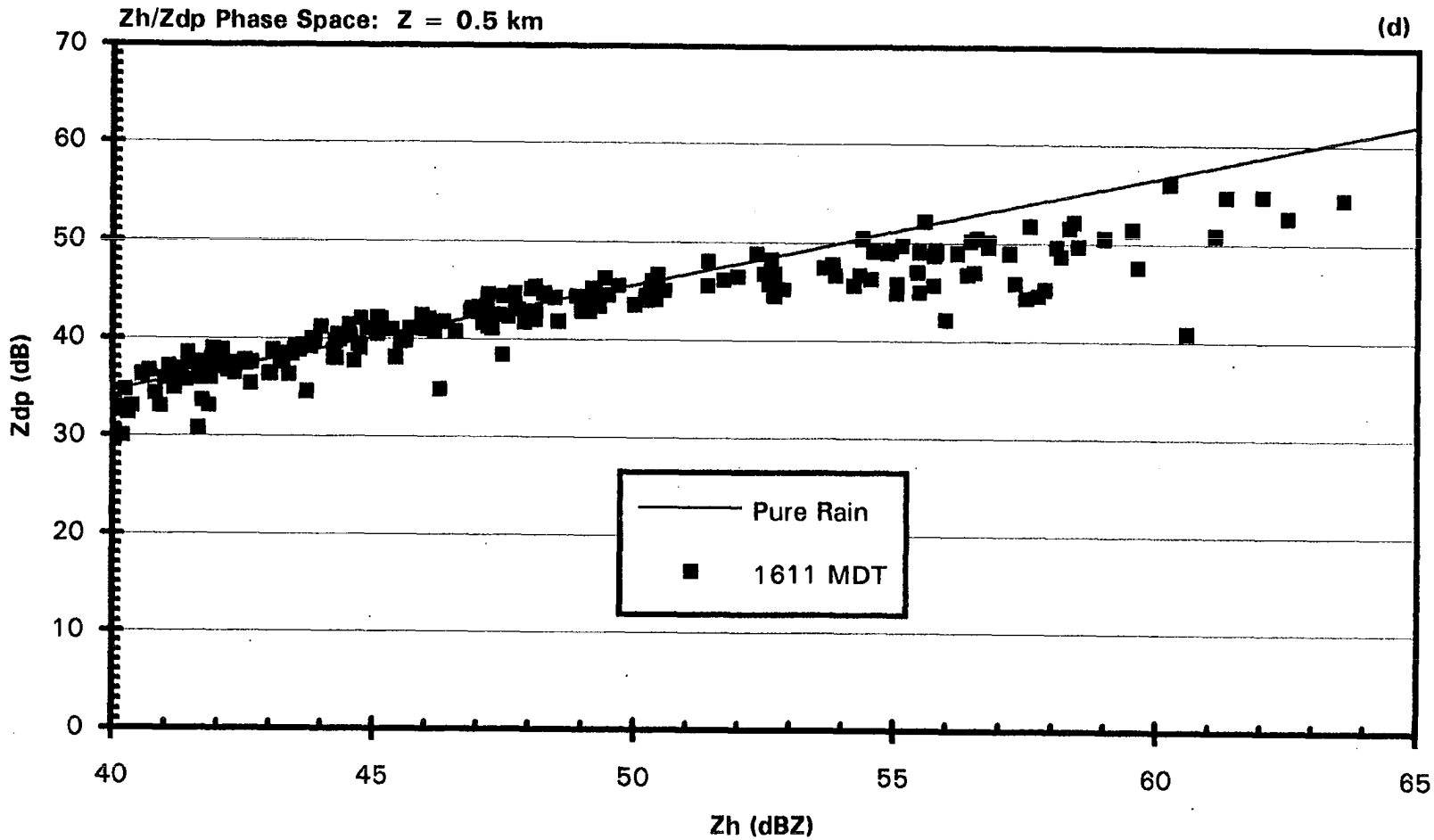

Fig. 5.13 d) Results at 1611 MDT.

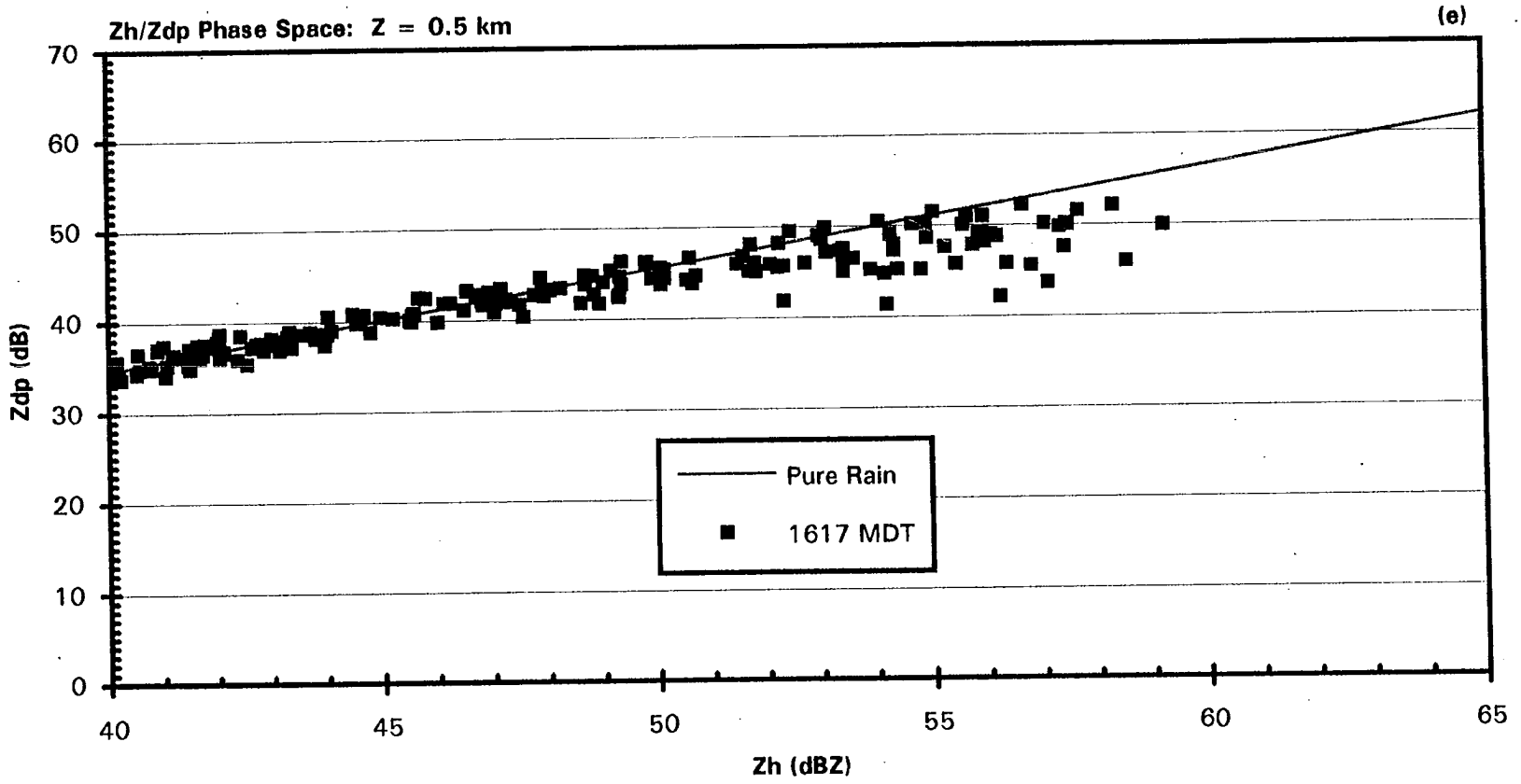

Fig. 5.13 e) Results at 1617 MDT.

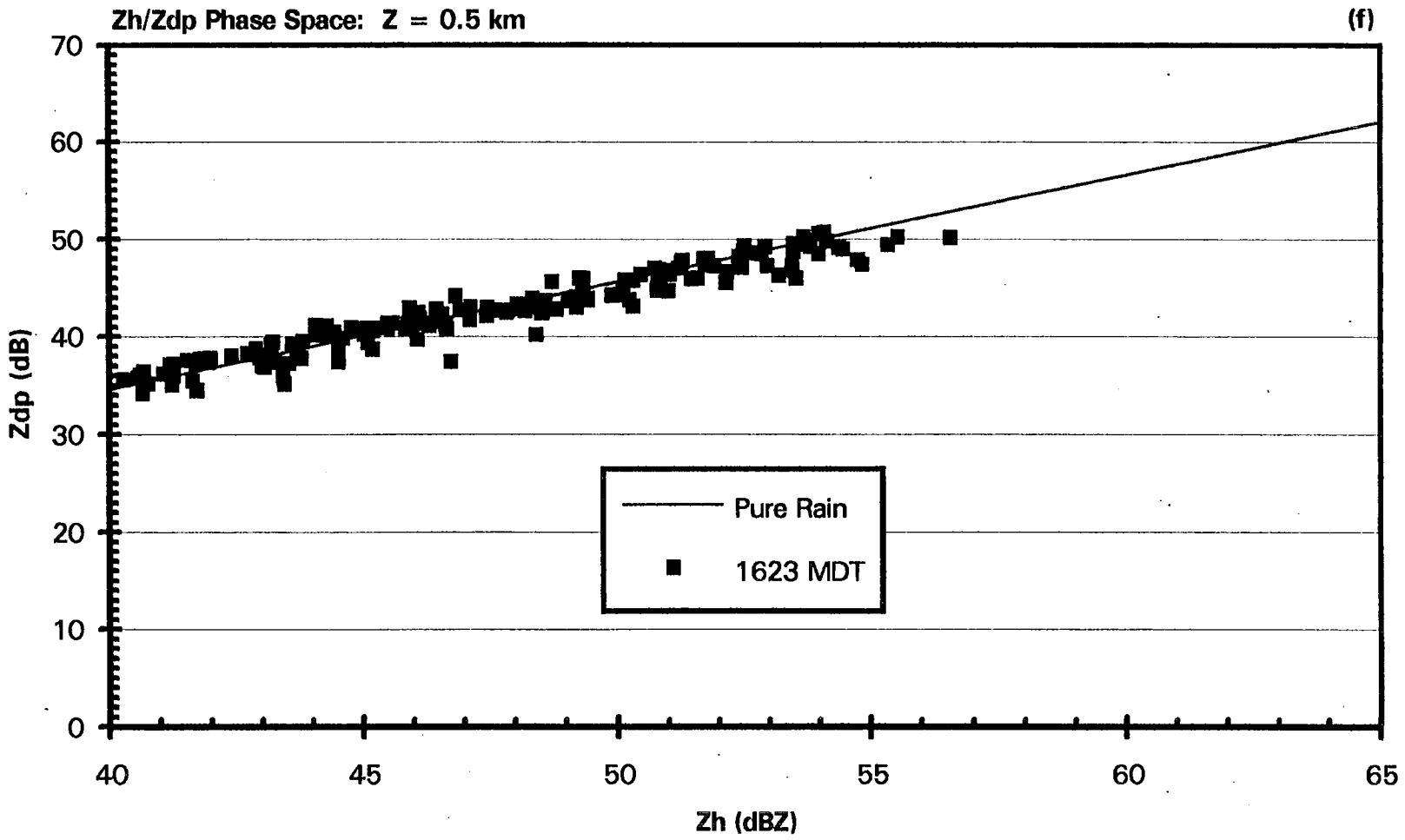

Fig. 5.13 f) Resutls at 1623 MDT.

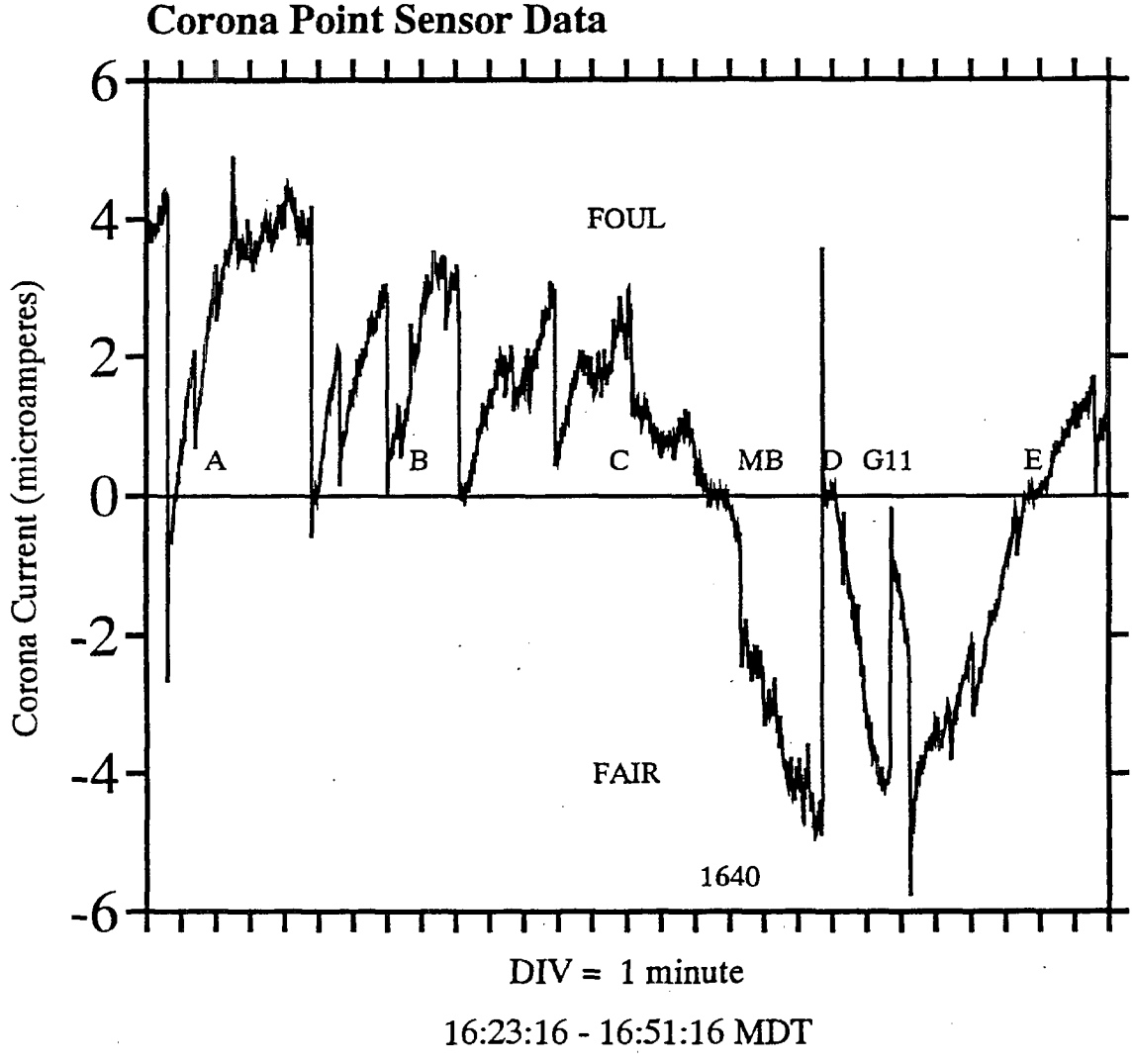

Fig. 5.14 Corona point sensor data during a field excursion associated with precipitation which occurs at approximately 1640 MDT. The corona current is in microamperes, is positive for a foul-weather electrostatic field (indicating negative charge aloft), and is negative for a fair-weather electrostatic field (indicating positive charge aloft). "MB" refers to a microburst detected in single-Doppler radar data at approximately 1641 MDT. "G11" refers to a peak wind gust of 11 m s^{-1} recorded by a nearby observational site at 1645 MDT. The letters "A-D" are time markers placed for comparison with Fig. 5.16.

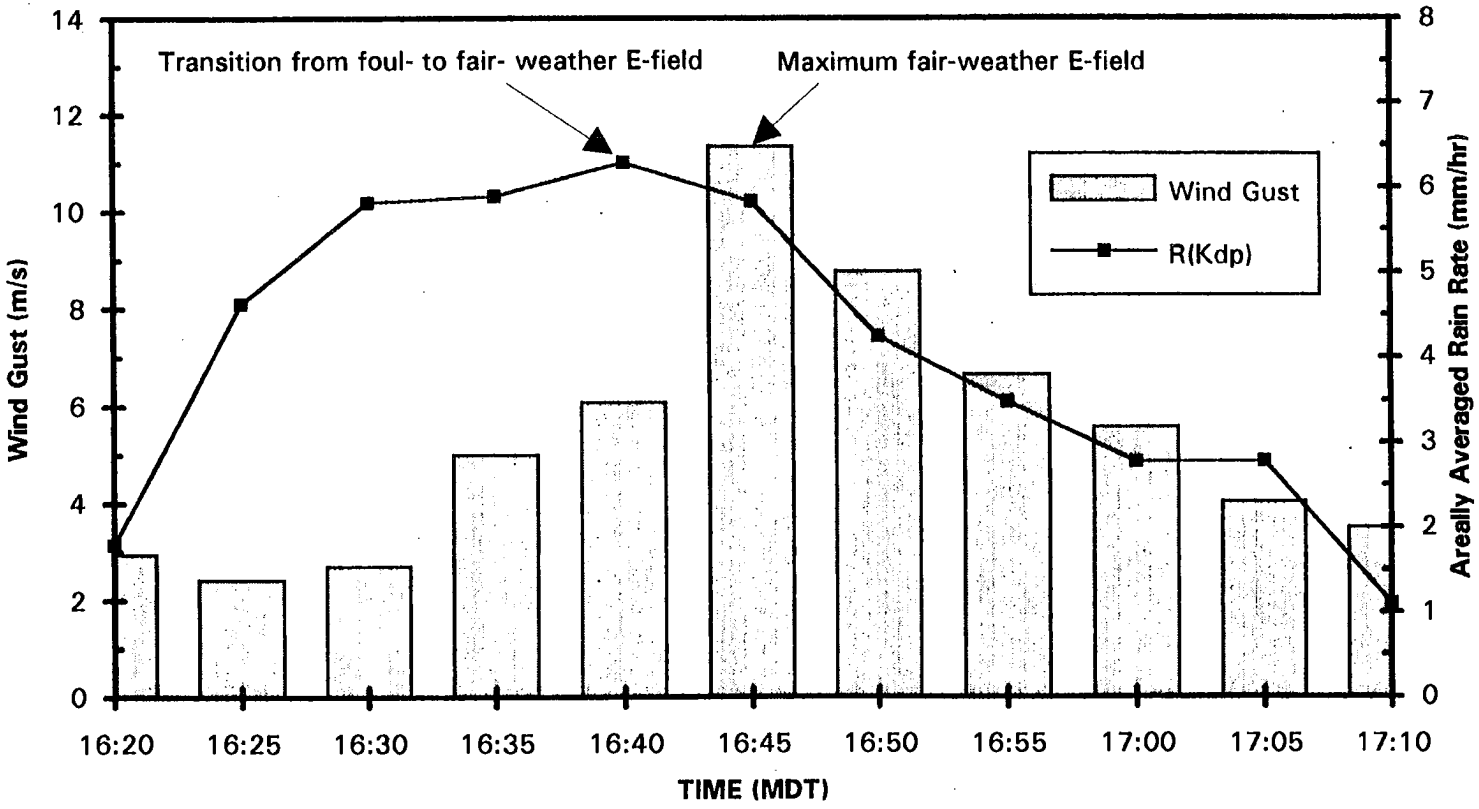

Fig. 5.15 Areally averaged rain rates (mm hr^{-1}) calculated using K_{dp} and peak wind gust (m s^{-1}) measured in the vicinity of a field excursion associated with precipitation at five-minute resolution.

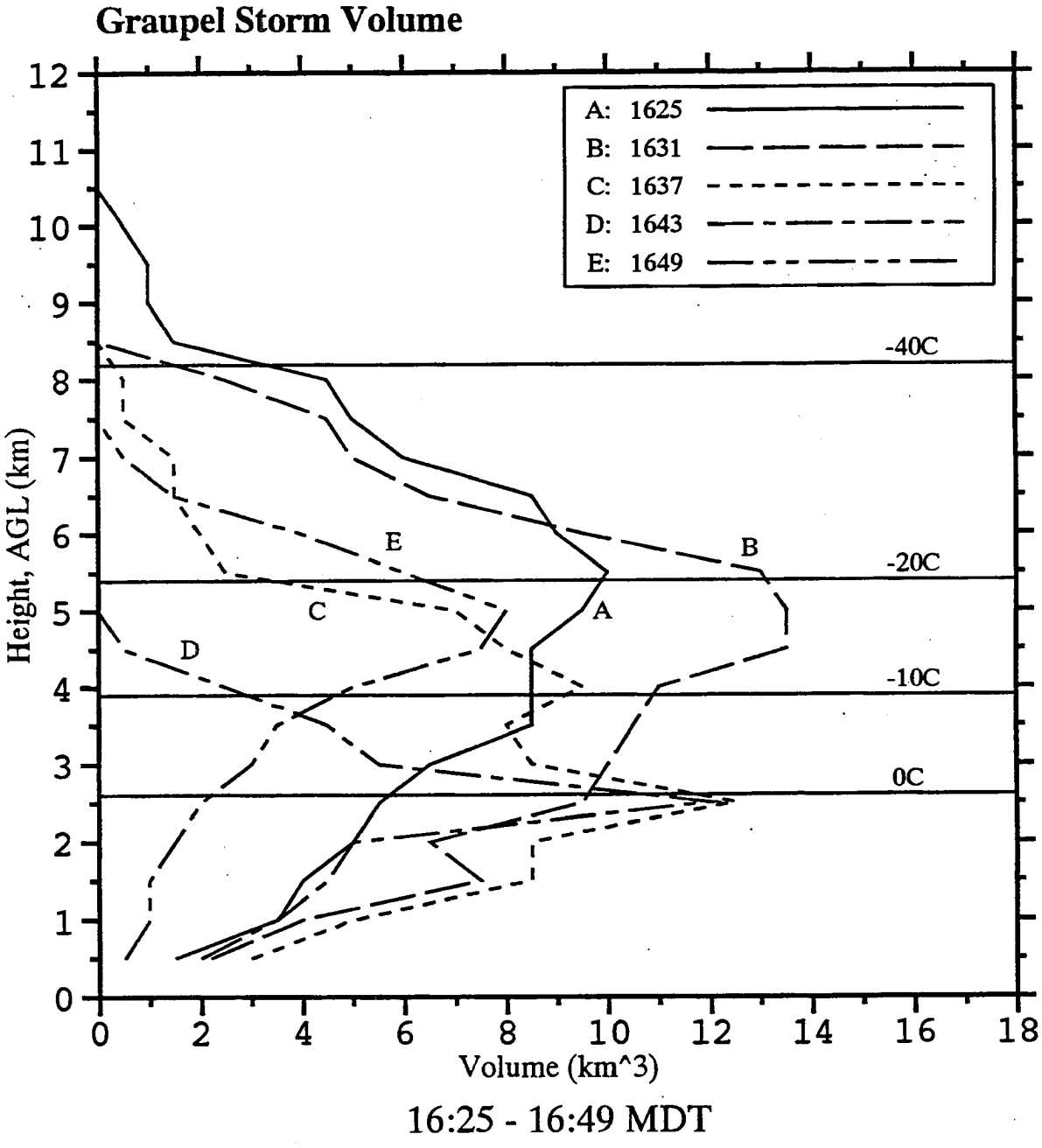

Fig. 5.16 Same as Fig. 5.7 except for 1623 - 1643 MDT in the vicinity of a field excursion associated with precipitation.

CHAPTER 6

CASE STUDY 2

A SEVERE SQUALL LINE

In this chapter, we investigate correlations between the radar inferred kinematic and microphysical evolution of a developing squall line and the evolution of lightning type and frequency. We present detailed observations and analyses of positive differential reflectivity (Z_{dr}) columns above the freezing level within the low level convergence zone along a merging gust front. In correlating ice-phase microphysics with squall line electrification, we speculate on the impact of these positive Z_{dr} columns on the in-cloud and cloud-to-ground flash rates during squall line development.

6.1 Atmospheric conditions

The morning upper air sounding (1200 UTC) for Denver on 28 May 1993 revealed a potentially unstable atmosphere with a significant capping inversion at low levels (surface to 0.5 km AGL) as shown in Figure 6.1. Surface conditions were relatively moist for the Front Range area with dewpoint temperatures near 9° C. The freezing level was at 2.6 km AGL and the wet bulb freezing level was calculated at 3.0 km AGL. Analysis of the sounding data gives a convective temperature of 25° C (77° F), a lifted condensation level (LCL) of 700 mb (1.5 km AGL), a level of free convection (LFC) of 630 mb (2.5 km AGL), and an equilibrium level of 230 mb (9.5 km AGL). At 1200 UTC, winds were weak (1-3 m s^{-1}) and out of the south near the surface. Winds veered with height such that the steering level winds (500 mb) were out of the west at about 5 - 10 m s^{-1}. To more accurately gauge the potential instability in the atmosphere, a modified sounding was

created with a surface temperature equal to the convective temperature and a surface dew point temperature of 10° C. Using this modified sounding, we calculate convective available potential energy (CAPE) of about 2000 J kg^{-1}, convective inhibition (CIN) of approximately 150 J kg^{-1}, and a lifted index of -3° C.

The 1200 UTC upper air data at 500 mb (Fig 6.2) showed a high amplitude shortwave trough over the Pacific coast and an associated short wave ridge axis oriented from northwest to southeast passing through Colorado. A weak shortwave trough whose southern edge terminated near the northeast corner of Colorado is evident in the 500 mb wind and pressure data. Although not apparent in the 500 mb pressure analysis, another weak short wave was evident in infrared satellite data (not shown) over the Gunnison River Valley (south central Colorado on the windward side of the Rocky Mountains) during the early morning hours. Given the southwesterly flow aloft, this feature moved to the northeast at about 10 m s^{-1}, bringing it to the Front Range area during the mid-afternoon (around 2100 UTC or 1500 MDT).

The winds aloft continued to be weak and out of the west to southwest at 10 m s^{-1} while the near surface winds backed to the east through southeast and intensified to about 5 - 10 m s^{-1}. This upslope flow at the surface was the result of a weak stationary front over northeastern Colorado (CO) and the associated anticyclonic flow over the Great Plains due to a high pressure center near the Great Lakes as seen in the 2100 UTC (1500 MDT, UTC = MDT + 6 h) surface analysis (Fig. 6.3). There was little temperature and moisture contrast across this boundary in Colorado. This is confirmed by the Front Range mesonet data at 2100 UTC as seen in Fig. (6.4). The most noticeable feature in the afternoon mesonet data was the strong surface upslope out of the east to southeast in northeastern CO which maintained a continual supply of warm, moist air despite the erosion of the morning surface inversion and the resulting afternoon mixing of the boundary layer. As seen in Fig. 6.4, temperatures in the vicinity of the CSU-CHILL radar

(ie, Greeley, GLY) had reached the convective temperature (25° C or 77° F) by 2100 UTC and dewpoints remained near 10° C (50° F).

The two key features of the atmospheric conditions on this day were 1) abundant low level moisture due to southeasterly upslope flow and 2) relatively weak westerly flow aloft. Doswell (1980) showed that severe convective activity in northeastern Colorado is usually favored under conditions of terrain induced upslope flow out of the east. When moist upslope flow at the surface combines with relatively weak westerly winds aloft, conditions are favorable for flash flooding due to the slow propagation speeds of squall lines formed under these conditions (Maddox et al., 1980). Given the abundant CAPE (2000 J kg^{-1}) associated with the moist surface conditions by 1500 MDT, all that was required to initiate potentially severe thunderstorms with the possibility of flash flooding was a triggering mechanism to overcome the remaining convective inhibition. Due to the advancing short wave trough over the Rocky Mountains, enhanced heating at higher elevations, and moist surface upslope, convection first began over the mountains west of the Front Range.

6.2 Overview of Squall Line Formation

In Figs. 6.5 a-g, we present the initial development of a broken-areal squall line (Bluestein and Jain, 1985) as seen in horizontal cross-sections of CSU-CHILL horizontal reflectivity at 2 km AGL. At 1559 MDT (Fig. 6.5a), decaying convection exited the foothills (see Fig 3.1 for the topography of the region) 35 km to the northwest of the CSU-CHILL radar and isolated convective cells were evident 25 km to the west-southwest and 40 km to the north. By 1611 MDT (Fig 6.5b), isolated cells continued to develop to the north and the cell exiting the foothills to the northwest (x = -33 km, y= 15 km) was raining out. The small grouping of cells to the west-southwest had undergone explosive convective growth during the previous 12 minutes and reportedly produced a

short lived F0 tornado (5 km southeast of Loveland) at 1612 MDT and spawned several funnel clouds during the next half-hour (Storm Data, 1993).

A plausible cause for this non-supercell tornado (sometimes called landspouts; Bluestein, 1985) can be seen in CSU-CHILL radial velocity data at 2.5° in elevation for 1612 MDT (Fig 6.6a). Cool tones (ie, green and violet) are negative and indicate wind flowing toward the radar and warm tones (ie, yellow and red) are positive and indicate wind flowing away from the radar. First, note that a wide band of decayed convection was present 40 km and further to the west of the CSU-CHILL radar that was not evident in Fig 6.5a. The large area of green and violet radial velocity data in this decayed convection over the foothills indicates the presence of a cold pool which resulted from downbursts driven by sub-cloud evaporation and melting (Srivastava, 1987). The gust front along the leading edge of this cold pool had advanced eastward into the Front Range area by 1612 MDT. It is visible in Fig. 6a as a convergence zone that is oriented along a north-to-south line with its northern (detectable) extent at about 40 km in range and 323° in azimuth and its southern extent at about 30 km in range and 240° in azimuth. The convergence zone was formed by the eastward advancing cold pool (green tones, 8 - 12 m s^{-1}) colliding with the strong westward moving upslope flow (yellow tones, 3 - 8 m s^{-1}). Note that by 1612 MDT the gust front has collided with a rapidly developing cell to the west-southwest of the radar (240° - 270° at about 30 km in range), in the vicinity of the F0 tornado report which also occurred at 1612 MDT.

Further evidence for the existence of a cold pool originating in the foothills that combines with upslope flow to form a convergence zone can be found in the Front Range mesonet data shown in Figs. 6.7 a and b. Fig 6.7a is a plot of temperature, dew point temperature, wind speed and direction, pressure, and solar radiation versus time at Fort Collins. Notice that the temperature drops rapidly, wind speed increases, and the wind shifts from 120° (upslope) to 330° at about 2130 UTC (1530 MDT). The temperature at Fort Collins drops by 6° F and the winds remain out of the west from 2130 UTC to 2210

UTC as would be expected during the passage of a surface cold pool originating in the foothills . A surface plot of the mesonet data at 2210 UTC (1610 MDT) in Fig 6.7b reveals the convergence zone located about half way between Fort Collins (FOR) and Greeley (GLY, approximate site of the CSU-CHILL radar) as depicted by a dashed line. Note that the location of the convergence line (4.3 km southeast of Loveland, LVE, at 1610 MDT) is approximately collocated with the reported position of a tornado about 3 miles (4.8 km) southeast of Loveland at 1612 MDT.

Wakimoto and Wilson (1989) present visual and radar data of 27 similar non-supercell tornadoes collected during CINDE (Convection INitiation and Downburst Experiment), a field project conducted during the summer of 1987 in the Front Range area of Colorado. They determined that a non-supercell tornado originates as a low-level vortex produced by shearing (or Helmholtz) instability along a convergence boundary. The vortex propagates along the convergence line and reaches tornado intensity when it becomes collocated with the updraft of a rapidly developing storm, due to vorticity stretching. Wakimoto and Wilson (1989) present a similar case study in which a westerly surge of cool air produced by thunderstorms collided with an upslope induced convergence zone, spawning an F1 tornado. This phenomena appears to be fairly common in northeast Colorado during periods of southeasterly flow along a terrain induced convergence zone, often called the Denver convergence zone (e.g., Brady and Szoke, 1988). Since the gust front in Fig 6.6a appears to be colliding with the most intense cell to the west-southwest of the radar at the same time as the tornado report, it is likely that this was the tornado producing mechanism in this case. Also, note that an inflow notch of lower reflectivity (reminiscent of a hook echo at higher radar resolution associated with a tornado) along the leading edge of the gust front in Fig. 6.5a at (x = -25.5 km, y = -12 km) was coincident with a region of cyclonic-shear in the radial velocity data (Fig 6.6a) at a range of 28 km and an azimuth of 245°. This is further evidence that the F0 tornado was formed by the mechanism put forth by Wakimoto and Wilson (1989).

By 1623 MDT, there were still at least three separate, irregularly spaced radar echoes as shown in Fig. 6.5c. The group of cells to the west-southwest continued to intensify and exhibit weak reflectivity in-flow notches. This is consistent with persistent reports of funnel clouds to the west of Greeley during this time by National Weather Service (NWS) severe weather spotters. Radar echoes to the north continue to develop slowly and the convection to the northwest continues to dissipate.

The collection of cells described above began to take on the characteristics of a line by 1635 MDT as the storms to the north-northwest and west had rapidly strengthened during the preceding twelve minute period (Fig. 6.5d). The eastward surging cold pool seen in Fig. 6.6b was probably the driving mechanism for this intensification. The convergence line at the head of the gust front can be seen in this figure as a transition from inbound to outbound radial velocities, oriented a few degrees clockwise of north to south about 20 km west of the radar. By this time, the gust front had just reached the western edge of the precipitation echo associated with the developing line of cells to the north-northwest and was along the leading edge of the echo to the west. The outflow from the thunderstorm to the west apparently combined with the original cold pool causing a forward bend in the convergence line as seen in Fig 6.6c at about 245° in azimuth and 20 km in range. Another interesting feature in the radial velocity data in Fig 6.6c is an extension of outbound (yellow) radial velocities from the convergence line about 22 km due west of the CSU-CHILL radar that curves cyclonically toward the south that is collocated with an in-flow notch of weak reflectivity in Fig 6.5d. The cyclonic shear formed by the couplet of inbound and outbound radial velocities at this location suggests the possibility of cyclonic rotation associated with a mesocyclone. This would be consistent with weather spotter reports of a rotating cloud base and funnel clouds at 1635 MDT west of Greeley.

After the eastward advancing cold pool collided with the group of cells to the north of the radar, explosive convective growth occurred as can be seen in the rapid increase of the areal extent of radar echo with $Z_h > 50$ dBZ from 1635 MDT to 1647 MDT (Figs 6.5d

and e). This process continued through 1653 MDT (Fig 6.5f). By 1659 MDT, the formation of the broken-areal squall line was complete with continuous, intense precipitation (Z_h > 40 dBZ) along a 60 km line oriented from northeast to southwest. From 1647 to 1659 MDT, there continued to be several reflectivity discontinuities or notches along the leading edge of the convergence line seen in the radial velocities of CSU-CHILL radar at 1659 MDT in Fig. 6.6d. The most prominent of these notches occurred in the range 10 km < y < 20 km as seen in Figs 6.5e-g. Comparing the reflectivity structure in Fig. 6.5g at 1659 MDT to the radial velocity structure at the same time in Fig. 6.6d, notice that two of these reflectivity discontinuities are associated with inflections in the shear line as suggested by Carbone (1982). These inflections are identified by the change in slope of the zero velocity (white) line in Fig. 6.6d. For example, the inflection in the shear line at a range of 20 km and an azimuth of 330° is approximately coincident with the reflectivity discontinuity at x = -10 km and y = 17 km. Similarly, the inflection in the shear line at a range of 15 km and an azimuth of 325° is collocated with the reflectivity corrugation at x = -8.5 km and y = 12.5 km. Carbone (1982) suggested that these inflections could be caused by a Helmholtz (1886) instability along strong horizontal shear zones. This explanation is in agreement with the hypothesis put forth by Wakimoto and Wilson (1989) for their explanation of the origins of tornado producing vortices along gust fronts in their study.

After 1711 MDT, the squall line propagated over the CSU-CHILL and continued to move very slowly to the east-northeast. Due to the close proximity of the squall line to the radar for the next one hour, temporal and spatial sampling of the surrounding convection was insufficient for electrification studies. The storm produced significant flooding and continued reports of large hail during this period in the vicinity of the radar. NWS weather spotters reported wide spread flooding of farm fields in the vicinity of the CSU-CHILL radar. At the radar, golf ball-sized hail was reported at 1729 MDT and heavy rain at 1743 MDT. NWS spotters also reported flooding in Ault, CO

(approximately 20 km to the north-northeast of the CSU-CHILL radar) with 2 feet of water in the streets at 1739 MDT.

In summary, we have presented the evolution of radar reflectivity and velocity data during the formation of a broken areal squall line. The radar data in combination with mesonet observations suggest that irregularly spaced convection was organized along a convergence line formed by the opposing flows of moist southeasterly upslope and an eastward surging cold pool formed by convection in the foothills. The reports of several funnel clouds and an F0 tornado were shown to be coincident with inflow notches in the reflectivity field and cyclonic shear (suggesting rotation) in the radial velocity field. We demonstrated that the formation of the tornado was consistent with the mechanism suggested by Wakimoto and Wilson (1989) in which a pre-existing vortex propagating along a convergence zone collides with a vigorous updraft and intensifies into a tornado.

6.3 Dual-Doppler and dual-polarization radar analyses of the developing squall line

As shown in the last section, the organizing mechanism in the development of this squall line was the presence of an eastward advancing cold pool or gust front, resulting from thunderstorm downdrafts in the foothills. The gust front is an example of a gravity current which can be defined as a mass of high-density fluid flowing along a horizontal bottom and displacing ambient fluid of lesser density (Simpson, 1987). A gust front can trigger new convection by lifting less dense environmental air to the LFC. In this way, convective inhibition (CIN) in the atmosphere can be overcome and all of the convective available potential energy (CAPE) can be realized. Intersecting gust fronts or a gust front which encounters pre-existing thunderstorm cells can trigger deep convective development.

The resulting reflectivity structure of the squall line is fairly similar in appearance to that of previous studies of mid-latitude squall lines (e.g., Kessinger et al., 1983; Bluestein and Jain, 1985; Smull and Houze, 1985; Rutledge et al., 1988 among others) but may

resemble more the structure of the narrow cold-frontal rainband (NCFR) as studied by Matejka et al. (1980), Hobbs and Persson (1982), and Carbone (1982) among others. NCFRs are a boundary layer phenomenon caused by the surge of high density fluid associated with cold fronts and they usually occur in an environment of little or no CAPE. The precipitation structure is often composed of elliptically-shaped precipitation cores and gap regions which are oriented clockwise to the cold front at 30° - 35° angles (Hobbs and Persson, 1982). Note that the squall line in this study shown in Fig. 6.5g is about 30° clockwise of the convergence zone depicted in Fig 6.6c. The cores form in areas of preferred low-level convergence resulting from wind shifts zones due to irregularities in the shape of the mesoscale outflow boundary. The boundary layer convergence produces a narrow updraft whose velocity can be up to a few meters per second. The gap regions (called corrugations by Browning and Harrold, 1970; and reflectivity discontinuities by Carbone, 1982) are similar to the low-reflectivity in-flow notches discussed above. Although the squall line shown in Fig. 6.5f contains significant precipitation along its entire length, there are individual precipitation cores with $Z_h > 50$ dBZ associated with the lower reflectivity notches at fairly regular intervals. The lack of true gaps in the precipitation along the squall line's extent can be attributed to the difference in CAPE between the environment in which NCFRs develop (low CAPE) and this study (2000 J kg^{-1}). The breakup of the NCFRs into cores is believed to be either the result of gravity current dynamics (high density fluid overtaking a lower-density fluid) as suggested by Hobbs and Persson (1982) or instabilities produced by strong horizontal shear as proposed by Carbone (1982). As demonstrated in the next section, the squall line depicted in Figs. 6a-g appears to be similar in kinematic and precipitation structure to a NCFR in a high CAPE environment with an advancing gust front providing the required forcing mechanism.

6.3.1 Kinematic and precipitation structure

The NCFR can be considered the non-convective counterpart (i.e., resulting from forced convection rather that free convection) of the broken line or broken areal squall line. In the case of the squall line in this study, the cold pool associated with the gust front is equivalent to the cold front in a NCFR. The similarities between the reflectivity structure and the kinematic structure between these two phenomena is striking. To further emphasize this point, dual-Doppler synthesized horizontal winds at 1.5 km AGL from 1653 and 1659 MDT are shown in Figs. 6.8a and b. At both times, the upslope enhanced in-flow is from the southeast at about 5 - 15 m s^{-1} and the surging cold pool is seen as strong northwesterly flow at 15 m s^{-1}. Note that the reflectivity discontinuities centered on y = 12 km in Fig 6.8a and y = 15 km in Fig 6.8b are characterized by sharp zones of cyclonic shear and convergence similar to the findings of Carbone (1982) in his study of a severe NCFR. These areas are strongly convergent with average values on the order of 10^{-3} s^{-1} and peak values of 8 x 10^{-3} s^{-1} and are characterized by positive vorticity also on the order of 10^{-3} s^{-1}. These values are somewhat weaker than the 10^{-2} s^{-1} average values found by Carbone in his analysis of a tornado producing vortex in an associated reflectivity notch. Note that there were no reports of a tornado or funnel cloud at this time for the 28 May 1993 storm. However, this type of vortex may have been responsible for the tornado which occurred earlier at 1612 MDT. Both Carbone (1982) and Wakimoto and Wilson (1989) suggest that shear instability may be the source of tornado producing vortices in their studies.

In Figs. 6.9a and b, we present the vertical kinematic and precipitation structure of the squall line with east to west (east to the right) vertical cross-sections of reflectivity, differential reflectivity, and relative velocity at 1653 MDT and 1659 MDT. Each figure focuses on a unique low-level precipitation structure revealed by Z_{dr} within the intense precipitation core on the northern edge of the previously discussed cyclonically convergent reflectivity notch. Within the low-level updraft forced by boundary layer

convergence, there are elevated values of differential reflectivity (Z_{dr} > 0.5 dB) that extend 1 to 1.5 km above the wet-bulb freezing level located at z = 3 km AGL. Differential reflectivity values above 3 km AGL exceed 2 dB in Fig 6.9a and 1.5 dB in 6.9b. At one-half kilometer above the wet-bulb freezing level (T = -7° C), precipitation in Colorado thunderstorms is typically in the form of conical graupel (Heymsfield, 1978) with supercooled drops being fairly rare. As discussed in Ch. 4, differential reflectivity is the reflectivity weighted measure of precipitation axis ratio. Graupel particles are typically characterized by Z_{dr} < 0.5 dB due to their nearly spherical shapes (semi-minor to semi-major axis ratios between 0.75 and 1.0) and a dielectric constant of low density ice that is as low as 5% to 10% that of water. As a result, the precipitation particles in these "positive Z_{dr} columns" must be more oblate and have larger dielectric constants than graupel.

Caylor and Illingworth (1987), Illingworth et al. (1987), Goodman et al. (1988), Tuttle et al. (1989), and Bringi et al. (1994) all attribute similar Z_{dr} structures to the presence of large supercooled raindrops rising or being suspended by strong ascending motion. They hypothesize that the raindrops within these columns are initially formed by the collision-coalescence process within developing updrafts characterized by high liquid water contents. On the other hand, Conway and Zrnic (1993) suggest that the hydrometeors responsible for the positive Z_{dr} column in their study of a severe Colorado hailstorm originate primarily from melted hydrometeors that fall from the back-sheared anvil, through the embryo curtain, and are recirculated into the storm updraft. We will consider in detail the microphysical evolution of this unique region as revealed by multiparameter radar data later in this section. First, we discuss further the vertical kinematic structure of the squall line as seen in Figs 6.9a and b.

At 1653 MDT (Fig 6.9a), the main updraft was located just to the west of the positive Z_{dr} column at x = -14 km. Vertical velocities in this region ranged from 15 to 25 m s^{-1} with the peak updraft occurring at 8 km AGL. The updraft tilts slightly in the downshear

direction before diverging aloft, consistent with the tilt in the reflectivity contours. A mid-level (7-8 km) reflectivity overhang developed in response to the downshear tilting of the eastern portion of the main updraft. This reflectivity overhang and the wind velocity through this region is similar in appearance to that of an embryo curtain (Browning and Foote, 1976). There appears to be a recirculation feature in the winds at about x = -10 km which exits the embryo curtain at about 8 km AGL. A recirculating ice particle such as graupel could exit the embryo curtain here, rapidly descend in a weak downdraft, melt, and become swept up into the updraft in the vicinity of the positive Z_{dr} column due to the strong low level in-flow from the east. A similar recirculation feature at this level was also found by Kessinger (1983) in a Doppler radar analysis of a squall line. Note that the upward vertical velocities east of x = -11 km may have been underestimated due to insufficient sampling of the upper level divergence in this region. As a result, the magnitude of the downdraft may be slightly exaggerated here. However, the presence of a weak downdraft is consistent with an increase in both the reflectivity and the differential reflectivity which occurs at the wet-bulb freezing level (3 km AGL) due to the melting of descending, large ice particles such as graupel. It is interesting to note that the positive Z_{dr} column is tilted along the same axis as the updraft just west of this feature. Updraft velocities in the positive differential reflectivity column were strong enough to loft raindrops and partially melted graupel particles above 3 km AGL and also vigorous enough to suspend larger raindrops, wet ice, and frozen drops once above this level with values ranging from 8 to 15 m s^{-1}.

The vertical kinematic structure of the squall line suggests that the hydrometeors responsible for the positive Z_{dr} column in this study originated from ice particles which descended below the melting level from a mid-level reflectivity overhang in a weak downdraft. As the multiparameter radar data will show, hydrometeors below the melting level in this region consisted of both partially melted ice and raindrops. These hydrometeors were then rapidly swept back up into the updraft due to the strong cyclonic

convergence discussed earlier. This explanation is similar to the one offered by Conway and Zrnic (1993) in their dual-Doppler trajectory analysis of a similar event. To support this argument, we calculate an approximate recirculation time for hydrometeors originating from below the melting level in the precipitating downdraft just east of the positive Z_{dr} column (e.g., x = -11 km and z = - 2.5 km AGL). The average vertical velocity along a trajectory into the column is about 11 m s^{-1}. Referring to the rain-ice boundary of Aydin (1986) seen in Fig 4.1, we find that the reflectivity (50 dBZ) and differential reflectivity (2 dB) at this point is representative of pure rain. Herzegh and Jameson (1992) calculated a relationship between raindrop diameter and Z_{dr} using the drop-size shape relationship of Beard and Chuang (1987). Using these results, we find that Z_{dr} = 2 dB is representative of a 3.4 mm drop. We then substitute this value into a terminal fallspeed and drop diameter (D) relationship derived by Atlas et al. (1973) using a vertically pointing radar.

$$V_t(D) = 9.65 - 10.3 \exp(-0.6D) \quad \text{m s}^{-1} \qquad (\text{D in mm}) \qquad (6.1)$$

Obtaining V_t = 8 m s^{-1}, we calculate a particle vertical velocity of $w = W - V_t$ = 3 m s^{-1}. The average horizontal velocity along a trajectory into the column (in the plane of Fig. 6.9a) is about 6 m s^{-1}. After a period of only six minutes (resolution of radar data) the raindrop would be within the positive Z_{dr} column above the wet-bulb freezing level at x = -13 km and z = 3.5 km AGL. As will be demonstrated later in the section, this time scale is consistent with the column genesis time as seen in CSU-CHILL radar data.

A similar vertical cross-section through the same positive Z_{dr} column at 1659 MDT is shown in Fig. 6.9b. The upper level divergence on the east side of the updraft was again undersampled suggesting that the mid- and upper-level vertical velocities there may have been underestimated. However, the low-level values (1 - 4 km) should be reasonable since the updraft was primarily driven by low-level convergence. There are a couple of key differences between Fig. 6.9a and b that should be discussed. The updraft in Fig. 6.9b no longer has a component which is tilted downshear. As a result, the reflectivity

contours no longer tilt in the downshear direction either. The vertical velocities in the positive Z_{dr} column have weakened slightly by 1659 MDT with values ranging from 5 to 10 m s^{-1}. Consequently, the maximum raindrop size that can be suspended by the updraft has decreased. This can be seen in the lower maximum values of Z_{dr} found above the freezing level at 1659 MDT compared to 1653 MDT. For example, the average vertical velocity at 1659 MDT (Fig. 6.9b) is about 8 m s^{-1}. Using Eqn. 6.1 above, we find that the average drop size that would be suspended in such an updraft is about 3 mm. Referring to Herzegh and Jameson (1992) once again, a raindrop with a 3 mm diameter would be associated with a Z_{dr} = 1.6 dB which is consistent with the area of differential reflectivity between 1.5 and 2 dB just above the wet-bulb freezing level. On the other hand, the stronger vertical velocities at 1653 MDT (Fig. 6.9a) would be able to support a larger raindrop according to Eqn. 6.1 which is consistent with the larger values of Z_{dr}, reaching up to 3 dB, at this time.

6.3.2 Multiparameter radar analyses of positive differential reflectivity columns

To obtain an understanding of the horizontal morphology of the positive Z_{dr} columns during the formation of the 28 May 1993 squall line, horizontal cross-sections at 3.5 km AGL (0.5 km above the wet-bulb freezing level) of horizontal reflectivity and differential reflectivity from 1647 to 1705 MDT are presented in Figs. 6.10a-d. Beginning at 0.5 dB, differential reflectivity is contoured at 0.5 dB intervals. Note that enhanced values of Z_{dr} (> 0.5 dB) along radar echo boundaries are probably associated with either a low signal-to-noise ratio or mismatched antenna illumination functions at horizontal and vertical polarizations (Herzegh and Carbone 1984).

There are several observations that can be made regarding the regions of enhanced differential reflectivity above the freezing level: 1) Most Z_{dr} columns appear to be near the inflection point of a reflectivity discontinuity or notch which is also a region of strong cyclonic convergence; 2) They appear to be spaced at fairly regular intervals along the

gust front at the leading edge of the squall line; and 3) They seem to propagate (through discrete new growth) toward the south along the gust front.

It is not surprising that the positive Z_{dr} columns were collocated with the reflectivity notches in this study since they were preferred regions of the low-level convergence necessary to produce an updraft sufficient to loft hydrometeors from below the freezing level. However, it is interesting to note that other investigations of positive differential reflectivity columns along the Front Range such as Conway and Zrnic (1993) and Bringi et al. (1994) were also associated with reflectivity discontinuities and cyclonic convergence. This similarity between the three studies in Colorado may suggest something about the origins of positive Z_{dr} columns in this region.

The columns were numerous and spaced at fairly regular intervals once the merging gust front organized convection along a line. Analyses of Figs. 6.10a-d reveal that 4 to 6 positive Z_{dr} columns were present from 1647 to 1705 MDT In this case, we have defined a positive Z_{dr} column as a distinct area with $Z_{dr} > 0.5$ dB associated with a reflectivity discontinuity at 3.5 km AGL. Measuring from center to center of the Z_{dr} maxima, the columns were found to be separated by an average distance of 8 km with values ranging from 6 to 11 km. The associated reflectivity corrugations were separated by an average distance of 9 km with values ranging from 6.5 to 13 km. This is similar to the findings of Carbone (1982) who determined that the reflectivity discontinuities and associated inflections in the shear line in his study of a severe NCFR occurred at 13 km intervals. He suggested that this phenomena could be caused by a Helmholtz (1886) instability along strong horizontal shear zones. He also noted that similar instabilities have been shown to amplify for wavelengths on the order of 10 km in early studies on the development of polar front waves (Solberg, 1930). Therefore, it is possible that the dynamical forcing responsible for the reflectivity discontinuities and the associated positive Z_{dr} columns in this study were associated with shear instability along the leading edge of a merging gust front. Recall that this instability mechanism was also suggested as the source of a vortex

which intensified into a tornado due to vorticity stretching in a developing updraft at 1612 MDT as hypothesized by Wakimoto and Wilson (1989). To further strengthen the connection between reflectivity notches, differential reflectivity columns, and cyclonic vortices, we note that the positive Z_{dr} columns in this study did tend to propagate along the gust front similar to the vortices discussed in Wakimoto and Wilson (1989).

Having associated these differential reflectivity columns with a dynamical forcing mechanism, we now investigate the microphysical properties of these columns as inferred from the use of all available multiparameter radar variables. Once these detailed analyses are complete, we will comment on the consistency of the microphysical findings with the suggested dynamical forcing mechanism. We begin characterizing the positive Z_{dr} column and surrounding convection by analyzing two range plots of Z_h, Z_{dr}, K_{dp}, and $\rho_{hv}(0)$. The first range plot shown in Fig. 6.11a is a ray of radar data from 1655 MDT through the differential reflectivity column depicted in Fig. 6.9a. Note the features in the four variables at a range near 21 km, corresponding to a height of 3.7 km AGL. There is a relative maximum in horizontal reflectivity (Z_h > 50 dBZ), a maximum in differential reflectivity (Z_{dr} > 3 dB), a maximum in the specific differential phase (K_{dp} > 0.7° km^{-1}), and a minimum in the correlation coefficient ($\rho_{hv}(0)$ < 0.95). These values are characteristic of conditions within the positive differential reflectivity column seen in Fig. 6.10b at x = -13 km and y = 16 km. Note that the Z_{dr} maxima here is less than seen in Fig 6.11a. This is due to the smoothing effect of the interpolation process which occurs while gridding the data. The large values of Z_{dr} in the column suggest the presence of large raindrops as seen in the rain-ice boundary of Aydin et al. (1986) in Fig. 4.1. The maximum in K_{dp} also suggests the presence of raindrops since it is proportional to the precipitation liquid water content (Jameson, 1985). However, given the large values of reflectivity, we would expect higher values of K_{dp} for pure rain. Referring to the rain-ice boundary of Balakrishnan and Zrnic (1990a) in Z-K_{dp} space depicted in Fig. 4.3, we find

that a Z_h = 53 dBZ and a K_{dp} = 0.9° km^{-1} falls well within the region characterized by a mixture of rain and hail.

This apparent contradiction can be resolved by recalling that differential reflectivity is a measure of the *reflectivity weighted* hydrometeor axis ratio. If raindrops dominate the reflectivity in a rain-ice mixture, then Z_{dr} will correspond closely to pure rain. For this reason, Balakrishnan and Zrnic (1990a) concluded that the combination of reflectivity and specific differential phase is a superior method for characterizing precipitation in a mixed-phase environment. Further evidence for the presence of mixed-phase precipitation can be found in the lowering of the correlation coefficient. Balakrishnan and Zrnic (1990b) determined that the correlation coefficient is reduced in mixed-phase precipitation due to a broader spread in the composite distribution of shapes and sizes compared to that of a single precipitation type. They found that a correlation coefficient in the range of 0.94 < $\rho_{hv}(0)$ < 0.96 as in the positive Z_{dr} column is associated with a rain and small hail (< 2 cm) mixture. Other potential causes for the lowering of $\rho_{hv}(0)$ such as a large protuberance to diameter ratio for hail (i.e., lobes) or the effect of Mie scattering for very large hail (> 5 cm) can be discounted. If hailstones in the positive Z_{dr} column had protuberances large enough to lower the correlation coefficient, they would have produced Z_{dr} close to 0 dB due to random tumbling. If the hail had been large enough to enter the Mie scattering regime and cause significant backscatter phase shift, there would have been rapid oscillations in Z_{dr} giving it a distribution near zero and the correlation coefficient would have been much less than observed (Balakrishnan and Zrnic, 1990b).

The second range plot depicted in Fig. 6.11b is representative of conditions at the top of and just above the positive Z_{dr} column when the range is near 21-22 km, corresponding to a height of 4.6 km AGL. Horizontal reflectivity here is larger than within the high Z_{dr} regions of the column ($Z_h \geq$ 55 dBZ). Differential reflectivity is near zero (-0.5 dB $\leq$ Z_{dr} $\leq$ 0.5 dB) and the specific differential phase still shows values above the noise level (0.5° km^{-1} $\leq$ K_{dp} $\leq$ 0.7° km^{-1}). The correlation coefficient is significantly depressed

with values as low as 0.92. Using similar reasoning as above, we suggest that the top of the differential reflectivity column was also comprised of a rain and ice mixture. In this region however, there is less precipitation liquid water as suggested by the lower values of K_{dp} and the ice dominates the reflectivity signal as suggested by the near zero values of differential reflectivity. We speculate that this ice is in the form of frozen drops that may serve as hail embryos and of rapidly growing hail in a water-rich environment. In regions of mixed-phase precipitation, the correlation coefficient is at a minimum when the contribution to the reflectivity factor from rain is approximately equal to that of hail (Balakrishnan and Zrnic, 1990b). Using the method of Golestani et al. (1989) reviewed in Ch. 4 for Z_h = 55 dBZ and Z_{dr} = 0.5 dB, we calculate a reflectivity weighted ice fraction of f_i = 70 %. Since the correlation coefficient at the top of the positive Z_{dr} column is lower than within the column and since the ice fraction is still larger than 50 % in the former location, we suggest that the hail at the top of the column is larger than within the high Z_{dr} region. This is consistent with the larger values of vertical velocity (w = 15 - 18 m s^{-1}) at the top of the column than within the column (w = 10 - 12 m s^{-1}) that would be necessary to suspend larger hail. This also implies an active and rapid hail growth process in this region which is consistent with the continued presence of significant precipitation liquid water as indicated by K_{dp}.

Another potential mechanism for forming the minimum in the correlation coefficient could be the presence of large hail with protuberances. Small protuberances or lobes can form on hail when large (say millimeter-sized) supercooled rain drops are captured in the wake of a large hailstone, strike the stone from above, and freeze in place (List, 1985). As discussed in Sec. 4.2.4, $\rho_{hv}(0)$ is lowered for hail with a protuberance to diameter ratio $\geq$ 0.1 (Balakrishnan and Zrnic, 1990b). Although the required supercooled drops were present near the top of the positive Z_{dr} column, lobes typically form on large ($\geq$ 4 cm) hail only. Since there was no ground reports or multiparameter radar data consistent with

hail this large, it is unlikely that hail with a large protuberance to diameter ratio caused the minimum in $\rho_{hv}(0)$.

Having established the presence of both rain and ice in the differential reflectivity columns, we now attempt to determine the origins of the hydrometeors in this column. We have already shown that the dynamic force behind the sudden lofting of hydrometeors was most likely a low-level updraft induced by regions of cyclonic convergence along the gust front of the developing squall line. We have also suggested a potential recirculation mechanism that could maintain a steady supply of raindrops, and partially melted graupel. The possibility of such a recirculation mechanism is not sufficient evidence to discount a potential role for warm rain collision-coalescence in the origin of these positive Z_{dr} columns. To investigate this further, we present the evolution of the most prominent positive Z_{dr} column for this squall line (y = 16 km in Fig. 6.10b) from 1642 to 1653 MDT as seen in vertical cross-sections of Z_h with contoured overlays of Z_{dr}, K_{dp}, and $\rho_{hv}(0)$ (1642 MDT: Figs 6.12a-c; 1647 MDT: 6.13a-c; 1653 MDT: 6.14a-c).

The portion of the squall line depicted in Figs. 6.12a-c has the characteristics of typical mature convection along the Front Range. The 40 dBZ echo top extends to 9 km AGL at 1642 MDT and an intense ($Z_h \geq 55$ dBZ) precipitation core appears to be descending below the melting level. Within the intense reflectivity core centered on x = -14 km, differential reflectivity increases steadily with increasing distance below the wet-bulb freezing level (3 km AGL) as seen in Fig. 6.12a. This pattern suggests the gradual melting of graupel and hail as the frozen precipitation descends toward the surface (Bringi et al., 1986b). Once below the wet-bulb freezing level, K_{dp} also tends to increase with decreasing altitude within the same region (Fig. 6.12b), implying an increase in precipitation liquid water content toward the surface. This corroborates the suggestion that the precipitation core centered on x = -14 km consists of gradually melting ice. Further evidence for this hypothesis can be found in Fig. 6.12c. As discussed earlier, $\rho_{hv}(0)$ decreases in regions of mixed-phase precipitation. Balakrishnan and Zrnic (1990b)

empirically determined that the mean correlation coefficient from pure rain would be larger than about 0.97. The correlation coefficient for precipitation consisting of pure ice such as graupel and hail is expected to have similar values, assuming that the hail is not large enough to cause Mie scattering or have a large protuberance to diameter ratio (Balakrishnan and Zrnic, 1990b). The correlation coefficient is lowered below 0.97 in the intense precipitation core below the wet-bulb freezing level and continues to decrease systematically with decreasing altitude, reaching a minimum of 0.95 (Fig 6.12c). Balakrishnan and Zrnic (1990b) demonstrate that this systematic decrease of $\rho_{hv}(0)$ is associated with mixed-phase precipitation and, more specifically, an increasing contribution of raindrops to the reflectivity factor due to melting.

By 1647 MDT, the reflectivity core discussed above continued to descend but just east of this feature the squall line experienced sudden explosive growth as seen in Figs. 6.13a-c. This rapid redevelopment along the convective line was coincident with the arrival of the gust front to the northern portion of the developing squall line. The 40 dBZ echo reached up above 10.5 km AGL and a new 50 dBZ radar echo extended to 8.5 km AGL. Convergence along the advancing gust front apparently forced a strong low-level updraft allowing the cell to undergo renewed growth. In Fig. 6.13a, another response of the squall line to this new low-level updraft can be seen in the bulging of the differential reflectivity field upward above the wet-bulb freezing level. Centered on x = -13 km, the 0.5 dB contour reaches up to 4.5 km AGL and maximum values of Z_{dr} above the freezing level now exceed 2 dB. Similarly, the $K_{dp} = 0.3^\circ$ km^{-1} contour also protrudes slightly above the wet-bulb freezing level in Fig. 6.13b. The sudden upward bulging of significant values of Z_{dr} and K_{dp} above the freezing level indicates the presence of lofted raindrops. As before however, we would expect slightly larger values of K_{dp} given values of reflectivity near 50 dBZ for pure rain (refer to Fig. 4.3). As a result, we suspect that a mixture of raindrops, partially melted graupel, and still frozen graupel was lofted above the freezing level by the gust front induced low-level updraft. Note that the $\rho_{hv}(0) \leq$

0.97 contour also protrudes above the wet-bulb freezing level in the same region as the positive Z_{dr} column and the K_{dp} bulge. As discussed above, this is further evidence that the origins of the differential reflectivity columns in this study were related to the lofting of mixed-phase precipitation above the freezing level by a low-level updraft forced by boundary layer convergence along a merging gust front.

By 1653 MDT, the cell centered on y = 16 km had 40 dBZ echo tops up to 11.5 km AGL and 50 dBZ echo tops reaching just under 10 km AGL (Figs. 6.14a-c). The reflectivity structure began to take on the characteristics of a potentially severe hailstorm with a weak echo region (not quite bounded) centered on x = -12 km, a reflectivity overhang or embryo curtain, and a reflectivity core directly below the overhang which descended below the melting level (Cotton and Anthes, 1989). As seen in Fig. 6.14a, the positive Z_{dr} column still extends up to 4.5 km AGL and now has peak values exceeding 2.5 dB. Collocated with the differential reflectivity column is a bulging of the K_{dp} field as shown in Fig. 6.14b. Values of specific differential phase within the column range from 0.3° km^{-1} to 0.6° km^{-1}. As before, the $\rho_{hv}(0) \leq 0.97$ contour extends well above the wet-bulb freezing level and is collocated with the protrusions of Z_{dr} and K_{dp}. This suggests the continued presence of significant precipitation liquid water and mixed-phase precipitation above the freezing level

As seen in Fig. 6.14c, a significant lowering of the correlation coefficient below 0.96 is coincident with a maximum in the reflectivity field in the interface zone at the top of the positive Z_{dr} column(between 4 and 5 km AGL centered on x = -12.5 km). This interface zone is characterized by a decrease in Z_{dr} from 2 dB at the bottom of the $\rho_{hv}(0)$ minimum/Z_h maximum to below 0.5 dB at the top of the feature. Since the precipitation liquid water content is fairly constant through the feature as inferred from the K_{dp} contours, we speculate that the $\rho_{hv}(0)$ minimum and rapid decrease in Z_{dr} is caused by increasing hail size and freezing of the drops. As mentioned earlier, a lowering of $\rho_{hv}(0)$ below 0.96 in a region of mixed-phase precipitation is typically associated with the

presence of small hailstones with diameters between 1 and 2 cm (Balakrishnan and Zrnic, 1990b). Recall that vertical velocities in this region were on the order of 15 m s^{-1}. Matson and Huggins (1980) derived the following best fit expression relating hailstone diameter (mm) to terminal fallspeed (m s^{-1}) by comparing their own measured values in several Colorado hailstorms to theoretical and empirical expressions for terminal fallspeeds of hailstones.

$$V_t = 3.62\sqrt{D} \qquad (\text{m s}^{-1}) \tag{6.2}$$

For a hailstone to be suspended in the $\rho_{hv}(0)$ minimum, the condition w - V_t = 0 must be met. Substituting V_t = w = 15 m s^{-1} into Eqn. 6.2 above and inverting to solve for hailstone diameter, we find that the dual-Doppler synthesized updraft could suspend a hailstone with a diameter of 1.7 cm, consistent with the above multiparameter radar data inference of 1-2 cm hail. Given the proximity of the Z_{dr} column, it is also reasonable to speculate that embryos for hailstones growing within this region consist of frozen drops. If hailstones were suspended in this region with significant precipitation liquid water as suggested by the data, then hailstone growth would be very rapid and potentially in the wet growth regime. Using the Schumann-Ludlam limit as a boundary between wet and dry growth (e.g., Young, 1993; Fig. 8.6), we find that hailstones with diameters ranging from 1 to 2 cm suspended within the correlation coefficient minimum where T $\approx$ -13° C would require liquid water contents in excess of 2.7 to 1.5 g m^{-3} respectively in order to experience wet growth. Since the adiabatic liquid water content (estimated from sounding data) in this region was 3.6 g m^{-3} , we conclude that wet growth was indeed possible.

Goodman et al. (1988) presented similar observations collected during the Cooperative Huntsville Meteorological Experiment (COHMEX) of a positive Z_{dr} column (although this term was not in wide use at the time) and an associated reflectivity maximum at the top of the column where Z_{dr} < 0.5 dB. With only Z_h and Z_{dr} available for their study, they suggested that the region characterized by a reflectivity maximum and low differential reflectivity was associated with graupel and small hail. Bringi et al. (1994)

presented dual-polarization radar data of a Florida storm collected during the Convective and Precipitation/Electrification Experiment (CAPE) which contained a very similar feature associated with a positive Z_{dr} column. They also associated the $\rho_{hv}(0)$ minimum and Z_h maximum in the Z_{dr} interface zone with the presence of water-coated hailstones growing rapidly in a water-rich environment. Apparently, positive Z_{dr} columns are favored hail growth regions because of the availability of frozen drop hailstone embryos, the presence of a significant updraft necessary to suspend large hydrometeors and allow them to grow, and the availability of ample liquid water for accretional growth.

To obtain a quantitative understanding of positive Z_{dr} column development, we present Z_{dp}/Z_h plots in the region discussed qualitatively above from 1642 to 1653 MDT. Fig. 6.15a is a plot of Z_{dp}/Z_h during the pre-development stage at 1642 MDT. Between 1-2 km AGL, most grid points are on or above the pure rain line, inferring the presence of mostly rain. With increasing height, deviation below the pure rain line increases, indicating the increased presence of ice (Golestani et al., 1989). The distribution of points in this plot is consistent with steadily melting graupel below the freezing level. Hydrometeors above the freezing level are primarily ice as expected. Precipitation below 3 km AGL consists of mixed-phase precipitation with an increasing contribution from rain with proximity to the surface. The Z_{dp}/Z_h plot for 1647 MDT (Fig. 6.15b) demonstrates the emergence of a developing positive Z_{dr} column above the wet-bulb freezing level with several points from 3-4 km AGL falling along the rain line. Below three km AGL, mixed-phase precipitation is still inferred with points falling on or above the rain line (rain) and points falling below this line (mixed-phase precipitation). By 1653 MDT, the positive Z_{dr} column is clearly established as depicted in Fig. 6.15c. Approximately 55% of all grid points between 3 and 4 km AGL are characterized by mixed-phase precipitation while 45% indicate the presence of pure rain. It is interesting to note that the rain fraction between 4 and 5 km AGL was as high as f_r = 63 % (corresponding to Z_h = 56 dBZ and Z_{dp} = 50 dB) at 1653 MDT as compared to 1642 MDT when the rain fraction was

negligible at this altitude. The effect of lofted raindrops was felt as far as 2 km above the wet-bulb freezing level during the mature phase of the differential reflectivity column.

We also present plots of Z/K_{dp} in the differential reflectivity column from 1642 to 1653 MDT (Figs. 6.16a-c) and briefly discuss the microphysical implications. In our discussion of these figures, we compare the measured data with the empirical rain/mixed-phase boundary in Z/K_{dp} space derived by Balakrishnan and Zrnic (1990a) shown in Fig. 4.3 and the Z/K_{dp} variations for modeled mixtures of rain and wet spherical hail shown in Fig. 4.4 (also from Balakrishnan and Zrnic, 1990a). Comparison of Fig. 6.16a for the pre-development phase at 1642 MDT with Fig. 4.4 demonstrates that the precipitation echo consisted of mixed-phase precipitation with an increasing contribution from rain toward the surface resulting from the melting of graupel and hail. This supports the above findings using the Z_{dp}/Z_h method and is our final piece of evidence suggesting that the origins of the positive Z_{dr} columns in this study were from lofted mixed-phase precipitation and not necessarily from the collision coalescence process. It is possible that the warm rain process played a secondary role in the development of large drops after the column was developed but it was clearly not the original raindrop producing mechanism. Comparing Figs. 6.16a-c for grid points above the wet-bulb freezing level (3-4 km AGL) while considering the modeled results in Fig. 4.4, it is apparent that the fraction of rain in the rain-hail mixture increased significantly from 1642 MDT to 1653 MDT in response to the development of the positive Z_{dr} column. This can also be recognized by comparing the proximity of the grid points for 3-4 km in the three Figs. to the mixed-phase boundary. For a fixed value of Z and for points above the boundary, the closer the point is to the mixed-phase boundary, the higher the fraction of rain is. This is simply a graphical representation of the simple idea that for fixed reflectivity, the precipitation liquid water content increases for larger values of K_{dp}.

Although the majority of previous studies regarding the origins of positive Z_{dr} columns have concluded that collision-coalescence was the initial raindrop producing

mechanism (as opposed to the melting of accretionally grown ice in this study), we suggest that our conclusions are not at odds with most of these papers. The majority of these studies observed positive Z_{dr} columns during initial convective development. (e.g., Caylor and Illingworth, 1987; Illingworth et al., 1987; Goodman et al., 1988; and Tuttle et al. 1989). In these studies, large values of differential reflectivity above the freezing level were collocated with moderate values of reflectivity (i.e., 25 dBZ < Z_h < 50 dBZ). Therefore, these studies attributed such observations to a low concentration of large drops. In contrast, the differential reflectivity columns in this study occurred within mature convection and were collocated with large values of reflectivity (Z_h > 50 dBZ). Several of these studies occurred in regions where warm rain processes are common due to typically moist low-levels and warm cloud bases (e.g., Florida: Bringi et al., 1994; Alabama: Goodman et al., 1988; Tuttle et al. 1989). In contrast, initial reflectivity development in northeastern Colorado storms typically occurs above the melting level (Dye et al., 1974; Knight et al., 1984).

Moist surface conditions (T_d > 10° C) from surface upslope does appear to be a common feature for Front Range thunderstorms with positive Z_{dr} columns (this study; Conway and Zrnic, 1993; and Bringi et al., 1994). Although a moist boundary layer can be considered a necessary condition for the occurrence of warm rain processes, it is not a sufficient condition. For example, Foote (1985) proposed that the continental initial drop spectrum of Colorado clouds which exhibit a lower concentration of smaller drops and an absence of large drops does not allow enough time for coalescence processes to occur within typical updrafts. Conway and Zrnic (1993) suggest that the very presence of large drops in positive Z_{dr} columns may indicate a localized, broad initial spectrum of sizes. Although this may be true, it is also possible to observe large drops in the positive Z_{dr} columns of mature Colorado convection resulting from the melting of lofted, large ice particles. In a wind tunnel and theoretical study of melting ice spheres, Rasmussen et al. (1984) determined that a 0.77 cm ice sphere (which exhibited no shedding) would have an

axis ratio of about 0.7 when only 40% of the original ice mass was converted to melt water. Langleben and Gunn (1952) studied the reflectivity of melting ice spheres and found that an ice sphere with 40% of its mass melted had essentially the same reflectivity (or dielectric constant) as an all-water drop of the same radius. Referring to Herzegh and Jameson (1992), we find that a hydrometeor with an axis ratio of 0.7 and the effective dielectric properties of a raindrop will have a Z_{dr} = 3.5 dB. Thus, lofted, melting ice could easily explain the presence of large Z_{dr} above the freezing level in this study. Both this study and Conway and Zrnic (1993) suggest that melted ice was the primary source of lofted drops in their analyses of Colorado differential reflectivity columns with the collision-coalescence process playing a secondary role. Bringi et al. (1994) suggest the reverse for their case study. Of course, the higher values of surface dewpoint temperatures in Bringi et al. (1994) may have led to an efficient coalescence process in their storm.

Having established the probable origins of the positive Z_{dr} columns in this study and having suggested that these columns were favored regions for the development of hail, we present multiparameter evidence and some surface observations to support this claim. This is particularly important for inferring the possible effect of these columns on the electrification of the storm. According to the precipitation theory for storm electrification, increased gravitational power associated with falling precipitation should increase the upper limit of the possible electrical output as measured by lightning flash rates (Williams and Lhermitte, 1983). In Fig. 6.17, we present a vertical cross-section of reflectivity and differential reflectivity taken through the same portion of the storm as the mature Z_{dr} column presented in Fig. 6.14a (y = 16 km) but 12 minutes later at 1705 MDT. Remnants of the Zdr column can be seen centered on x = 8 km. However, the feature of note is the 2 km wide region centered on y = - 14 km that is characterized by Z_h > 55 dBZ and Z_{dr} < 0.5 dB. Bringi et al. (1986a) defined this anti-correlated pattern (i.e., high Z_h and low Z_{dr}) as the differential reflectivity hail signature. Using Eqn. (4.13), we calculate the

Aydin et al. (1986) hail signal for this region as $H_{dr} \geq 18.5$, clearly suggesting the presence of hail. The presence of a large hail shaft is supported by storm spotter reports of 0.75" (2 cm) hail mixed with heavy rain to the north of the CSU-CHILL radar near this time. In addition, golf-ball sized, spongy hail ($\approx$ 3 cm) was reported at the CSU-CHILL radar at 1729 MDT, possibly in association with the developing positive Z_{dr} columns within 10 km to the west at 1705 MDT as shown in Fig. 6.10d. Further multiparameter radar evidence for the possible hail producing abilities of the positive Z_{dr} columns is shown in a plot of Z_{dp} versus Z_h for a 9 km^2 area at 1 km AGL to the west of the column from 1653 MDT to 1705 MDT (Fig. 6.18). Significant deviation below the rain line at 1659 MDT and especially 1705 MDT suggests that some hail was produced near the surface within 6 minutes of the mature phase of the positive Z_{dr} column and that the majority of the hail fell within 12 minutes.

It should be noted that the rapid increase in Z_{dr} near x = -11.5 km in Fig. 6.17 was associated with a maximum in K_{dp} of 2.2° km^{-1} and is probably indicative of an intense rain shaft mixed with some hail. Using a rain rate equation from Balakrishnan and Zrnic (1990a) for λ = 10.7 cm, $R(K_{dp}) = 40.7\ (K_{dp})^{0.866}$, this region can be characterized by heavy rain with peak rain rates near 80 mm hr^{-1}, consistent with several reports of flooding to the north-northwest of the radar.

6.4 Relation of storm kinematics and microphysics to electrical evolution

With some understanding of the kinematic and microphysical properties of the developing squall line, we now compare the evolution of the in-cloud and cloud-to-ground flash rates to these characteristics. The comparison between flash rates and radar inferred storm properties is only accomplished for the development period of the squall line. We were unable to perform similar analyses for the rest of the squall line life-cycle due to insufficient spatial and temporal sampling of the squall line. Analyses which required good vertical sampling of the convection, such as graupel volume above the melting layer, were

halted at 1705 MDT. Low-level analyses such as hail rates and graupel volume below the melting layer were continued until 1711 MDT. After this time, all analyses were halted due to insufficient horizontal, vertical, and temporal scanning of the storm.

6.4.1 IC lightning and the updraft accumulation of graupel and hail

In this section, we strengthen the evidence first presented in Sec. 5.3.1 that the accumulation of graupel particles above the melting level is correlated with the in-cloud lightning flash rate. As discussed in Sec. 2.2, several studies (Lhermitte and Krehbiel, 1979; Lhermitte and Williams, 1984; Goodman et al., 1988; and Williams et al. 1989a among others) have demonstrated that the IC lightning flash rate rises in parallel with the cloud vertical development. The IC lightning results from a combination of particle scale charge separation via the non-inductive mechanism by collisions between ice particles in the presence of supercooled liquid water and of cloud scale charge separation by differential particle motions in the upper dipole region. By comparing the evolution of the IC lightning flash rate to the graupel volume above the melting level, we provide further evidence to support this hypothesis. The method of bulk hydrometeor identification using all available multiparameter radar variables as discussed in Sec. 4.3.3 and as depicted in Table 4.1 was used to infer the amount of graupel above the melting level.

As can be seen in Fig. 6.19, the updraft accumulation of graupel was highly correlated to the IC flash rate during squall line development. The initial increase in the graupel volume aloft which occurred from 1547 to 1611 MDT was associated with the rapidly developing cell along a gust front to the west-southwest (WSW) of the radar. At the conclusion of this explosive growth in the graupel volume, an F0 tornado was reported (at 1612 MDT) below the cell to the WSW. The tornado, explosive growth in the graupel volume, and the associated increase in the IC flash rate were all apparently related to the vigorous vertical storm growth occurring along the gust front.

Both the graupel volume and the IC flash rate continued to increase from 1611 to 1635 MDT. The IC flash rate increased by over a factor of five during this period while

the graupel volume only increased by a factor of two. During this period, there were several official reports of funnel clouds and cloud base rotation associated with the group of cells to the WSW. Radial velocity data at 1635 MDT (Fig. 6.6b) suggest the presence of a cyclonic mesocyclone at low levels associated with shear instability along a convergence line. In their study of the Binger tornadoes (F2 and F4) of 22 May 1981, MacGorman et al. (1989) found a temporary reduction in the CG flash rate and an enhanced IC flash rate associated with an intensifying mid-level cyclone. They hypothesized that the mesocyclone strength determines lightning type and frequency during the thunderstorm's tornadic phase through the modulation of the updraft and cyclonic shear intensity. Although there are key differences in the dynamics between this non-supercell storm and the Binger supercell (i.e., mesocyclone formed within boundary layer in response to pre-existing vortices along gust front in this study), we speculate that similar dynamical mechanisms may have also altered the electrical characteristics of the developing squall line in this study by modifying the flow field and thereby redistributing charge carried on precipitation particles. For example, since the upward vertical velocities were enhanced during the formation of the mesocyclone, negative charge carried by precipitation particles may have accumulated at mid-levels where it may not have been energetically favorable to transfer the negative charge to ground in CG lightning (Williams et al., 1989a). This would help explain the disparity in growth between the graupel volume aloft and the IC flash rate from 1611 to 1635 MDT.

From 1635 to 1641 MDT, both the graupel volume aloft and the IC flash rate decreased. A large change in the in-cloud flash rate was associated with only a modest decrease in the graupel volume. During this period, reflectivity features in the group of cells to the WSW were descending and the mesocyclone was dissipating. Although dual-Doppler analysis was not possible for this time, we speculate that the cell to the WSW had entered the mature stage in which precipitation is descending in weak upward vertical velocities or even downward air motion. One potential cause for the onset of the mature

phase is that the gust front had moved ahead of this group of cells, cutting them off from a supply of warm, moist air from the east. As discussed in Williams et al. (1989a), this stage of a thunderstorm is typically associated with a decrease in the IC flash rate and an increase in the CG flash rate.

The IC flash rate did not continue to decrease after 1641 MDT in this squall line as it typically does in a an isolated, single-cell storm. Instead, the IC flash rate and the graupel volume increased from 1641 to 1705 MDT. This rapid growth in the IC flash rate (7.5 min^{-1} at 1641 MDT to 30 min^{-1} at 1705 MDT) coincides with the rapid development of the cells to the north of the radar, the formation of precipitation along an organized line, and the emergence of the positive Z_{dr} column as a dominant microphysical feature along the convergence line of the developing squall line. It is interesting to note that the IC flash rate increased by a factor of three more than the graupel volume during this period. Since the reflectivity discontinuities at low levels, associated strong cyclonic shear and convergence, and associated positive Z_{dr} columns are the dominant features of the developing squall line, it is worthwhile to consider their possible influences on storm electrification.

The strength and number of these reflectivity discontinuities may affect the predominate lightning type and frequency through the modification of updraft velocity and the intensity of cyclonic shear (similar to the influence of a mesocyclone). Dual-Doppler analyses of these features reveal that they are associated with enhanced cyclonic shear up to 5 km AGL. Updraft velocities in the vicinity of these reflectivity discontinuities also appear to be enhanced. Maximum updraft values are about 25 m s^{-1} above the positive Z_{dr} columns while they are closer to 15 m s^{-1} elsewhere in the storm where these columns are not present. It is possible that a release of latent heat associated with the freezing of drops at the top of the Z_{dr} columns increased the convective available potential energy (CAPE) of the storm locally. Since the maximum realizable vertical velocity is related to the CAPE by $w_{max} = \sqrt{2(CAPE)}$ (Bluestein, 1993), an increase in CAPE caused by the

latent heat of fusion would increase the updraft velocity. The explosive growth which occurred in the northern portion of the squall line from 1642 to 1653 MDT (as seen in the evolution of Z_h and Z_{dr} depicted in Figs. 6.12a, 6.13a, and 6.14a) may have been related to a sudden increase in the CAPE by the freezing of lofted drops within the positive Z_{dr} columns. Both of these kinematic features could redistribute existing charge in such a way that IC lightning is more electrically favorable. Increased updraft velocities would also provide more cloud liquid water, thereby increasing ice growth by riming and affecting the sign and magnitude of charge separated during collisions with ice crystals (Saunders, 1994).

The microphysics of the positive Z_{dr} column could also potentially affect storm electrification. This region is characterized by enhanced values of liquid water content which affects electrification as mentioned above. One speculative suggestion is that these positive Z_{dr} columns may contain elevated concentrations of ice crystals due to secondary ice processes. Goodman et al. (1988) presented observations of a positive Z_{dr} column followed by a rapid increase in the total flash rate. They speculated that the large liquid water contents in the columns would result in a very efficient ice production rate. Most observations of enhanced ice crystal concentrations were obtained in cumulus clouds which contained large supercooled drops (Young, 1993). One possibility is the Hallett-Mossop mechanism which suggests that ice splinters form as droplets larger than 12 μm in radius are collected by a large graupel particle at temperatures between -3° C (3 km AGL in this study) and -8° C (4 km AGL). The positive Z_{dr} columns occur within this temperature range and most likely contain droplets of this size. Another possibility is the shattering or partial fragmentation of freezing drops. Observations suggest that drops of diameter $\geq$ 250 μm are required, that temperatures between -10° C and -20° C are favored, and that the enhancement factor can be as high as 10 (Pruppacher and Klett, 1978). The positive Z_{dr} columns contain drops of this size as revealed by dual-polarization radar data and we can infer from the location of the rapid decrease in Z_{dr} that

most drops are probably freezing at a temperature near -12° C (4.5 km AGL). In the non-inductive charging mechanism, graupel charging is proportional to the ice crystal concentration (e.g., Takahashi, 1978) As a result, a tenfold increase in the ice crystal concentration could result in a tenfold increase in graupel electrification. Clearly, the possible effect of positive Z_{dr} column microphysics and kinematics on electrification is quite complex and requires more observational and modeling studies to bring it out of the realm of speculation.

6.4.2 CG lightning and the descent of graupel and hail

Several studies have demonstrated that the onset of cloud-to-ground lightning is well correlated to the descent of a reflectivity core associated with heavy precipitation (e.g., Workman and Reynolds, 1949; Lhermitte and Krehbiel, 1979; Lhermitte and Williams, 1984; and Goodman et al., 1988). Lhermitte and Krehbiel (1979) observed the onset of CG lightning activity in a Florida storm coincident with the initial descent of the 55-dBZ reflectivity core beneath the level of the inferred main negative charge. Williams et al. (1989a) suggest that cloud-to-ground lightning is favored when ice particles descend below the level of the main negative charge because they acquire positive charge through the process of charge reversal microphysics. This lower positive charge results in the electrical bias necessary for negative charge to transfer to ground as CG lightning.

To investigate this correlation further, we have inferred the hail volume aloft (T<0° C) by employing the multiparameter radar method of bulk hydrometeor identification as shown in Table 4.1. The results depicted in Fig. 6.20 demonstrate that the appearance of hail aloft leads the CG flash rate by six minutes. Each peak in the CG flash rate is preceded by a maximum in the hail volume aloft. This result is in agreement with observations from the previous case (Sec. 5.3.2), assuming that the hail can descend below the level of the main negative charge and then charge positively within six minutes. Using Eqn. 6.2, the terminal fallspeed for a 2 cm hailstone is approximately $V_t = 16$ m s^{-1}. Our analysis reveals that the bulk of the hail was found between 4 and 6.5 km AGL. We

assume a level of main negative charge of 4 km AGL associated with T = -10° C (Williams, 1989). Recall that we calculated a conservative "charge reversal time" on the order of 4 minutes in Sec. 5.6. We estimate that a majority of the hail would have time to descend below the level of main negative charge and charge positively within the required six minutes in the presence of a weak updraft of 6 m s^{-1}. Note that the there must be a sufficient ice crystal concentration (say 100 l^{-1}) and at least a weak updraft maintaining a supply of cloud liquid water while the hail is descending for the non-inductive charging mechanism to be operative. This may be the reason why the onset of CG lightning is well correlated with the initial descent of the largest precipitation particles (hail in this study and 55 dBZ echo in Lhermitte and Krehbiel, 1979). Smaller hydrometeors with lower terminal fallspeeds will contribute to this process later than the large ones.

The most striking features of Fig. 6.20 are the rapid increase in the hail aloft after 1629 MDT and in the CG lightning after 1635 MDT. Positive Z_{dr} columns began appearing in the northern portion of the developing squall line by 1629 MDT and were prevalent throughout much of the convection by 1653 MDT. In sections 6.3.1 and 6.3.2, we compiled the following supporting evidence suggesting that positive Z_{dr} columns are prodigious producers of hail: 1) ample supply of frozen drop embryos, 2) evidence in the correlation coefficient for the prolonged presence (12 minutes) of hail in the interface zone at the top of the column, 3) dual-Doppler synthesized vertical velocities in the interface zone sufficient to suspend the particles, 4) ample liquid water for rapid growth of hail (probably wet growth in some regions), 5) reflectivity and differential reflectivity data showing the presence of a 2 km wide hail shaft adjacent to a column within 6 to 12 minutes 6) evidence from Conway and Zrnic (1993) from a similar Colorado storm demonstrating that several hail trajectories passed through the column, and 6) confirming evidence for numbers 1, 2, 4, and 5 above in several other studies. As a result, we suggest that the rapid increase in the production of hail aloft and the subsequent increase in the CG

flash rate was at least partially caused by the presence of the positive Z_{dr} columns along the developing squall line after 1629 MDT.

As in Sec. 5.3.2, we also present a comparison of the CG flash rate and the hail and graupel volume below the melting level as calculated using Table 4.1 (Fig 6.21). The graupel and hail volume were combined in this figure because they exhibited the same temporal trends. The hail volume was typically equal to 10-20% of the graupel volume. As seen in Fig 6.21, each peak in the CG flash rate was accompanied by a corresponding peak in the descending graupel and hail mass. This supports the findings of previous lightning studies which relied on the use of reflectivity alone to discriminate precipitation size and type.

The absence of CG lightning during periods of tornado and funnel cloud reports at 1612 MDT and 1635 MDT is in agreement with the findings of MacGorman et al. (1989) during the Binger F2 and F4 tornadoes associated with a supercell and with the observations of Seimon (1993) during an F5 tornado associated with a supercell. In this study, the predominance of IC lightning during tornado development was associated with a period of rapid vertical growth as seen in multiparameter radar data. Cloud-to-ground lightning associated with the descent of ice mass followed the occurrence of the tornado and funnel cloud reports as shown in Fig 6.21. This temporal pattern is not universal however. MacGorman and Nielsen (1991) did not observe a similar reduction in CG activity during mesocyclone formation and a brief F3 tornado. Instead, they found in this case that the CG flashes clustered near the mesocyclone during intensification and tornado genesis. They attributed this finding to weaker mesocyclone organization and updraft intensity than in the Binger storm. Seimon (1993) suggested that this lull in CG activity might be a possible precursor signature for violent tornadoes in supercell storms. Given the findings in this study for a non-supercell tornado and the other references mentioned here, we submit that a lull in CG activity during tornado genesis is really an

indication of whether the tornado formation mechanism is associated with the updraft accumulation of ice and not necessarily of tornado intensity.

6.4.3 Observations of two field excursions associated with precipitation

After 1711 MDT the squall line slowly moved over the CSU-CHILL radar such that the spatial and temporal resolution of the radar data was insufficient for analysis. However, the squall line was electrically active within the operating range of the corona point sensor collocated with the radar. Observations of two Field Excursions Associated With Precipitation (FEAWP) were recorded by the corona point. The kinematic (microburst) and microphysical (strong precipitation) signatures of the FEAWP were measured by a nearby mesonet observation station.

Fig. 6.22 is a plot of the wind gust and rain rate as measured by the Greeley (GLY) meso-network observation station operated by NOAA/FSL. The mesonet station is located approximately 1 km southeast of the CSU-CHILL radar. Prior to 1710 MDT, no precipitation was recorded and winds were typically gusting to 8 m s^{-1} in response to the approaching squall line to the west. By 1720 MDT, winds in the vicinity of the radar began to gust to over 17 m s^{-1}. Since moderate rain (27.5 mm h^{-1}) began by 1730 MDT, evaporation and melting of precipitation in a sub-saturated boundary layer was the probable cause of the initial onset of the downburst at 1720 MDT (Srivastava, 1987). Golf-ball sized, spongy hail was reported at the CSU-CHILL radar at 1729 MDT. Gusty winds associated with the downburst began to weaken after 1725 MDT and actually reached a minimum of only 7 m s^{-1} by 1740 MDT. Meanwhile, the precipitation increased in magnitude after 1730 MDT and reached a maximum of approximately 50 mm h^{-1} by 1740 MDT. Reports of heavy rain were noted by the CSU-CHILL radar operator at 1743 MDT.

As discussed in Sec. 5.5, a FEAWP is a pronounced excursion of the electric field to negative values (fair-weather field) during the active stage of a thunderstorm that is typically coincident with the arrival of a strong downdraft and a transient surge of

precipitation near the observing location. There is still some controversy as to whether the field excursion is caused by descending, positively charged precipitation or whether the accompanying downdraft transports some other positive charge downward.

Some evidence in favor of the descending, positively charged precipitation causing the FEAWP can be found in Fig. 6.23. It is readily apparent from the corona point data in Fig. 6.23 that the storm was extremely electrically active. Each sudden discontinuity is associated with a lightning flash. Note the two prominent excursions to negative values of corona current associated with predominately positive charge aloft. The first excursion occurred from about 1732:30 to 1733:30 MDT and the second, stronger excursion occurred from approximately 1740:30 to 1743:00 MDT. Comparing the times of these excursions to the onset of gusty winds and precipitation found in Fig. 6.22, we note that there was no excursion in the corona current during periods of peak downburst strength at 1720 and 1725 MDT. The first FEAWP was approximately coincident with the descent of large hail and moderate rain. The second FEAWP which contained the peak fair weather electric field was simultaneous with the peak rain rate at the mesonet station. Notice that several smaller excursions occurred from 1745 to 1751 associated with continued light to moderate rain.

At least in this case, the FEAWPs were highly correlated with the onset of precipitation at the surface and offset from the period of maximum downburst strength. This appears to favor the hypothesis that descending, positively charged precipitation causes the transient excursion in the electric field. Jayaratne et al. (1983) first suggested that the source of the lower positive charge in thunderstorms might be graupel particles falling below the charge reversal level that acquire positive charge during collisions with ice crystals via the non-inductive mechanism. Williams et al (1989b) speculated that the lower positive charge and associated field excursion observed with a similar corona point sensor in a Denver thunderstorm were caused by the action of charge reversal microphysics on descending graupel. It is interesting to note the massive discontinuity

which occurred at approximately 1741 MDT associated with the second FEAWP. The lightning flash which caused this discontinuity was so intense that it saturated the corona point sensor for almost 20 seconds. It is apparent from the upward extension of this discontinuity that net positive charge aloft was neutralized by this lightning flash. In other words, either an in-cloud lightning flash terminating on the lower positive charge center or a positive cloud-to-ground lightning strike neutralized charge within the lower positive charge region. Although the former event is most common, the magnetic direction finder network confirms that a positive CG lightning strike occurred at approximately 1741 MDT to the south-southwest of the radar at 19.5 km in range. The magnitude of the positive CG flash was quite large (201 LLP units), explaining the saturation of the corona point instrument.

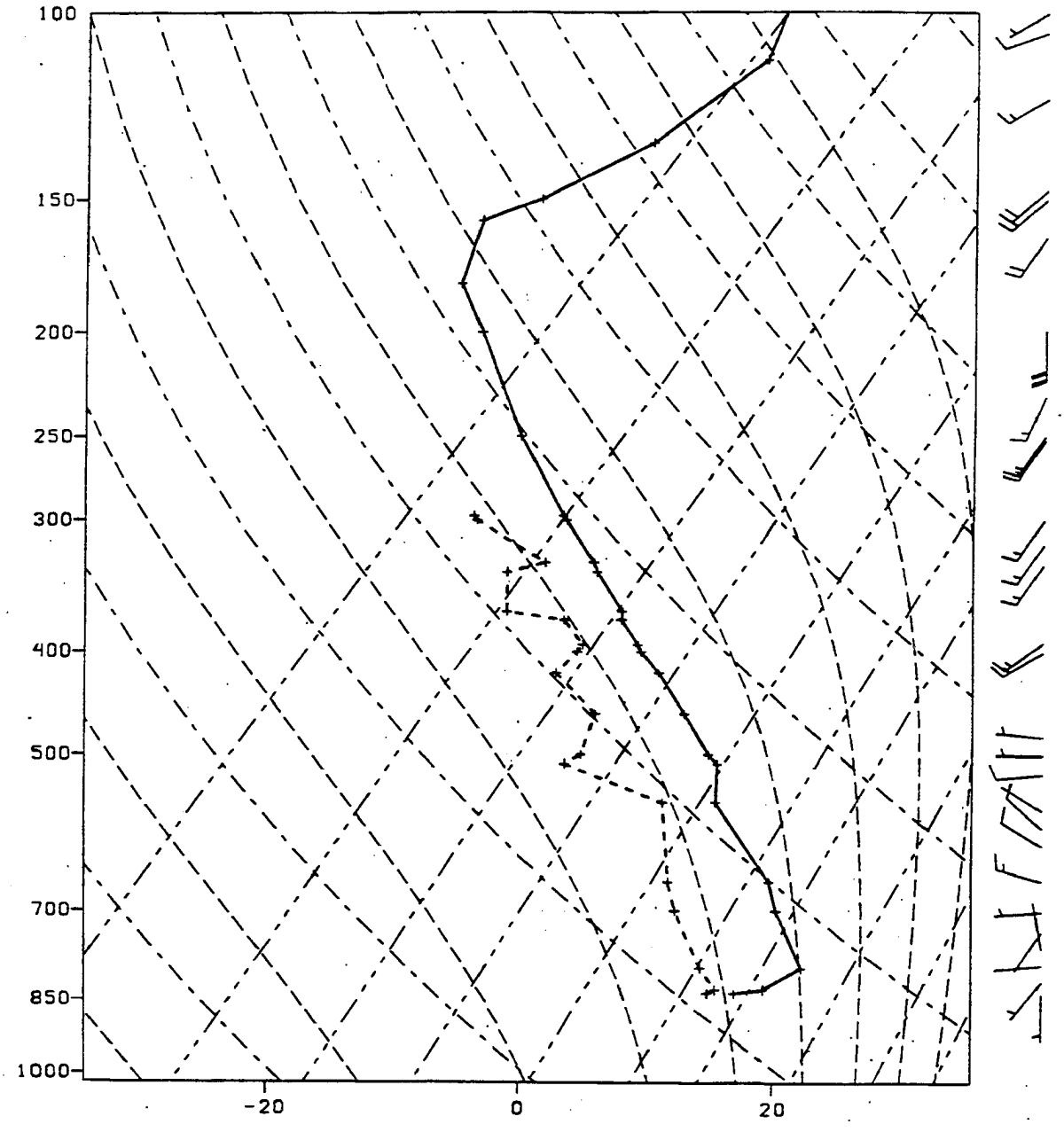

Fig. 6.1 Skew T - Log P plot of upper air sounding data for Denver, Colorado on 28 May 1993 at 1200 UTC. Temperature (solid line) and dewpoint temperature (dashed line) are in degrees Celsius. Wind barbs are in m s^{-1}.

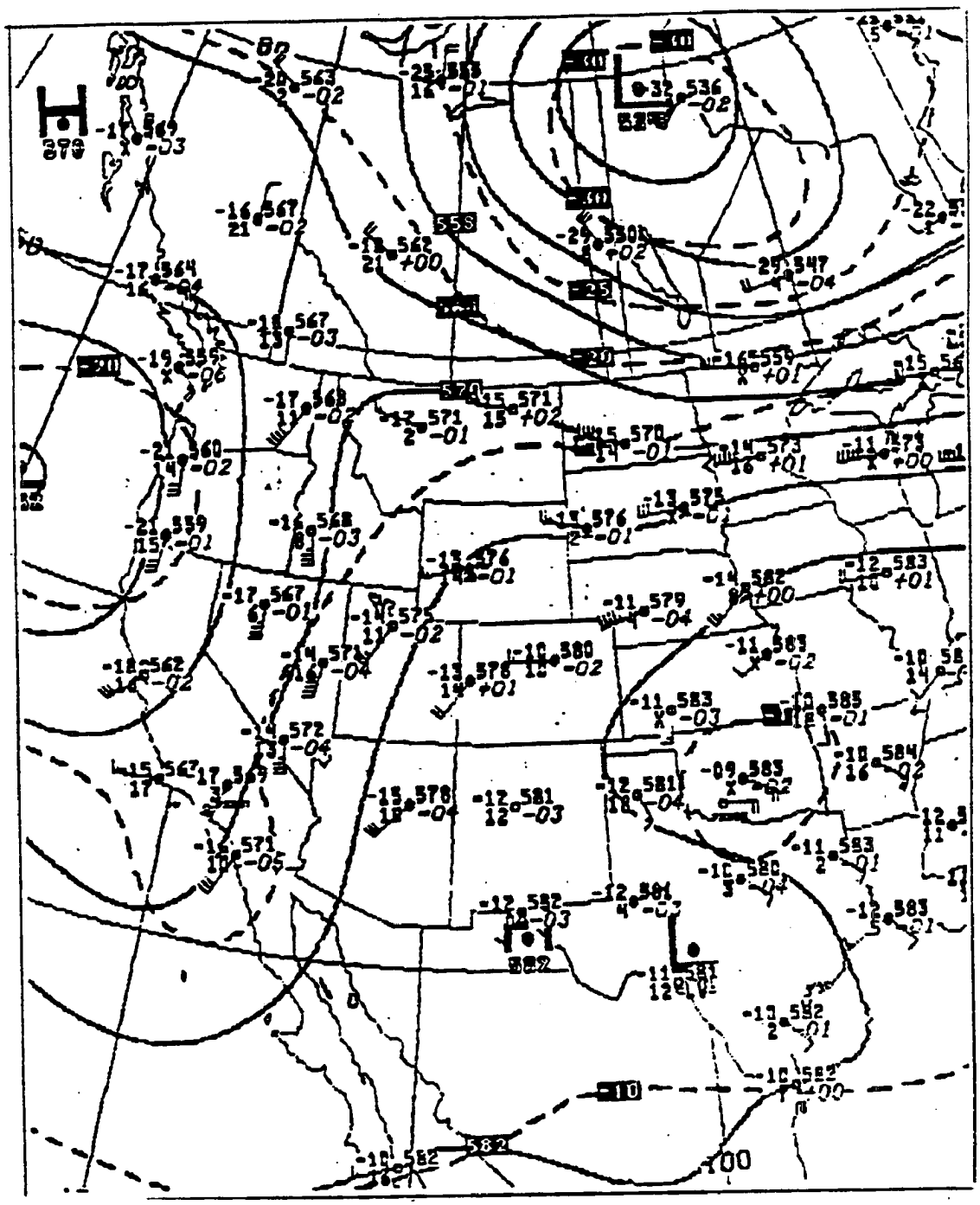

Fig. 6.2 500 mb height analysis of western United States on 28 May 1993 at 1200 UTC.

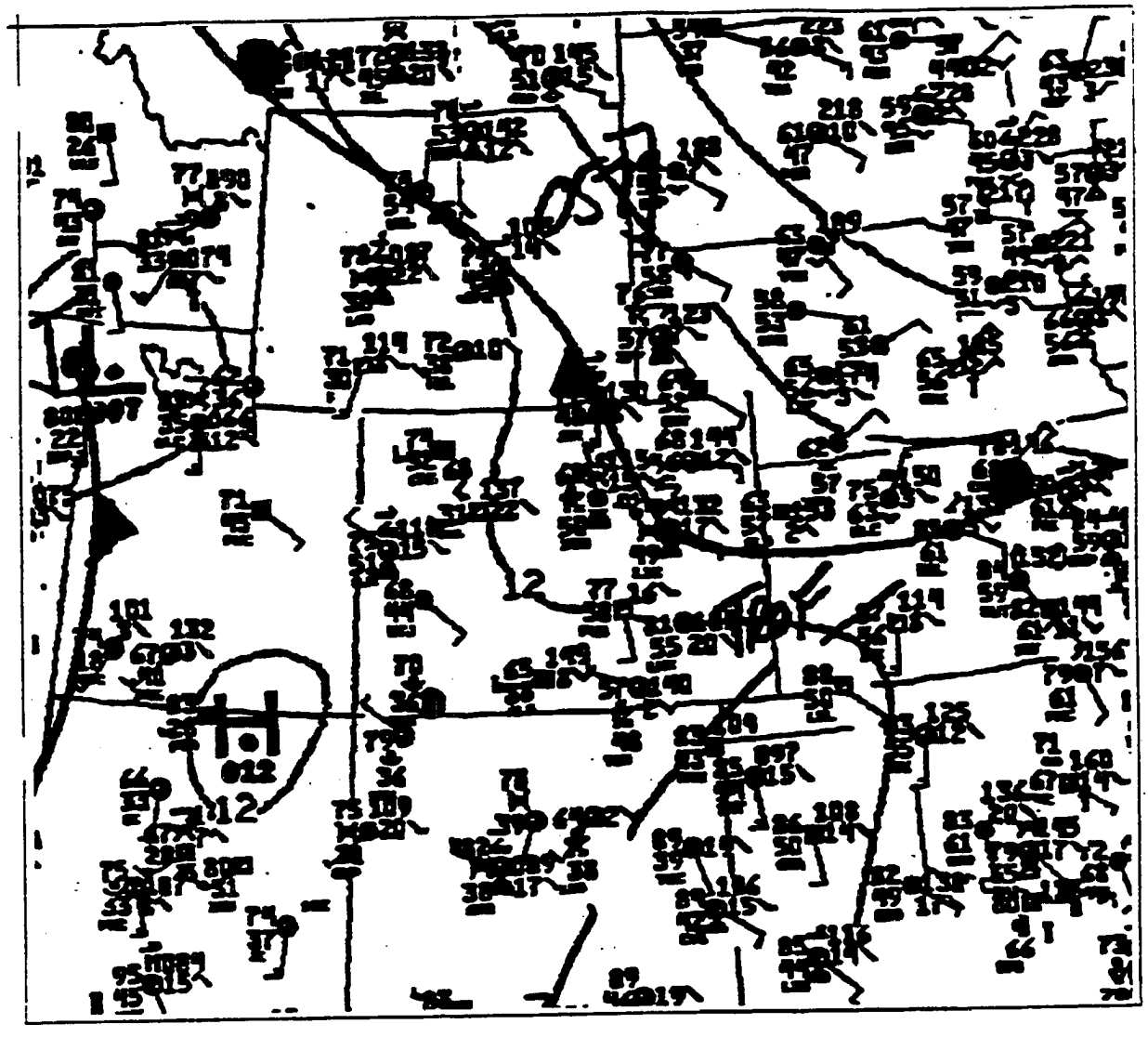

Fig. 6.3 National Weather Service (NWS) frontal analysis of western United States on 28 May 1993 at 2100 UTC.

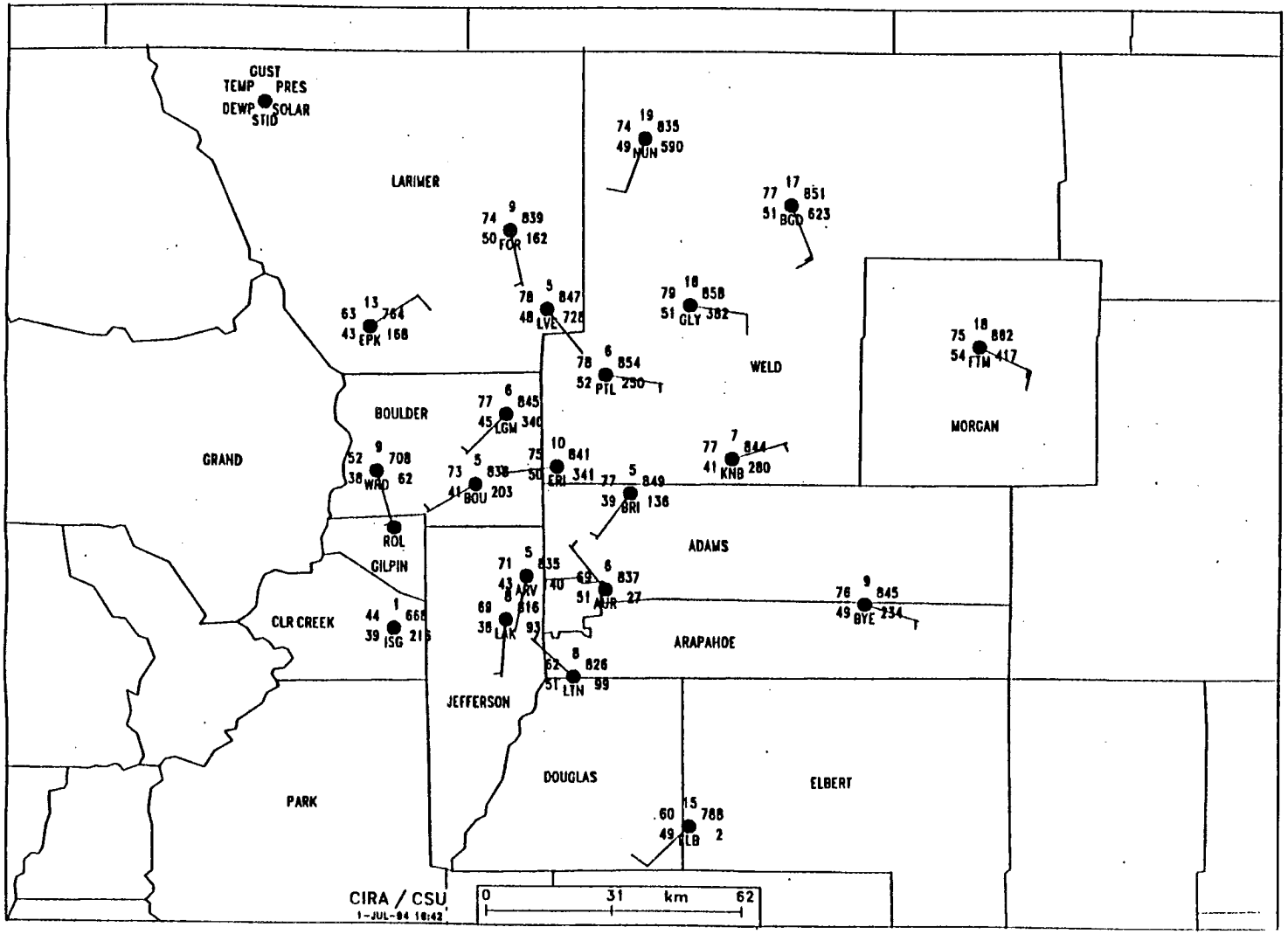

Fig. 6.4 Front Range Mesonet surface data for 28 May 1993 at 2100 UTC depicting temperature and dewpoint temperature in degrees Fahrenheit; wind direction; wind speed and gust magnitude in knots; pressure in millibars; and solar radiation in W m-2. Note key at top left hand corner of figure.

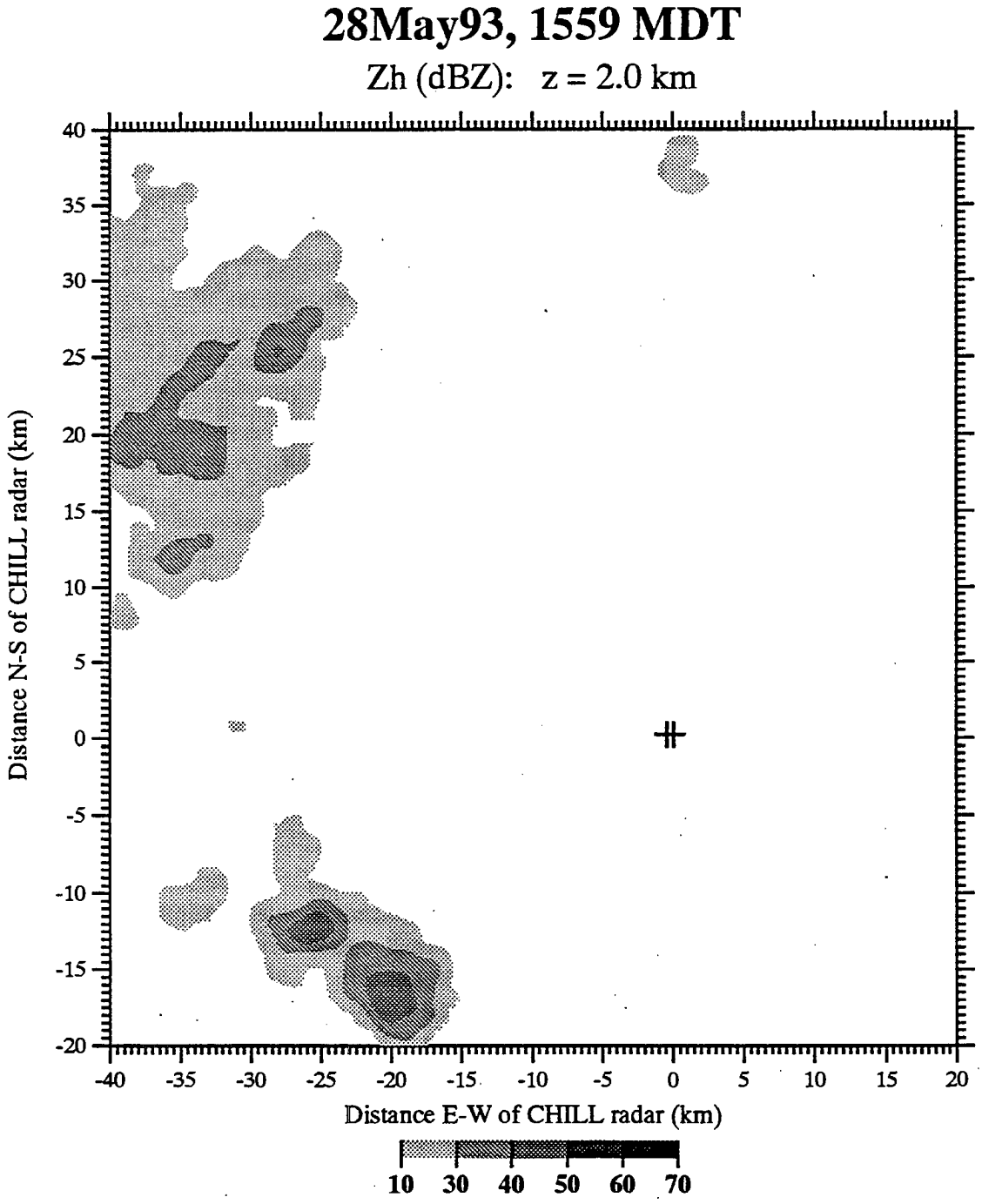

Fig. 6.5 Horizontal cross-sections of horizontal reflectivity (dBZ) at 2 km AGL during squall line formation. a) Results at 1559 MDT.

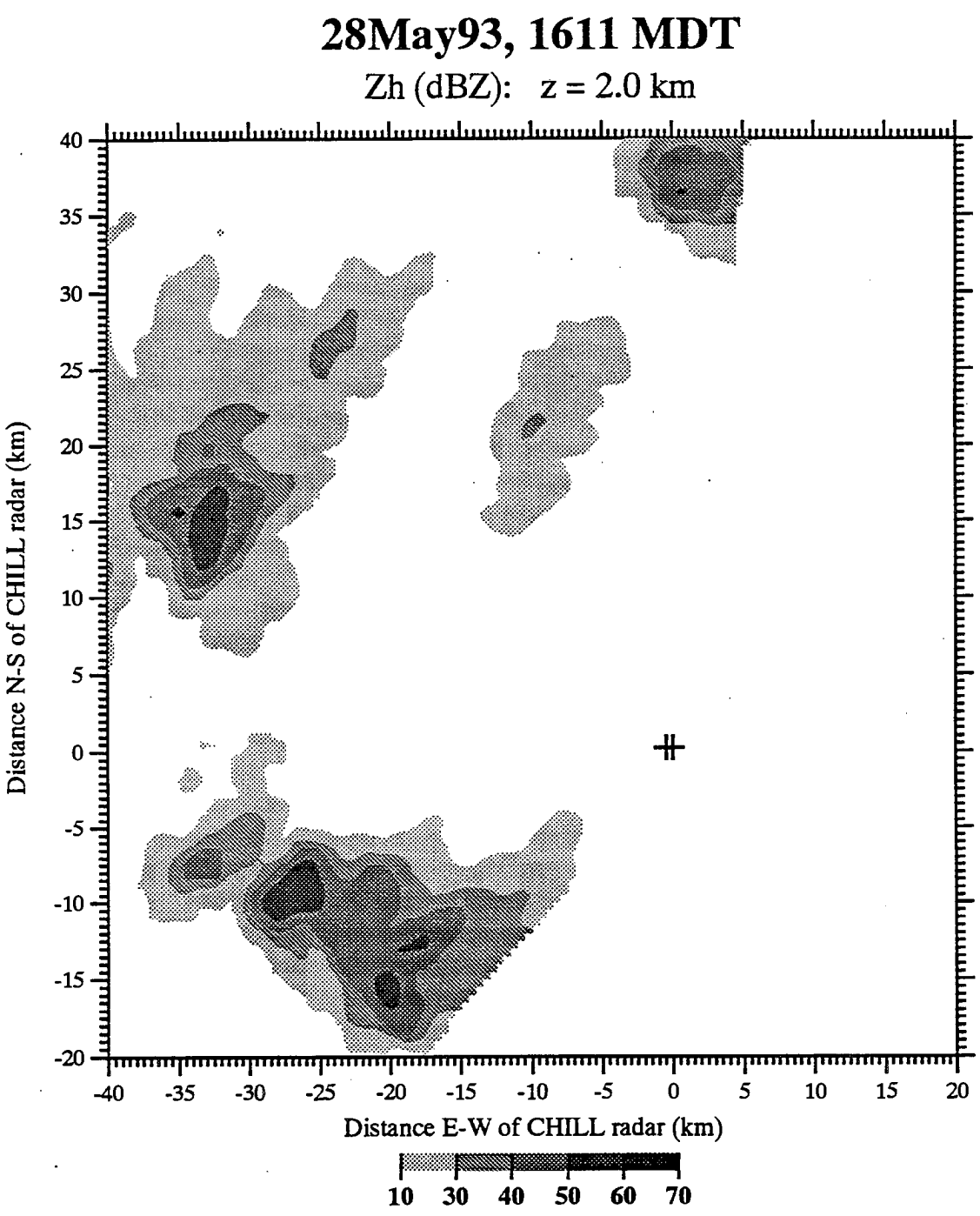

Fig. 6.5 b) Results at 1611 MDT.

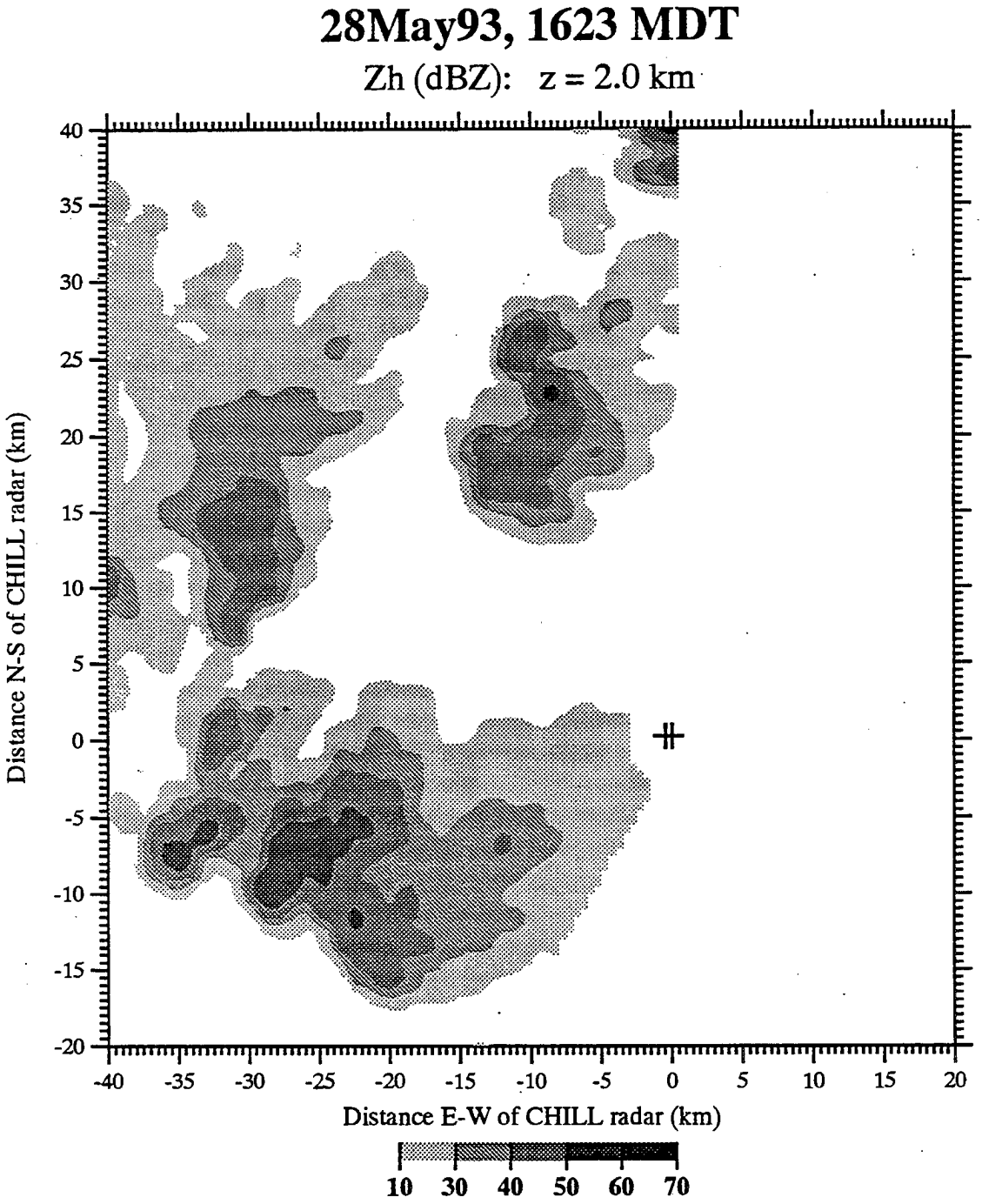

Fig. 6.5 c) Results at 1623 MDT.

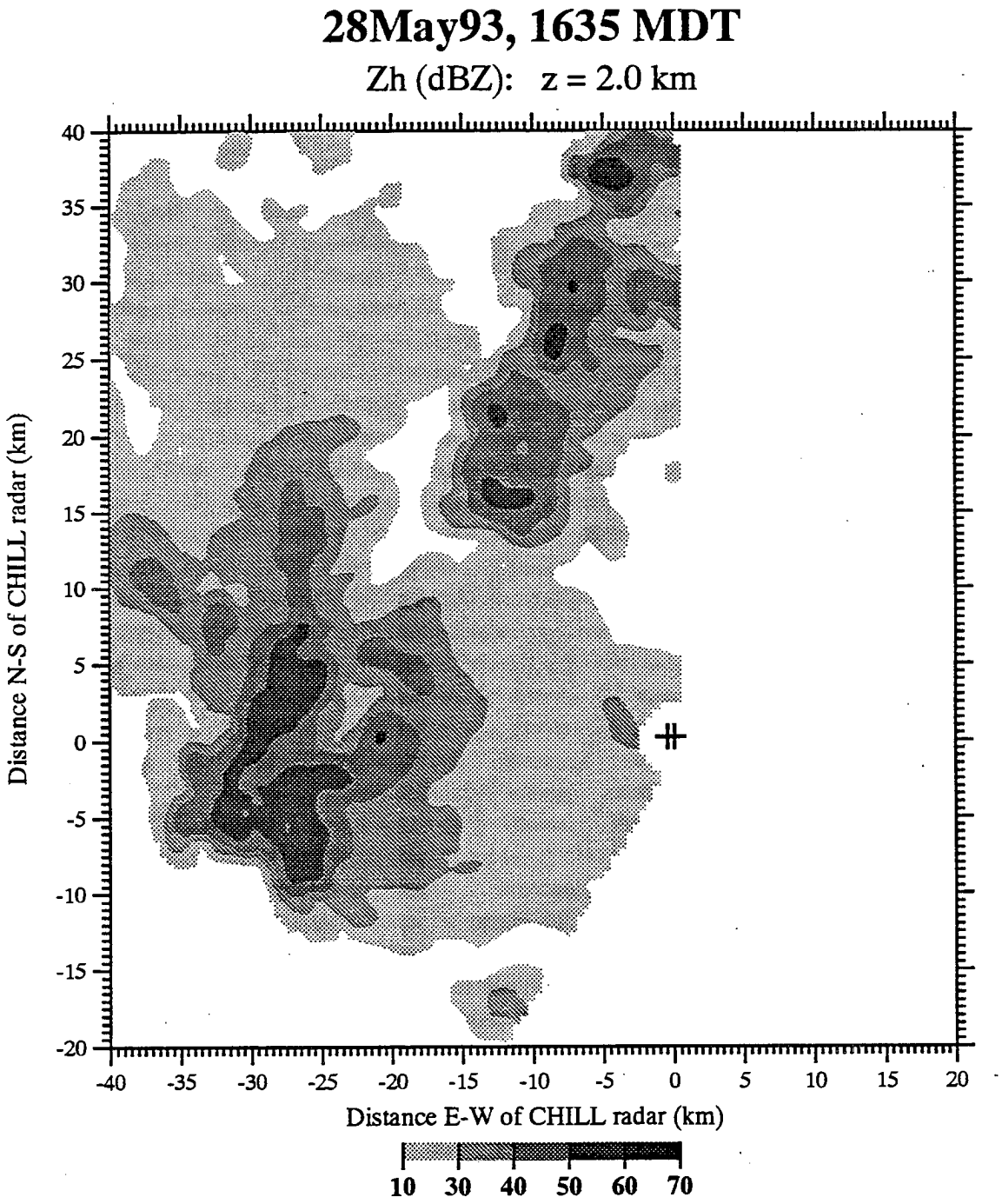

Fig. 6.5 d) Results at 1635 MDT.

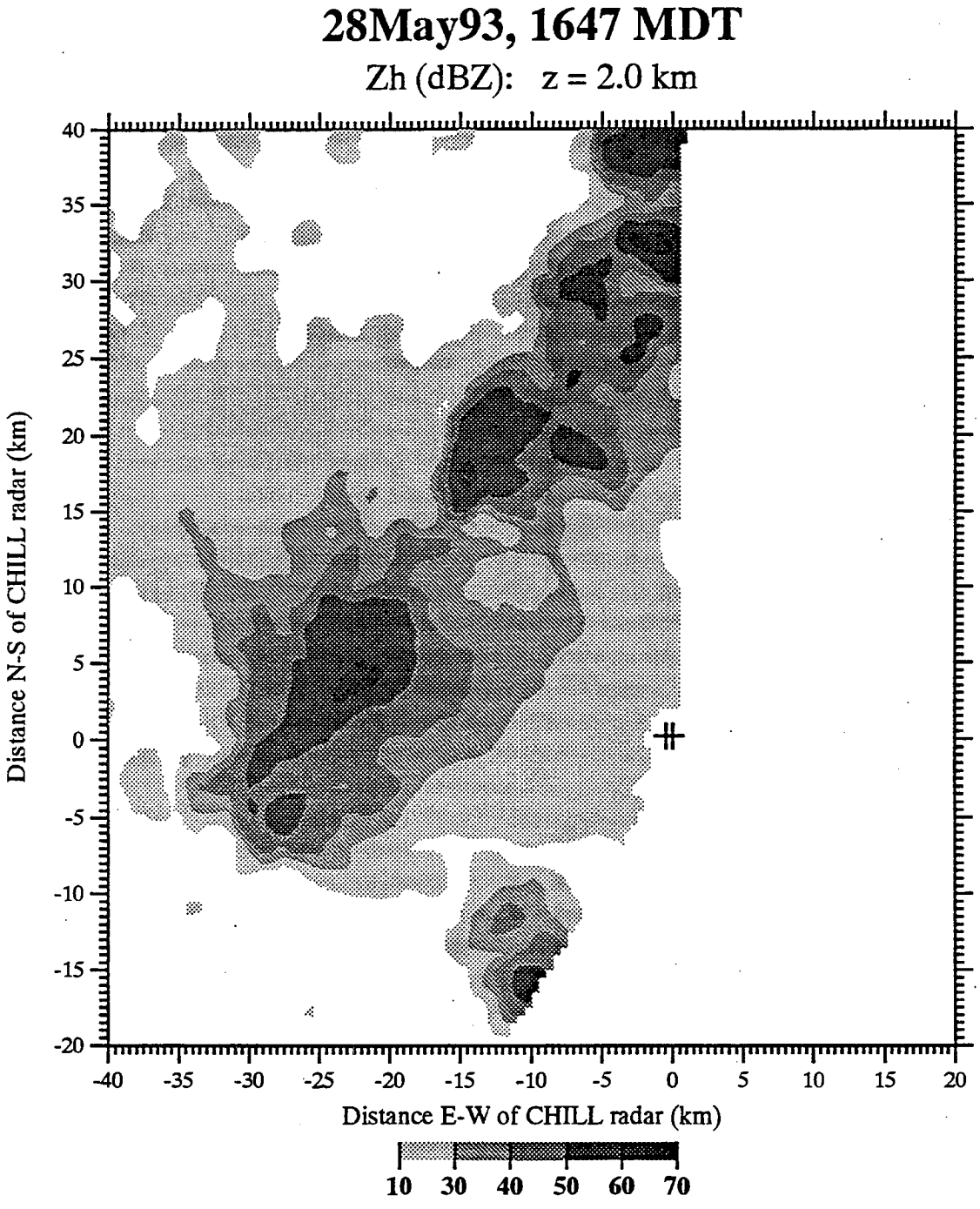

Fig. 6.5 e) Results at 1647 MDT.

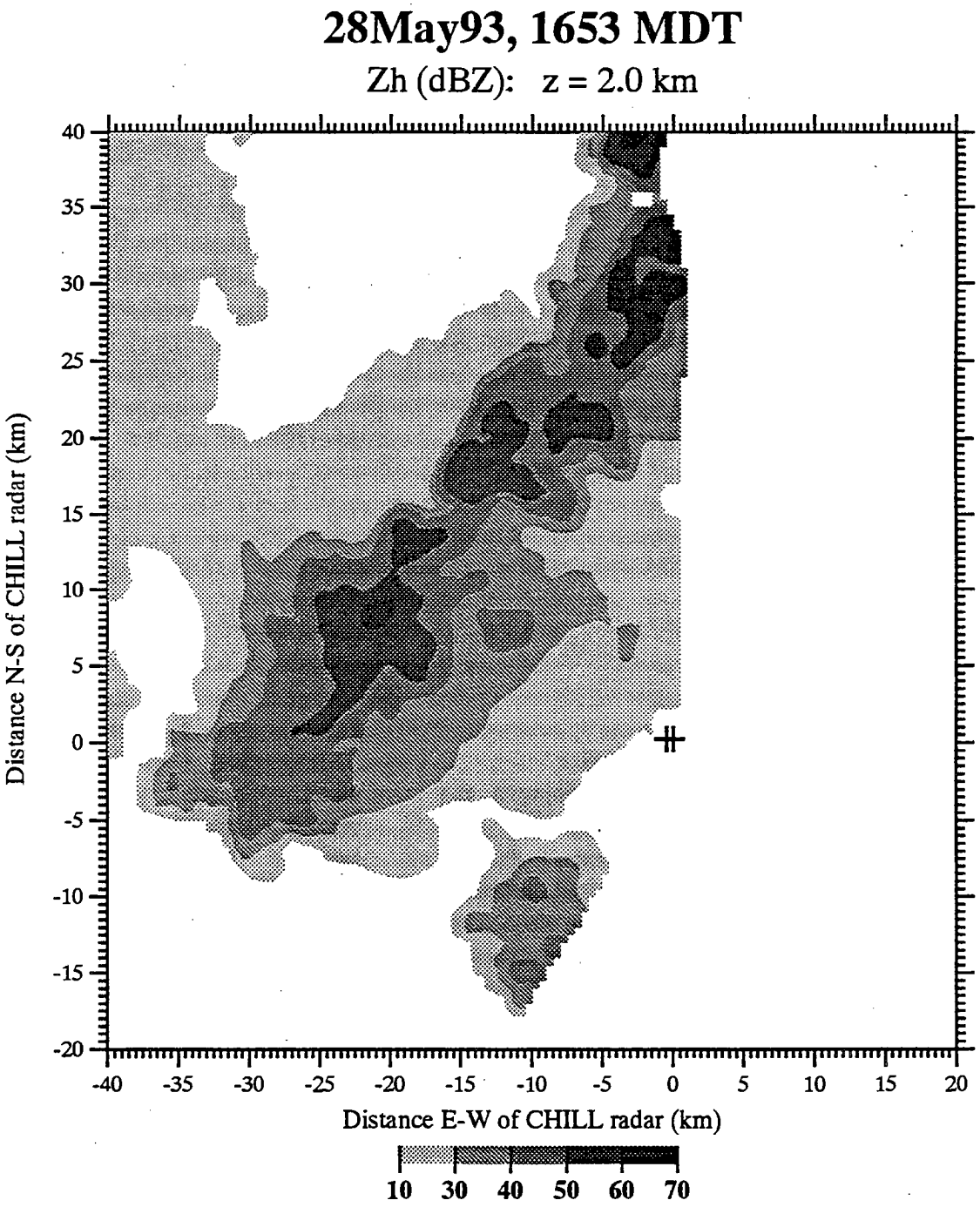

Fig. 6.5 f) Results at 1653 MDT.

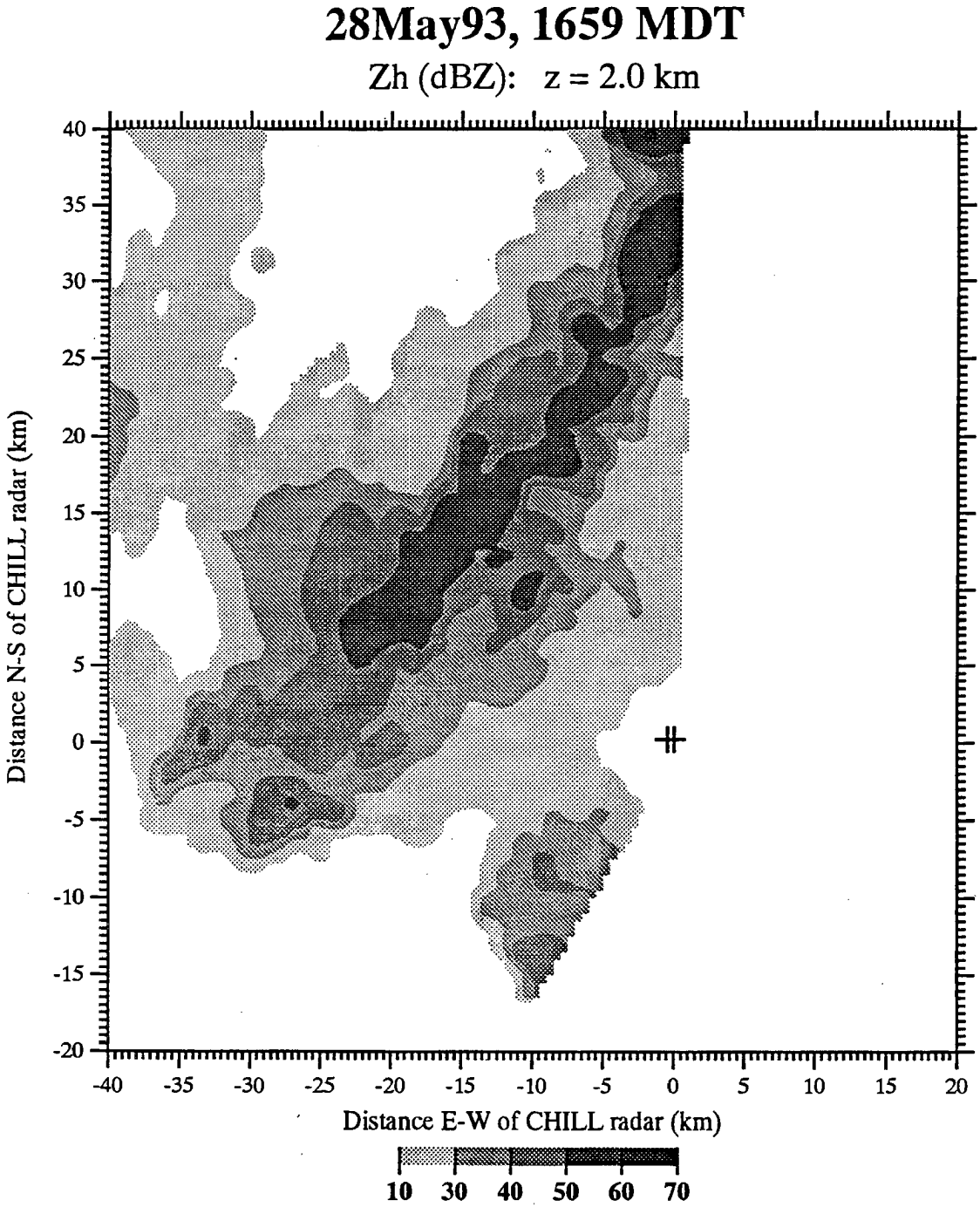

Fig. 6.5 g) Results at 1659 MDT.

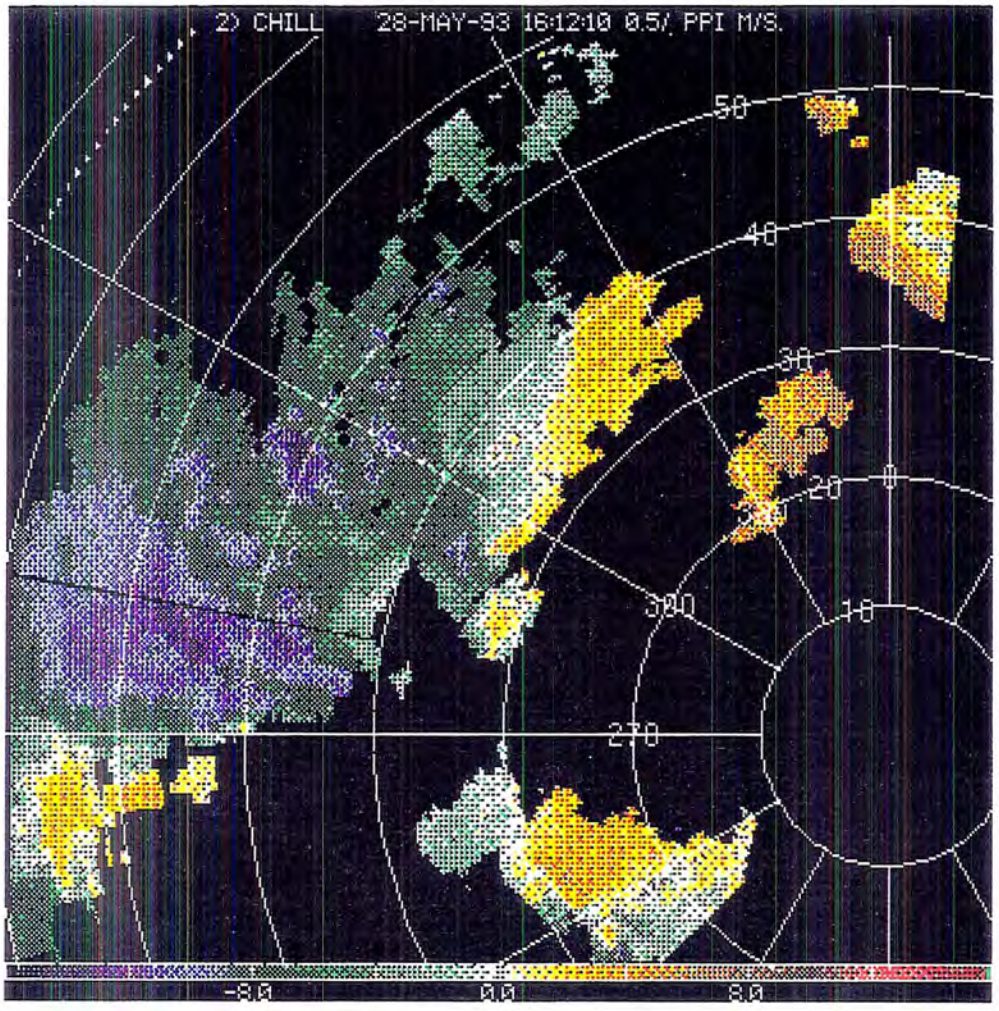

Fig. 6.6 Radial velocities at an elevation angle of 2.5° . Warm tones (such as yellow and red) are positive and indicate a wind direction away from the radar. Cool tones (such as green and violet) are negative and indicate wind direction toward the radar. a) Results at 1612 MDT.

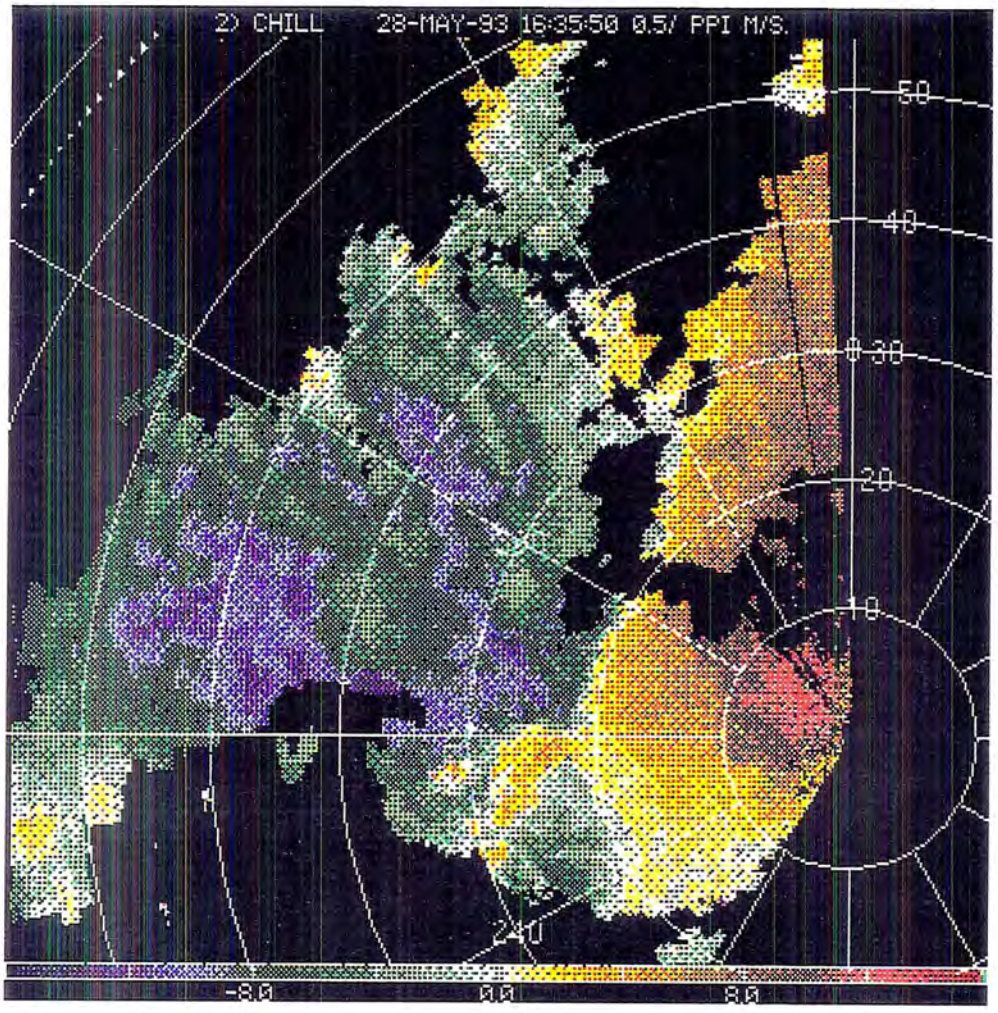

Fig. 6.6 b) Results at 1635 MDT.

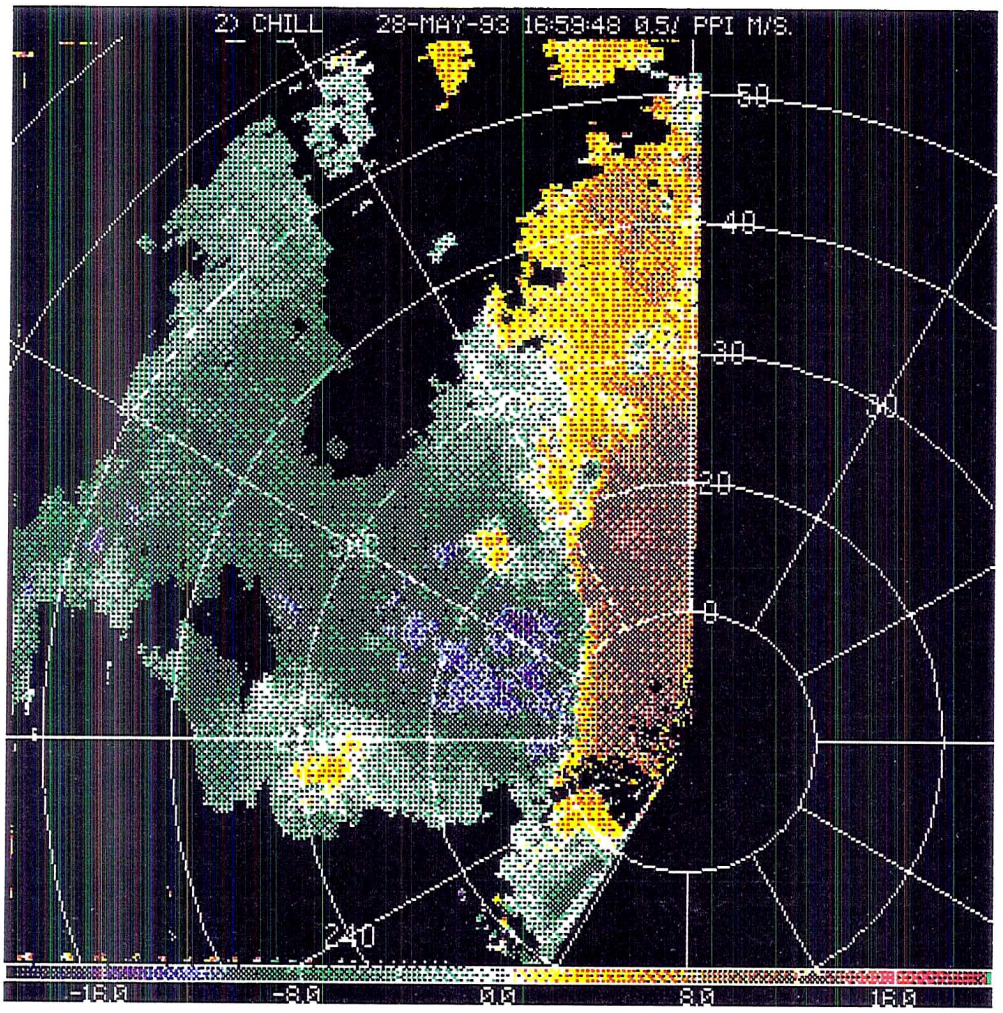

Fig. 6.6 c) Results at 1659 MDT.

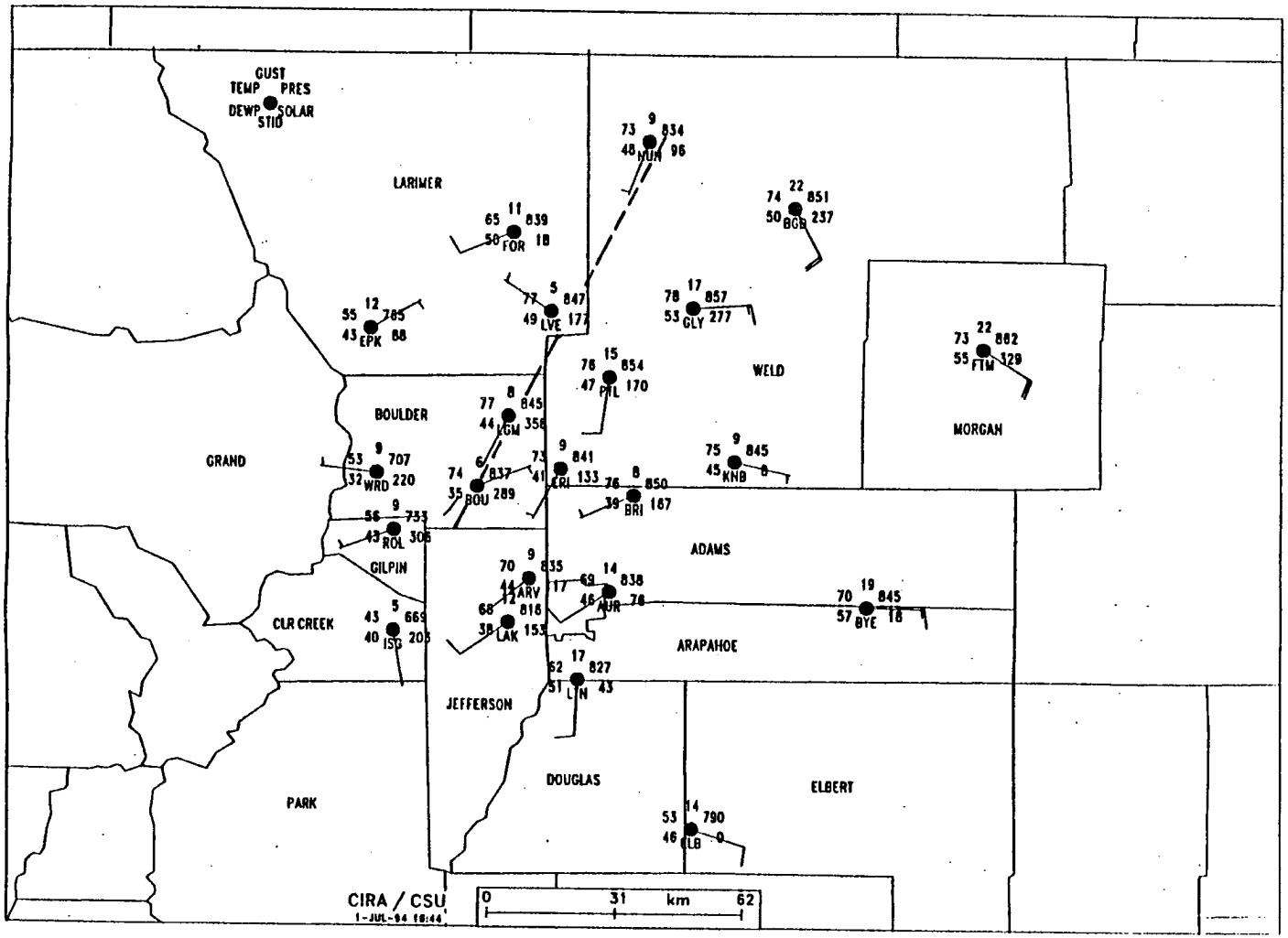

Fig. 6.7 a) Same as 6.4 except for 2210 UTC.

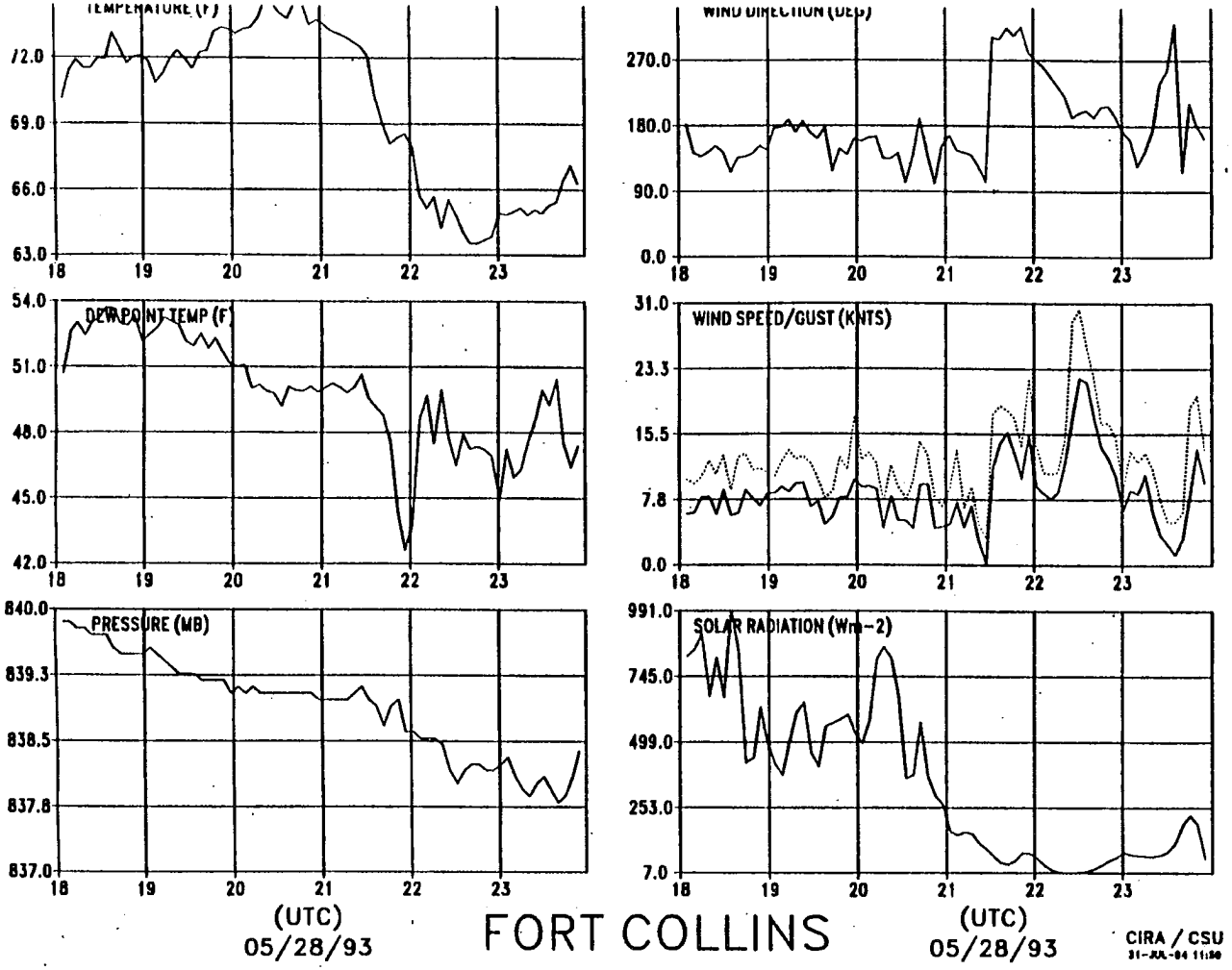

Fig. 6.7 b) Front Range Mesonet temporal evolution of temperature (°F), dewpoint temperature (°F), pressure (mb), wind direction (deg.), wind speed and gust (knots), and solar radiation (W $m.^{-2}$) from 1800 to 2355 UTC on 28 May 1993 for Fort Collins, Colorado.

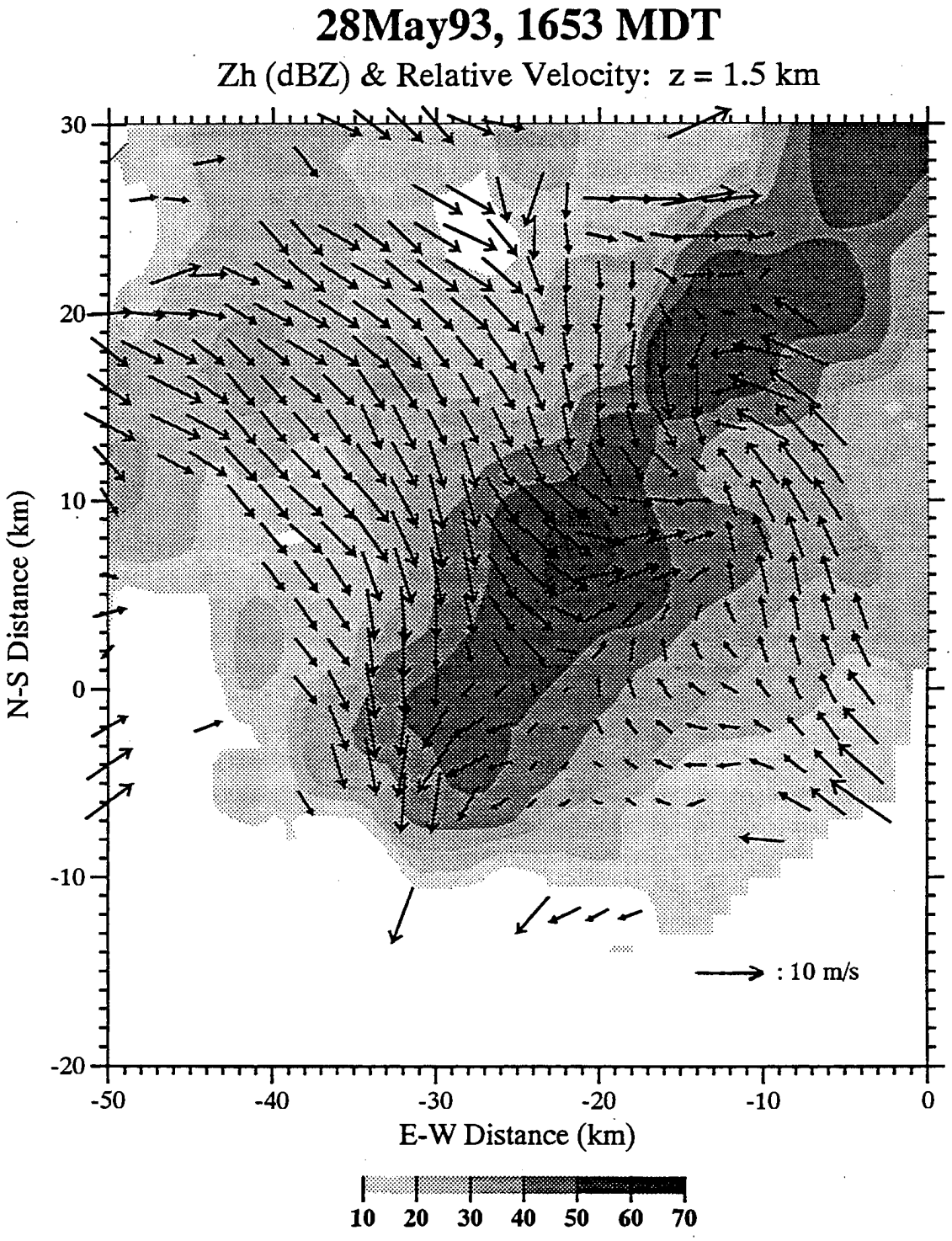

Fig. 6.8 Horizontal cross-section of horizontal reflectivity (dB) and dual-Doppler synthesized horizontal, relative velocity vectors at z = 1.5 km AGL.. a) Results at 1653 MDT.

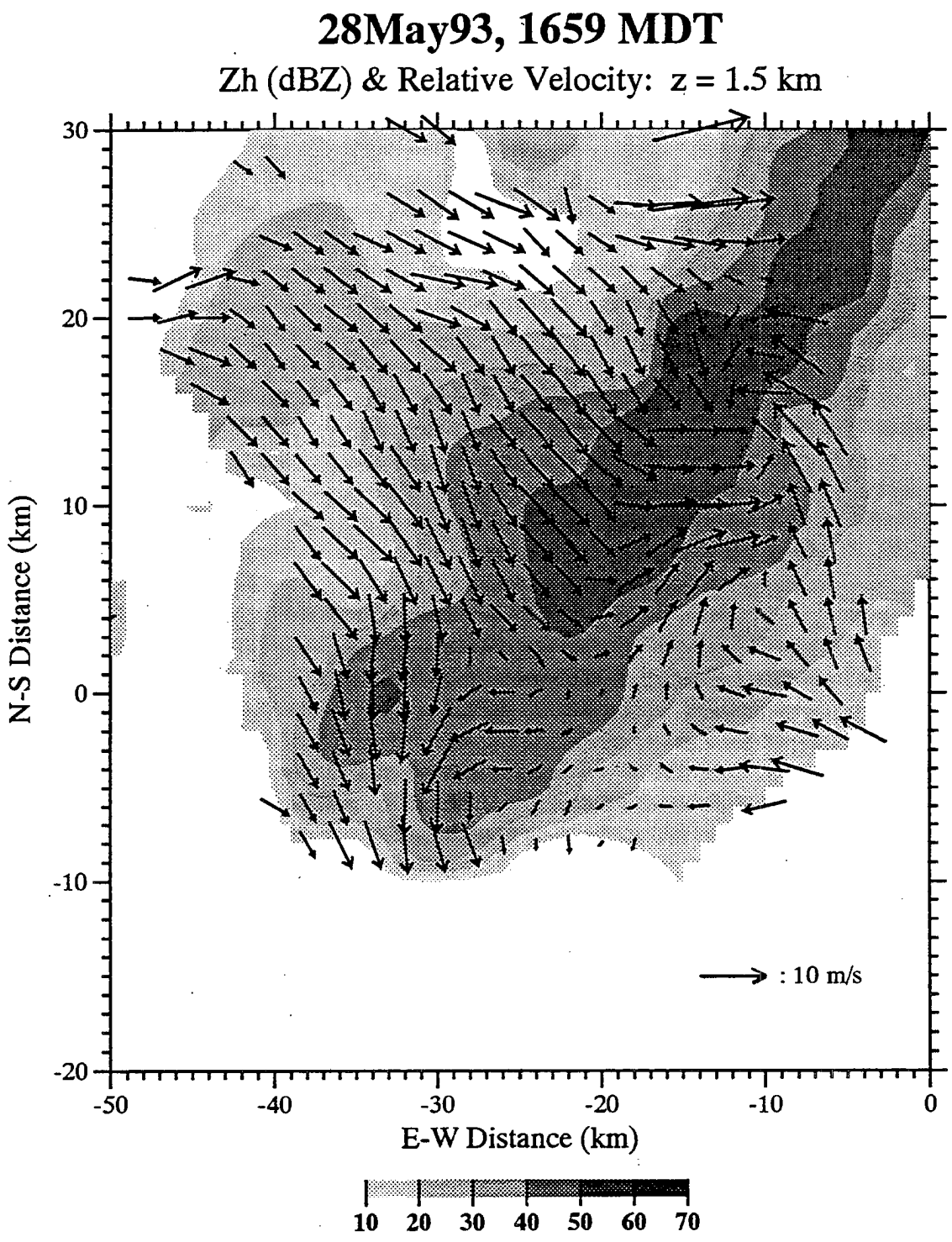

Fig. 6.8 b) Results at 1659 MDT.

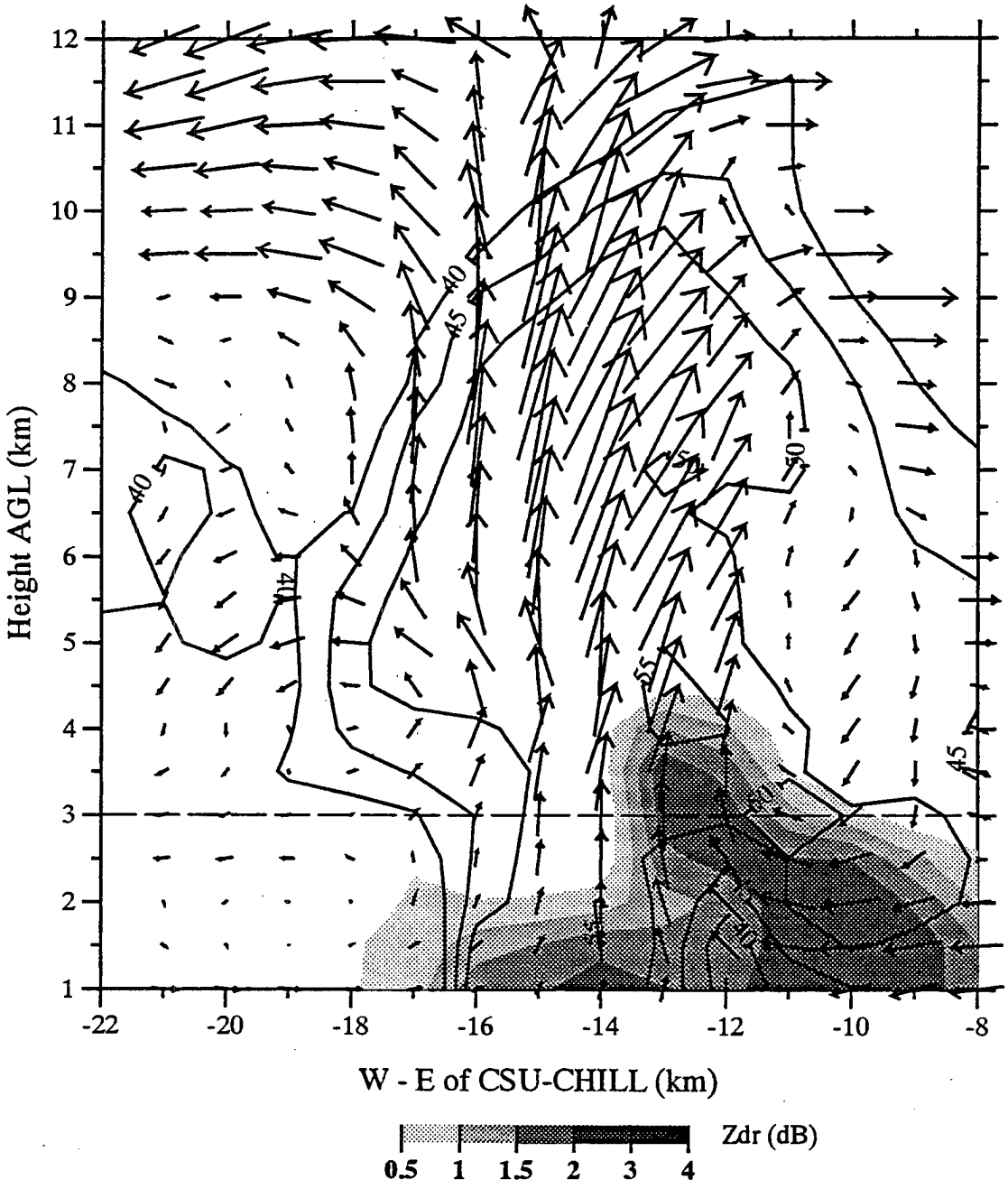

Fig. 6.9 Vertical cross-section of contoured horizontal reflectivity (dBZ), shaded differential reflectivity (dB), and relative velocity vectors at y = 16 km. (Scale: 1 cm = 10 m s^{-1}) a) Results at 1653 MDT.

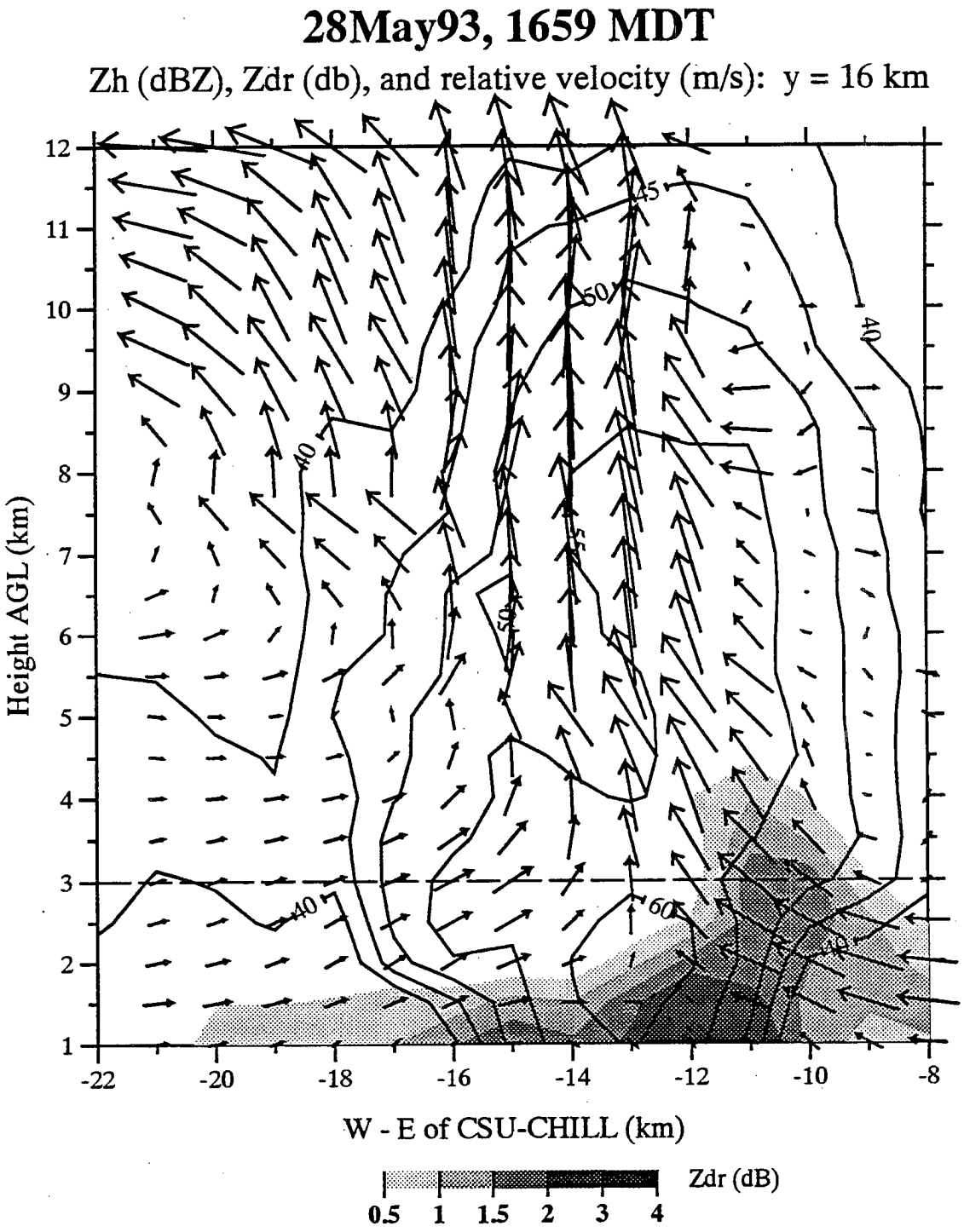

Fig. 6.9 b) Results at 1659 MDT.

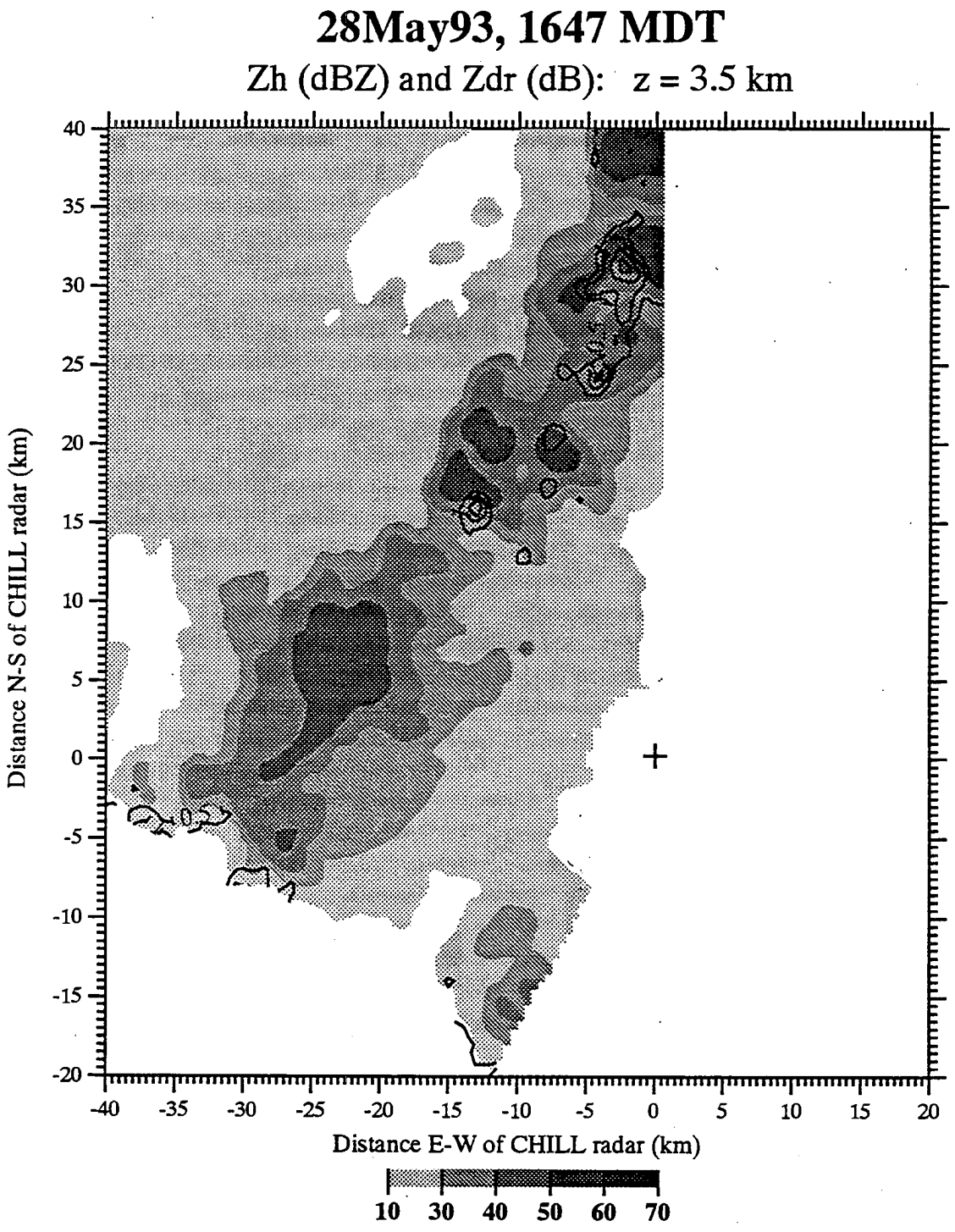

Fig. 6.10 Horizontal cross-section of horizontal reflectivity (dBZ) and contoured differential reflectivity (dB) at z = 3.5 km AGL. a) Results at 1647 MDT.

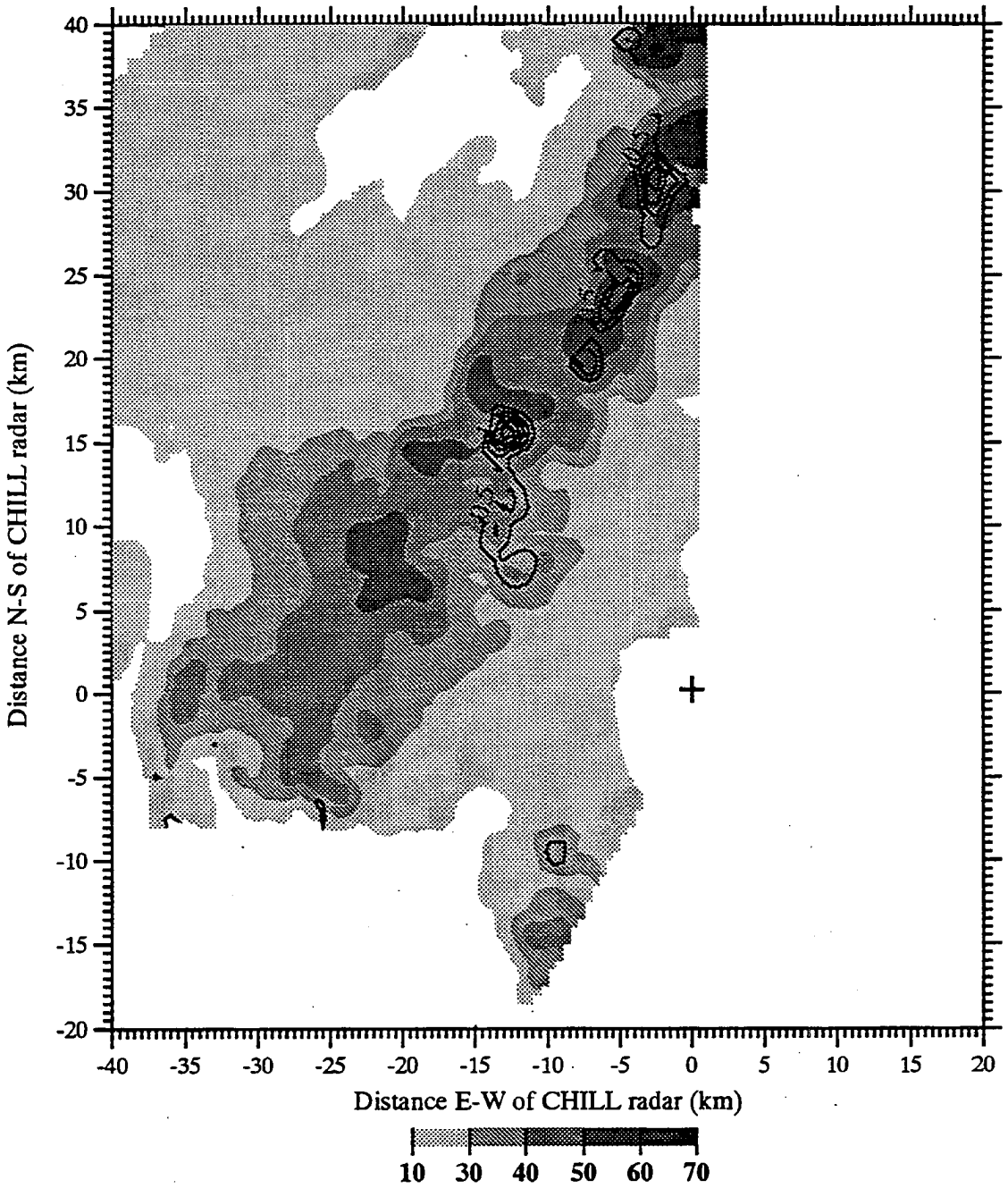

Fig. 6.10 b) Results at 1653 MDT.

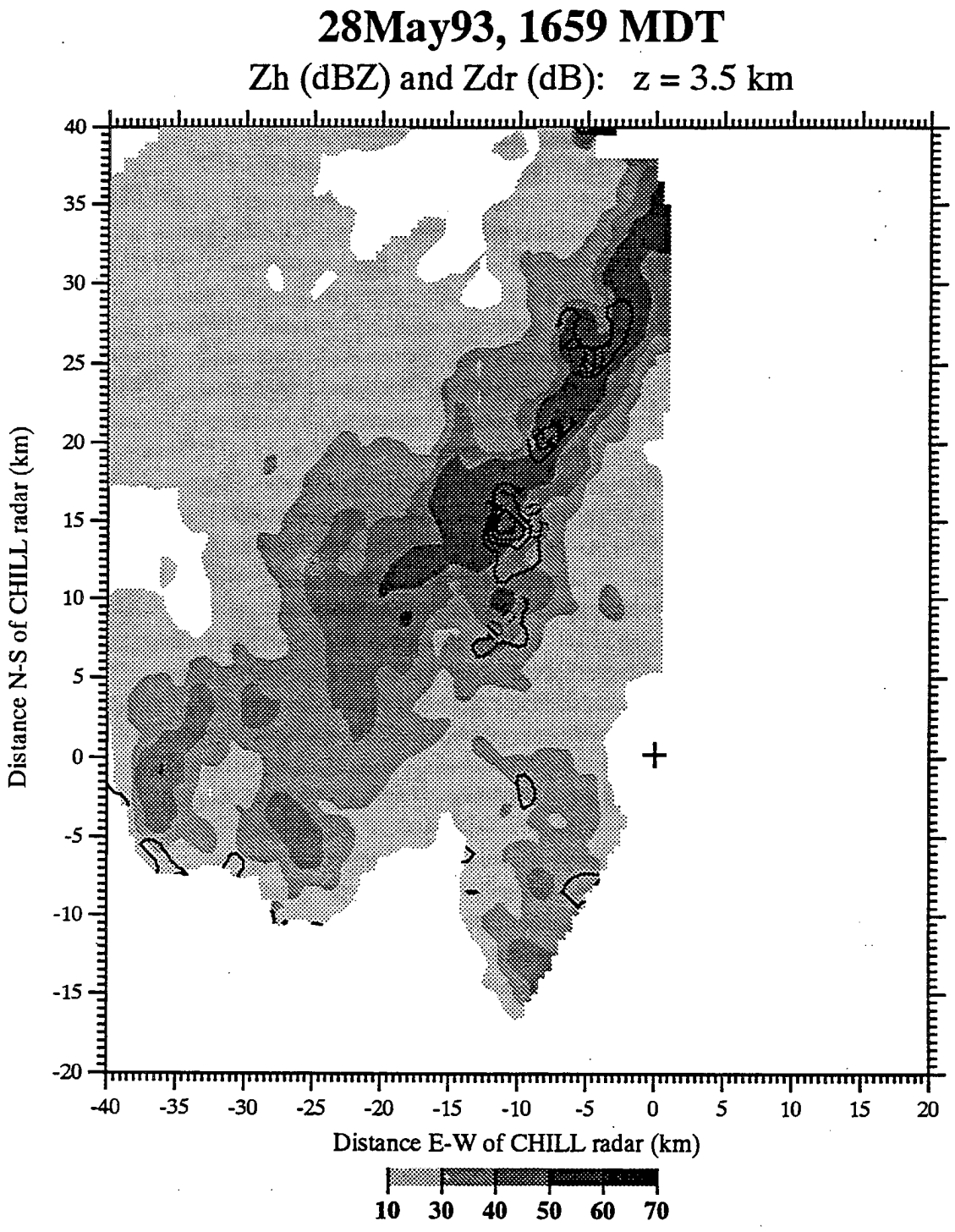

Fig. 6.10 c) Results at 1659 MDT.

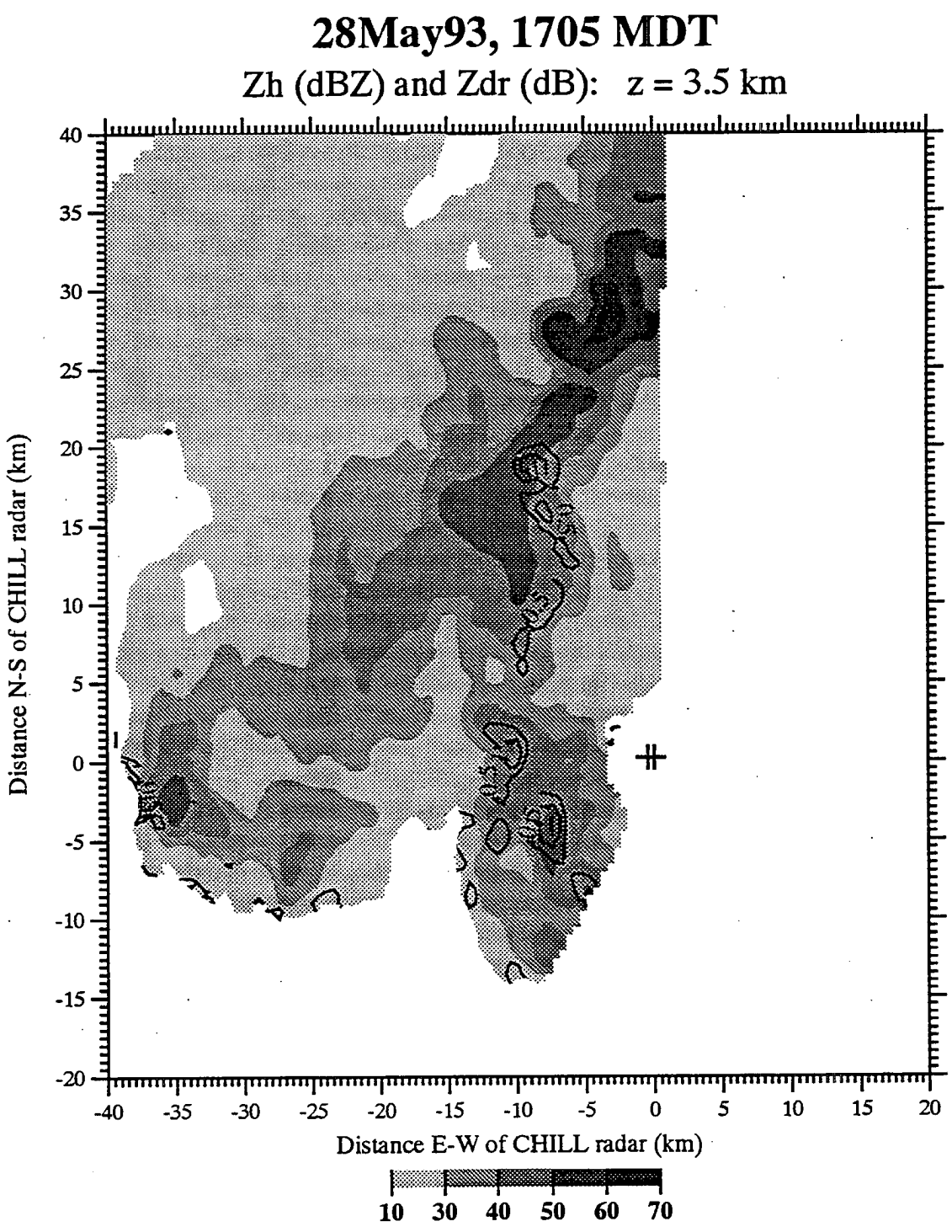

Fig. 6.10 d) Results at 1705 MDT.

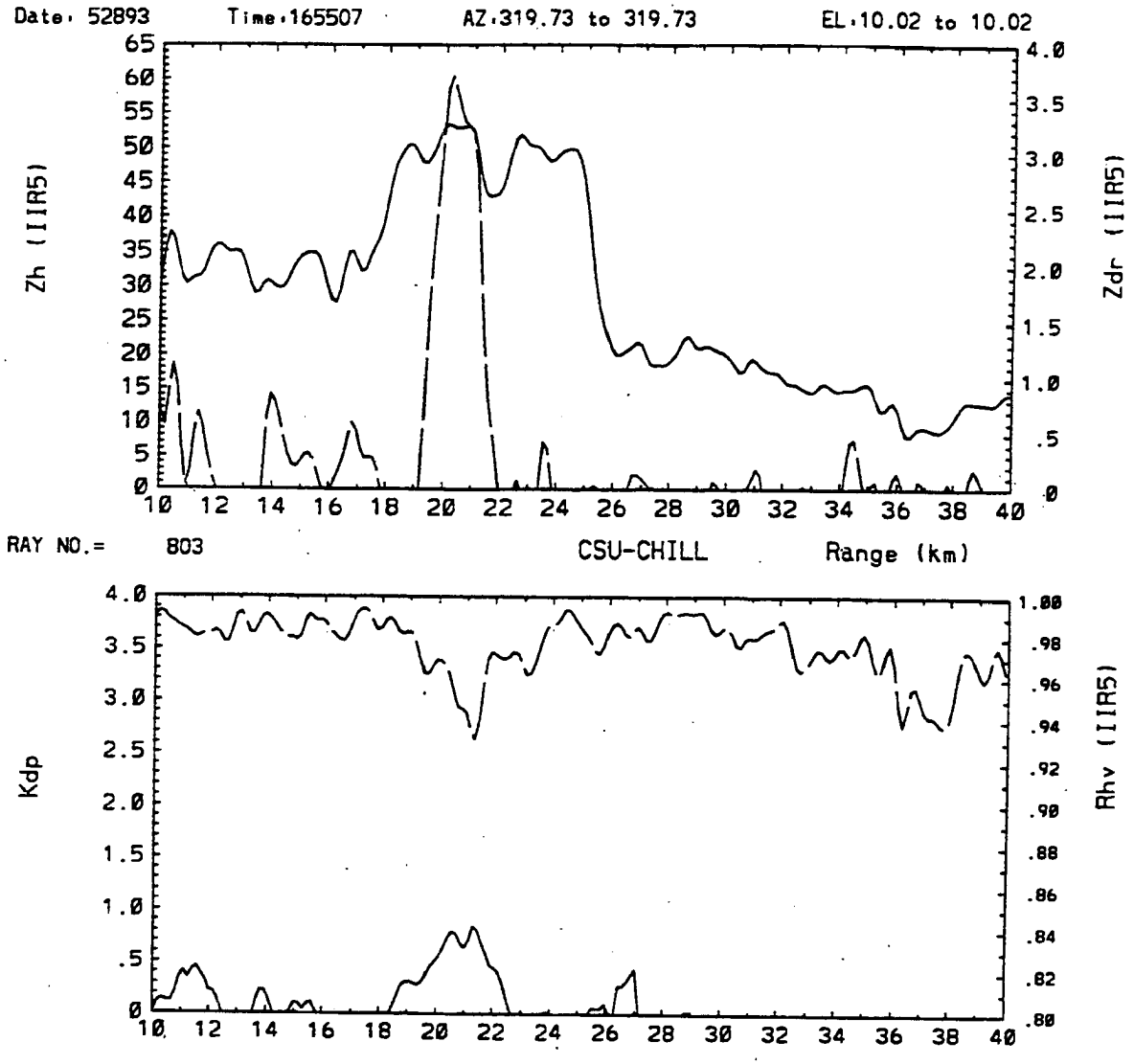

Fig. 6.11 Range plots of Z_h (dBZ, solid line), Z_{dr} (dB, dashed line), K_{dp} (° km^{-1}, solid line), and $\rho_{hv}(0)$ (dashed line) at 1655 MDT. a) an azimuth of 319.73°, an elevation of 10.02°, and a range from 10 to 40 km.

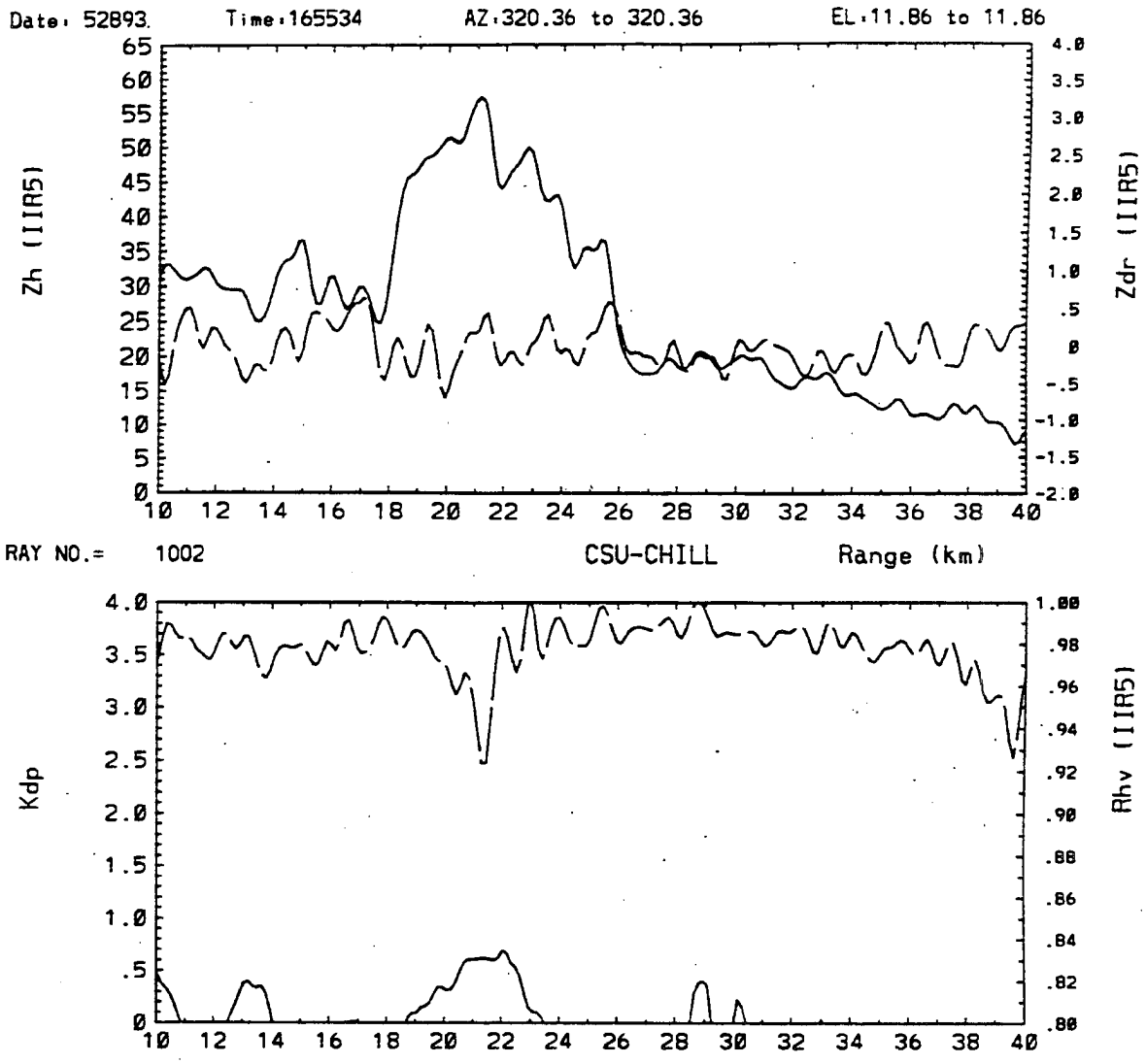

Fig. 6.11 b) an azimuth of 320.36°. an elevation of 11.86°, and a range of 10 to 40 km.

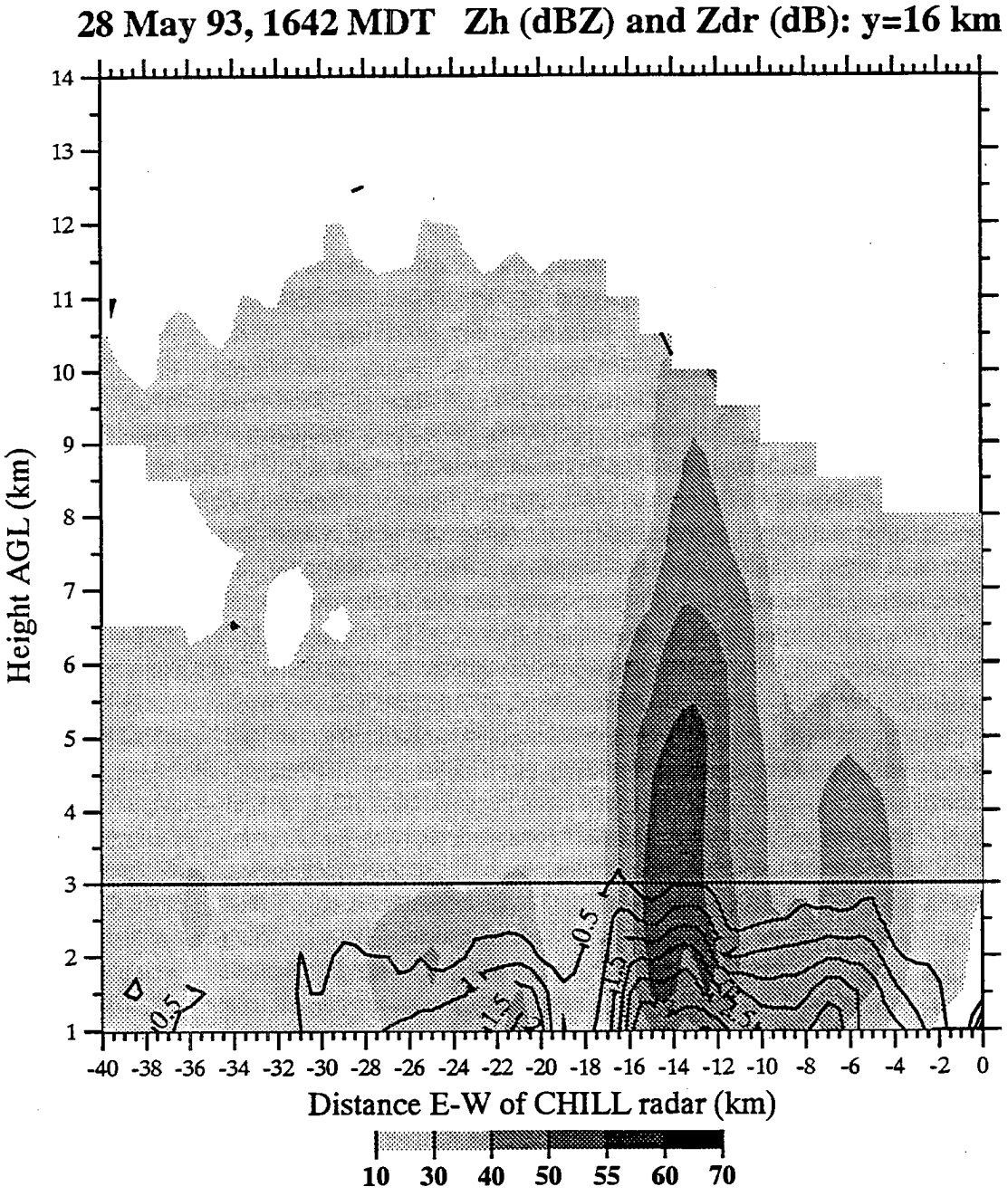

Fig. 6.12 Vertical cross-sections at 1642 MDT along y = 16 km (with the wet bulb freezing level depicted as a solid line at y = 3 km AGL) of reflectivity (dBZ) and contours of a) differential reflectivity (every 0.5 dB beginning at 0.5 dB);

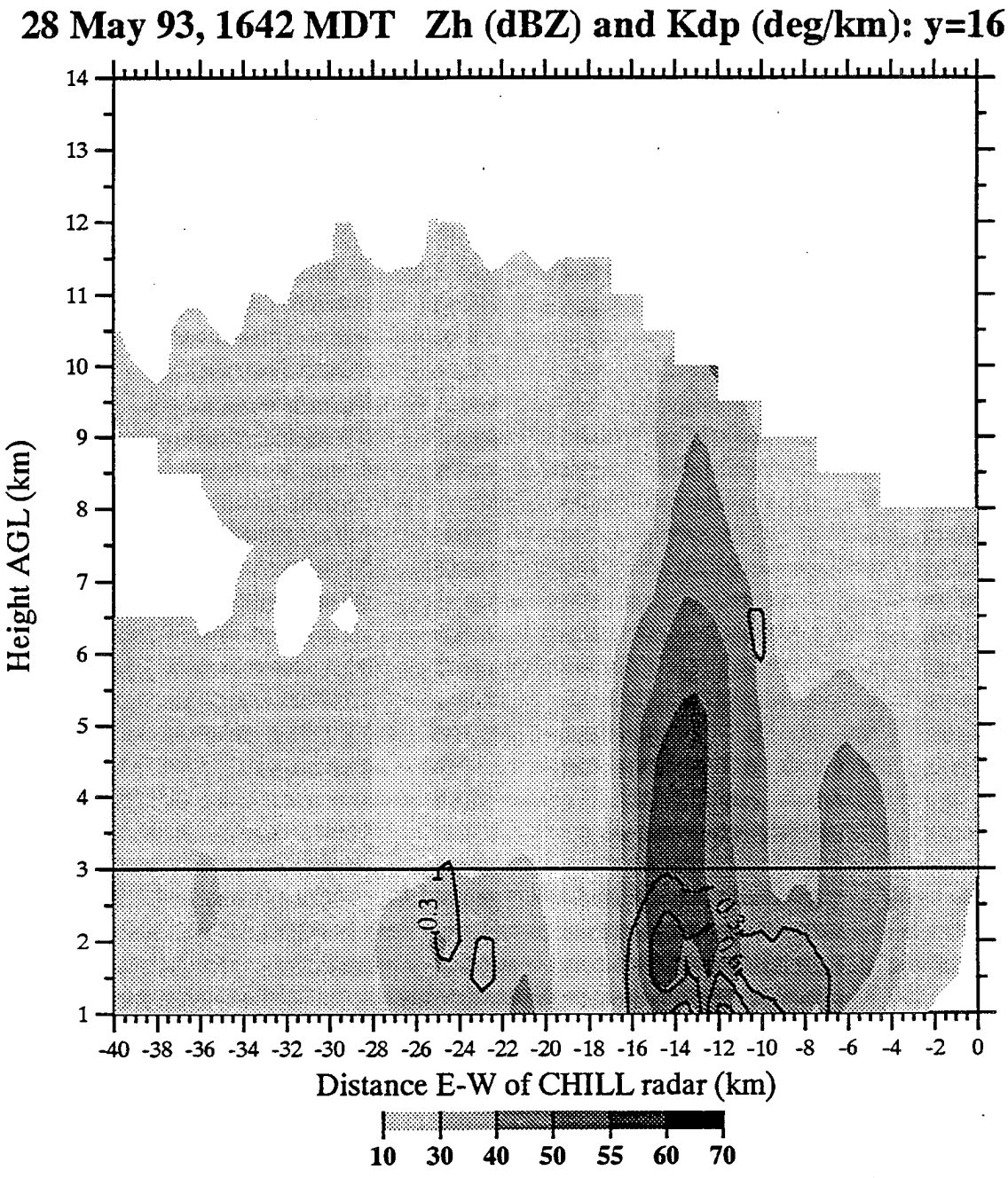

Fig. 6.12 b) specific differential phase (every 0.3 ° km^{-1} beginning at 0.3 ° km^{-1});

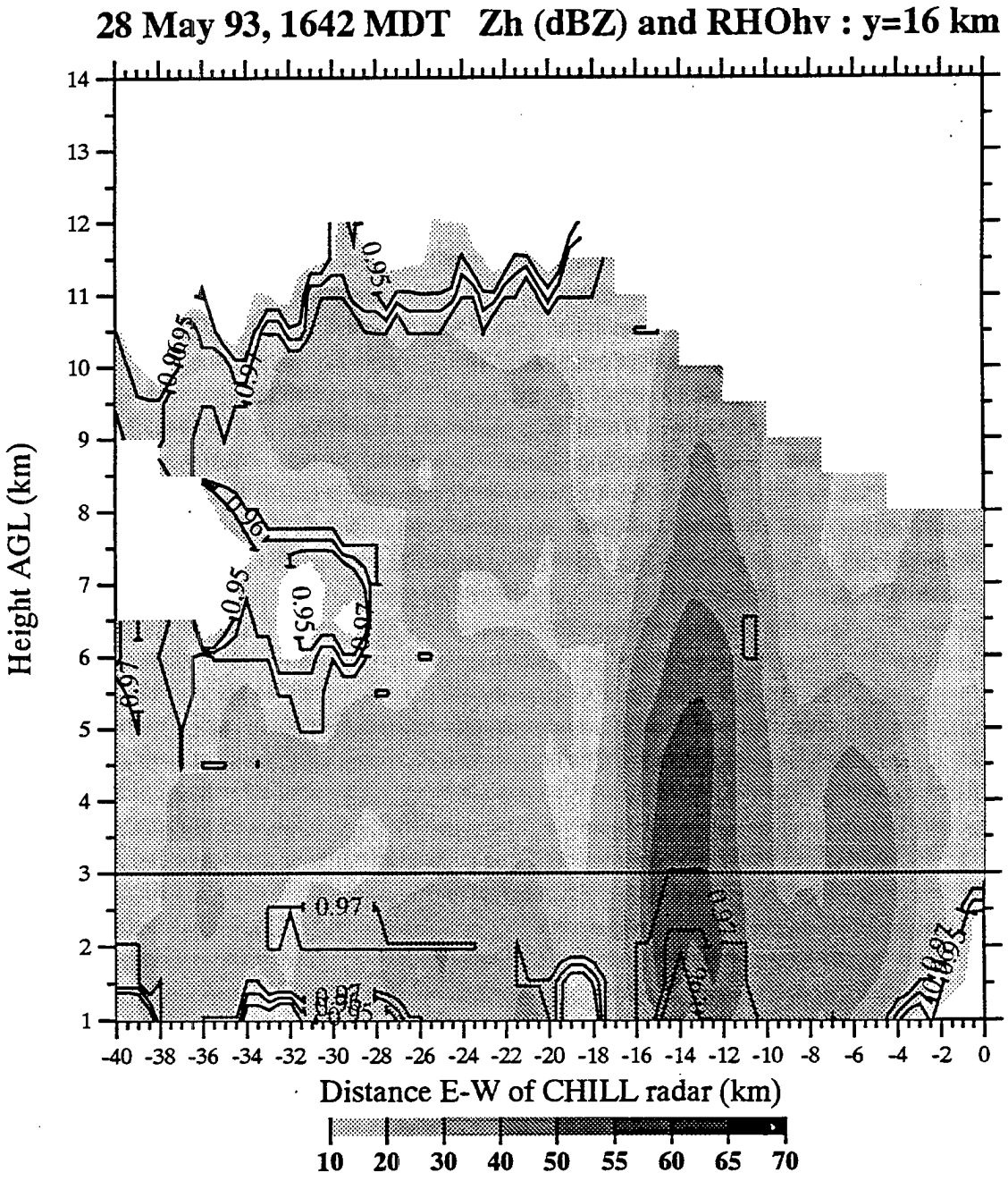

Fig. 6.12 c) and correlation coefficient (every 0.01 for values $\leq$ 0.97).

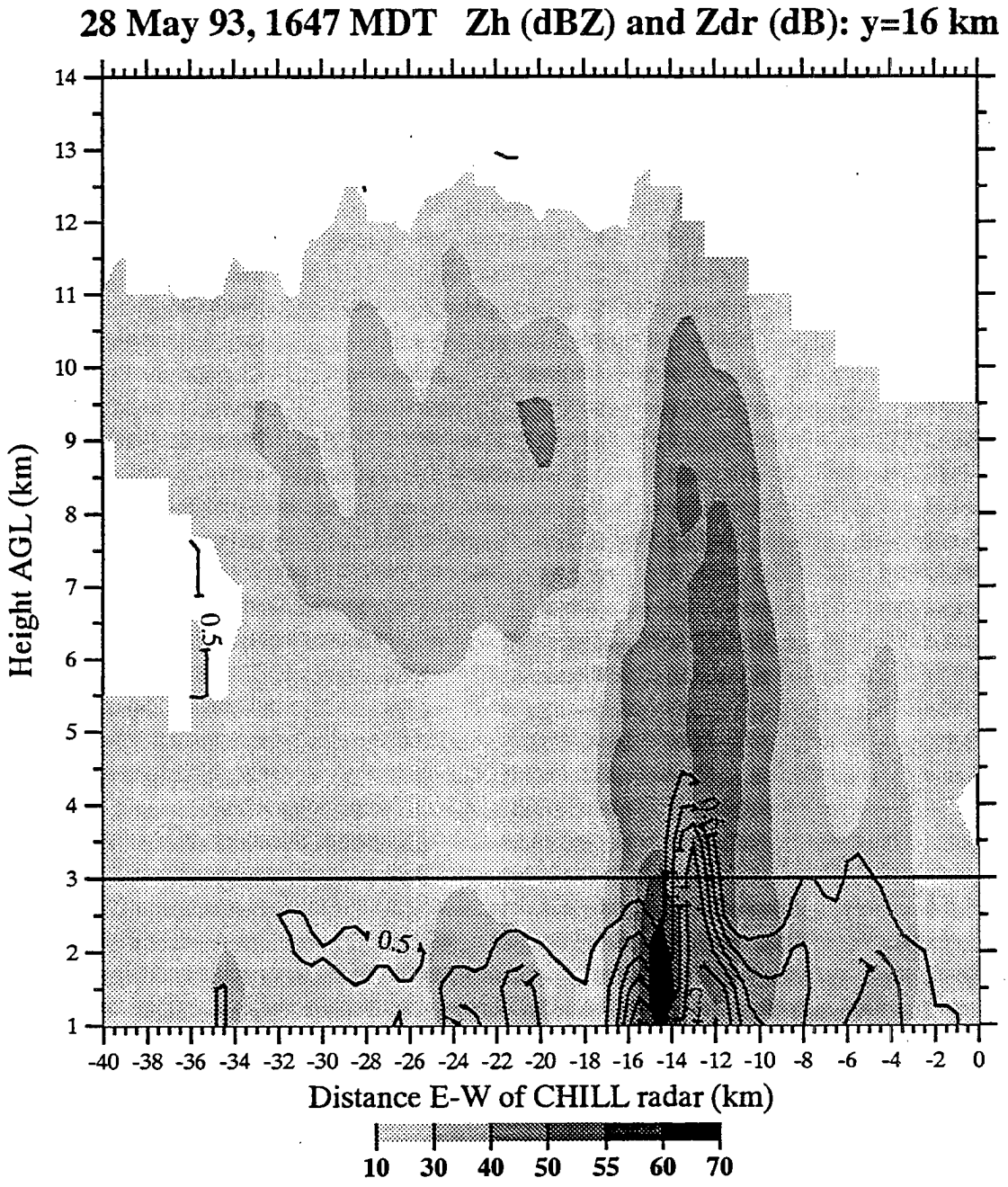

Fig. 6.13 Vertical cross-sections at 1647 MDT along y = 16 km (with the wet bulb freezing level depicted as a solid line at y = 3 km AGL) of reflectivity (dBZ) and contours of a) differential reflectivity (every 0.5 dB beginning with 0.5 dB);

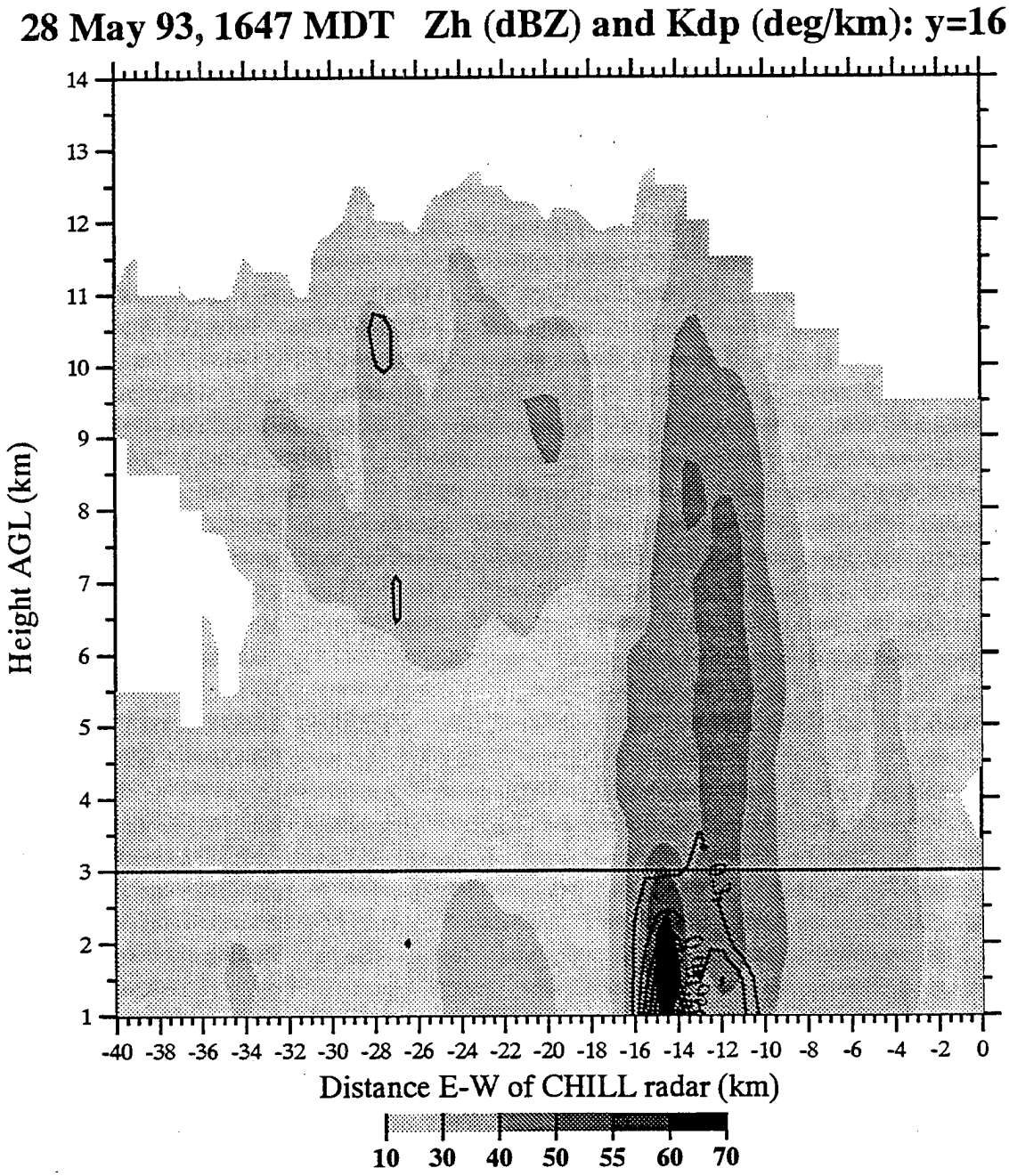

Fig. 6.13 b) specific differential phase (every 0.3° km^{-1} beginning with 0.3° km^{-1});

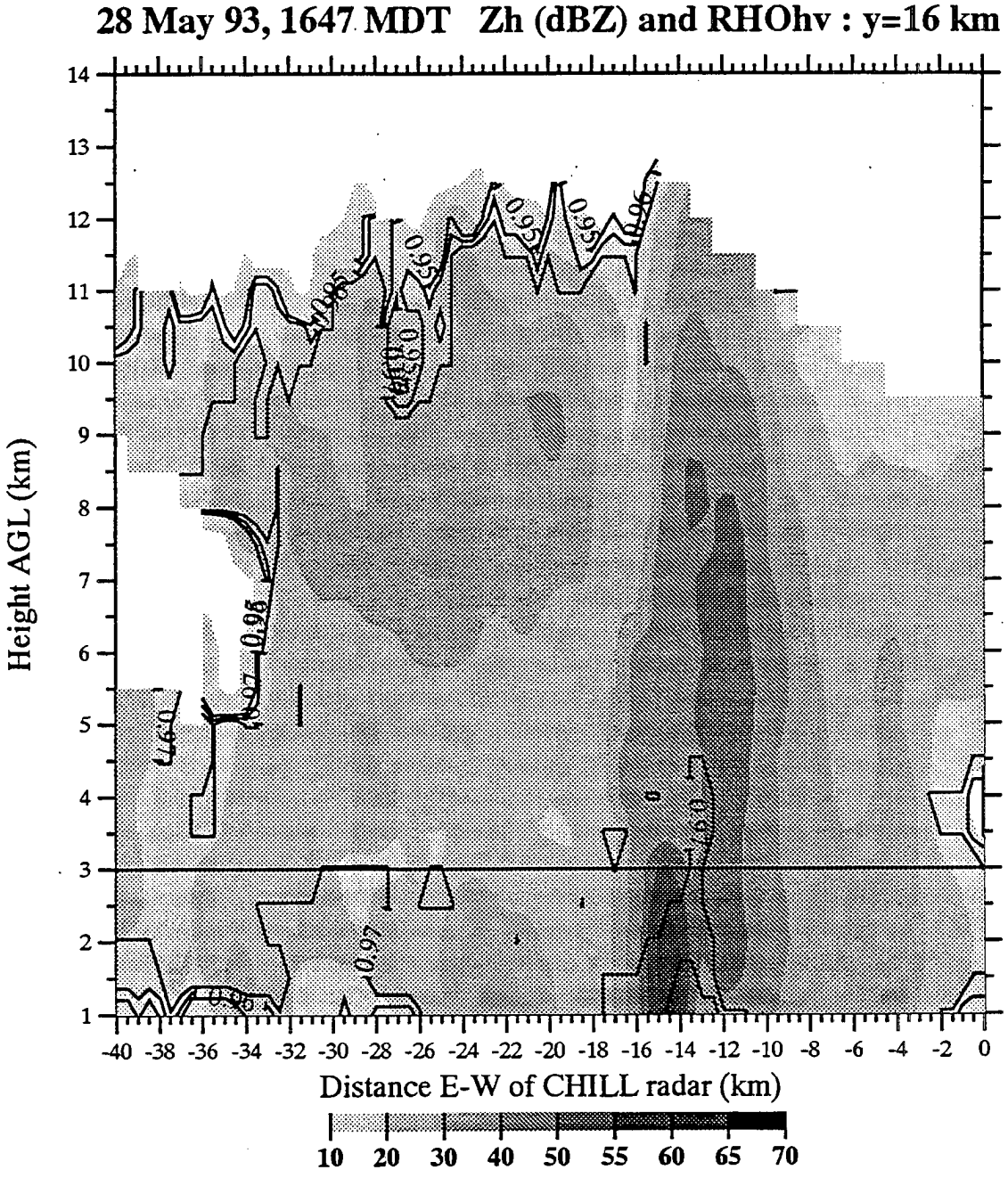

Fig. 6.13 c) and correlation coefficient (every 0.01 for values ≤ 0.97).

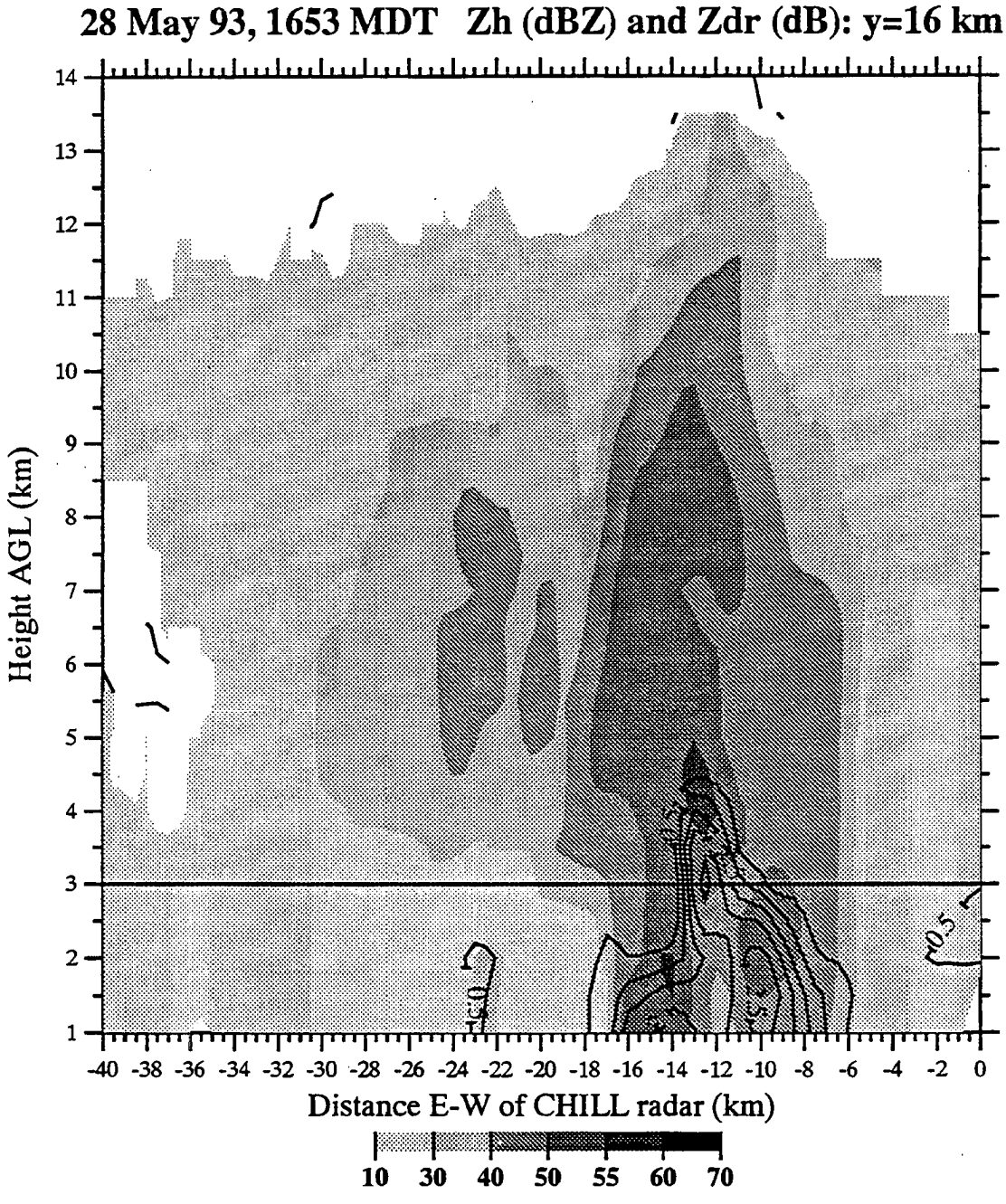

Fig. 6.14 Vertical cross-section at 1653 MDT along y = 16 km (with the wet bulb freezing level depicted as a solid line at y = 3 km AGL) of reflectivity (dBZ) and contours of a) differential reflectivity (every 0.5 dB beginning with 0.5 dB);

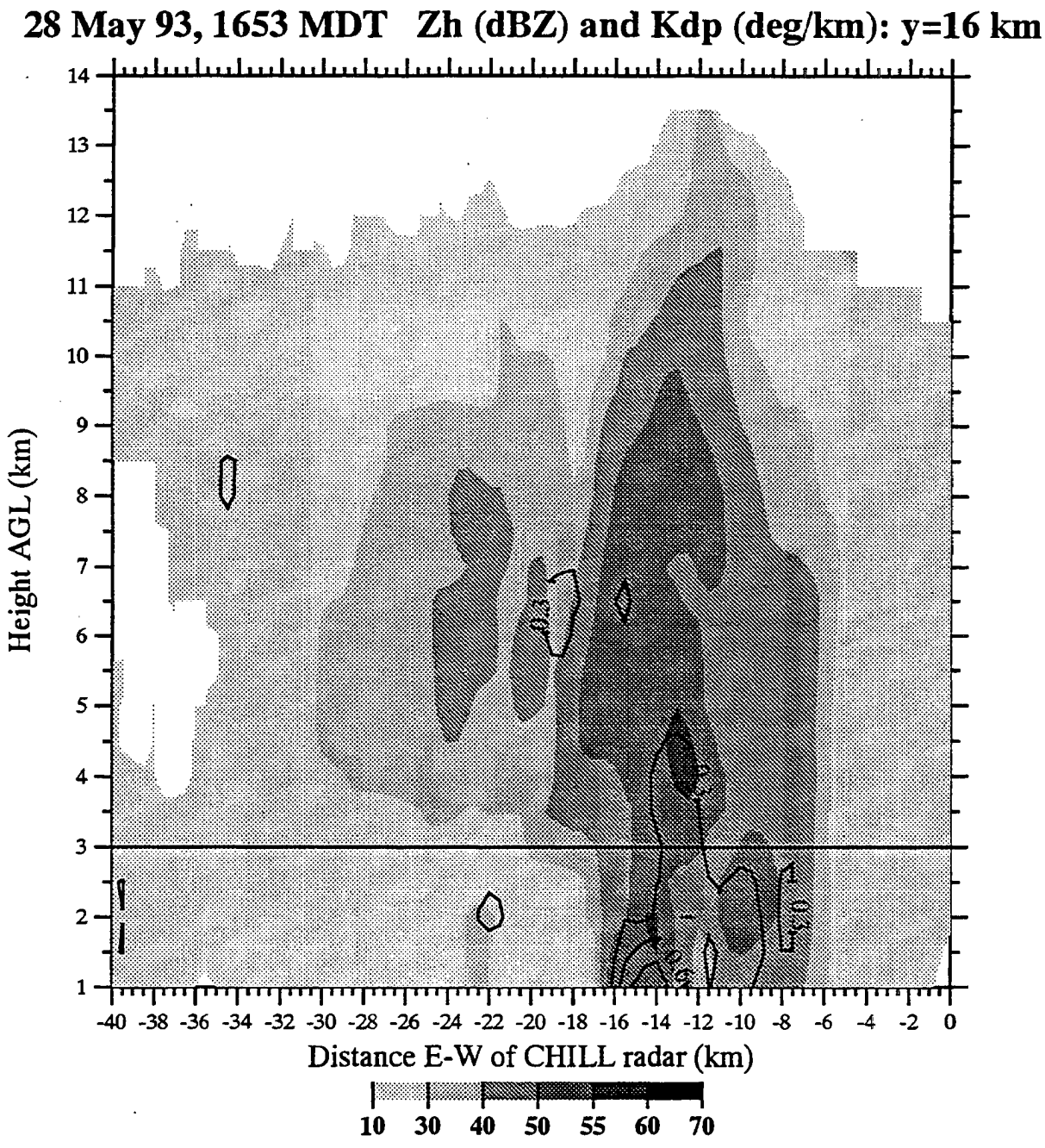

Fig. 6.14 b) specific differential phase (every 0.3 ° km^{-1} beginning with 0.3 ° km^{-1});

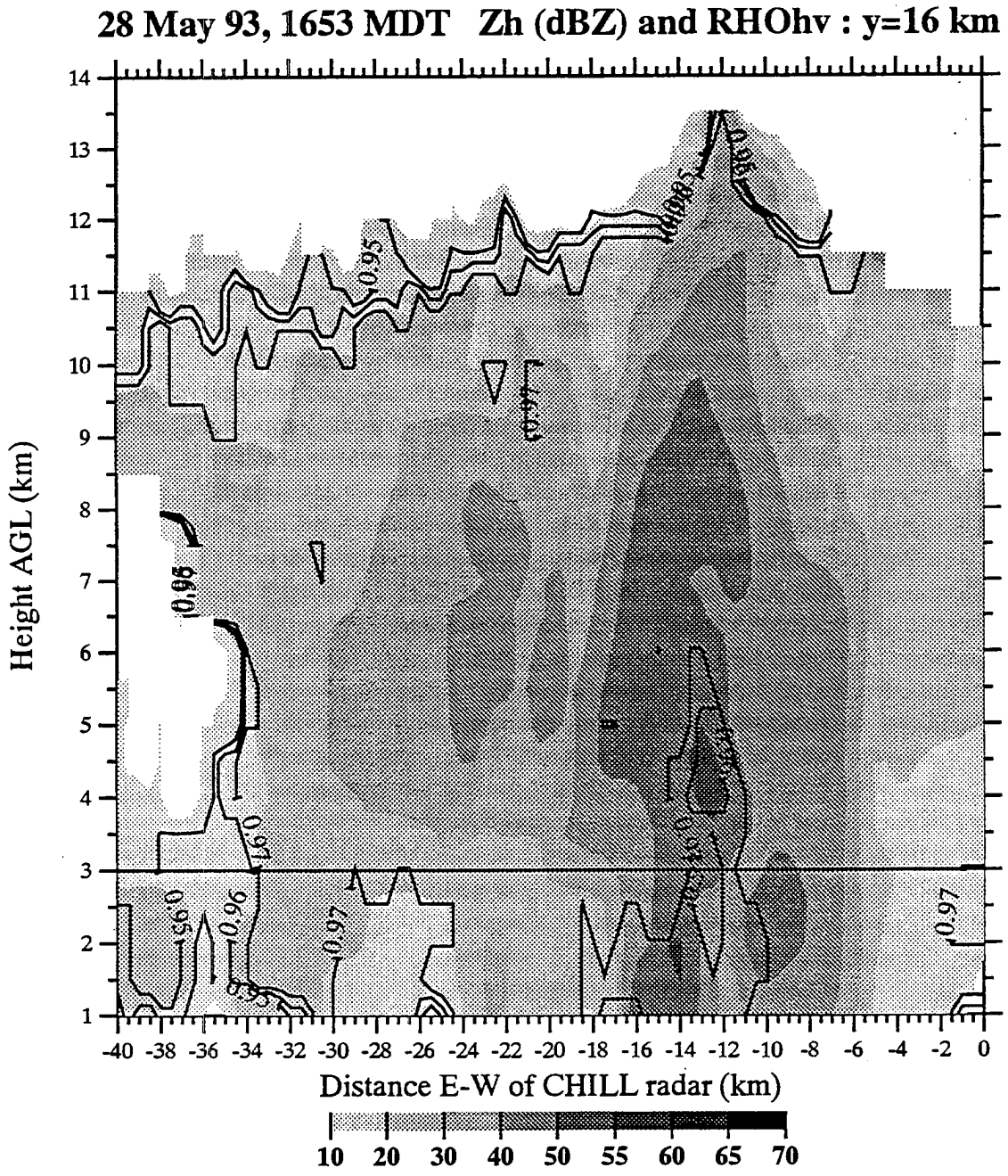

Fig. 6.14 c) and correlation coefficient (every 0.01 for values ≤ 0.97).

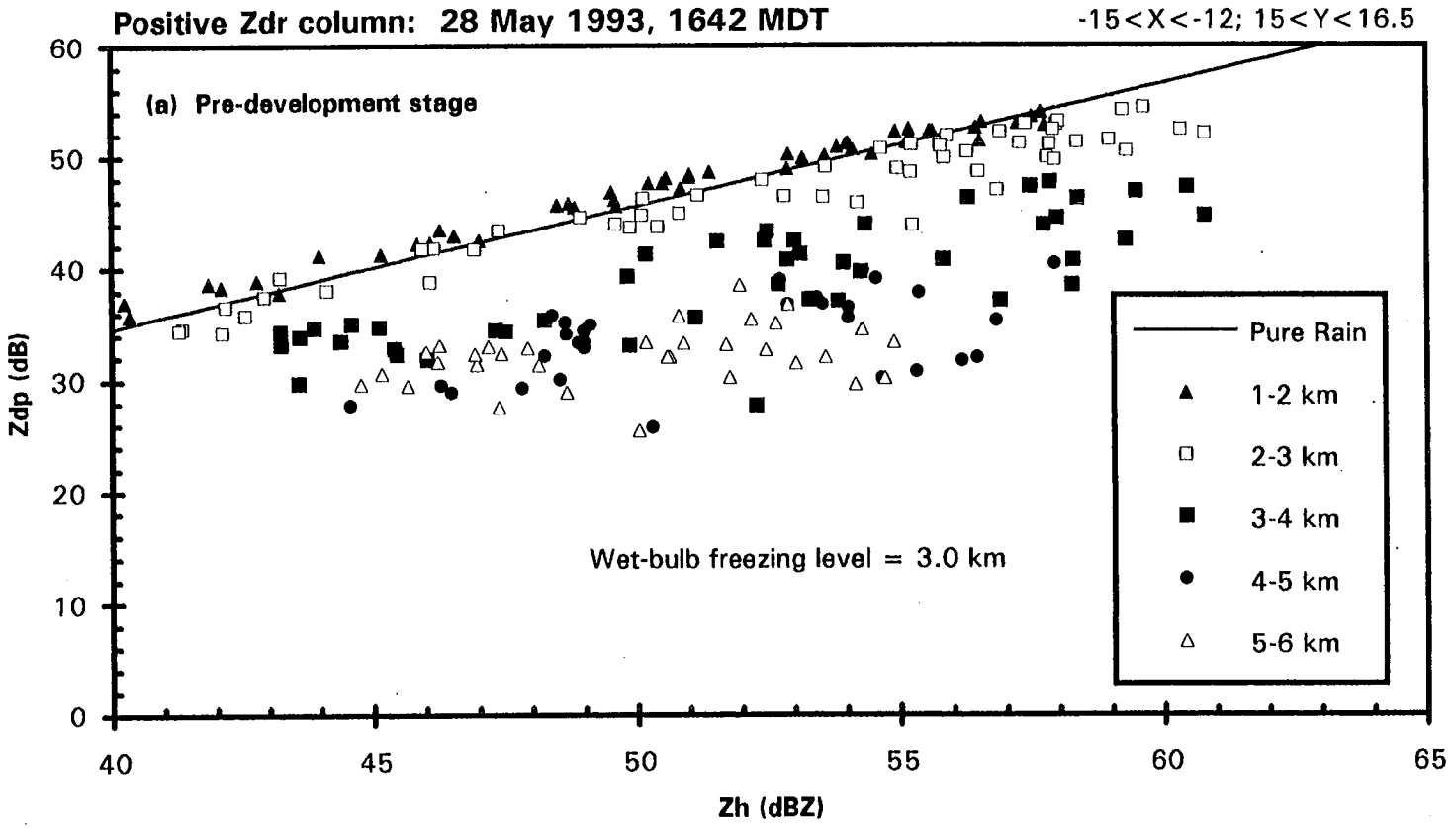

Fig. 6.15 Plot of Z_{dp} (dB) versus Z_h (dBZ) depicting the conditions in the positive Z_{dr} column. a) Results at 1642 MDT.

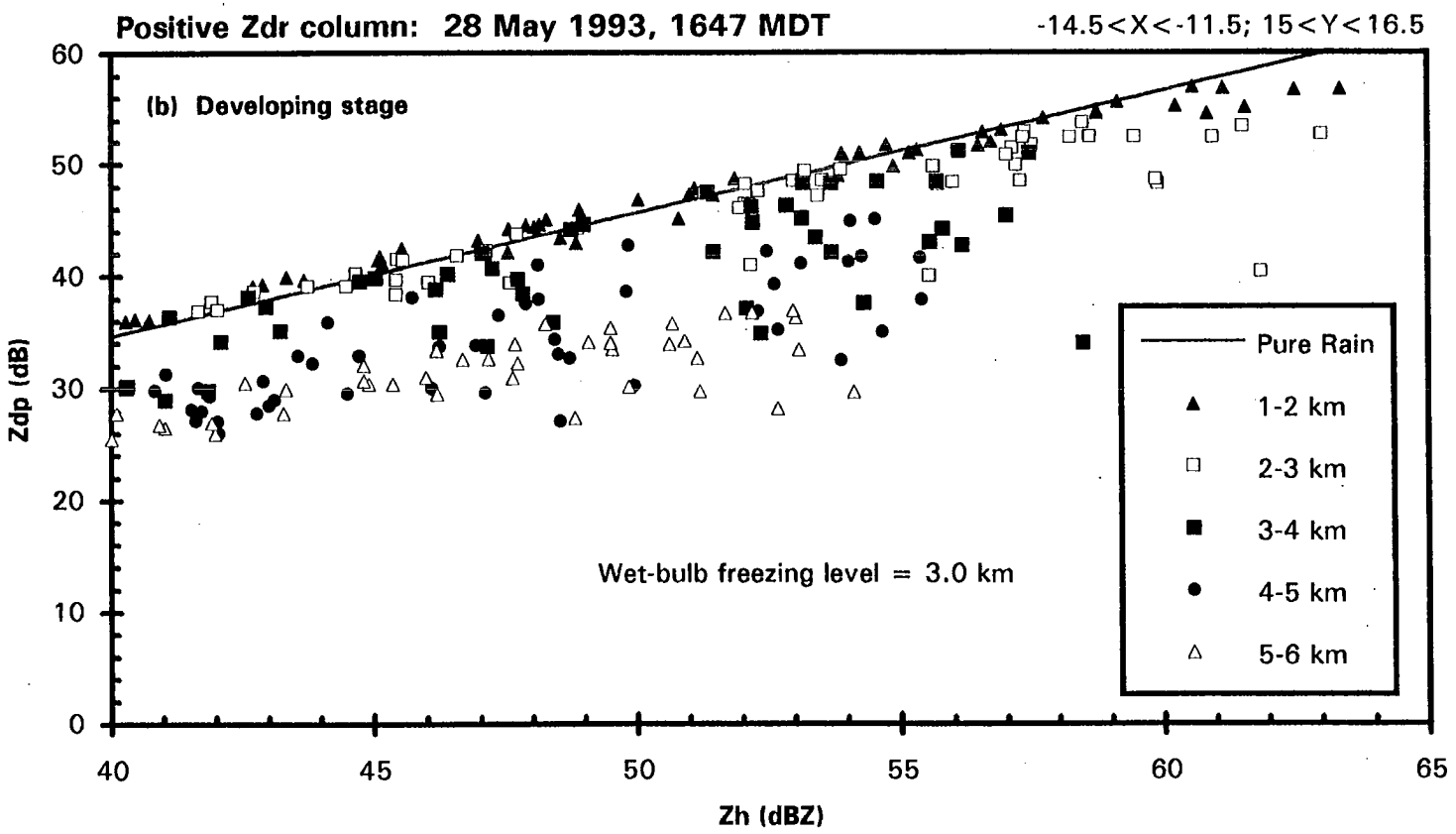

Fig. 6.15 b) Results at 1647 MDT.

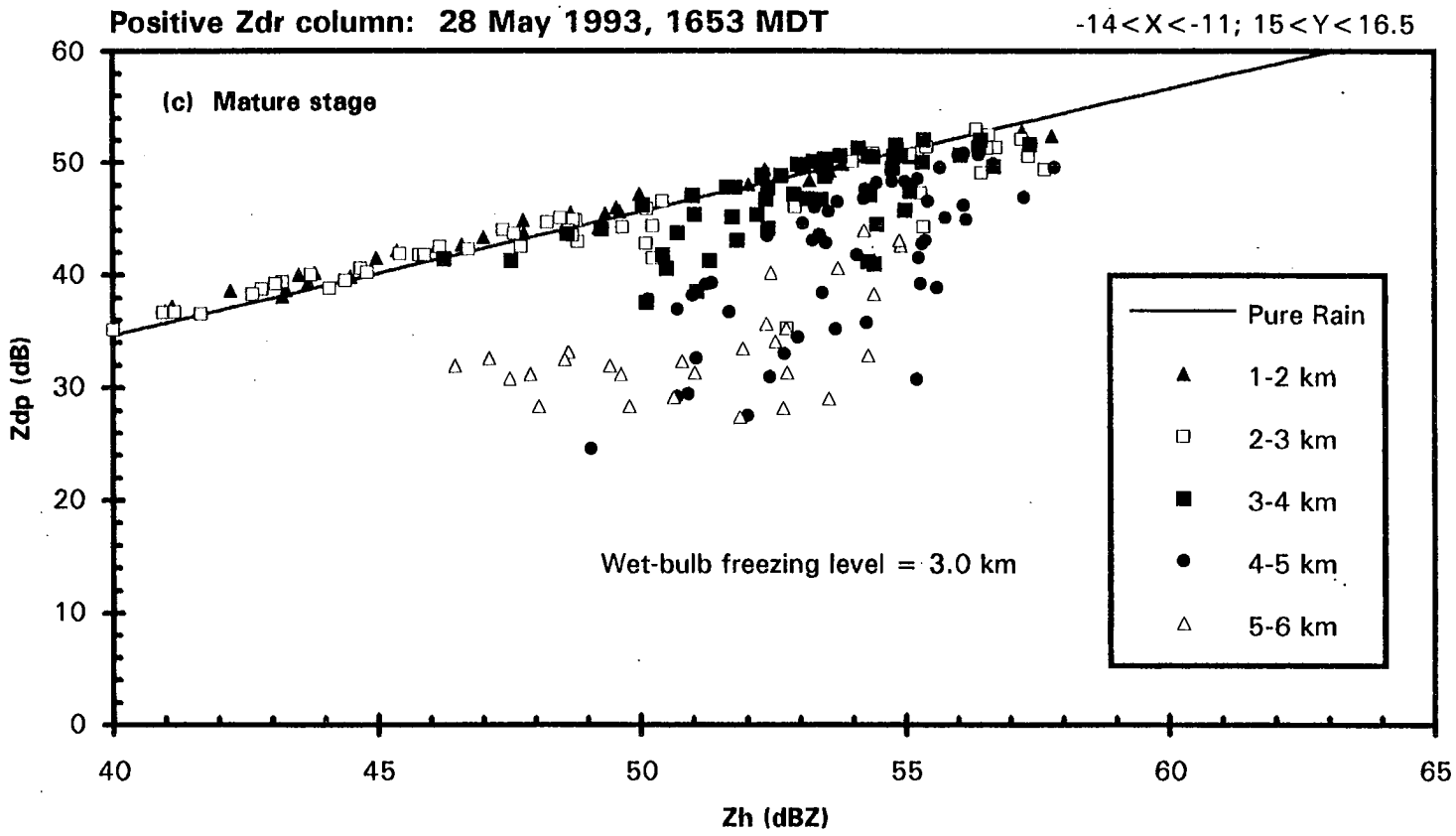

Fig. 6.15 c) Results at 1653 MDT.

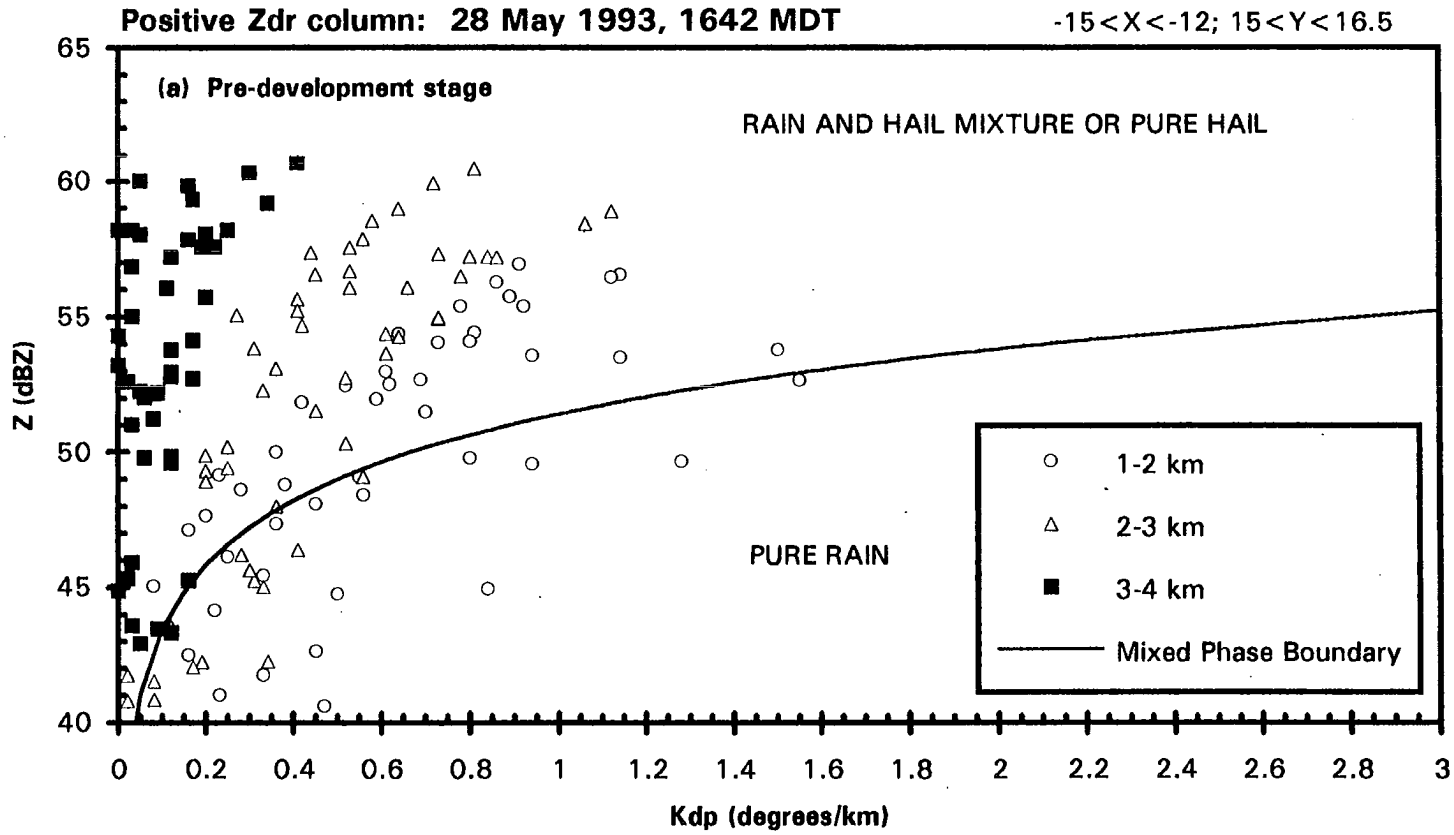

Fig. 6.16 Plot of Z_h (dBZ) versus K_{dp} (° km^{-1}) depicting the conditions in the positive Z_{dr} column. a.) Results at 1642 MDT.

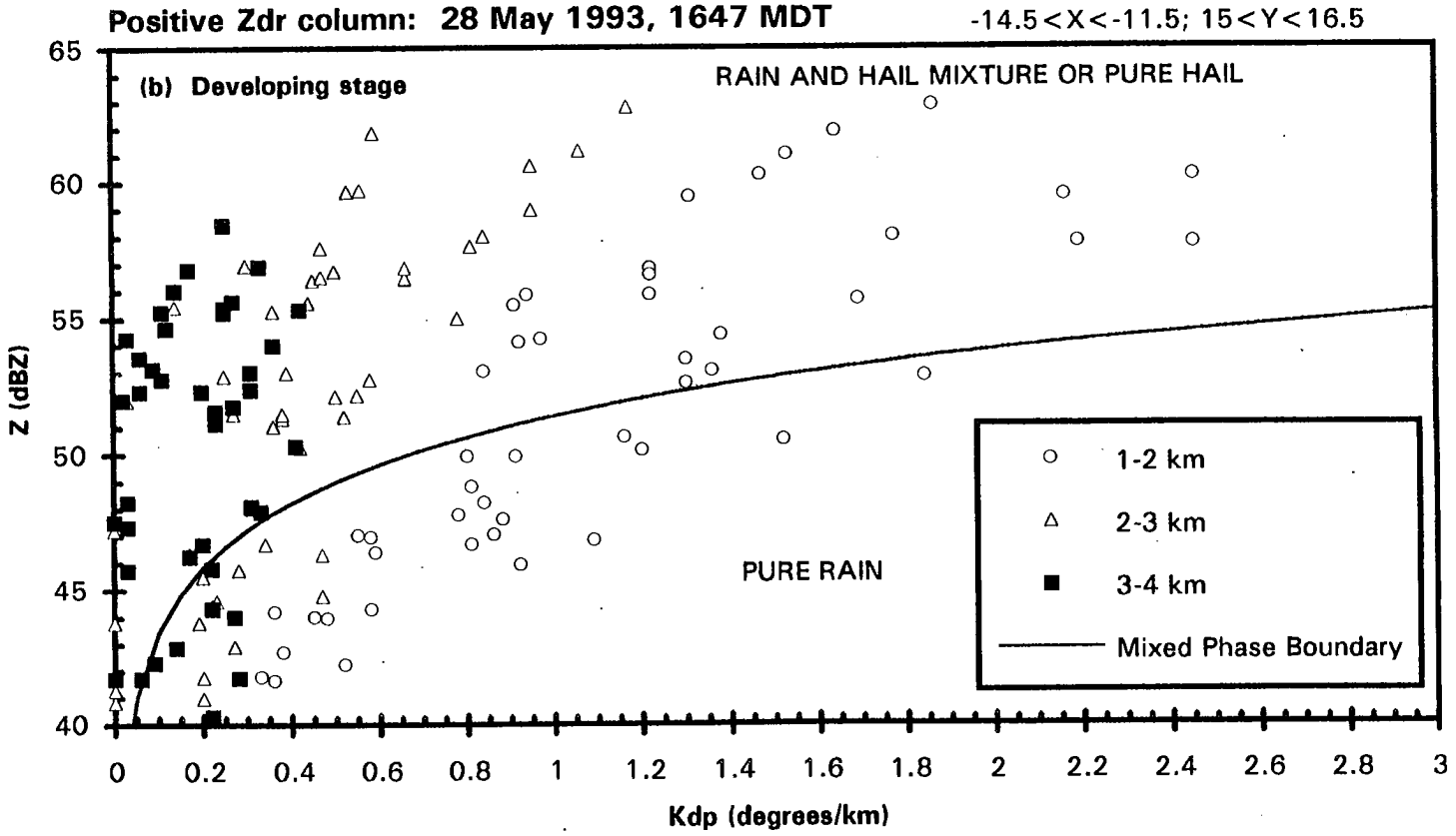

Fig. 6.16 b) Results at 1647 MDT.

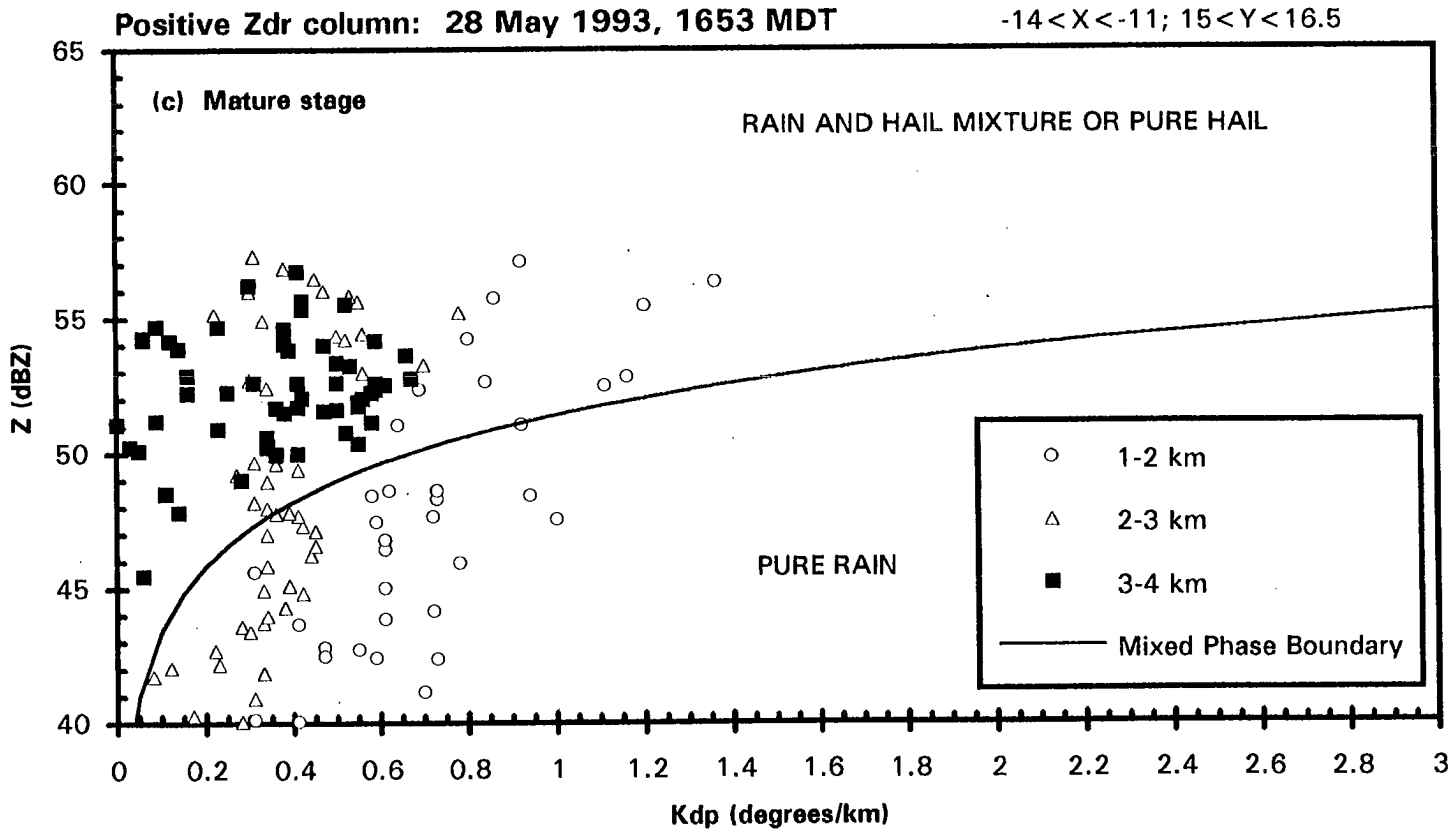

Fig. 6.16 c) Results at 1653 MDT.

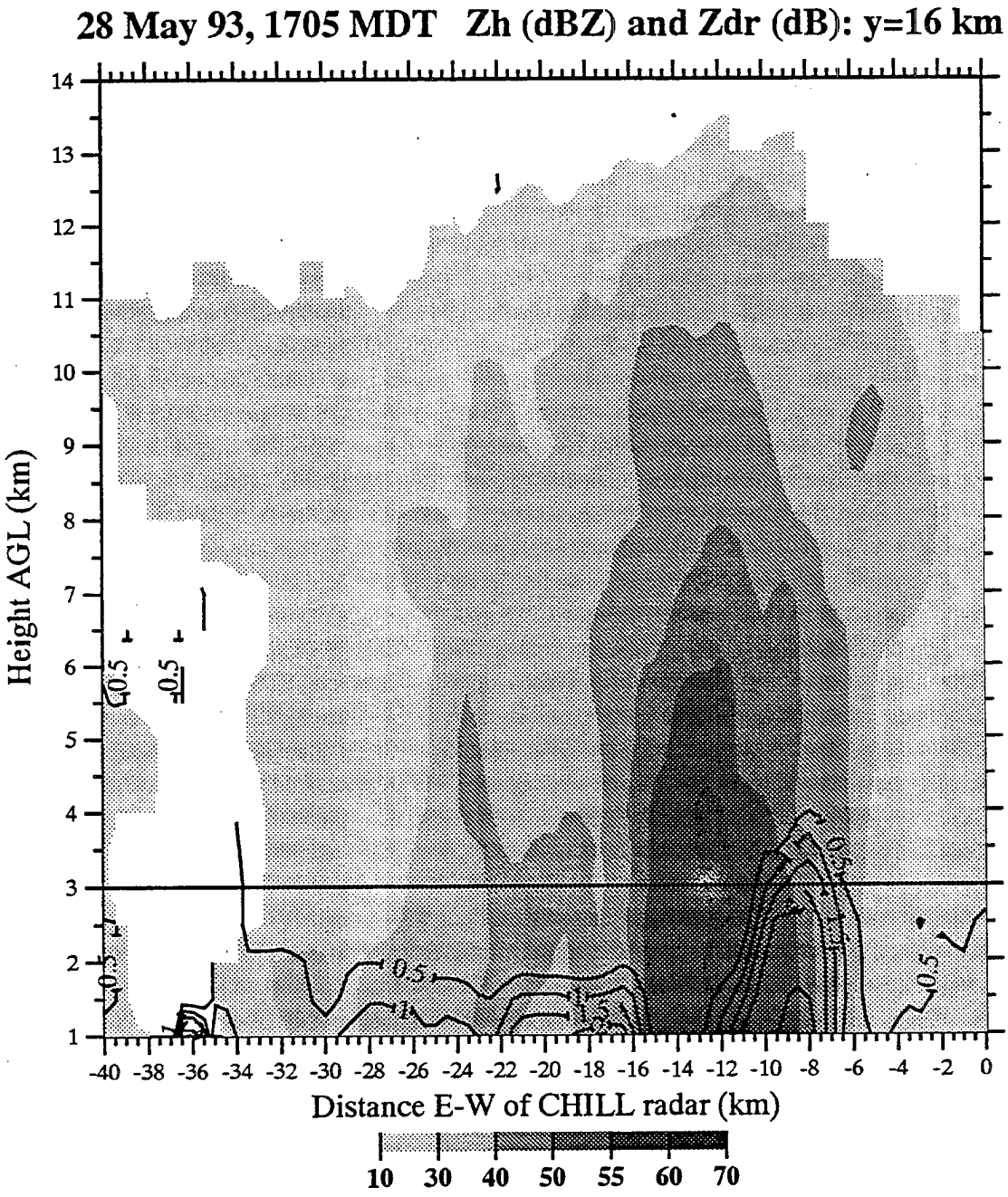

Fig. 6.17 Vertical cross-section of reflectivity (dBZ) and differential reflectivity (dB) along y = 16 km at 1705 MDT, depicting a hail shaft.

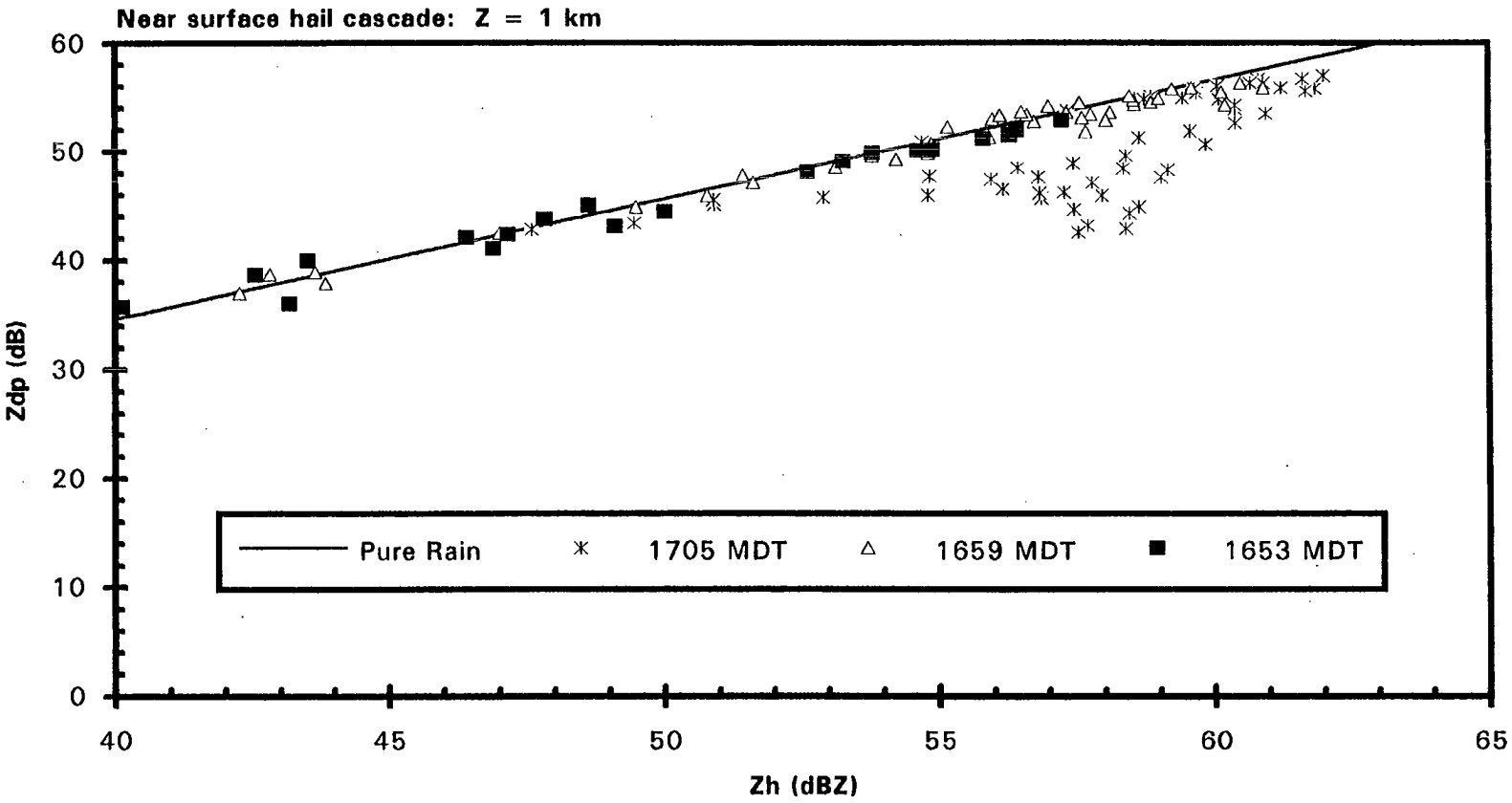

Fig. 6.18 Plot of Z_{dp} (dB) versus Z_h (dBZ) depicting the conditions in a hail shaft immediately to the west of a positive Z_{dr} column at 1 km AGL from 1653 to 1705 MDT.

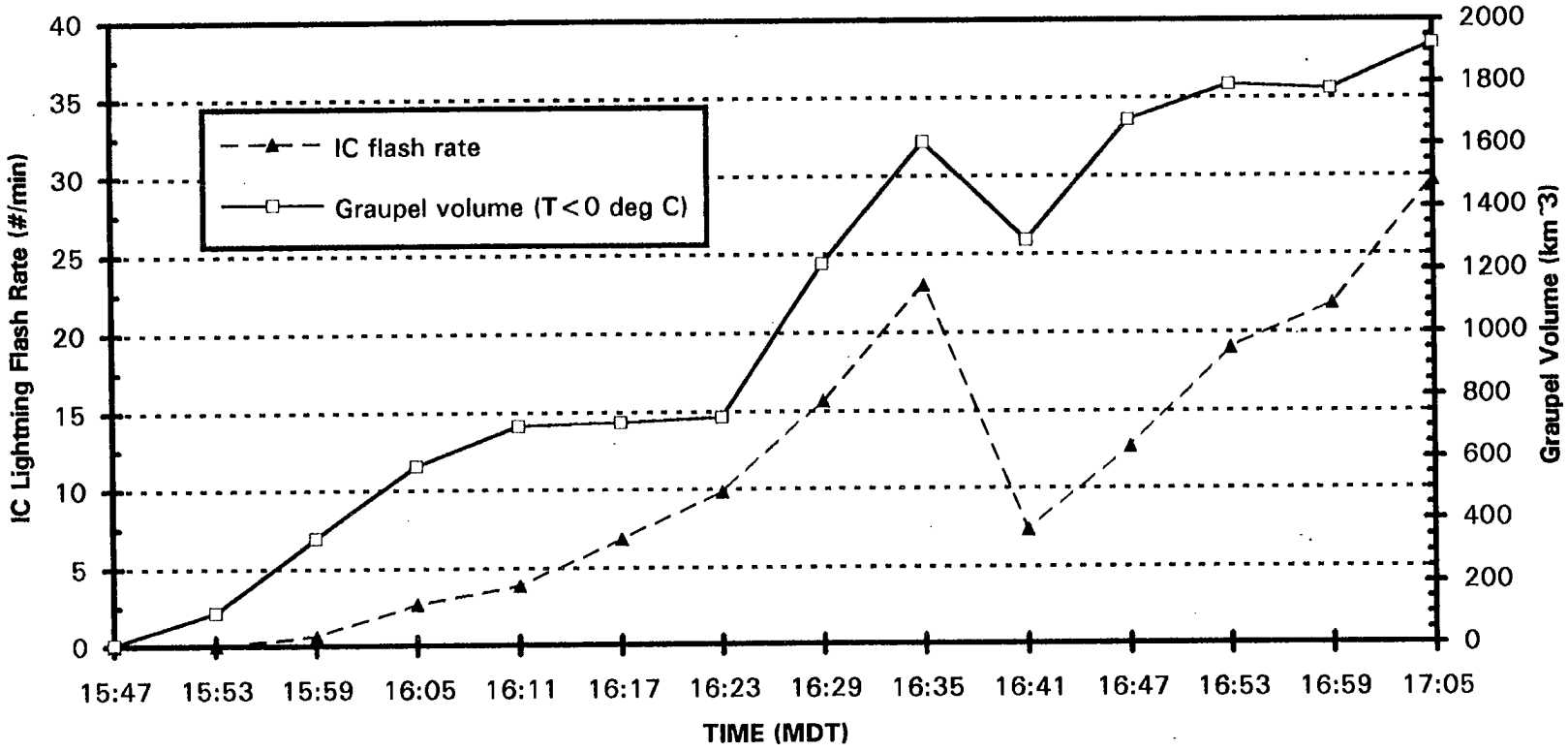

Fig. 6.19 Evolution of the in-cloud lightning flash rate (min^{-1}) and graupel volume (km^3) above the melting level during squall line development from 1547 to 1705 MDT.

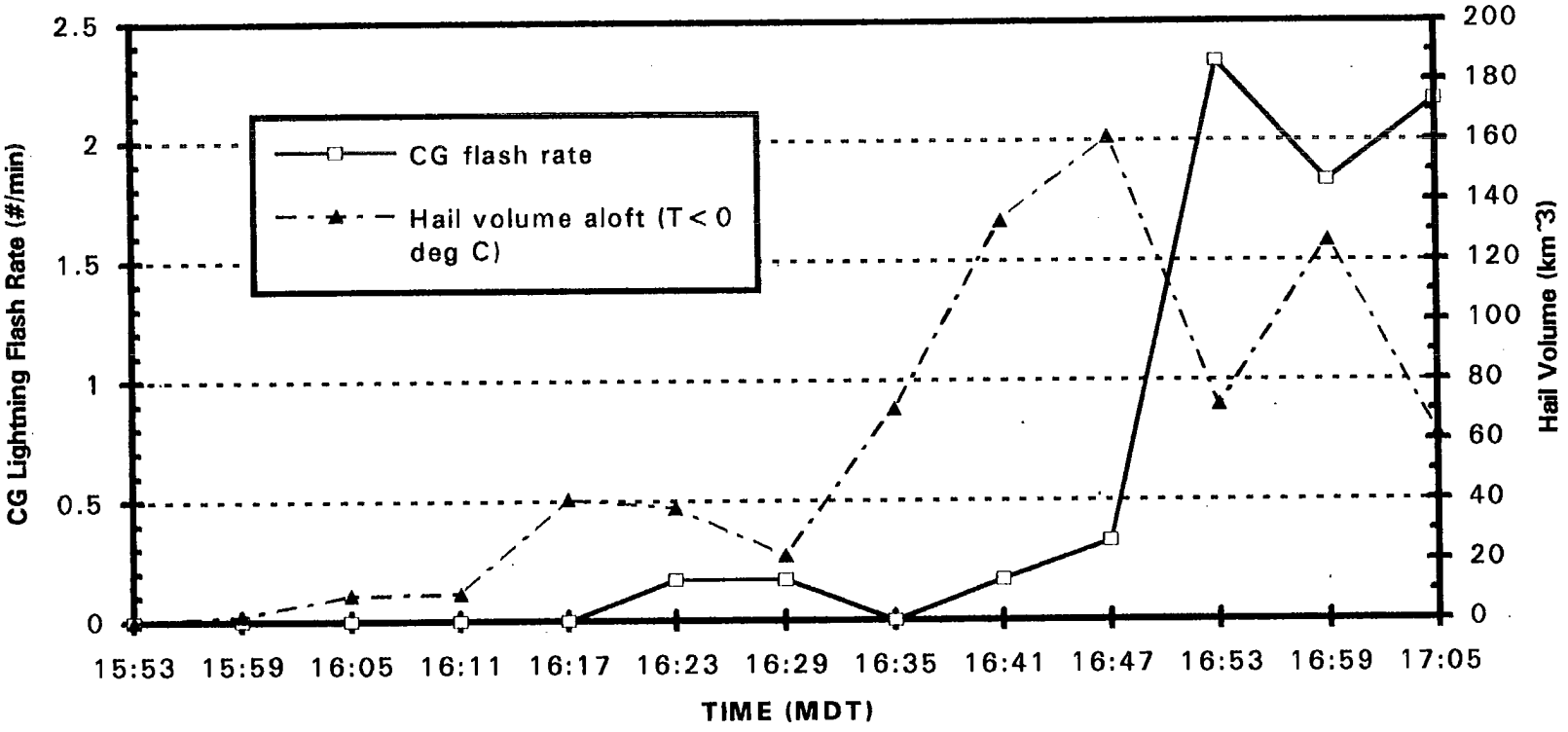

Fig. 6.20 Evolution of the cloud-to-ground lightning flash rate (min^{-1}) and hail volume (km^3) above the melting level during squall line development from 1547 to 1705 MDT.

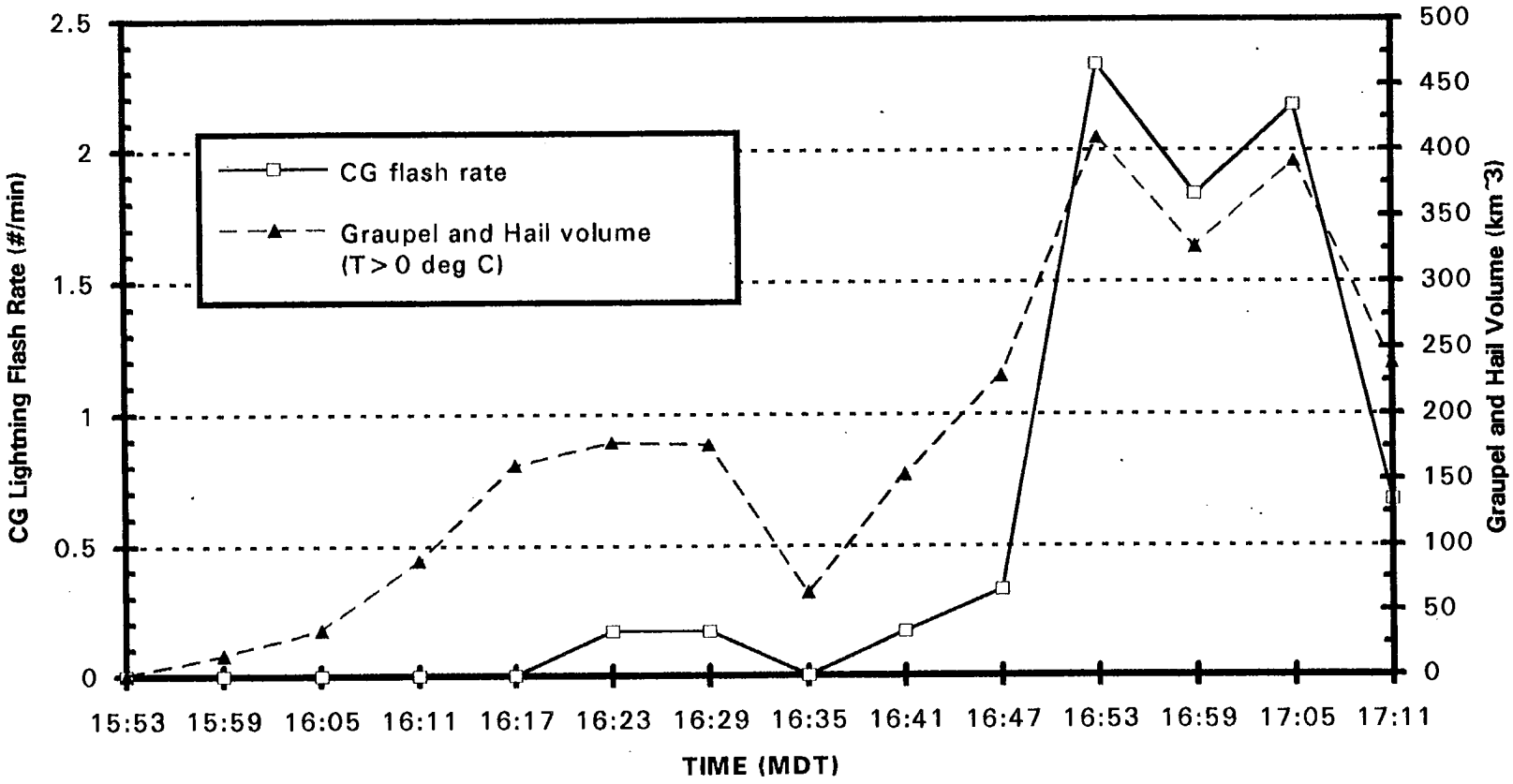

Fig. 6.21 Evolution of the cloud-to-ground lightning flash rate (min^{-1}) and graupel and hail volume (km^3) below the melting level during squall line development from 1553 to 1711 MDT.

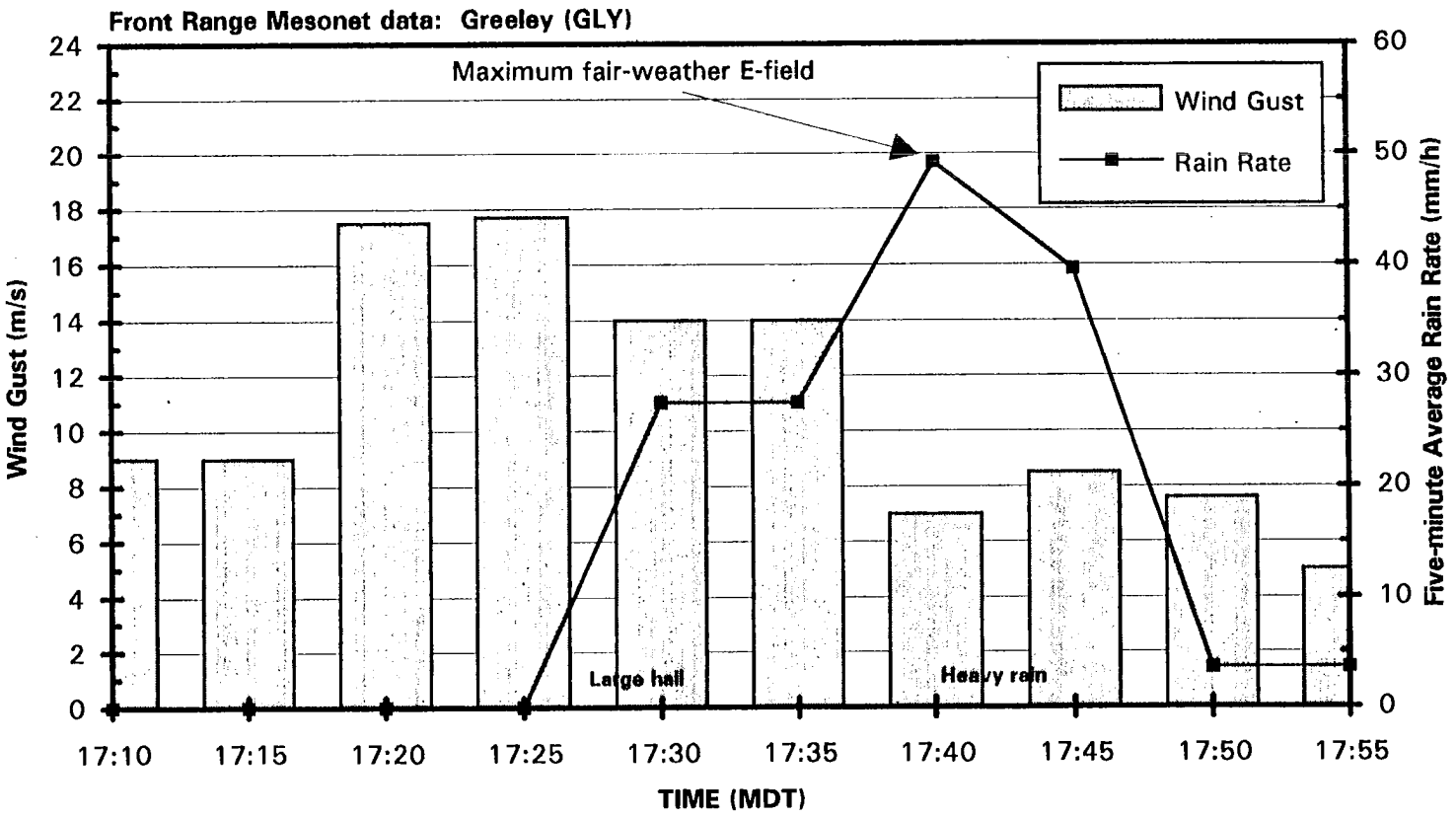

Fig. 6.22 Temporal evolution of wind gust (m s^{-1}) and rain rate (mm h^{-1}) as measured by the Greeley mesonet observation station from 1710 to 1755 MDT. Large hail was reported at the CSU-CHILL radar at 1729 MDT and heavy rain at the CSU-CHILL radar at 1743 MDT.

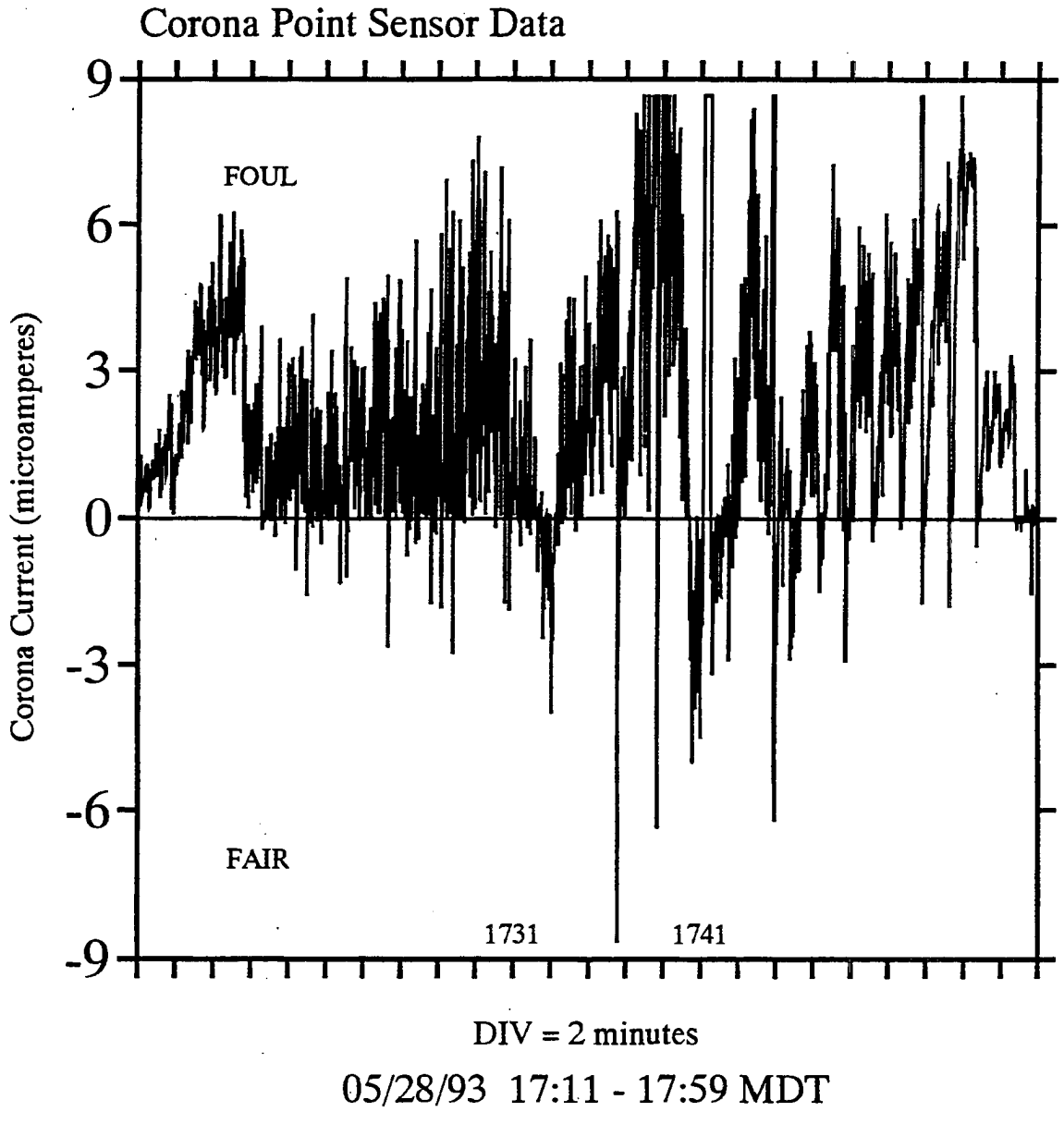

Fig. 6.23 Temporal evolution of corona point current (μA) from 1711 to 1759 MDT. Horizontal axis divisions are two minutes. Positive values of corona current are indicative of a foul-weather E-field (predominant negative charge) aloft. Negative values of corona current are indicative of a fair-weather E-field (predominant positive charge) aloft.

CHAPTER 7

CONCLUSIONS AND RECOMMENDATIONS FOR FUTURE RESEARCH

7.1 Further evidence for the role of ice in thunderstorm electrification

We have examined the integrated kinematic, microphysical, and electrical evolution of a multi-cell storm and a squall line which occurred along the Front Range of Colorado. Dual-Doppler data was collected during the initial development of each storm through synchronous operation between the CSU-CHILL and NCAR Mile High radars. Electrification and lightning data were collected with a flat plate antenna and corona point sensor co-located at the CSU-CHILL site and a network of three magnetic direction finders. The resultant data were used to correlate the lightning type and frequency, and electrostatic field strength and polarity to the evolution of storm kinematics (based on single- and dual-Doppler analyses) and cloud microphysical properties (as inferred from CSU-CHILL multiparameter variables). Emphasis was placed on utilizing recent advances in radar polarimetry to identify and quantify the ice-phase precipitation processes relevant to the precipitation theory of thunderstorm electrification.

For the multi-cell storm on 21 May 1993, we found that the fate of ice particles in the storm was well correlated to both electrical and kinematic events. We began by demonstrating that there were sufficient upward vertical velocities in the storm to support the riming growth of graupel particles and small hail. Multiparameter radar observables were used to suggest the presence of hail in the developing storm. We then offered evidence that the accumulation of graupel and hail particles suspended by vigorous updrafts in the upper-portion of the storm was highly correlated to the IC flash rate. This

was accomplished by comparing the evolution of the graupel storm volume as inferred from a four-dimensional partitioning of the multiparameter radar data to the IC flash rate. Both parameters grew exponentially during initial storm development, reached a quasi-steady state after attaining their respective peaks, and rapidly decayed in unison. The IC flash rate was found to slightly lag the graupel storm volume during the period of exponential storm growth. This was attributed to the required time to allow the gravitational sedimentation of larger graupel and hail particles from oppositely charged, smaller ice crystals. We supported this argument by calculating an estimate of the vertical charge separation which would occur as a result of the lag in electrical start-up. The calculated distance of 3 km is consistent with observed separation distances between positive and negative charge centers at first lightning, thus lending credence to our argument. We demonstrated that the exponential increase in the IC flash rate occurred while the graupel volume was increasing in overall magnitude and vertical extent and that the rapid decay in the IC flash rate was coincident with the descent of graupel and hail in the storm. These results are consistent with the non-inductive charging mechanism which entails collisions between graupel particles and ice crystals in the presence of supercooled water to separate charge in thunderstorms.

The action of charge reversal microphysics on descending ice has been proposed to provide the necessary electrical bias required to cause cloud-to-ground lightning (Williams et al., 1989a). As a result, we attempted to relate the presence of graupel and hail at low altitudes in the multi-cell storm to the CG flash rate. We found that maxima in the graupel volume as inferred from a four-dimensional partitioning of the multiparameter radar measurements and the hail rate as determined from Z and K_{dp} were well correlated to peaks in the CG flash rate. Three distinct maxima in the CG flash rate were coincident with peaks in the hail rate. We employed established multiparameter methods involving two-dimensional plots of K_{dp}/Z and Z_h/Z_{dp} to further confirm the presence of graupel and hail in mixed-phase precipitation during a period of peak CG lightning.

As part of this case study, we presented radar and corona point sensor observations of a field excursion associated with precipitation (FEAWP) which occurred in a cell 7 km southwest of the CSU-CHILL radar. The average precipitation rate as calculated from specific differential phase, K_{dp}, peaked simultaneously with the transition from foul- to fair-weather electrostatic field. Furthermore, the storm outflow reached its maximum at about the same time as the peak in the measured fair-weather field. From this data, it is impossible to determine whether the field transition was caused by the precipitation or some other source of charge carried by the storm drafts. On the other hand, the field excursion was also shown to be coincident with the descent of graupel and small hail below the charge reversal level. If collisions between graupel/hail and smaller ice crystals resulted in positive charge being transferred to the graupel/hail as expected from the non-inductive charging mechanism at these temperatures, then the observed field excursion may have been caused by the presence of the descending, positively charged graupel and hail. The subsequent descent of graupel and hail below the melting layer was well correlated with the observation of a microburst in the single-Doppler data and a significant increase in the wind gusts as measured by a nearby observing station.

The role of ice in driving storm outflow for the 21 May multi-cell storm was explored by comparing the evolution of hail rate at low elevations and microburst strength as estimated from the maximum differential radial velocity. We found a consistent temporal evolution beginning with peak CG flash rate, followed by a maxima in the hail rate, and concluding with a peak in storm outflow. Typically, the maximum hail rate lagged the peak CG flash rate by two to six minutes and preceded the strongest storm outflow by (at most) six minutes. The peak IC flash rate did not consistently precede the maximum CG flash rate as in previous studies of isolated convection. This discrepancy with our results for multi-cell convection was attributed to the simultaneous contribution of multiple cells to the IC flash rate at differing phases in their evolution.

Using corona point and multiparameter radar observations of the FEAWP, we presented a comparative speculation on the microphysics of the lower positive charge and the applicability of the various laboratory studies. By assuming values for the liquid water content, ice crystal concentration, and graupel size and terminal velocity appropriate for deep convection, we estimated the non-inductive charging time scale. Assuming that graupel particles falling in a weak updraft through the level of the charge reversal temperature charge positively during collisions with ice crystals (as suggested by laboratory studies), the excursion of the corona point sensor to negative values (i.e., predominately positive charge aloft) should lag the descent of the graupel mass below the level of the inferred charge reversal temperature by the estimated non-inductive charging time scale. Using this premise, we inferred a range for the charge reversal temperature within the 21 May 1993 multi-cell storm of $-17° C \leq T \leq -10° C$. This range is in close agreement with measured charge reversal temperatures in New Mexico storms, which are climatologically similar to Colorado storms. This temperature range is also consistent with the laboratory results of Takahashi (1978) and those of Saunders et al. (1991) for graupel collection efficiencies between 0.5 and 0.6.

In the second case study (28 May 1993), we investigated correlations between the radar inferred kinematic and microphysical evolution of a developing severe squall line and the evolution of lightning type and frequency. First, we showed that the atmospheric conditions in which the storm formed along the Front Range of Colorado were favorable for the development of a slow-moving, potentially severe squall line. We then presented an overview of the squall line formation process as seen in the evolution of radar reflectivity and radial velocity data and related this process to the aforementioned environmental conditions. In the context of this data, we suggested that merging outflow boundaries from previously decayed convection over the foothills were responsible for forming the convergence zone along which the broken-areal squall line developed. Next

we presented observations of positive differential reflectivity (Z_{dr}) columns above the freezing level within the low level convergence zone of the developing squall line.

We then analyzed the kinematic and microphysical evolution of these columns in detail. Using multiparameter radar data, we inferred the presence of mixed phase precipitation, or a mixture of supercooled rain drops and wet ice, which is suspended above the freezing level in the low level updraft forced by the convergence zone. Given the observed radar data, we argued that the source of these large supercooled drops is primarily the result of the recycling of melted graupel into the vigorous low-level updraft. Unique observations of a local minimum in the correlation coefficient collocated with a maximum in the reflectivity and specific differential phase at the top of the positive Z_{dr} column were presented. Based on these observations, we suggested that this region was a water-rich interface zone consisting of supercooled drops, wet frozen drops, and rapidly growing hail. Evidence of abundant hail precipitating out of the adjacent downdraft within six to twelve minutes of initial formation of this feature were presented to support this hypothesis.

We presented correlations between the in-cloud flash rate and the production of graupel and hail aloft in the 28 May squall line. The volume of ice aloft was determined to be well correlated to the IC flash rate as is expected if non-inductive charging is the dominant mechanism leading to thunderstorm electrification. Similarly, excellent correlations between the descent of this graupel and hail mass and the CG flash rate were found. We provided evidence to suggest that the rapid increase in both the IC and CG flash rates associated with explosive development of the squall line was partially related to the presence of positive Z_{dr} columns. Three mechanisms were proposed that could link the enhancement of the observed flash rates to the emergence of the positive Z_{dr} columns: 1) their prodigious hail producing ability, 2) the increase in the CAPE and hence the updraft velocity caused by latent heat release associated with the freezing of drops within the columns, and 3) favorable conditions for ice multiplication processes such as the

shattering of freezing drops and the Hallett-Mossop process. Lastly, observations of a FEAWP over the radar site were compared to the wind and rain measurements of a nearby mesonet station. Negative excursions in the corona point sensor data (indicating positive charge overhead) were shown to be coincident with periods of moderate to heavy rainfall, consistent with the role of positively charged precipitation particles in producing these electric field reversals.

By utilizing recent multiparameter radar methods to remotely infer precipitation type and amount in convective storms, we have provided further evidence for the role of ice in thunderstorm electrification. Previous electrification studies which relied on conventional radar (no polarization diversity) demonstrated that the lightning and electric fields produced by convective storms are correlated to the development of precipitation aloft. Many of these radar studies speculated that this correlation is the result of the non-inductive charging mechanism which relies on the collision of graupel/hail particles with ice crystals in the presence of supercooled liquid water. To support this hypothesis with data from two detailed case studies, we proposed a four-dimensional partitioning of the available multiparameter radar variables to remotely infer the presence and amount of graupel and hail in convective storms. Consistent with previous studies, we determined that the convective state is closely related to storm electrification. We found that the accumulation of graupel and hail in upper-portions of a storm by a vigorous updraft is highly correlated to the in-cloud lightning flash rate and to the presence of a foul-weather electric field beneath the storm (i.e., predominately negative charge aloft). Next, we revealed that the subsequent descent of graupel and hail within a weakening updraft, below the height of the inferred negative charge region is associated with cloud-to-ground lightning and a fair weather electric field beneath the storm (i.e., predominately positive charge aloft). Lastly, we demonstrated that the further descent of graupel and hail below the melting level results in a microburst at the surface due to precipitation loading and cooling associated with melting and sub-cloud evaporation.

Based on the research in this thesis and the work of previous investigators, the correlation between the convective state (i.e., updraft strength and three-dimensional precipitation structure) and electrical and lightning characteristics of deep, convective storms appears to be a persistent feature in both the mid-latitudes and the tropics. As a result, remotely sensed lightning and electric field data should add supplemental information to our understanding of global, cloud precipitation structure that is not always available from more conventional means such as infrared or visible satellite imagery.

7.2 Future use of multiparameter radar observations in electrification studies

A key goal in this research was to categorize all available multiparameter radar observables such that a unique determination of graupel and hail amounts in thunderstorms could be made and related to electrification processes. The four-dimensional categorization of Z_h, Z_{dr}, K_{dp}, and $\rho_{hv}(0)$ used in this thesis resulted in graupel and hail volumes which were well correlated to lightning type and frequency and electric field strength and polarity. Even with these four variables, there were still some ambiguities between melting (i.e., wet) graupel and rain in this study. Inclusion of the linear depolarization ratio (LDR) into this partitioning effort would help alleviate these ambiguities and improve the reliability of the algorithm overall. Doviak and Zrnic (1993) and Straka and Zrnic (1993) have proposed a five-dimensional multiparameter radar partitioning scheme to identify bulk hydrometeor types which includes LDR.

The linear depolarization ratio is defined as the ratio of the cross-polar signal power to the co-polar power. During descent, oblate spheroid particles wobble (e.g., falling graupel wobbles; Pflaum et al., 1978), thus producing an increase in the distribution of canting angles and hence an increase in the value of LDR. The values of LDR rise as the particles either become more oblate or their refractive index increases. The linear depolarization ratio in rain is small (-27 to -34 dB) while values for wet graupel usually range from -20 to -25 dB (Doviak and Zrnic, 1993). The discrimination afforded by LDR would provide a much more reliable method of distinguishing wet graupel from rain.

Since the refractive index for dry graupel is small compared to wet or melting graupel, dry graupel has values of LDR which are typically less than -30 dB. This suggests a potential multiparameter radar method to differentiate dry growth conditions from wet growth conditions above the freezing level. If this process occurs on scales of one or more radar gates (say > 150 m), LDR should be able to detect the presence of wet growth graupel. This would be very useful in investigating the current controversy over the non-inductive charging behavior of wet growth graupel. Williams et al. (1991; 1994) suggest that wet growth graupel would charge positively during collisions with ice crystals and propose that the lower positive charge observed in thunderstorms could be caused by the transition of graupel from dry growth to wet growth as the graupel particles descend toward the melting level. On the other hand, Saunders and Brook (1992) found that graupel particles in wet growth experience no charging during ice crystal collisions which they attributed to the complete capture of ice crystals. The presence of enhanced LDR (-20 to -25 dB) associated with graupel above the freezing level that is correlated with either a fair weather electric field or positive CG lightning beneath the thunderstorm could be considered evidence in support of the hypothesis of Williams et al. (1991; 1994).

Another worthy research effort is to extend the results of this study to different types of electrified clouds. The four-dimensional partitioning accomplished in this thesis is specific to mid-latitude deep convection. To extend this method to the stratiform regions of mid-latitude (or tropical) mesoscale convective systems (MCS) or to the convective regions of tropical or oceanic convection, significant alterations may be required. Using four polarimetric radar observables [Z_h, Z_{dr}, K_{dp}, and $\rho_{hv}(0)$], a one-dimensional cloud model, and aircraft observations, Zrnic et al. (1993b) inferred the presence of aggregates, graupel, and supercooled liquid water in the stratiform region of a MCS. These inferred conditions could be favorable for the local generation of charge within the stratiform region via the non-inductive charging mechanism (e.g., Engholm et al., 1990; Rutledge et al., 1990). Additional polarimetric radar observations, electrical observations, and cloud

modeling of MCSs would be useful in supporting the above conclusions of Zrnic et al. (1993a) and the in-situ charge generation mechanism for the electrification of the stratiform region of MCSs proposed by Rutledge et al. (1990) and Rutledge and Petersen (1994).

Perhaps the most important goal in any future research involving the identification of bulk-hydrometeor types using multiparameter radar data should be the pursuit of an extensive verification program. Ideally, this would consist of the in-situ measurement of particle phases, sizes, shapes, and fall behavior and the simultaneous scanning of the same cloud volume with a multiparameter radar. This would be possible for stratiform precipitation regions and the initial development of convective cells. However, in-situ sampling is usually not possible in regions of active, deep convection. As a result, the combined modeling of kinematic and microphysical fields with a coupled electromagnetic backscatter model would be necessary to effectively verify the method presented in this thesis. Bringi et al. (1986b) successfully accomplished a verification effort of this sort with a rigorous computation of Z_h, Z_{dr}, and LDR using an electromagnetic model that was coupled to a one-dimensional microphysical model of melting graupel. In order to properly model some of the precipitation features in this thesis, a more sophisticated model would probably be necessary such as the application of a three dimensional, explicit microphysical model coupled to an electromagnetic backscatter model.

REFERENCES

Armijo, L., 1969: A theory for the determination of wind and precipitation velocities with Doppler radar. *J. Atmos. Sci.*, **26**, 570-573.

Atlas, D., R. C. Srivastava, and R. S. Sekhon, 1973: Doppler radar characteristics of precipitation at vertical incidence. *Rev. Geophys. Space. Phys.*, **2**, 1-35.

Avila, E. E., and G. M. Caranti, 1991: Charge transfer during individual collisions in ice growing by riming, paper presented at International Aerospace and Ground Conference on Lightning and Static Electricity, IAMAP, Cocoa Beach, 109A1-109A14.

—, and —, 1992: A laboratory study of static charging by fracture in ice growing by riming, in *Proceedings of the Ninth Int. Conf. on Atmospheric Electricity,* A. I. Voyeykov Geophysical Observatory, St. Petersburg, Russia, 100-103.

Aydin, K., T. A. Seliga, and V. N. Bringi, 1984: Differential radar scattering properties of model hail and mixed phase hydrometeors. *Radio Sci.*, **19**, 58-66.

—, —, V. Balaji, 1986: Remote sensing of hail with a dual linear polarization radar. *J. Climate Appl. Meteor.*, **25**, 1475-1484.

—, Y. Zhao, and T. A. Seliga, 1990: A differential reflectivity radar hail measurement technique: Observations during the Denver hailstorm of 13 June 1984. *J. Atmos. Oceanic Technol.*, 7, 104-113.

Baker, M. B., and J. G. Dash, 1989: Charge transfer in thunderstorms and the surface melting of ice. *J. of Crys. Growth,* **97,** 770-776.

—, and —, 1994: Mechanism of charge transfer between colliding ice particles in thunderstorms. *J. Geophys. Res.*, **99,** 10621-10626.

Balakrishnan, N., and D. S. Zrnic', 1990a: Estimation of rain and hail rates in mixed-phase precipitation. *J. Atmos. Sci.*, **47**, 565-583.

—, and —, 1990b: Use of polarization to characterize and discriminate large hail. *J. Atmos. Sci.*, **47**, 1525 - 1540.

Battan, L. J., 1973: *Radar Observations of the Atmosphere.* Univ. Chicago Press, Chicago, Illinois, 324 pp.

Beard, D. V., and D. Chuang, 1987: A new model for the equilibrium shape of raindrops. *J. Atmos. Sci.*, **44,** 1509-1524.

Beard, K. V. K., and H. T. Ochs, 1986: Charging mechanisms in clouds and thunderstorms, in *The Earth's Electrical Environment*, Washington D. C., National Academy Press, 114-130..

Bergeron, T, 1935, On the physics of clouds and precipitation, *Proc. 5th Assembly UGGI, Lisbon* **2**, 156.

Biggerstaff, M. I., and R. A. Houze, Jr., 1993: Kinematics and microphysics of the transition zone of the 10-11 June 1985 squall line. *J. Atmos. Sci.*, **50,** 3091-3110.

Biron, P. J., and M. A. Isaminger, 1989: An analysis of microburst characteristics related to automatic detection from Huntsville, Alabama and Denver, Colorado. Preprints, 24th Conference on Radar Meteorology, Tallahassee, Florida, 269 - 273.

Bluestein, H. B., and M. H. Jain, 1985: Formation of mesoscale lines of precipitation: Severe squall lines in Oklahoma during the spring. *J. Atmos. Sci.*, **42,** 1711-1732.

—, 1993: *Synoptic-Dynamic Meteorology in Midlatitudes, Vol II, Observations and Theory of Weather Systems.* Oxford University Press, New York, 594 pp.

Brady, R. H., and E. Szoke, 1988: The landspout - A common type of northeast Colorado tornado. Preprints, 15th Conf on Severe Local Storms, Baltimore, Amer. Meteor. Soc., 312-315.

Bringi, V. N., T. A. Seliga, and K. Aydin, 1984: Hail detection using a differential reflectivity radar. *Science,* **225**, 1145-1147.

—, J. Vivekanandan, and J. D. Tuttle, 1986a: Multiparameter radar measurements in Colorado convective storms. Part II: Hail detection studies. *J. Atmos. Sci.*, **43,** 2564- 2577.

—, R. M. Rasmussen, and J. Vivekanandan, 1986b: Multiparameter radar measurements in Colorado convective storms. Part I: Graupel melting studies. *J. Atmos. Sci.*, **43,** 2 545-2563.

—, V. Chandrasekar, P. Meischner, J. Hubbert, and Y. Golestani, 1991: Polarimetric radar signatures of precipitation at S- and C-bands. *IEE Proceedings-F,* **138**, No. 2, 109-119.

—, I. J. Caylor, J. Turk, and L. Liu, 1993: Microphysical and electrical evolution of a convective storm using multiparameter radar and aircraft data during CaPE. *Preprints, 26th Conf. Radar Meteor.* Norman, Oklahoma, Amer. Meteor. Soc., 312-314.

—, L. Liu, P. C. Kennedy, V. Chandrasekar, and S. A. Rutledge, 1994: Dual multiparameter radar observations of intense convective storms: The 24 June 92 case study. *J. Meteor. and Atmos. Phys.*, (accepted).

Browning, K. A., and T. W. Harrold, 1970: Air motion and precipitation at a cold front. *Quart. J. Roy. Meteor. Soc.*, **96,** 369-389.

—, and G. B. Foote, 1976: Airflow and hail growth in supercell storms and some implications for hail suppression. *Quart. J. Roy. Meteor. Soc.*, **102,** 499-533.

Byrne, G. J., A. A. Few, M. F. Stewart, A. C. Conrad, and R. L. Torczon, 1987: In situ measurement and radar observations of a severe storm: Electricity, kinematics, and precipitation. *J. Geophys. Res.*, **92,** 1017-1031.

Caracena, F., J. McCarthy and J. Flueck, 1983: Forecasting the likelihood of microbursts along the front range of Colorado. *Preprints, 13th Conf. on Severe Local Storms*, Tulsa, Amer. Meteor. Soc., 262-264.

Caranti, J. M., A. J. Illingworth, and S. J. Marsh, 1985: The charging of ice by differences in contact potential, *J. Geophys. Res.*, **90,** 6041-6046.

Carbone, R. E., 1982 A severe frontal rainband. Part I: Stormwide hydrodynamic structure. *J. Atmos. Sci.*, **39**, 258-279.

Caylor, I. C., and A. J. Illingworth, 1987: Radar observations and modeling of warm rain initiation. *Quart. J. Roy. Meteor. Soc.*, **113,** 1171-1191.

Chandrasekar, V., and V. N. Bringi, 1988: Error structure of multiparameter radar and surface measurements of rainfall, Part 1: Differential Reflectivity. *J. Atmos. Oceanic Technol.*, **5,** 783-795.

—, V. N. Bringi, N. Balakrishnan, and D. S. Zrnic′, 1990: Error structure of multiparameter radar and surface measurements of rainfall. Part III: Specific differential phase. *J. Atmos. Oceanic Technol.*, **7**, 621-629.

Chauzy, S. M. Chong, A Delannoy, and S Desipiau, 1985 The June 22 tropical squall line observed during COPT '81 experiment: Electrical signature associated with dynamical structure and precipitation. *J. Geophys. Res.*, **90,** 6091-6098

Church, C. R., 1966: The electrification of hail, Ph.D. thesis, Univ. of Durham, England.

Clarence, N. D., and D. J. Malan, 1957: Preliminary discharge processes in lightning flashes to ground. *Q. J. R. Meteorol. Soc.*, **83**, 161-172.

Conway, J. W., and D. S. Zrnic′, 1993: A study of embryo production and hail growth using dual-Doppler and multiparameter radars. *Mon. Wea. Rev.*, **121**, 2511-2528.

Cotton, W. R., and R. A. Anthes, 1989: *Storm and cloud dynamics, Academic Press, Inc., 883 pp.*

Cressman, G. P., 1959: An operational objective analysis system. *Mon. Wea. Rev.*, **87**, 367-374.

Davies-Jones, R. J., 1979: Dual-Doppler radar coverage area as a function of measurement accuracy and spatial resolution. *J. Appl. Meteor*, **9**, 1229-1233.

Doswell, C. A., 1980: Synoptic-scale environments associated with high plains severe thunderstorms. *Bull. Amer. Soc.*, **61**, 1388-1400.

Doviak, R. J., P. S. Ray, R. G. Strauch, and L. J. Miller, 1976: Error estimation in wind fields derived from dual-Doppler radar measurement. *J. Appl. Meteorol.*, **15**, 868-878.

—, and D. S. Zrnic′, 1993: *Doppler Radar and Weather Observations*, 2nd Ed., San Diego, CA, Academic Press, 562 pp.

Dye, J. E., C. A. Knight, V. Toutenhoofd, and T. W. Cannon, 1974: The mechanism of precipitation formation in northeastern Colorado cumulus: III. Coordinated microphysical and radar observations and summary. *J. Atmos. Sci.*, **31**, 2152-2159.

—, J. J. Jones, W. P. Winn, T. A. Cerni, B. Gardiner, D. Lamb, R. L. Pitter, J. Hallett, and C. P. R. Saunders, 1986: Early electrification and precipitation development in a small isolated Montana cumulonimbus, *J. Geophys. Res.*, **91**, 1231-1247.

—, J. J. Jones, A. J. Weinheimer, and W. P. Winn, 1988: Observations within two regions of charge during initial thunderstorm electrification., *Q. J. R. Meteorol. Soc.*, **14**, 1271-1290.

—, W. P. Winn, J. J. Jones, and D. W. Breed, 1989: The electrification of New Mexico thunderstorms 1. Relationship between precipitation development and the onset of electrification. *J. Geophys. Res.*, **94**, 8643-8656.

Elster, J., and H. Geital, 1913: Zur Influenztheorie der Niederschlagselek-trizitat. *Phys. Z.*, **14**, 1287.

Engholm, C. D., E. R. Williams, and R. M. Dole, 1990: Meteorological and electrical conditions associated with positive cloud-to-ground lightning. *Mon. Wea. Rev.*, **118**, 470-487.

Fankhauser, C. J., I. R. Paluch, W. A. Cooper, D. W. Breed, and R. E. Rinehart, 1982: Air motion and thermodynamics, Chap. 6 in *Hailstorms of the Central Hail Plains, Vol. I,* The National Hail Research Experiment. C. A. Knight and P. Squires, Eds. 280 pp.

Findeisen, W., 1940: Uber die Entstehung der Gewitterelektrizitat, *Meteorol. Z.*, **57,** 201.

Foote, G. B., 1985: Aspects of cumulonimbus classification relevant to the hail problem. *J. Rech. Atmos.*, **19,** 61-74.

Fujita, T. T., R. M. Wakimoto, 1983: Microbursts in JAWS depicted by Doppler radars, PAM, and aerial photographs. *Preprints, 21st Conf. on Radar Meteorology,* Edmonton, Amer. Meteor. Soc., 638-645.

Gaskell, W., A. J. Illingworth, J. Latham, and C. B. Moore, 1978: Airborne studies of electric fields and the charge and size of precipitation elements in thunderstorms, *Q. J. R. Meteorol. Soc.*, **112**, 149-163.

—, 1979: Field and laboratory studies of precipitation charge. Ph.D. Thesis, Univ. of Manchester.

—, and A. J. Illingworth, 1980: Charge transfer accompanying individual collisions between ice particles and its role in thunderstorm electrification. *Q. J. R. Meteorol. Soc.*, **106,** 841-854.

Golestani, Y., V. Chandrasekar, and V. N. Bringi, 1989: Intercomparison of multiparameter radar measurements. *Proc. 24th Conf. Radar Meteorology,* Tallahassee, FL, Amer. Meteor. Soc., 309-314.

Goodman, S. J., D. E. Buechler, P. D. Wright, and W. Rust 1988: Lightning and precipitation history of a microburst-producing storm. *Geophys. Res. Let.*, **15**, 1185-1188.

—, Raghavan, S., 1993: Investigating the relation between precipitation and lightning using polarimetric radar observations. *Preprints, 26th Conf. Radar Meteor.* Norman, Oklahoma, Amer. Meteor. Soc., 793 - 795.

Hane, C. E., 1986: Extratropical squall lines and rainbands. Chap. 16 of *Mesoscale Meteorology and Forecasting,* ed. Peter S. Ray, Amer. Meteor. Soc., 359-389.

von Helmholtz, H., 1886: Uber discontinuirliche Flussigkeitsbewegungen, *Berlin Akad Monastber.*

Herzegh, P. H., and R. E. Carbone, 1984: The influence of antenna illumination function characteristics on differential reflectivity measurements. Preprints, *22d Radar Meteor. Conf.*, Zurich, Switzerland, Amer. Meteor. Soc., 281-286.

——, and A. R. Jameson, 1992: Observing precipitation through dual-polarization radar measurements. *Bull. Amer. Meteor. Soc.*, **73**, 1365-1374.

Heymsfield, A. J., 1978: The characteristics of graupel particles in northeastern Colorado cumulus congestus clouds. *J. Atmos. Sci.*, **35**, 284-295.

Hjelmfelt, M. R., H. D. Orville, R. D. Roberts, J. P. Chen, and F. J. Kopp, 1989: Observational and numerical study of a microburst line-producing storm. *J. Atmos. Sci.*, **46**, 2731-2743.

Hobbs, P. V., 1974: *Ice Physics*. Oxford Press, Bristol. 837 pp.

——, O. G. Persson, 1982: The mesoscale and microscale structure and organization of clouds and precipitation in midlatitude cyclones. Part V The substructure of narrow cold-frontal rainbands. *J Atmos. Sci.*, **39,** 280-295.

Holden, D. N., C. R Holmes, C. B. Moore, W. P. Winn, J. W. Cobb, J. E. Griswald, and D. M. Lytle, 1983: Local change concentrations in thunderclouds. *Proceedings in Atmospheric Electricity.* L. H. Ruhnke , L. Latham, and A. Deepak, eds, Hampton, VA.

Hubbert, J., V. Chandrasekar, V. N. Bringi, P. Meischner, 1993: Processing and interpretation of coherent dual-polarized radar measurements. *J. Atmos. Oceanic Technol.*, **10,** 155-164.

Illingworth, A. J., and J. Latham, 1977: Calculations of electric field structure and charge distributions in thunderstorms. *Q. J. R. Meteorol. Soc.*, **103,** 281-295.

——, J. W. F. Goddard, and S. M. Cherry, 1987: Polarization radar studies of precipitation development in convective storms. *Q. J. R. Meteorol. Soc.*, **113**, 469-489.

Jacobson, E. A., and E. P. Krider, 1976: Electrostatic field changes produced by Florida lightning. *J. Atmos. Sci.*, **33,** 103-117.

Jameson, A. R., 1985: Microphysical interpretation of multiparameter radar measurements in rain. Part III: interpretation and measurement of propagation

differential phase shift between orthogonal linear polarizations. *J. Atmos. Sci*, **42**, 607-614.

Jayaratne, E. R., C. P. R. Saunders, and J. Hallet, 1983: Laboratory studies of the charging of soft hail during ice crystal interactions. *Q. J. R. Meteorol. Soc.*, **109**, 609-630.

Karr, T. W., and R. L. Wooten, 1976: Summer radar echo distribution around Limon, Colorado. *Mon. Wea. Rev.*, **104**, 728-734.

Keith, W. D., and C. P. R. Saunders, 1989: Charge transfer during multiple large ice-crystal interactions with a riming target. *J. Geophys. Res.*, **94**, 13,103-13,106.

—, and —, 1990: Further laboratory studies of the charging of graupel during ice crystal interactions, *Atmos. Res.*, **25**, 445-464.

Kessinger, C. J., 1983: An Oklahoma squall line: A multiscale observational and numerical study. M.S. thesis, University of Oklahoma, Norman 211pp.

—, P. S. Ray, and C. E. Hane, 1983: An Oklahoma squall line: A multiscale observational and numerical study. CIMMS Report No. 34, University of Oklahoma, Norman , 211 pp.

Kitigawa, N., and K. Michimoto, 1994: Meteorological and electrical aspects of winter thunderclouds. *J. Geophys. Res.*, **99**, 10713-10721.

Krehbiel, P. R., M. Brook, and R. A. McCrory,1979: An analysis of the charge structure of lightning discharges to ground, *J. Geophys. Res.*, **84**, 2432-2456.

—, 1981: An analysis of the electric field change produced by lightning, PhD thesis, Univ. Manchester, England

—, M. Brook, S. Khanna-Gupta, C. L. Lennon, and R. Lhermitte, 1984: A comparative study of the initial sequence of lightning in a small Florida thunderstorm, *Proc. VII International Conference on Atmospheric Electricity,* Amer. Meteor. Soc., 388-393.

—, 1986: The electrical structure of thunderstorms, in *The Earth's Electrical Environment*, Washington D. C., National Academy Press, 90-113.

Knight C. A., and N. C. Knight, 1970: Falling behavior of hailstones. *J. Atmos. Sci.*, **27**, 672-681.

—, W. A. Cooper, D. W. Breed, I. R. Paluch, P. L. Smith, and G. Vali, 1982: Microphysics, Chap.7 in *Hailstorms of the Central Great Plains,* Vol 1., The National Hail Experiment, C. A. Knight, and P. Squires, Eds., 280pp.

—, W. D. Hall, and P. M. Roskowski, 1984: Visual cloud histories related to first radar echo formation in northeast Colorado cumulus. *J. Climate Appl. Meteor.*, **22,** 1022-1040.

Krider, E. P., R. C. Noggle, and M. A. Uman, 1976: A gated, wideband magnetic direction finder for lightning return strokes. *J. Appl. Meteor.*, **15**, 301-306.

Langleben M. P., and K. L. S. Gunn, 1952: Scattering and absorption of microwaves by a melting ice sphere. Sci. Rept. MW-5. Montreal: Stormy Weather Group, McGill Univ.

Latham, J., 1963: The electrification of frost deposits, *Q. J. R. Meteorol. Soc.*, **89,** 265-270.

—, 1981: The electrification of thunderstorms, *Q. J. R. Meteorol. Soc.*, **107,** 277-298.

Leitao, M. J., and Watson, P. A., 1984: Application of dual linearly polarized radar data to prediction of microwave path attenuation at 10-30 GHz. *Radio Science,* **19,** 209-221.

Lhermitte, R. M., and P. R. Krehbiel, 1979: Doppler radar and radio observations of thunderstorms. *IEEE Trans. Geosci. Electron.*, **GE-17(4)**, 162-171.

—, and E. R. Williams, 1984: Doppler radar and electrical activity observations of a mountain thunderstorm. *Preprints, 22nd Conf. on Radar Meteorology*, Amer. Meteor. Soc., Zurich, Switzerland.

—, and —, 1985: Thunderstorm electrification: A case study. *J. Geophys. Res.*, **90**, 6071-6078.

List, R., 1985: Properties and growth of hailstones. In *Thunderstorm Morphology and Dynamics,* Ed Kessler, ed., University of Oklahoma press, Norman Oklahoma. 259-276

López, R. E., and R. L. Holle, 1986: Diurnal and spatial variability of lightning activity in northeastern Colorado and central Florida during the summer. *Mon. Wea. Rev.*, **114**, 1288-1312.

MacGorman, D. R., D. W. Burgess, V. Mazur, W. D. Rust, W. L. Taylor, and B. C. Johnson, 1989: Lightning rates relative to tornadic storm evolution on 22 May 1981, *J. Atmos. Sci.*, **46**, 221-250.

—, and K. E. Nielsen, 1991: Cloud-to-Ground lightning in a tornadic storm on 8 May, 1986. *Mon Wea. Rev.*, **119,** 1557-1574.

Maddox, R. A., F. Canova, and L. E. Hoxit, 1980: Meteorological characteristics of flash rate flood events over the Western United States. *Mon. Wea. Rev.*, **108,** 1866-1877.

Maier, L. M., and E. P. Krider, 1986 The charges that are deposited by cloud-to-ground lightning in Florida. *J. Geophys. Res.*, **91**, 13275-13289.

Malan, D.J., 1952: Les décharges dans l'air et la charge inférieure positive d'un nuage orageux, *Ann. Geophys.*, **8**, 385-401.

Markson, R., and B. Anderson, 1987: The influence of space charge on ground level electric fields under thunderclouds at Kennedy Space Center. *Eos Trans. AGU,* **68,** 1218.

Marshall, T. C., and W. P. Winn, 1982: Measurements of charged precipitation in a New Mexico thunderstorm: Lower positive charge centers. *J. Geophys. Res.*, **87,** 7141-7157.

—, 1985: A thunderstorm sounding of precipitation charges and electric field, *Eos. Trans. AGU,* **66**, 840.

—, and W. D. Rust, 1991: Electric filed soundings through thunderstorms, *J. Geophys. Res.*, **96,** 22297-22306.

Matejka, T. J., R. A. Houze, Jr., and P. V. Hobbs, 1980: Microphysics and dynamics of clouds associated with mesoscale rainbands in extratropical cyclones. *Q. J. R. Meteorol. Soc.*, **106,** 29-56.

Matson, R. J., and A. W. Huggins, 1980: The direct measurement of the sizes, shapes and kinematics of falling hailstones. *J. Atmos. Sci.*, **37** 1107-1125.

Moore, C. B., 1976: Reply to "Further comments on Moore's criticisms of precipitation theories of thunderstorm electrification," *Q J. R. Meteorol. Soc.*, **102,** 935-939.

—, and B. Vonnegut, 1977: The thundercloud, in *Lightning, Vol. 1,* R. H. Golde, ed., New York, Academic Press, 51-98.

—, 1977: An assessment of thunderstorm electrification mechanisms, in *Electrical Processes in Atmospheres,* pp. 333-352, Stenkipff, Darmstadt.

—, W. P. Winn, and A. S. Cooper, 1983: The effect of transport time delays on convective cloud electrification, in *Proceedings in Atmospheric Electricity*, edited by L. H. Ruhnke and J. Latham, pp 267-276, A. Deepak, Hampton, Va.

Mohr, C. G., and L. J. Miller, 1983: A software package for Cartesian space editing, synthesis and display of radar fields under interactive control. Preprint, 21st Conf on Radar Meteorology, Edmonton, Alberta, Amer. Meteor. Soc., 569-574.

Nelson, S. P., and R. A. Brown, 1982: Multiple Doppler radar derived vertical velocities in thunderstorms. NOAA Tech. Memo. ERL NSSL-94, 21 pp.

—, and —, 1987: Error sources and accuracy of vertical velocities computed from multiple-Doppler radar measurements in deep convective storms. *J. Atmos. Oceanic Technol.*, **4**, 233-238.

Oguchi, T., 1983: Electromagnetic wave propagation and scattering in rain and other hydrometeors. Proc. IEEE, **71**, 1029-1078.

Oye, R., and R. E. Carbone, 1981: Interactive Doppler editing software. *Proc. 20th Conf. Radar Meteorology*, Boston, Amer. Meteor. Soc., 683-689.

Petersen, W. A., S. A. Rutledge, D. J. Boccipio, and E. R. Williams, 1993: The electrification of tropical oceanic convective clouds observed during TOGA COARE. *Severe Local Storms, St. Louis, Missouri.* 796-802.

Pflaum, J. C., J. J. Martin, and H. R. Pruppacher, 1978: A wind tunnel investigation of the hydrodynamic behavior of growing, freely falling graupel. *Q. J. R. Meteorol. Soc.*, **104,** 179 - 187.

Pflaum, J. C., and H. R. Pruppahcer, 1979: A wind tunnel investigation of the growth of graupel initiated from frozen drops. *J. Atmos. Soc.*, **36,** 680-689.

—, J. J. Martin, and H. R. Pruppahcer, 1978: A wind tunnel investigation of the hydrodynamic behavior of growing, freely falling graupel. *Q. J. R. Meteorol. Soc.*, **104,** 179-187.

Price, C., and D. Rind, 1993: What determines the cloud-to-ground lightning fraction in thunderstorms? *Geophys. Res. Letters.*, **20**, 463-466.

Pruppacher, H. R., and K. V. Beard, 1970: A wind tunnel investigation of the internal circulation and shape of water drops falling at terminal velocity in air. *Quart. J. Roy. Meteor. Soc.*, **96**, 247-256.

—, and J. D. Klett, 1978, *Microphysics of Clouds and Precipitation.* D. Reidel Publishers, Dordrecht, 714 pp.

Rasmussen, R. M., V. Levizzani, and H. R. Pruppacher, 1984: A wind tunnel and theoretical study on the melting behavior of atmospheric ice particles: III. Experiment and Theory for Spherical Ice Particles of Radius > 500 μ m. *J. Atmos. Sci.*, **41,** 381-388.

Rawlins, F., 1982: A numerical study of thunderstorm electrification using a three dimensional model incorporating the ice phase. *Q J R Meterol. Soc.*, **108,** 779-800.

Raymond, D. J., and A. M. Blyth, 1989: Precipitation development in a New Mexico thunderstorm. *Q. J. R. Meteorol. Soc.*, **115**, 1397-1423,

Reynolds, S. E., M. Brook, and M. F. Gourley, 1957: Thunderstorm charge separation, *J. Meteorol.*, **14**, 426-436.

Roberts, R. D., and J. W. Wilson, 1984: Precipitation and kinematic structure of microburst producing storms. *Preprints, 22nd Conf. on Radar Meteorology,* Zurich, Amer. Meteor. Soc., 71-76.

Rutledge, S. A., R. A. Houze, Jr., M. I. Biggerstaff, and T. Matejka, 1988: The Oklahoma-Kansas Mesoscale Convective System of 10- 11 June 1985: Precipitation structure and single-Doppler radar analysis, *Mon. Wea. Rev.*, **116,** 1409-1430.

—, C. Lu, and D. MacGorman, 1990: Positive Cloud-to-Ground Lightning in Mesoscale Convective Systems, *J. Atmos. Sci.*, **47,** 2085-2100.

—, V. N. Bringi, E. A. Mueller, D. A. Brunkow, P. C. Kennedy, and K. Pattison, 1991: New capabilities of the CSU-CHILL radar. *Preprints, 25th Conf. on Radar Meteorology,* Paris, Amer. Meteor. Soc., 852-854.

—, E. R. Williams, and T. D. Keenan, 1992: The Down Under Doppler and Electricity Experiment (DUNDEE): Overview and preliminary results. *Bull. Amer. Meteorol. Soc.*, **73,** 3-16.

—, and W. A. Petersen, 1994: Vertical radar reflectivity structure and cloud-to-ground lightning in the stratiform region of MCSs: Further evidence for in-situ charging in the stratiform region. *Mon. Wea. Rev.*, Special issue on thunderstorm electrification, in press.

Rydock, J. R., and E. R. Williams, 1991: Charge separation associated with frost growth, *Q. J. R. Meteor. Soc.*, **117,** 409-420.

Sachidananda, M., and D. S. Zrnic', 1985: Z_{dr} measurement considerations for a fast scan capability radar. *Radio Sci.*, **20**, 907-922.

—, and —, 1986: Differential propagation phase shift and rainfall rate estimation. *J. Atmos. Oceanic Tech.*, **4**,

—, and —, 1987: Rain rate estimates from differential polarization measurements. *J. Atmos. Oceanic Technol.*, **4**, 588-598.

Saunders, C. P. R., W. D. Keith and R. P. Mitzeva, 1991: The effect of liquid water on thunderstorm charging. *J. Geophys. Res.*, **96**, 11007-11017.

—, and I. M. Brooks, 1992: The effects of high liquid water content on thunderstorm charging, *J. Geophys. Res.*, **97**, *14671-14676.*

—, 1993: Reply, *J. Geophys. Res.*, **98**, 10823-10825.

—, M. Hickson, M. D. Malone, and J. von Richtofen, 1993: Charge separation during the fragmentation of rime and frost. *Atmos. Res.*, **29**, 261-270.

—, 1994: Thunderstorm electrification laboratory experiments and charging mechanisms. *J. Geophys. Res.*, **99**, 10773-10779.

Seimon, A., 1993: Anomalous cloud-to-ground lightning in an F5-tornado-producing supercell thunderstorm on 28 August 1880, *Bull. Amer. Meteor. Soc.*, **74**, 189-203.

Seliga, T. A., and V. N. Bringi, 1976: Potential use of differential reflectivity measurements at orthogonal polarizations for measuring precipitation. *J. Appl. Meteor.*, **15**, 69-76.

Selvam, A. M., R. Vijayakumar, G. K. Manohar, and A. S. R. Murty, 1991: Electrical, microphysical, and dynamical observations in summer monsoon clouds. *Atmos. Res.*, **26**, 19-32.

Simpson, J. E., 1987: *Gravity Currents in the Environment and the Laboratory.* John Wiley and Sons, New York, 244 pp.

Simpson, G. C., and F. J. Scrase, 1937: The distribution of electricity in thunderclouds, *Proc. R. Soc. London, Ser. A, 161, 309-352.*

Smull, B. F., and R. A. Houze, Jr., 1985: A mid-latitude squall line with a trailing region of stratiform rain: Radar and satellite observations. *Mon. Wea. Rev.*, **113**, 117-133.

Solberg, H., 1930: *Verhandl. III Intern. Kongr. tech. Mechanik,* Stockholm

Srivastava, R. C., 1987: A model of intense downdrafts driven by the melting and evaporation of precipitation. *J. Atmos. Sci.*, **44**, 1752-1773.

Standler, R. B. and W. P. Winn, 1979: Effects of corona on electric fields beneath thunderstorms, *Q. J. R. Meteorol. Soc.*, **105,** 285-302.

Straka, J. M., and D. S., Zrnic' 1993: An algorithm to deduce hydrometeor types and contents from multiparameter radar data. *Preprints, 26th Conf. Radar Meteor.* Norman, Oklahoma, Amer. Meteor. Soc., 513-515.

Takahashi, T., 1978: Riming electrification as a charge generation mechanism in thunderstorms. *J. Atmos. Soc.*, **35**, 1536-1548.

Toth, J. J., and R. H. Johnson, 1985: Summer surface flow characteristics over northeast Colorado. *Mon. Wea. Rev.*, **113,** 1558-1649.

Tuttle, J. D., V. N. Bringi, H. D. Orville and F. J. Kopp, 1989: Multiparameter radar study of a microburst: Comparison with model results. *J. Atmos. Soc.*, **46**, 601-620.

Uman, M. A., 1987: *The Lightning Discharge.* Academic Press, Orlando, FL. 377 pp.

Vali, G., J. Cupal, C. P. R. Saunders, and W. P. Winn, 1984: Airborne measurements of the electrical charges of hydrometeors, *Proc. Int. Cloud Phys. Conf. Tallinn,* **9**, 751-754.

Vasiloff, S. V., E. A. Brandes, R. P. Davies-Jones, and P. S. Ray, 1986: An investigation of the transition from multicell to supercell storms. *J Clim. and Appl. Meteorol.*, **25,** 1022-1036.

Vonnegut, B., 1953: Possible mechanism for the formation of thunderstorm electricity, *Bull. Am. Meteorol. Soc.*, **34**, *378-381.*

—, 1963: Some facts and speculations concerning the origin and role of thunderstorm electricity, *Meteorol. Monogr.*, **5,** 224-241.

Wagner, P. B., and J. W. Telford, 1981: Cloud dynamics and an electric charge separation mechanism in convective clouds, *J. Rech. Atmos.*, **15**, 97-120.

Wakimoto, R. M., 1985: Forecasting Dry Microburst activity over the high plains. *Mon. Wea. Rev.*, **113**, 1131-1143.

—, and V. N. Bringi, 1988: Dual-polarization observations of microbursts associated with intense convection: the 20 July storm during the MIST project. *Mon. Wea. Rev.*, **116**, 1521-1539.

—, and J. W. Wilson, 1989: Non-supercell Tornadoes. *Mon. Wea Rev.*, **117,** 1113-1140.

Weber, M. E., M. F. Stewart, and A. A. Few, 1983: Corona point measurements in a thundercloud at Langmuir Laboratory, *J. Geophys. Res.*, **88**, 3907-3910.

Weinheimer, A. J., J. D. Dye, D. W. Breed, M. P. Spowart, J. L. Parrish, T. L. Hoglin, and T. C. Marshall, 1991: Simultaneous measurements of the charge, size,, and shape of hydrometeors in an electrified cloud, *J. Geophys. Res.*, **96,** 20809-20829.

Williams, E. R., and R. M. Lhermitte, 1983: Radar tests of the precipitation hypothesis for thunderstorm electrification. *J. Geophys. Res.*, **88,** 10984-10992.

—, 1985: Large-scale charge separation in thunderclouds. *J. Geophys. Res.*, **90**, 6013-6025.

—, C. M. Cooke, and K. A. Wright, 1985: Electrical discharge propagation in and around space charge clouds, *J. Geophys. Res.*, **90**, 6059-6070.

—, 1989: The tripole structure of thunderstorms. *J. Geophys. Res.*, **94**, 13,151-13,167.

—, M. E. Weber and R. E. Orville, 1989a: The relationship between lightning type and convective state of thunderclouds. *J. Geophys. Res.*, **94**, 13,213-13,220.

—, M. E. Weber and C. D. Engholm, 1989b: Electrical characteristics of microburst-producing storms in Denver. *Proc. 24th Conf. Radar Meteorology,* Tallahassee, FL, Amer. Meteor. Soc., 89-92.

—, 1990: Lightning and microbursts in convective clouds. *Conf. on Atmos. Electricity,* Kananaskis Park, Alta., Canada, Amer. Meteor. Soc., 738-743.

—, R. Zhang, and J. Rydock, 1991: Mixed-phase microphysics and cloud electrification, *J. Atmos. Sci.*, **48**, 2195-2203.

—, and R. Zhang, 1993: Comments on "The Effect of Liquid Water on Thunderstorm Charging" by C. P. R. Saunders et al., *J. Geophys. Res.*, **98**, 10819-10821.

—, R. Zhang, and D. Boccippio, 1994: Microphysical growth state of ice particles and large-scale electrical structure of clouds. *J. Geophys. Res.*, **99**, 10787-10792.

Wilson, C. T. R., 1920: Investigations on lightning discharges and on the electric field of thunderstorms, *Philos. Trans.* A, **221**, 73-115.

Winn, W. P., C. B. Moore, C. R. Holmes, and L. G. Byerley, 1978: Thunderstorm on July 16, 1975, over Langmuir Laboratory: A case study. *J. Geophys Res.*, **83**, 3079-3092.

Workman, E. J., and S. E. Reynolds, 1949: Electrical activity as related to thunderstorm cell growth, *Bull Am Meteorol. Soc.*, **30**, 142-149.

Xiao, R., V. N. Bringi, D. Garbrick, E. A. Mueller and S. A. Rutledge, 1993: Copolar and crosspolar pattern measurement of the CSU-CHILL antenna. *Preprints, 26th Conf. Radar Meteor.* Norman, Oklahoma, Amer. Meteor. Soc., 363-365.

Zeigler, C. L., 1978: "A Dual-Doppler Variational Objective Analysis as Applied to Studies of Convective Storms," NOAA Tech. Memo. ERL NSSL-85. Natl. Severe Storms Lab, Norman Oklahoma.

Zrnic', D. S., V. N. Bringi, N. Balakrishnan, K. Aydin, V. Chandrasekar and J. Hubbert, 1993a: Polarimetric measurements in a severe hailstorm. *Mon. Wea. Rev.*, **121**, 2223-2238.

——, N. Balakrishnan, C. L. Ziegler, V. N. Bringi, K. Aydin and T. Matejka, 1993b: Polarimetric signatures in the stratiform region of a mesoscale convective system. *J. Appl. Meteor.*, **32**, 678-693.

——, R. Raghavan and V. Chandrasekar, 1994: Observations of copolar correlation coefficient through a bright band at vertical incidence. *J. Appl. Meteor.*, **33**, 45-52.